



THE UNIVERSITY
of ADELAIDE

Development and Application of a Method for Gas-phase Temperature Measurements in Particle-laden Flows

ELLIOTT W. LEWIS

School of Mechanical Engineering
The University of Adelaide
Adelaide, Australia

*Thesis submitted in partial fulfillment of the
requirements for the degree of Doctor of Philosophy
in June, 2022.*

Ph. D. Thesis

23rd June 2022

School of Mechanical Engineering
The University of Adelaide
Adelaide, Australia

Typeset by the author using \LaTeX .
Printed in Australia.

Copyright © 2022 Elliott W. Lewis, and The University of Adelaide, Australia.

All right reserved. No part of this report may be used or reproduced in any form or by any means, or stored in a database or retrieval system without prior written permission of the university except in the case of brief quotations embodied in critical articles and reviews.

Abstract

Suspensions of particles in a carrier flow of gas are utilised in, or being developed for, several high-temperature industrial processes. These include for material transformations in calciners and kilns, as fuel in particulate burners and as the medium for radiation absorption in concentrated solar thermal receivers. The efficiency, stability, and emissions from such systems is strongly dependent on the temperature distribution of both the particle and fluid phases, each of which can be highly variable both spatially and temporally. While these systems are widely utilised, there is still a lack of fundamental understanding of the heat transfer processes due to the complexity of turbulent particle-laden flows with a high particle volume fraction. Therefore, this work aims to provide insight into these processes for future optimisation of non-isothermal particle-based systems. This is performed by adapting and applying the technique of laser induced fluorescence (LIF) to measure the gas-phase temperature in a particle-laden flow that is heated using high-flux radiation.

This thesis presents the first demonstration of LIF in the densely loaded conditions present in particle-laden flows relevant to industrial application, with the potential for strong optical interference from elastic scattering of radiation from the excitation laser by particles. The two-colour method for thermometry, with toluene as the fluorescent tracer, was used to provide spatially resolved measurements from a < 1 mm thick planar cross-section of the flow. The particle distribution was measured simultaneously with the temperature by imaging the laser light scattered by particles (particle nephelometry). The accuracy and precision of the two-colour LIF method was assessed for a series of particle materials and diameters, including materials that luminesce following absorption of the excitation laser light. The results show that optical filters effectively suppress the detection of elastically scattered light, with other sources of measurement uncertainty including particle luminescence, laser attenuation, and signal trapping identified and assessed. The systematic error in the measurement from these combined

sources was shown to increase with local particle loading, but be independent of particle diameter.

The two-colour LIF and particle nephelometry methods were applied to simultaneously measure the gas-phase temperature and particle distributions in a particle-laden flow heated using high-flux radiation, evaluated for systematically varied series of particle diameter, particle volumetric loading, and heating power. The measurements were recorded in a particle-laden jet flow issuing from a long, straight pipe with well-defined inlet and co-flow conditions, with the particles heated using an axisymmetric, well-characterised infra-red radiative source generating a beam with a peak flux of up to 42.8 MW/m^2 on the axis. The resulting gas-phase temperature profile increased monotonically with distance down-stream from the start of the heating region, at up to $2,200 \text{ }^\circ\text{C/m}$ on the jet centreline. Additionally, attenuation of the heating beam was shown to lead to an asymmetric temperature profile in the jet flow.

The rate of increase of the gas temperature was shown to be directly proportional to both the heating flux and the time-averaged particle volumetric loading, within the range of conditions investigated. The temperature decreased significantly with an increase in particle diameter, due to the dependence of radiative and convective heat transfer processes to different exponents of the diameter. The experimental results for the temperature rise on the jet centreline were shown to match the trends from a simplified analytical model. Importantly, the model also predicts that the particle temperature is significantly greater than the gas, from the heating region to the edge of the measurement region investigated. The asymmetry of the flow temperature due to attenuation of the heating beam is also shown to increase with an increase in the particle loading and a decrease in the particle diameter (i.e., an increase in the total cross-sectional area of particles in the flow).

The instantaneous distributions of both the gas-phase temperature and particle locations were demonstrated to be highly non-uniform in the radiatively heated particle-laden flow. The particle distributions were analysed using Voronoi diagrams to determine the locations of particle clusters. Void regions (i.e., with no nearby particles) were also identified. The gas-phase temperature around particles was shown to be dependent on the local particle loading, with the measured temperature inside of clusters also greater than that outside of clusters. Localised regions of relatively high or low temperature compared to their surroundings were also identified from the instantaneous images, with these regions shown to remain coherent to the downstream edge of the measurement region. The high temperature regions are shown to be typically associated with regions of high local particle-loading,

while regions with low temperature are shown to be in the void regions or with a low particle loading. These results suggest that the structures in the flow are long-lived with a sufficient particle-gas temperature difference, both within the heating region and in the near-field downstream, for convection between the particles and gas to influence the gas-phase temperature field more significantly than entrainment, mixing, and convection within the gas flows.

Contents

Abstract	i
Contents	iv
Declaration	vii
Acknowledgements	ix
Papers Produced	xi
List of Figures	xiii
List of Tables	xix
Nomenclature	xxi
1 Introduction	1
1.1 Background	1
1.2 Thesis aims	4
1.3 Thesis outline and paper synopses	4
2 Literature Review	9
2.1 Particle-laden flows	9
2.2 Heat transfer equations	13
2.3 Heat transfer in particle-laden flows	17
2.4 Scattering of radiation by particles	23
2.5 Gas-phase temperature measurement of particle-laden flows .	23
2.6 Summary and Research Gaps	31
3 Methods	33
3.1 Wind tunnel and jet	34
3.2 Screw feeder	36

3.2.1	Output flow rate	38
3.2.2	Output steadiness	39
3.2.3	Particle properties	42
3.3	Two-colour toluene LIF	43
3.3.1	Toluene seeding	45
3.4	Experimental arrangements	46
3.4.1	Arrangement for Experiment I	46
3.4.2	Arrangement for Experiment II	50
3.4.3	Spectroscopic measurements	55
3.5	Analytical heat transfer model	56
3.6	Random particle distribution simulation	58
3.7	Two-colour LIF calibration	59
3.8	Image processing	60
3.8.1	LIF	60
3.8.2	Hot and cold region determination	62
3.8.3	Particle loading	65
3.8.4	Particle cluster determination	66
4	Results	69
4.1	Interference to two-colour LIF in a particle-laden flow	69
4.1.1	Spectral emission measurements	70
4.1.2	Measurements of the pre-heated flow without particles	72
4.1.3	Measurements for Experiment I	74
4.1.4	Measurements for Experiment II	78
4.2	Time-averaged measurements of a radiatively heated particle-laden flow	80
4.2.1	Particle number density and velocity measurements	81
4.2.2	Gas-phase temperature measurements	83
4.3	Instantaneous measurements of a radiatively heated particle-laden flow	89
5	Conclusions and recommendation for future work	99
5.1	Conclusions	99
5.2	Recommendation for future work	101
A	Wind tunnel characterisation	103
B	Screw feeder	109
C	Paper I - Luminescence interference to two-colour toluene laser-induced fluorescence thermometry in a particle-laden flow	119

D Paper II - Insights from a new method providing single-shot, planar measurement of gas-phase temperature in particle-laden flows under high-flux radiation	157
E Paper III - The effect of particle size and volumetric loading on the gas temperature distributions in a particle-laden flow heated with high-flux radiation	199
F Paper IV - The effect of instantaneous particle distributions on the gas-phase temperature in an unsteady particle-laden jet heated with high-flux radiation	237
Bibliography	283

Declaration

I certify that this work contains no material which has been accepted for the award of any other degree or diploma in my name, in any university or other tertiary institution and, to the best of my knowledge and belief, contains no material previously published or written by another person, except where due reference has been made in the text. In addition, I certify that no part of this work will, in the future, be used in a submission in my name, for any other degree or diploma in any university or other tertiary institution without the prior approval of the University of Adelaide and where applicable, any partner institution responsible for the joint-award of this degree.

The author acknowledges that copyright of published works contained within the thesis resides with the copyright holder(s) of those works. I also give permission for the digital version of my thesis to be made available on the web, via the University's digital research repository, the Library Search and also through web search engines, unless permission has been granted by the University to restrict access for a period of time.

I acknowledge the support I have received for my research through the provision of an Australian Government Research Training Program Scholarship.

Elliott W. Lewis
23rd June 2022

Acknowledgements

It is only with a great deal of assistance that I have made it to this point, and I would like to gratefully acknowledge the contributions of everyone who has helped me through all aspects of life during the wild ride that has been PhD research.

To my academic supervisors and co-authors, you have often clarified the potential paths forward for me, no matter how murky it seemed to be. Your advice over the years for professional and technical skills have greatly improved the efficiency and quality of my work. To Prof. Gus Nathan, your leadership of not just my project and the two-phase group but the CET as a whole have exemplified the universal goal of research in looking to the future. I am also grateful to A/Prof. Zeyad Alwahabi, for providing the original concept and techniques for my research; to Dr Tim Lau, for always making yourself available to help me work through any issues that occurred in the lab or during the analysis of results and being the first to read, and try to make sense of, most of my drafts; and to Dr Zhiwei Sun, for guiding me through the theory and practice of laser diagnostic techniques and your calm presence in the lab when it seemed that nothing was working.

I would also like to thank the Faculty of ECMS and the School Mechanical Engineering at the University of Adelaide, and all of the workshop staff that I relied on often for design, manufacturing, 3D-printing, plumbing, and electronics. There was always someone available to help with troubleshooting the constant pesky little problems. In particular, I would like to mention Mr Hayden Westell, for his assistance and patience to find solutions for my obscure and complex 3D-printed parts, and to Mr Jason Peak, for his monumental efforts in building most of my second experimental arrangement, modifying the lab to suit, and for being my go-to man for any minor issues.

This journey has been made much more enjoyable over the years because of my friendly officemates and fellow PhD colleagues, who were able to keep all in perspective and provide advice when needed. I greatly enjoyed our (occasionally long) lunches, end of week catch-ups, and weekends away for

discussing all the great issues of the world.

To all my friends away from uni, we have had many great times these past few years and I thank all of you for being there to help me laugh, relax, and escape from the at times all-consuming world of research.

Finally, and most importantly, to my family, for your endless patience and support throughout the journey. Without all you have taught me in life, I would never have made it to this point - hopefully soon I can answer the question of 'when will you get a real job'.

Cheers folks

Papers Produced

Journal papers included in the present thesis by publication.

1. Lewis, E. W., Lau, T. C. W., Sun, Z., Alwahabi, Z. T. and Nathan, G. J. (2020), "Luminescence interference to two-colour toluene laser-induced fluorescence thermometry in a particle-laden flow." *Experiments in Fluids* 61(4): 101.
2. Lewis, E. W., Lau, T. C. W., Sun, Z., Alwahabi, Z. T. and Nathan, G. J. (2021), "Insights from a new method providing single-shot, planar measurement of gas-phase temperature in particle-laden flows under high-flux radiation", *Experiments in Fluids* 62(4).
3. Lewis, E. W., Lau, T. C. W., Sun, Z., Alwahabi, Z. T. and Nathan, G. J. (2022), "The effect of particle size and volumetric loading on the gas temperature distributions in a particle-laden flow heated with high-flux radiation", *International Journal of Heat and Mass Transfer* 182.
4. Lewis, E. W., Lau, T. C. W., Sun, Z., Alwahabi, Z. T. and Nathan, G. J. (2022), "The effect of instantaneous particle distributions on the gas-phase temperature in an unsteady particle-laden jet heated with high-flux radiation", *International Journal of Multiphase Flow* 153.

Conference papers relevant to, but not included in this thesis.

1. Lewis, E. W., Lau, T. C. W., Sun, Z., Nathan, G. J. and Alwahabi, Z. T. (2018). "Gas-phase temperature measurement of particle-laden jets." *Proceedings of the 11th Australasian Heat and Mass Transfer Conference*. RMIT University, Melbourne, Australia.
2. Lewis, E. W., Lau, T. C. W., Sun, Z., Nathan, G. J. and Alwahabi, Z. T. (2018). "Effect of Particle Loading on Interference in Planar Laser Induced Fluorescence Thermometry." *Proceedings of the 21st Australian Fluid Mechanics Conference*. T. C. W. Lau and R. M. Kelso. Adelaide, Australia.
3. Lewis, E. W., Lau, T. C. W., Sun, Z., Alwahabi, Z. T. and Nathan, G. J. (2019). "Interference Modes in Laser Induced Fluorescence Thermometry Applied to Particle-Laden Flows." *Proceedings of the Ninth Australian Conference on Laser Diagnostics*. Z. T. Alwahabi and P. R. Medwell. Adelaide, Australia, The University of Adelaide.
4. Extended abstract: Lewis, E. W., Sun, Z., Lau, T. C. W., Alwahabi, Z. T. and Nathan, G. J. (2020). "Simultaneous 2D gas- and particle-phase thermometry with single laser excitation." Submitted to the *International Conference on Phosphor Thermometry*.

List of Figures

2.1	A diagram illustrating the typical dominant heat transfer processes and flow conditions for a particle-laden flow subjected to radiation, such as occurs in a particle-based CST receiver. The background shading represents the local heating flux, and the arrow length of the heat transfer processes indicates their typical relative magnitudes. The subscripts 1 and 2 represent each particle displayed.	14
2.2	Typical molecular energy excitation levels for Rayleigh and Raman scattering. The arrows indicate photons absorbed/emitted. The excited energy levels do not necessarily represent stable molecular energy levels.	26
2.3	Simplified Jablonski diagram for an organic molecule, showing example relaxation mechanisms following electronic excitation. S_0 and S_1 denote the ground and first excited singlet states, respectively while T_1 denotes the first excited triplet state. Note that not all energy levels available for transitions are shown.	29
3.1	The wind tunnel that was designed to provide optically accessible measurements of a particle-laden jet flow.	35
3.2	Diagram of design parameters for the screws used to analyse the particle volumetric flow rate and the steadiness of output from the screw feeder.	37
3.3	Screws that were manufactured to investigate the effect of pitch, core diameter and number of flights on the magnitude and steadiness of the particle mass flow rate.	38
3.4	The acrylic screw feeder assembly and aluminium enclosure used to seed particles into the gas flow.	39
3.5	Time series of Mie scattering intensity from particles in the flow for screws with 1, 2, and 4 flights (a), together with the fast Fourier transform for the same screws (b), normalised by the time-averaged mean.	41

3.6	The normalised fluorescence emission spectra of toluene following 266 nm excitation for a series of temperatures together with example wavelength bands λ_1 and λ_2 used for two-colour LIF thermometry, denoted using the shaded regions (the emission spectra data are adapted from Faust et al. [107]).	45
3.7	Schematic diagram of the bubbler manufactured to seed toluene in flows. The view is sectioned to show internal detail.	46
3.8	Experimental arrangement of the particle-laden jet system used for simultaneous measurements of gas temperature using two-colour LIF and particle number density from Mie scattering.	47
3.9	Combined optical density (OD) as a function of wavelength for all filters used to form each channel for two-colour LIF.	49
3.10	Experimental arrangement of the radiatively heated particle-laden jet used for simultaneous measurements of gas temperature, using two-colour LIF, and of particle number density, using Mie scattering.	51
3.11	Schematic diagram of the measurement region with key co-ordinates and dimensions shown (a) and the axial profile of the heating laser intensity normalised by the peak intensity, I/I_{peak} (b).	53
3.12	The measured volume-weighted particle diameter distribution of the particles used for Experiment II.	54
3.13	Arrangement used to measure the spectral response of the particle materials used (PMMA, ZnO:Zn, alumina) to the 266 nm light used for two-colour LIF.	55
3.14	The simulated temperature from the one-dimensional model of both the particle and gas (a) together with the absolute powers of the modelled particle heat transfer components (b) as a function of axial distance, for the parameters listed in Table ?? with $\bar{d}_p = 173 \mu\text{m}$, $\bar{\phi} = 1.4 \times 10^{-3}$ and $\dot{Q}_0 = 2840 \text{ W}$	57
3.15	Calibration curve relating the two-colour LIF intensity ratio to temperature, together with the fluorescence intensity in each channel.	60
3.16	Simultaneous images from the three channels used in Experiment II, S_{285} , S_{315} and S_{532} , together with the resultant temperature calculated using the two-colour ratio method.	62

- 3.17 Images to illustrate the method used to determine local areas of relative high and low temperature: (a) the instantaneous gas-phase temperature, $T_g - T_a$, (b) the time-averaged temperature, $\bar{T}_g - T_a$, (c) the axial profile of the time- and radially-averaged temperature in the region $|r/D| < 0.3$ after replication into an array across the width of the original image, $\bar{T}_{g,CL}(x) - T_a$, (d) the smoothed normalised temperature increase from ambient, Θ_S , (e) the thresholds used to determine hot and cold regions, $\epsilon_H(x)$ and $\epsilon_C(x)$, respectively, and (f) Θ_S together with the boundaries of the determined hot and cold regions. 64
- 3.18 The binary particle mask from S_{532} (a), the resultant particle centroids together with the calculated Voronoi cells and determined clusters (b), and the void locations (c) for a single image from the case with $\bar{d}_p = 173 \mu\text{m}$ and $\phi = 1.4 \times 10^{-3}$ 67
- 4.1 Normalised spectral response measured from toluene following illumination with 266 nm light for a series of fluences (a). The measured fluorescence intensity for each of the two-colour fluorescence channels together with the intensity ratio I_{315}/I_{285} as a function of toluene concentration (b). The errorbars represent one standard deviation for the measured shot-to-shot intensity and temperature. 71
- 4.2 Spectral response measured from the three particle materials used in Experiment I to illumination with 266 nm light. The wavelengths used to detect the emissions for two-colour LIF thermometry in the presented investigations were in the range 280-325 nm. 72
- 4.3 The axial profile of gas-phase temperatures above ambient ($\Delta T = (T_g - T_a)$) on the jet centreline measured using the two-colour LIF technique, normalised by the jet exit value, for a series of initial temperatures. Also presented are the scalar mixing values presented by Papadopoulos and Pitts [118] (denoted by P&P) for two initial density ratios ρ_e/ρ_∞ , where ρ_e is the density of the jet fluid and ρ_{inf} is the density of the surrounding flow. The inset presents the temperature above ambient measured for the case without heating, ΔT_{dep} 73

4.4	Single-shot images of the particle-laden flow at a series of instantaneous particle loadings for the 20 μm PMMA particles in the unheated jet, for the (i) intensity measured in LIF channel S_{285} , (ii) intensity measured in LIF channel S_{315} , (iii) the temperature difference from the actual ambient value calculated using the LIF ratio (ΔT_{dep}) and (iv) the local particle volumetric loading. The images in row (c) were from the flow with particles but without toluene seeded; note the different colourbar scale for the fluorescence intensities for this case.	76
4.5	Probability density functions of the measured temperature difference from ambient for the unheated flow with 20 μm PMMA particles for a series of instantaneous particle volumetric loadings, calculated in the jet region $ r/D < 0.4$ and $0.55 < x/D < 3$	77
4.6	The difference between the measured temperature and ambient value (ΔT_{dep}) as a function of local particle loading (ϕ) in the unheated jet for the three particle materials investigated. The error bars represent one standard deviation.	78
4.7	Typical instantaneous images from each camera, S_{285} , S_{315} , and S_{532} , together with the temperature calculated from the two-colour LIF ratio, T_g . The top row presents the case without particles and with the heating laser switched on with an output power of $\dot{Q}_0 = 2840$ W. The dotted lines and arrows represent the approximate boundary and direction of the heating laser, respectively. The bottom row presents the case with $\bar{\phi} = 1.4 \times 10^{-3}$ but with the heating laser switched off, with the inset showing the important features of attenuation of the light sheet and signal trapping by particles in greater detail.	80
4.8	Radial profiles of the particle number density normalised by the centreline value measured at $x/D = 1.5$ (a) and $x/D = 3$ (b) for both $r/D > 0$ and $r/D < 0$ for the flow with $\dot{Q}_0 = 0$ and 2840 W, $\bar{d}_p = 173$ μm and $\bar{\phi} = 1.4 \times 10^{-3}$	82
4.9	Radial profiles of the particle velocity normalised by the centreline value measured at $x/D = 1, 2,$ and 3 for the unheated flow and with $\dot{Q}_0 = 2840$ W. For each case, $\bar{d}_p = 173$ μm and $\bar{\phi} = 1.4 \times 10^{-3}$	83
4.10	The time-averaged temperature distributions of the radiatively heated particle-laden jet for a series of heating powers (\dot{Q}_0) with a median particle diameter of $\bar{d}_p = 173$ μm and average particle volumetric loading of $\bar{\phi} = 1.4 \times 10^{-3}$ (top), a series of \bar{d}_p with $\dot{Q}_0 = 2840$ W and $\bar{\phi} = 1.4 \times 10^{-3}$ (middle), and a series of $\bar{\phi}$ with $\dot{Q}_0 = 2840$ W and $\bar{d}_p = 205$ μm	85

4.11	The average rate of gas-phase temperature increase with axial distance on the jet centreline over the region $2 < x/D < 3$ for both the measurements and the one-dimensional model, as a function of heat flux for a series of \bar{d}_p with $\bar{\phi} = 1.4 \times 10^{-3}$ (a) and as a function of volumetric loading for a series of \bar{d}_p with $\dot{Q}_0 = 2840$ W (b).	87
4.12	Comparison of the measured (Meas) and simulated (Sim) power of the SSSTS beam transmitted through the particle-laden flow, normalised by the total beam power, as a function of particle diameter for each volumetric loading investigated. The measured results presented are for the cases with $\dot{Q}_0 = 2840$ W.	88
4.13	Typical instantaneous images of the temperature calculated from the two-colour LIF ratio, the fluorescence intensity in the channel S_{285} and the binary particle mask for each particle size investigated with $\phi = 1.4 \times 10^{-3}$ and $\dot{Q}_0 = 2840$ W. Also presented is a reference case with the heating laser switched off, for the $\bar{d}_p = 406$ μm particles. The dotted lines represent the upper and lower extent of the heating laser, where used, while the arrowheads indicate its direction. The regions with hatching correspond to where the fluorescence signal from either S_{285} or S_{315} is below the threshold for reliable measurements.	90
4.14	Selected instantaneous images of the gas-phase temperature for two particle diameters, the corresponding normalised, smoothed temperature Θ_S with the detected hot and cold region boundaries and the simultaneous particle locations, both inside and outside of clusters, and the void regions.	93
4.15	Ensemble average of the measured particle volumetric loading within the detected hot and cold regions, ϕ_{reg} , normalised by the time-averaged loading at the same location, $\bar{\phi}(x)$, as a function of axial location for a series of Sk_D with $\bar{\phi} = 1.4 \times 10^{-3}$ and $\dot{Q}_0 = 2410$ W.	95
4.16	The ensemble average of the temperature above ambient as a function of the local particle volumetric loading, for the regions around particles inside clusters, outside clusters and in voids, for a series of Sk_D with $\bar{\phi} = 1.4 \times 10^{-3}$ and $\dot{Q}_0 = 2410$ W measured in the region immediately downstream from the heating laser of $2 < x/D < 2.25$ (a) and for a series of axial locations with $Sk_D = 86$, $\bar{\phi} = 1.4 \times 10^{-3}$ and $\dot{Q}_0 = 2410$ W (b).	97

A.1	Radial profiles of axial velocity of the jet and co-flow for a series of jet Reynolds numbers measured near to the jet exit plane at $x/D = 0.5$ (a), the velocity normalised by the centreline value (b). The insets present the detail of the velocity in the jet flow for $ r/D < 0.6$, with the analytical profiles for both laminar and turbulent pipe jets also presented for the middle sub-figure. The vertical dashed lines indicate the jet diameter ($\cdot\cdot$), annular pipe diameter ($\cdot-$) and the wind tunnel walls ($--$).	105
A.2	Radial profile of the standard deviation of velocity fluctuations for a series of jet Reynolds numbers measured near to the jet exit plane at $x/D = 0.5$	106
A.3	Velocity measurements from hot-wire anemometry of the jet and co-flow at a series axial distances for $Re_D = 20,000$, normalised by the jet exit velocity. The inset shows the detail of the velocity in the jet flow, for $ r/D < 0.6$. The vertical dashed lines indicate the jet diameter ($\cdot\cdot$), annular pipe diameter ($\cdot-$) and the wind tunnel walls ($--$).	107
A.4	Measured velocity in the co-flow for a series of fan controller positions, normalised by the velocity at the maximum speed. . .	108
B.1	(Continued next page)	110
B.1	Particle mass flow rate from screw feeder as a function of rotational speed for screws with varying pitch (c_p , a), core diameter (c_i , b), and number of flights (F , c), for 40 μm diameter spherical PMMA particles. The inset in each sub-figure presents the linear fit to the data, $d\dot{m}/d\omega$, as a function of c_p , c_i and F , respectively.	111
B.2	(Continued next page)	113
B.2	Time series of intensity from particle scattering for screws with varying pitch (a) and number of flights (b), together with that for one screw at a series of rotational speeds (c), normalised by the time-averaged mean.	114
B.3	(Continued next page)	116
B.3	The fast Fourier transform of the time series of scattering intensity for screws at constant speed with varying pitch (a) and number of flights (b), along with for one screw at rotational various speeds (c), with the frequency normalised by the rotational speed.	117

List of Tables

2.1	Summary of previous measurements within particle-laden flows heated by external radiation. Abbreviations for technique: LIP – laser induced phosphorescence, TC – thermocouple, CW – cold wire probe, NM – numerical model, CFD – computational fluid dynamics, DNS – direct numerical simulation; for parameters: \bar{d}_p – median particle diameter, Sk – particle Stokes number, \dot{Q}''_{peak} – peak heating flux, T_g – gas-phase temperature, T_p – particle-phase temperature, ϕ – particle loading, U_p – particle velocity.	21
3.1	Design parameters of the series of screws manufactured	37
3.2	Particle properties. The value in the Emissions column are those recorded following 266 nm illumination	42
3.3	Flow parameters used for Experiment I.	50
3.4	Flow parameters used for Experiment II.	54
3.5	Input parameters used for the analytical heat transfer model. The particle properties used were those previously measured for the Carbobead CP particles or similar [22, 30, 103]. The properties used for the gas were those of pure nitrogen. Temperature dependent parameters are indicated within the brackets in the Symbol column.	57

Nomenclature

Symbols	Units	Description
A_{cell}	(m ²)	Voronoi cell area
Bi	(-)	Biot number
c_i	(-)	Screw inner to outer diameter ratio
c_p	(-)	Screw pitch to diameter ratio
$c_{p,e}$	(-)	Screw effective pitch to diameter ratio
$c_{p,p}$	(J/kgK)	Particle specific heat capacity
$c_{p,f}$	(J/kgK)	Fluid specific heat capacity
C	(%vol/vol)	Tracer concentration
d_p	(m)	Particle diameter
D	(m)	Pipe diameter
D_ϵ	(m)	Effective diameter of jet
D_i	(m)	Screw inner diameter
D_o	(m)	Screw outer diameter
e_p	(-)	Voronoi method threshold
F	(-)	Number of screw flights
h	(W/m ² K)	Convective heat transfer coefficient
I	(W/m ²)	Heating beam intensity
I_λ	(W/m ²)	Fluorescence emission intensity
I_{peak}	(W/m ²)	Peak heating beam intensity
J_e	(kgm/s)	Jet exit momentum flux
k	(-)	Multiplier for hot/cold region threshold calculation
k_p	(W/mK)	Particle thermal conductivity
k_f	(W/mK)	Fluid thermal conductivity
L	(m)	Length
L_S	(m)	Smoothing length scale
m_p	(kg)	Mass of a single particle
\dot{m}	(kg/s)	Particle mass flow rate
M_e	(kg/s)	Jet exit mass flux
N	(m ⁻³)	Particle number density

Nu	(-)	Nusselt number
p	(N/m ²)	Flow pressure
P	(m)	Screw pitch
Pr	(-)	Prandtl number
Q''	(J/m ²)	Laser fluence
\dot{Q}_{abs}	(W)	Radiative heat absorbed by particle
\dot{Q}_{conv}	(W)	Convective heat transfer
\dot{Q}_{emit}	(W)	Radiative heat emitted by particle
\dot{Q}_p	(W)	Total heat transfer to particle
\dot{Q}_0	(W)	Outlet SSSTS power
\dot{Q}_{rad}''	(W/m ²)	Radiative heating flux
\dot{Q}_{peak}''	(W/m ²)	Peak radiative heating flux
r	(m)	Radial co-ordinate of jet
Re	(-)	Reynolds number
S_λ	(counts)	Measured signal for each channel
Sk	(-)	Stokes number
t	(s)	Time
T_a	(K)	Ambient temperature
T_f	(K)	Fluid temperature
T_g	(K)	Gas temperature
$T_{g,Hi}$	(K)	Gas temperature in regions near to particles within clusters
$T_{g,Lo}$	(K)	Gas temperature in regions near to particles outside of clusters
$T_{g,Vd}$	(K)	Gas temperature in void regions
T_{film}	(K)	Film temperature
T_p	(K)	Particle temperature
u'	(m/s)	Velocity fluctuation
U_f	(m/s)	Fluid velocity
$U_{g,b}$	(m/s)	Bulk mean flow velocity
U_p	(m/s)	Particle velocity
U_{slip}	(m/s)	Slip velocity between particles and fluid
\dot{V}_f	(m ³ /s)	Fluid volumetric flow rate
\dot{V}_p	(m ³ /s)	Particle volumetric flow rate
x	(m)	Axial co-ordinate of jet
\mathbf{x}	(m)	Spatial location
X	(m)	Co-ordinate of SSSTS parallel to x
α	(-)	Particle absorptivity
ΔT	(K)	Temperature above ambient
ϵ	(-)	Particle emissivity
ϵ_H	(-)	Threshold for determination of hot regions

ϵ_C	(-)	Threshold for determination of cold regions
Θ	(-)	Normalised temperature
Θ_S	(-)	Smoothed normalised temperature
λ	(m)	Emission wavelength
μ	(Ns/m ²)	Fluid dynamic viscosity
ρ_b	(kg/m ³)	Powder bulk density
ρ_f	(kg/m ³)	Fluid density
ρ_p	(kg/m ³)	Particle density
σ	(W/m ² K ⁴)	Stefan Boltzmann constant
σ_{abs}	(cm ⁻²)	Tracer absorption cross section
σ_T	(K)	Standard deviation of temperature
τ_f	(s)	Characteristic fluid time scale
τ_p	(s)	Particle response time
ϕ	(-)	Particle volumetric loading or volume fraction
ϕ_{loc}	(-)	Particle volume fraction around individual particle
ϕ_{reg}	(-)	Particle volume fraction within hot/cold regions
Φ	(-)	Tracer fluorescence quantum yield
ω	(s ⁻¹)	Screw rotational speed

Abbreviation	Description
CARS	Coherent anti-Stokes Raman spectroscopy
CFD	Computational fluid dynamics
CST	Concentrated solar thermal
DFWM	Degenerate four-wave mixing
DNS	Direct numerical simulation
FRS	Filtered Rayleigh scattering
LIF	Laser induced fluorescence
LIP	Laser induced phosphorescence
LITGS	Laser induced thermal grating spectroscopy
Nd:YAG	Neodymium-doped yttrium aluminium garnet laser
OD	Optical density
PDF	Probability density function
PMMA	Polymethyl methacrylate
PTV	Particle tracking velocimetry
RMS	Root mean square
SSSTS	Solid-state solar thermal simulator
TLAF	Two-line atomic fluorescence
ZnO:Zn	Zinc activated zinc oxide

Chapter 1

Introduction

1.1 Background

Industrial processes operating at high temperature ($> 400\text{ }^{\circ}\text{C}$) are currently responsible for more than 10% of the global energy demand [1], with the majority of these processes used for material transformations such as the refinement of iron in steel making and the production of cement. The predominant source of energy used to provide heat to existing systems is the combustion of fossil fuels, which contribute significantly to global greenhouse gas emissions [2]. With the global demand for these materials expected to increase continually in the near future, the development and implementation of low carbon energy sources is critical to reduce the environmental impact of high-temperature industrial processes [3]. Previously identified low carbon energy sources for industrial heating, to replace or be used in conjunction with fossil-fuel combustion, include hydrogen, electricity, and solar thermal [4]. To facilitate the transition to these sources through re-design of existing equipment in an efficient and cost-effective manner, more detailed understanding of the fundamental heat transfer processes present in such systems is required.

Solid particles are utilised in many high-temperature processes in industrial systems [5]. The particles in these systems can be used as a granular flow, such as in packed/moving bed reactors and rotary kilns in which the flow is predominantly of the bulk solid material [5, 6]. Alternatively, the particles can be a fine powder that is suspended in a carrier fluid (also known as particle-laden flows), such as for fluidised bed and flash reactors [7, 8]. The advantage of processing the material as a suspended powder flow is the increased material surface area available for reaction, which significantly decreases the conversion time of individual particles, and improved volumetric

throughput of material in the reactor, resulting in increased efficiency of the system [9]. Some examples of industrial processes utilising particle-laden flows include:

- suspension pre-heaters and calciners for cement and lime processing [10],
- fluid-flash calciners and fluidised beds for the production of alumina [8], and
- burners utilising solid fuels such as pulverised coal or biomass [11].

Particle-laden flows are also being developed:

- for the reduction of iron ore in fluidised beds [12], instead of the typical carbon-intensive blast furnace and direct reduction processes that account for 7% of all energy-related CO₂ emissions [1], and
- as the medium for solar energy absorption either directly, for material transformation processes [13], or indirectly, for sensible heat storage or electricity generation [14].

These industrial particle-laden flows typically have strong thermal gradients generated by the combustion of fuels and/or the absorption of high-flux radiation. The resultant heat transfer in the flow is highly complex, with the potential for gas-particle convection, radiation absorption, radiation emission by particles, inter-particle conduction, and thermodynamic chemical reactions to be simultaneously significant. These processes are further complicated by mutually-interacting non-linear particle-laden flow phenomena such as turbulence, preferential concentration of particles, and particle-fluid momentum transport [7, 15]. The significance of the particle-fluid interactions is characterised by the particle volumetric loading ($\phi = \dot{V}_p / \dot{V}_f$, where \dot{V}_p and \dot{V}_f are the respective volumetric flow rates of the particles and fluid), with three primary flow regimes identified [16]:

- the one-way coupling regime, in which the particles interact with the fluid structures but are sufficiently disperse ($\phi < 10^{-6}$) that the average structure of the flow is effectively identical to a single-phase flow;
- the two-way coupling regime, for $10^{-6} < \phi < 10^{-3}$, in which the momentum exchange between particles and fluid becomes sufficient to alter the flow structure, and;
- the four-way coupling regime, for $10^{-3} < \phi < 10^0$, where in addition to the interactions in the one-and two-way regimes particle-particle interactions, such as collisions, also become significant.

Typical industrial flows are sufficiently densely loaded to be in the two- or four-way coupling regimes [17–19]. However, such flows are currently poorly understood in comparison to single-phase and one-way coupled flows because of the additional non-linear interactions [7], particularly in heated flows [20].

The efficiency, stability and emissions of processes utilising non-isothermal particle-laden flows are strongly dependent on the heat transfer in the flow [18, 21]. Reliable predictable models, evaluated for the range of conditions relevant to industry, are required to cost-effectively optimise these processes. While previous investigations have provided qualitative understanding and insight into specific flows, the accuracy of predictive models are limited by the lack of quantitative understanding of the fundamental mutually-interacting, non-linear interactions present within non-isothermal particle-laden flows [7, 15]. The computational cost of fully resolved models is also prohibitive for large-scale datasets, with simplifying assumptions required to resolve existing models of the industrial-scale systems [22, 23]. As such, there is a need for experimental measurements of these flows to provide further insights into these processes and detailed data for model validation. Additionally, because such models are highly sensitive to the inflow and boundary conditions, it is necessary that such measurements are performed in flows with well-defined and characterised conditions

Direct measurements of heat transfer in non-isothermal particle-laden flows are currently not available due to challenges in acquiring well-resolved measurements of individual parameters (i.e., temperature, velocity, number density), let alone combinations [24, 25]. Laser based methods are commonly preferred for measurements of these parameters in these challenging environments because they can provide non-intrusive, in-situ measurements with high spatial and temporal resolutions [26, 27]. However, the application of these methods to obtain well-resolved data of radiatively heated particle-laden flows have been limited to measurements of the particle temperature for a single set of flow conditions with particles heated up to 400 °C [25, 28]. Previous investigations of radiatively heated particle-laden flows, both experimental and numerical, have demonstrated the importance of the flow conditions of heating flux, particle diameter, and particle volumetric fraction on both the heat transfer efficiency and temperature distribution [15, 20, 23, 29–31]. However, the effect of varying these flow conditions on the gas-phase temperature distribution and thermal gradients in the flow is yet to be investigated systematically for low temperature systems (< 200 °C), let alone for the high temperature systems of interest. Additionally, no method has been previously demonstrated that is able provide such measurements

in the flow conditions relevant to industry, which typically utilise particles of diameter 1-1,000 μm with particle volumetric loadings greater than 10^{-4} . The application and analysis of high-quality measurements of the gas-phase temperature in these non-isothermal particle-laden flows is a critical step towards the continued development and optimisation of industrial systems.

1.2 Thesis aims

The overall objective of the work presented in the present thesis is to provide new insights into the heat transfer processes within non-isothermal, non-reacting particle-laden flows with sufficiently dense particle loading to be in the two- and four-way coupling regimes. This is completed using simultaneous, spatially resolved measurements of the gas-phase temperature and particle volumetric loading in a flow with simplified, well-characterised inflow and boundary conditions relevant to practical applications, albeit with a relatively low peak temperature ($< 200\text{ }^{\circ}\text{C}$). In particular, the aims of the present thesis are as follows:

1. To assess the accuracy and identify the potential error sources of spatially resolved measurements of the gas-phase temperature using two-colour laser induced fluorescence in a densely loaded ($\phi > 10^{-4}$) non-isothermal particle-laden flow, for a series of particle diameters and volumetric loadings;
2. to investigate the effect of particle diameter and particle volume fraction on the temperature distributions in a particle-laden flow heated using high-flux radiation, for a systematically varied series of heating fluxes;
3. to evaluate the correlation between gas-phase temperature and local, instantaneous particle volumetric loading in a radiatively heated particle-laden flow.

1.3 Thesis outline and paper synopses

The format of the present thesis is a *thesis-by-publication* with the main body of work (Chapter 4) consisting of a summary of the key results from the four manuscripts produced for the present thesis, each of which are published in international peer-reviewed scientific journals. These papers are included in full in the appendices C - F of this document. The details of the work presented in each chapter and paper are provided below.

- Chapter 2 provides the background information on the particle-fluid interactions and heat transfer processes that occur in non-isothermal particle-laden flows, together with a review of the techniques available for temperature measurements in such flows.
- Chapter 3 presents an overview of the methods and systems used to develop the present thesis research for simultaneous, non-intrusive, planar measurements of the gas-phase temperature and particle loading in a non-isothermal particle-laden flow.
- Chapter 4 presents the key results from the experiments performed to meet the aims of the present investigation.
- Chapter 5 presents the main conclusions from the results presented in the present thesis, together with recommendations for future study.
- Appendix A presents the results from the flow characterisation of the wind tunnel arrangement used for the experiments performed.
- Appendix B presents the results from the calibration of the screw feeder, together with an investigation into the influence of select design parameters on the steadiness of mass flow output with time.
- Appendix C presents the first paper published as part of the present thesis, entitled: *Luminescence interference to two-colour toluene laser-induced fluorescence thermometry in a particle-laden flow* [32].

In particle-laden flows, laser-based methods are susceptible to interference and increased uncertainty from a range of sources including elastic scattering of the laser light, signal trapping, attenuation of the light sheet, and luminescence of particles. The influence of these sources on the temperature measurement technique of two-colour LIF was assessed in a particle-laden flow for the first time, using particles with a series of diameters and different luminescence interactions with the 266 nm beam used for LIF. Importantly, this work demonstrates the accuracy, precision and limitations of the method for a range of conditions with the given optical arrangement.
- Appendix D presents the second paper, entitled: *Insights from a new method providing single-shot, planar measurement of gas-phase temperature in particle-laden flows under high-flux radiation* [33].

A particle-laden flow heated at a series of powers from a high-flux

radiative heating source was investigated using simultaneous, spatially-resolved measurements of the gas-temperature and particle distributions. The system used is a simplified arrangement from the conditions present in a falling-particle receiver, with a well-defined flow and heating profile utilised to improve understanding of the heat transfer in the system. The gas temperature distribution was investigated both within and downstream from the region with strong particle heating due to the absorption of high-flux radiation. From these measurements, the relative significance of convective heat transfer, gas-phase mixing and buoyancy in the near field was evaluated qualitatively. Additionally, spatial variations in the gas-phase temperature distribution, for both the instantaneous and mean flow, due to the non-uniform particle distribution and attenuation of the heating beam were identified. The relative intensity distribution of the radiative heating flux within the measurement region was also characterised.

- Appendix E presents the third paper entitled: *The effect of particle size and volumetric loading on the gas temperature distributions in a particle-laden flow heated with high-flux radiation* [34].

This paper extends the method presented in Paper II to a systematically varied series of particle diameters and particle volumetric loadings. Each of these is known to affect both the radiation absorption and convective heat transfer in the flow, although the relative influence has not previously been evaluated with spatially resolved measurements in well-defined conditions. A simplified one-dimensional analytical model of the temperature rise with distance was also developed, with the results in good agreement with the trends seen in the experiments. Additionally, the transmission of the heating beam through the flow was modelled numerically using a random particle distribution, which also gave good agreement with the measured results.

- Appendix F presents the fourth paper entitled: *The effect of instantaneous particle distributions on the gas-phase temperature in an unsteady particle-laden jet heated with high-flux radiation* [35].

This paper analyses the instantaneous correlation between the spatial distributions of particle loading and temperature for the same conditions as in Paper III, to gain further insights into the significance of convective heat transfer, gas-phase mixing, and buoyancy. A new method was developed to identify and separate highly localised, coherent regions of high or low temperature in the instantaneous distribution, with the particle loading within these regions simultaneously

measured. Additionally, the instantaneous gas-phase temperature distribution was analysed separately into a series of local flow conditions: near to particles within clusters, near to those outside of clusters, and in void regions without particles.

Chapter 2

Literature Review

2.1 Particle-laden flows

The term 'particle' can be used to describe a multitude of different objects - of scale varying from sub-atomic to molecular to macroscopic. For the purposes of the present thesis, we define a 'particle' as a solid object with a diameter on the order of 0.1-1,000 μm . The interaction between particles and their surroundings is dependent not only on the particle properties but also those of the surrounding fluid. In the present thesis, the fluid of greatest interest is air at temperatures in the range 0-1000 °C and atmospheric pressure. Resultantly, the flows investigated in this thesis are in the continuum flow regime.

A particle-laden flow is the term used to describe a system in which solid particles are suspended and/or carried in a fluid. These flows are prevalent both in the natural world, such as the sediment in rivers and dust in the atmosphere, and for industrial applications, such as in fluid-flash calciners for the production of alumina [8], suspension preheating of material [36], flames with soot production [17], and particulate fuel burners [11]. Particles are also currently being investigated as the absorbing medium for use in concentrated solar thermal (CST) receivers, with the potential to sustain higher operating temperatures than typical molten salt based receivers leading to improved efficiency of the receiver [14]. Despite their widespread utilisation in practical systems, the highly complex nature of interactions within particle-laden flows means that, fundamentally, they are still relatively poorly understood [7].

Axisymmetric jets have been used extensively in past investigations of fundamental flow processes, for both particle-laden and single-phase flows, for two main reasons: firstly, because of their relevance to industrial systems, and, secondly, because the generated flow is relatively simple with well-

defined initial and boundary conditions. The simplest nozzle to provide a jet flow is the round pipe, with previous measurements of the velocity and/or number density fields of either phase in a particle-laden flow performed for a wide range of flow conditions [37–45]. Additionally, pipe jet flows have been utilised for measurements of the temperature, velocity, and species concentration of flames with droplets or soot particle formation [46]. From these measurements, flow conditions such as the jet spreading, mixing, and entrainment for certain jet configurations are well characterised. However, there is currently a paucity of data in such well-defined flows with high-flux radiation from an external source (i.e., to approximate the conditions in systems such as particle-based CST receivers), with measurements reported only for the particle temperature distribution [25, 28]. Pipe jets generate a relatively simple flow field and, as such, are the ideal configuration for measurements to provide fundamental insight into the particle-fluid interactions and heat transfer processes that occur in radiatively heated particle-laden flows.

Turbulence, particle-fluid coupling, and preferential concentration of particles are mutually-interacting, complex, non-linear phenomena that are commonly present in particle-laden flows, each of which can significantly influence the instantaneous and time-averaged flow fields of both phases and the particle distribution [7]. Turbulence, which is characterised by unsteady, irregular, chaotic flow motions, has been the subject of extensive investigation in single-phase flows and is among the most challenging topics in fluid mechanics due to the complexity of motions generated [47]. The extent of turbulence in the flow can often be characterised using the Reynolds number, which is defined as the ratio of the inertial to viscous forces in the flow, calculated from the equation:

$$Re_L = \frac{\rho_f UL}{\mu} \quad (2.1)$$

where

- ρ_f is the fluid density,
- U is a characteristic flow velocity,
- L is a characteristic length scale, and
- μ is the dynamic viscosity of the fluid.

In particle-laden flows, the interaction of turbulent structures with the particles leads to even greater complexity than for single-phase flows. Previous measurements and simulations have demonstrated that the turbulence

intensity of the particle-laden flow can be either greater or lesser than that of the single-phase flow, depending on the flow conditions [7, 48, 49]. The primary mechanisms that affect the turbulence in particle-laden flows are:

1. momentum exchange between the fluid and particles as the particles partially respond to the flow motions, which in turn attenuates the turbulence [50, 51],
2. the generation of turbulent structures from vortex shedding off particles, and
3. resonant oscillations in the wake of particles, both of which result in an increase in the turbulence intensity [49, 52].

The relative significance of these mechanisms is dependent on various flow parameters, including the time and length scales of both the particle and the turbulent structures in the flow, the particle-fluid density ratio, and the particle Reynolds number [49].

Particle-fluid coupling describes the level of interaction between the particles and fluid and is primarily dependent on the particle volumetric loading, defined as the fractional volume of particles in the flow:

$$\phi = \frac{\dot{V}_p}{\dot{V}_f}, \quad (2.2)$$

where \dot{V}_p and \dot{V}_f are the volumetric flow rates of the particles and fluid, respectively. The interactions within particle-laden flows can typically be separated into three regimes, namely the one-way, two-way, and four-way coupling regimes [7, 16].

- In the one-way coupling regime, the turbulent motions in the flow influence the particle distribution but the particles are sufficiently disperse ($\phi < 10^{-6}$) that the mean fluid flow field and turbulence of the flow closely approximate that of a single-phase flow.
- At higher volumetric loadings, for $10^{-6} < \phi < 10^{-3}$, in addition to the interactions in the one-way coupling regime the momentum exchange between the particles and the fluid is sufficient to alter the fluid flow field and turbulence structures. Flows in this regime are considered to be two-way coupled.
- More densely loaded flows, with $10^{-3} < \phi < 10^0$, are considered to be in the four-way coupling regime because particle-particle interactions,

such as collisions, agglomeration, and breakage, are significant in addition to the particle-fluid interactions present in the two-way coupling regime.

Typical particle-laden flows used in industrial processes or CST receivers operate in the four-way coupling regime, or the higher-loading end of the two-way coupling regime [17–19]. However, measurements of the particle-laden flows at the loadings relevant to these systems are currently limited, particularly for spatially resolved data, primarily due to the significant interferences and uncertainties associated with the particles in the flow that are introduced to common measurement techniques.

The distribution of particles in particle-laden flows is often highly non-uniform, with the potential for particles to preferentially concentrate in localised regions of the flow from aerodynamic interaction with the turbulent motions [42, 45, 53]. This can result in regions with a volumetric loading much higher than the mean (clusters) and regions without, or a sparse population of, particles (voids). The term ‘cluster’ used in the context of the variable particle distribution indicates a region of closely-spaced individual particles, and hence should not be confused with aggregates of particles that are physically connected. The level of clustering in the flow is characterised by the Stokes number (Sk) of the particles, defined as the ratio of particle response time, τ_p , to a characteristic fluid time scale, τ_f [54]. For bounded flows, such as a pipe jet, it is convenient to use the large-eddy time scale, so that the Stokes number is given by the equation:

$$Sk_D = \frac{\tau_p}{\tau_f} = \frac{\rho_p d_p^2 U_b}{18\mu D} \quad (2.3)$$

where

- ρ_p is the particle density,
- d_p is the particle diameter,
- U_b is the bulk-mean flow velocity, and
- D is the pipe diameter.

The Stokes number characterises the particle response to flow motions of a given scale, such that for $Sk \ll 1$ the particles closely follow the flow motions of that scale, for $Sk \gg 1$ the particle motions are mostly independent of the flow, and for $Sk \sim 1$ the particles partially respond to flow motions [7, 55]. Previous experiments have shown that clustering is most significant for

particles with Sk on the order of unity [54, 56]. Additionally, the particle distribution in a pipe flow has been shown to be dependent on Stokes number, with the particles of $Sk_D \leq 1.4$ preferentially concentrated toward the pipe edge while the particles of $Sk_D \geq 5.6$ were concentrated toward the pipe axis [44]. These differences in particle distribution were attributed to the relative significance of particle-size dependent aerodynamic forces flow, namely turbophoresis and Saffman lift [57]. As such, the combined effect of each of these mechanisms for preferential concentration of particles must be considered when analysing particle-laden flows.

The combination of the turbulent structures, particle-fluid interactions, and preferential concentration lead to challenges in predicting the flow fields and particle distributions in particle-laden flows, using either existing experimental data or numerical modelling. These challenges are further complicated in non-isothermal flows, with temperature gradients in the fluid generating additional buoyant and thermophoretic forces on the particles. The buoyant forces are driven by pressure gradients in the flow, such as from the gradients of temperature around radiatively heated particles, that lead to the formation of plumes [20]. The phenomenon of thermophoresis causes particles migrate towards regions of lower temperature. This occurs because the kinetic energy of molecules on the hot side of the particle is greater than that of molecules on the cold side, resulting in a net force on the particle from collisions [58]. Each of these phenomena that affect the particle motions, flow motions, or particle distributions in turn affect the heat transfer processes in non-isothermal flows.

2.2 Heat transfer equations

The primary heat transfer processes for a single particle in particle-laden flow without chemical reactions or phase changes are radiation absorption, thermal radiation emission, convection with the surrounding fluid (or conduction, if the particle is stationary relative to the fluid), and internal particle conduction [21, 29, 59]. The internal particle conduction is often neglected in models, because the internal thermal response (i.e., the time it takes for the particle temperature to reach a uniform state) is typically much faster than the convective/radiative processes. This is true when the particle Biot number:

$$Bi = \frac{hd_p}{k_p} \ll 1, \quad (2.4)$$

where h is the convective heat transfer coefficient and k_p is the thermal conductivity of the particle. As such, the heat transfer for a single, spherical

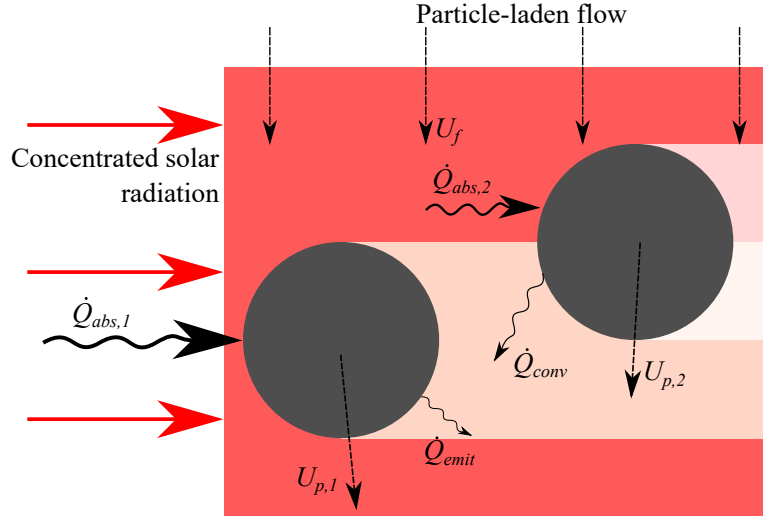


Figure 2.1: A diagram illustrating the typical dominant heat transfer processes and flow conditions for a particle-laden flow subjected to radiation, such as occurs in a particle-based CST receiver. The background shading represents the local heating flux, and the arrow length of the heat transfer processes indicates their typical relative magnitudes. The subscripts 1 and 2 represent each particle displayed.

particle in a non-isothermal particle-laden flow can be modelled using a simplified heat transfer balance equation [25]:

$$\dot{Q}_p = \dot{Q}_{abs} - \dot{Q}_{conv} - \dot{Q}_{emit} \quad (2.5)$$

where

- \dot{Q}_p is the rate of heat transfer to the particle (a positive value indicates particle heating),
- \dot{Q}_{abs} is the radiative heat absorbed by the particle,
- \dot{Q}_{conv} is the convection between the particles and surrounding gas, and
- \dot{Q}_{emit} is the radiative heat emitted from the particle.

A diagram illustrating these heat transfer processes is presented in Figure 2.1 for the flow with high-flux incident radiation, such as for particle-based CST receivers.

Each of these heat transfer processes can be expressed as a function of the system parameters and time (t), using the following equations applied to

a single, independent particle (i.e., these equations neglect particle-particle interactions, including shadowing).

The change in particle temperature is given by:

$$\dot{Q}_p = m_p c_{p,p}(T_p) \frac{\partial T_p(t)}{\partial t} \quad (2.6)$$

where

- T_p is the particle temperature,
- $m_p = \rho_p \pi d_p^3 / 6$ is the mass of a single particle, and
- $c_{p,p}(T_p)$ is the specific heat capacity of the particle as a function of particle temperature.

The radiation absorbed by the particle is given by:

$$\dot{Q}_{abs} = \frac{\alpha \pi d_p^2 \dot{Q}_{rad}''(t)}{4} \quad (2.7)$$

where

- α is the absorptivity of the particle, and
- \dot{Q}_{rad}'' is the radiative heating flux.

The particle-fluid convection is given by:

$$\dot{Q}_{conv} = h \pi d_p^2 [T_p(t) - T_f(t)] \quad (2.8)$$

where

- T_f is the fluid temperature,
- $h = Nuk_f(T_{film}) / d_p$ is the convective heat transfer coefficient,
- $T_{film} = (T_f - T_a) / 2$ is the film temperature at which the fluid properties are evaluated,
- T_a is the ambient temperature,
- $k_f(T_{film})$ is the fluid thermal conductivity evaluated at the film temperature.

The Nusselt number of a spherical particle in forced convection is given by:

$$Nu = 2 + (0.4Re_p^{1/2} + 0.06Re_p^{2/3})Pr^{0.4}, \quad (2.9)$$

where the particle Reynolds and Prandtl numbers are given by:

$$Re_p = \frac{\rho_f(T_{film})|U_{slip}|d_p}{\mu(T_{film})}, \quad (2.10)$$

and

$$Pr = \frac{c_{p,f}(T_{film})\mu(T_{film})}{k_f(T_{film})}, \quad (2.11)$$

respectively. Here,

- $|U_{slip}|$ is the absolute value of the particle-fluid velocity difference, and
- $c_{p,f}$ is the specific heat capacity of the fluid.

The radiation emitted from the particle is given by:

$$\dot{Q}_{emit} = \epsilon\sigma\pi d_p^2 [T_p^4(t) - T_a^4] \quad (2.12)$$

where

- ϵ is the emissivity of the particle and
- $\sigma = 5.67 \times 10^{-8} \text{ W/m}^2\text{K}^4$ is the Stefan-Boltzmann constant.

The rate of change of particle temperature with time can therefore be evaluated by substituting equations 2.6 - 2.12 into equation 2.5, with the resultant equation derived to be:

$$\frac{\partial T_p(t)}{\partial t} = \frac{6}{d_p c_{p,p}(T_p)\rho_p} \left[\frac{\alpha}{4} \dot{Q}_{rad}''(t) - h(T_p(t) - T_f(t)) - \epsilon\sigma(T_p^4(t) - T_a^4) \right]. \quad (2.13)$$

The rate of change of gas temperature can also be derived, using the assumptions that all convective heat transfer is to the surrounding fluid, the particles are evenly distributed within the fluid and heat the gas uniformly, and other heat transfer processes for the gas-phase are negligible. This is given by the equation:

$$\dot{Q}_{conv} = \rho_f V_f c_{p,f}(T_{film}) \frac{\partial T_f(t)}{\partial t} \quad (2.14)$$

where

- $V_f = V_p/\phi = \pi d_p^3/6\phi$ is the volume of fluid per particle and

- V_p is the particle volume.

Substituting this relationship into equation 2.8 and rearranging gives the rate of change of gas temperature as:

$$\frac{\partial T_f(t)}{\partial t} = \frac{6h\phi (T_p(t) - T_f(t))}{d_p c_{p,f}(T_{film}) \rho_f(T_{film})}. \quad (2.15)$$

To solve the equations derived for the change of temperature of both the particles and gas (equations 2.13 and 2.15, respectively) the initial temperatures were assumed to be equal at the ambient temperature of 20 °C. While these equations require significant assumptions and neglect the complex interactions discussed in Section 2.1, they are useful to determine the relative significance of the key parameters in the system and are used within the present thesis to estimate the temperature under experimental conditions.

2.3 Heat transfer in particle-laden flows

In real systems the complex phenomena in particle-laden flows (e.g., turbulence, preferential concentration, particle-fluid momentum transport) mutually interact with the convective heat transfer processes [15]. In particle-laden flows with radiative heat input this coupling also forms a feedback loop [20], the primary interactions of which are the particle-fluid momentum transport, convective heat transfer, and buoyancy.

- The particle-fluid momentum transport is proportional to the slip velocity (i.e., the difference in velocity between the particles and gas), which is dependent on the particle Stokes number and turbulent structures in the flow.
- The radiative energy absorbed by the particles is transferred to the gas through convection, the magnitude of which is also proportional to the slip velocity.
- The resultant gradients in the gas-phase temperature can then generate buoyant plumes in the flow. The buoyancy-induced motions alter both the velocity distribution and turbulent structures in the gas-phase, which in turn affects both the particle-fluid momentum transport and convective heat transfer.

This feedback loop can lead to the generation of self-sustaining turbulence in particle suspensions with constant radiative heating [20], which affects the velocity and temperature distributions of each phase.

Preferential concentration in radiatively heated particle-laden flows also significantly affects the spatial distribution of gas-phase temperature, with the instantaneous gas-phase temperature increasing with an increase in the local particle loading [31]. However, the effective convective heat transfer in the flow with significant particle clustering has been demonstrated to be lower than that of a random particle distribution, because the particles within clusters retain heat for longer than those outside [23]. Additionally, the variation of particle settling velocities, which can be influenced by buoyant plumes in radiatively heated flows, has been shown to be greater for flows with significant clustering than for a random distribution of particles [15].

The absorption of radiation by individual particles in systems such as particle-based CST receivers can be highly non-uniform, both spatially and temporally, because the particles attenuate the incident radiation and cast shadows in the down-beam direction [60]. This attenuation results in the average radiative heating flux, and therefore also particle temperature, decreasing with path length through the flow [61]. This is also illustrated in Figure 2.1, with one particle down-beam from the other receiving a lower radiative heating input.

The combination of these non-linear, mutually interacting processes can lead to significant spatial and temporal variations in the distributions of temperature and velocity for both phases, as well as the particle number density. Therefore, for full characterisation of a non-isothermal particle-laden flow, the spatial distributions of each of these flow parameters are required to be simultaneously known. Experimentally, such measurements are yet to be demonstrated because of the complex arrangements required to implement well-resolved measurement techniques for each individual parameter. Similarly, for fully resolved numerical models to incorporate all of the particle-fluid interactions and heat transfer processes direct numerical simulations are required [7], which become prohibitively expensive in terms of computational time for flows with more than ~ 1000 particles. Additionally, there is currently a lack of high-quality experimental data of individual flow parameters for validation of these models. As such, simultaneous, well-resolved measurements of several key flow parameters, conducted in systems with a well-defined flow and heating source, are critical to improve the current understanding of heat transfer in non-isothermal particle-laden flows.

The thermometry techniques used and parameters measured in previous investigations with radiative heating are summarised in Table 2.1. These previous measurements and numerical models of particle-laden flows with radiative heating have shown that the incident heating flux, particle diameter, and particle loading each significantly affect the particle-fluid interactions

and heat transfer.

- The rate of particle temperature increase through the heating region is proportional to the radiative heating flux [28, 30], with this temperature rise leading to convective heat transfer with the surrounding fluid. The subsequent thermal gradients in the fluid phase, which generate buoyant and thermophoresis motions that can influence both phases, is therefore also dependent on the radiative heating flux [15].
- For a constant particle volumetric loading, an increase in the particle diameter leads to a decrease on average of both the radiation absorption, which is proportional to the total cross-sectional area of particles in the flow, and convective heat transfer, which is proportional to the total particle surface area [21, 22, 29]. Additionally, the temperature increase of individual particles due to radiative heating is inversely proportional to the particle diameter (see also equation 2.15), because the radiation absorption is proportional to the particle cross-sectional area while the temperature change is proportional to the particle volume [62].
- For a constant particle diameter, the total radiation absorption increases with particle volumetric loading, although the average particle temperature decreases at sufficiently high loadings because attenuation/shadowing of the incident radiation becomes significant [21, 22, 30]. The influence of attenuation of the heating beam on non-uniformities in the spatial distribution of particle temperature is particularly significant in flows with preferential concentration of particles [23]. Additionally, the instantaneous fluid temperature in radiatively heated particle-laden flows has been found to be dependent on the local particle loading [31].

These results show that the distribution of gas-phase temperature has the potential to be highly variable both spatially and temporally, due to both system-dependent parameters, such as particle diameter, particle loading, and heating flux, and interactions within the particle-laden flow, such as particle clustering and buoyancy. However, previous measurements of the fluid temperature in radiatively heated flows have been limited to a single spatial location, with the instantaneous thermal gradients in the flow yet to be resolved experimentally. Furthermore, quantitative, systematic data evaluating the effect of the heating flux, particle diameter, and volumetric loading on the spatial distribution of the fluid-phase temperature, for both the time-averaged and instantaneous flow, are currently unavailable. Hence,

to improve understanding of the heat transfer and particle-fluid interactions in non-isothermal particle-laden flows, there is a need for systematic, well-resolved measurements of the fluid-phase temperature for series of particle diameters, volumetric loadings, and heat fluxes.

Table 2.1: Summary of previous measurements within particle-laden flows heated by external radiation. Abbreviations for technique: LIP – laser induced phosphorescence, TC – thermocouple, CW – cold wire probe, NM – numerical model, CFD – computational fluid dynamics, DNS – direct numerical simulation; for parameters: \bar{d}_p – median particle diameter, Sk – particle Stokes number, \dot{Q}''_{peak} – peak heating flux, T_g – gas-phase temperature, T_p – particle-phase temperature, ϕ – particle loading, U_p – particle velocity.

Author	Flow	Thermometry technique	Resolution	Analysed parameters	\bar{d}_p (μm)	Sk	Coupling regime	\dot{Q}''_{peak} (kW/m^2)
Experimental								
Banko et al., (2020) [31]	Square channel	TC, CW, NM	Point, 1D	T_g, ϕ	11.5	11.3	Two-way	245
Bertocchi et al., (2004) [63]	Particle receiver	TC	Point	T_g	< 0.6	n/a	Two-way (inferred)	< 4,900
Davis et al., (2017) [18]	Particle receiver	TC	Point	T_g	15.5	0.19	Two-way	1,070-2,190
Kueh et al., (2017, 2018) [25, 28]	Fluidised bed	LIP	Planar	T_p	2-50	n/a	Two-way	36,600
Meier et al., (2006) [64]	Rotary kiln	TC	Point	T_g	2,000 - 3,000	n/a	n/a	3,000
Monazam & Maloney (1992) [65]	Suspended particle	Pyrometer, NM	Volume average	T_p	50-150	n/a	n/a	\sim 64,000
Nikulshina et al., (2009) [66]	Particle receiver	TC	Point	T_g	6-35	n/a	Two-way (inferred)	1,096 - 1,884
Siegel et al., (2004) [30]	Particle curtain	TC	Point	T_g, U_p, ϕ	697	n/a	Four-way	\sim 1,100
Spjut et al., (1985) [67]	Suspended particle	Pyrometer	Volume average	T_p	10-50	n/a	n/a	\sim 10,000
Steinfeld et al., (1992) [13]	Particle receiver	TC	Point	T_g	n/a	n/a	Two-way	1162

Author	Flow	Thermometry technique	Resolution	Analysed parameters	\bar{d}_p (μm)	Sk	Coupling regime	\dot{Q}''_{peak} (kW/m^2)
Numerical								
Chen et al., (2006) [22]	Particle curtain	CFD	3D	T_p, U_g, U_p, ϕ	100-900	n/a	Four-way	920
Evans et al., (1987) [21]	Particle curtain	NM	2D	T_g, T_p, U_g, U_p	650	n/a	Four-way	920
Frankel et al., (2016) [15]	Particle suspension	DNS	3D	T_p, U_g, U_p, ϕ	40	0.18-0.58	Two-way	2,000
Grena (2009) [59]	Single particle	CFD	3D	T_p	400-800	n/a	n/a	920
Miller & Koenigsdorff (1991) [29]	Particle suspension	NM	3D	T_p, ϕ	0.1-10	n/a	n/a	5,000
Pouransari & Mani (2016) [23]	Square channel	DNS, NM	3D, 1D	T_g, T_p, ϕ	n/a	0.04-9.2	Four-way	n/a
Rahmani et al., (2018) [68]	Square channel	DNS, NM	3D, 1D	T_g, T_p, ϕ	4.6-15	0.1-4	Two-way	17,000
van Eyk et al., (2016) [69]	Particle gasifier	NM	1D	T_g, T_p	100	n/a	Two-way (inferred)	4,000
Zamansky et al., (2014) [20]	Particle suspension	DNS	3D	T_g, ϕ	n/a	0.003-7.34	Two-way	n/a

2.4 Scattering of radiation by particles

The interaction of electromagnetic radiation by particles is dependent on both the particle radius (r_p) and wavelength of incident light (λ). The resultant scattering can be roughly separated into three main regimes, dependent on the size parameter $\alpha_{sp} = \frac{2\pi r_p}{\lambda}$: 1) Rayleigh scattering, for $\alpha_{sp} \ll 1$; Mie scattering, for $\alpha_{sp} \approx 1$; and geometric optics, for $\alpha_{sp} \gg 1$ [70, 71].

Scattering from molecules or atoms in a gas using typical laser wavelengths for diagnostic measurements is in the Rayleigh regime. Rayleigh scattering describes the interaction of light with particles that are much smaller than the wavelength of incident light. It occurs when radiation is emitted from the atom/molecule due to oscillations induced by the electromagnetic field of incident light [72]. This process is effectively instantaneous and is termed elastic because the energy of the emitted photons is the same as that of the incident photons. The proportion of light that will be scattered from a single molecule, for a given wavelength and angle to the incident light, is described by the Rayleigh cross section of the molecular species [73]. This cross-section can also be determined for a mixture if the mole fraction and cross section of each species is known. Rayleigh scattering has previously been used extensively to measure the concentration or temperature of a gas.

Mie scattering is typically used to image particles of diameter 0.1-150 μm , such as are commonly used in industrial applications, and exhibits an angle-dependent intensity due to the summation of oscillations induced within the particle by electromagnetic radiation [70]. If the particle size distribution is mono-disperse and the particles are spherical, the Mie scattering intensity is proportional to the number density of particles. Measurements of Mie scattering can therefore be used to determine the local concentration/number density of particles in a flow, although corrections may be required for accurate measurement [60]. Particles with a greater diameter are in the geometric optics regime, with the interaction of light with the particle surface typically measured in terms of absorption, reflectance, and refraction.

2.5 Gas-phase temperature measurement of particle-laden flows

Temperature is one of the key parameters required for understanding of heat transfer processes in common fluid-based systems. For industrial particle-laden flows the carrier fluid is typically a gas (e.g. mineral processing [8], solid fuels [11]), with several techniques having been previously developed

for gas-phase temperature measurements in a wide range of flow conditions and configurations.

Among the simplest, most robust measurement devices are thermocouples, which are commonly used in particle-laden flows because they provide reliable, time-resolved measurements while being resistant to collisions with particles [18, 31, 74]. However, these probes are limited to single-point measurements and arrays are required to resolve spatial gradients in the flow with limited resolution. Additionally, the measurement using a thermocouple is intrusive, such that the physical probe can influence the flow field around the measurement volume. Furthermore, the measurement is of the probe temperature instead of directly from the gas-phase, with the output required to be corrected to estimate the actual gas temperature in systems with strong heat transfer. Alternative non-intrusive single point measurement methods suitable for particle-laden flows include pyrometry, which measures the thermal emission from the flow [75], and absorption/extinction, which measures the decrease in intensity of a beam of specific wavelength through the flow due to absorption by a species [76]. However, the signal from each of these methods is integrated over the path length through the flow, which results in a poor spatial resolution of the measurement.

Laser based methods are potentially well suited to provide non-intrusive planar measurements and have been applied to a wide range of flows, with much of the development for temperature measurements motivated by the need for improved understanding of harsh combustion environments [26, 27]. Methods using pulsed lasers are capable of providing accurate, spatially resolved measurements of the instantaneous flow, with temporally resolved measurements also possible using instruments with sufficiently high repetition rates. The thermometry signal from these planar laser-based techniques can be grouped into three typical processes:

1. the spontaneous scattering of radiation, the intensity of which is proportional to the species number density following the ideal gas law, such as Rayleigh scattering;
2. from coherent methods where the signal is generated as a laser-like beam, such as coherent anti-Stokes Raman spectroscopy (CARS), degenerate four-wave mixing (DFWM), and laser-induced thermal grating spectroscopy (LITGS);
3. emissions from molecular or atomic energy level transitions relevant to the Boltzmann distribution, such as spontaneous Raman scattering,

2.5 Gas-phase temperature measurement of particle-laden flows

laser induced fluorescence (LIF), two-line atomic fluorescence (TLAF), and laser induced phosphorescence (LIP).

Additionally, laser-induced breakdown spectroscopy, which measures the emissions from a plasma sample generated by the absorption of the beam from a laser, can be used for thermometry, although this method is practically limited to point-measurements and thus not considered for the present investigation.

The intensity of radiation Rayleigh scattering from a probe volume, for a constant incident light intensity, is proportional to the number density of molecules within the volume. If the pressure and composition of the gas is known, the temperature can then be calculated. A simplified example of the energy transitions of Rayleigh scattering is presented graphically in Figure 2.2. While the Rayleigh scattering method is relatively simple, requiring only a single laser and detector, it is highly susceptible to interference from other sources of elastically scattered light from the laser. This is particularly significant in particle-laden flows, with the intensity of Mie scattering from the (comparatively large) particles several orders of magnitude greater than the Rayleigh signal [77].

Filtered-Rayleigh scattering (FRS) utilises the fact that the Rayleigh signal is typically Doppler-broadened due to the molecular kinetic motions, while the interfering elastic scattering is from effectively static sources (e.g., particles and surfaces). The thermometry signal is isolated using a spectral line based filter centred at the laser wavelength, typically an iodine cell, that has high absorption at the laser wavelength but transmits the edge wavelengths of the broadened Rayleigh signal [72]. However, the transmitted FRS signal is greatly reduced from that of the unfiltered Rayleigh signal, and the method is practically limited to measurements in flows with $< 1 \mu\text{m}$ particles with negligible luminescence after filtering. Additionally, the Doppler-broadening, and therefore also the transmitted Rayleigh signal, is relatively weak in low-temperature (e.g., ambient) conditions.

The process of Raman scattering is similar to Rayleigh scattering, although the emitted photon is at a different wavelength to that absorbed (see Figure 2.2). If the wavelength of the emitted photon is longer than that of the absorbed photon (i.e., the molecular energy level increases from its initial state) the process is known as Stokes Raman scattering, while if the emitted photon is at a shorter wavelength (i.e., the molecular energy level decreases from its initial state) the process is known as anti-Stokes Raman scattering. The Raman signal intensity is proportional to the population distribution of the initial energy level, which is temperature dependent.

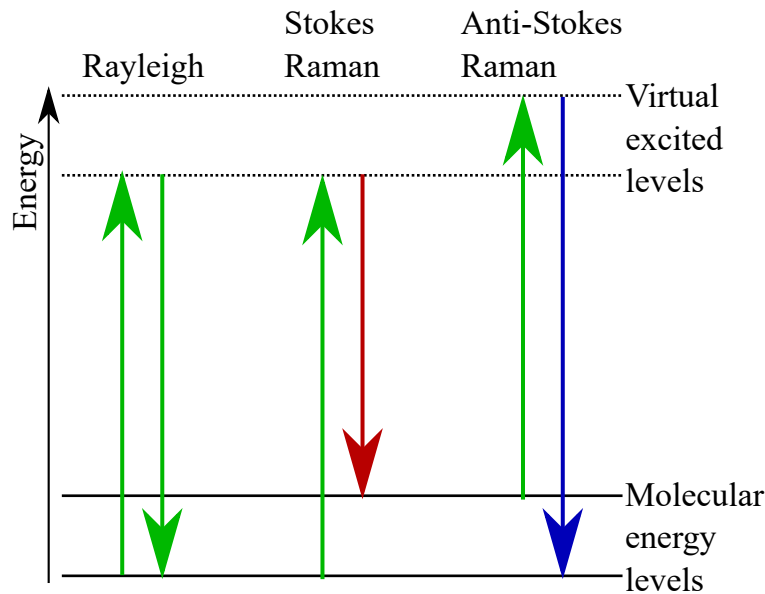


Figure 2.2: Typical molecular energy excitation levels for Rayleigh and Raman scattering. The arrows indicate photons absorbed/emitted. The excited energy levels do not necessarily represent stable molecular energy levels.

Therefore, the temperature can be derived from the intensity ratio of Stokes and anti-Stokes signals. However, the most broadly used Raman technique is anti-Stokes Raman spectroscopy, in which the signal from multiple anti-Stokes transitions are recorded simultaneously to increase the measurement accuracy. This can be utilised for temperature measurements with coherent anti-Stokes Raman spectroscopy (CARS), which uses three photons of specific molecule-dependent wavelengths and phase-matching to generate an anti-Stokes Raman transition [26]. The CARS technique has a high accuracy and relatively strong signal because the measured signal is coherent (i.e., the emission is a laser-like beam with low divergence) and can be separated optically from elastic scattering by particles. This method has been demonstrated for planar temperature measurements [78, 79] and in sooting flames [80], although it is typically applied for point measurements.

Similarly, the methods of DFWM and LITGS both require the interaction of three phase-matched beams to generate a coherent signal, from which the temperature can be measured [27, 81]. However, the generated signal beam is of the same wavelength as one (or all three) of the incident beams and therefore susceptible to interference from elastic scattering in particle-laden flows, although this interference can be reduced significantly using polarisation optics and by placing the detector sufficiently far from the measurement

volume for the scattering to become negligible [82]. Additionally, attenuation of the incident beams and signal trapping become increasingly significant in densely-loaded flows, and, while these methods have been demonstrated for planar measurement [83], the complex experimental arrangement leads to practical limitations.

For laser induced fluorescence (LIF) the wavelength of the probe beam is tuned to match an absorption line of a molecule or atom in the flow. The species is excited to a stable electronic energy level, with the fluorescence photon emitted to return the molecule to a lower state [84]. The emitted photons are of lower energy (i.e., longer wavelength) than the absorbed photon due to Stokes shift, which means that the fluorescence emissions can be separated from elastically scattered light using optical filtering. An example of fluorescence is shown by the $S_0 \rightarrow S_1$ transitions (the green dashed arrow) in the Jablonski diagram presented in Figure 2.3. This diagram also illustrates that non-radiative transitions (i.e., vibrational relaxation) or phosphorescence following internal conversion can return the molecule to the ground state, with the number of photons that are emitted through fluorescence per excited molecule characterised by the fluorescence quantum yield of the species [27].

The simplest method to measure the temperature using LIF requires only a single laser wavelength and detector, with the temperature determined from the intensity of the fluorescence emission [85]. However, the emission intensity is also proportional to the local tracer concentration and radiation flux, both of which must be kept constant or measured separately to accurately derive the temperature. This is particularly difficult in a particle-laden flow, because attenuation of the laser beam leads to significant spatial variations in the local radiation flux [60]. To overcome these issues the two-line, multi-line, and two-colour ratio methods were developed.

The two-line method utilises the temperature-dependent absorption spectrum of a molecule, with the ratio of the fluorescence intensity following excitation at two wavelengths measured to determine the temperature. This has been applied for conditions with strong interference, such as sooting flames, using the method of two-line atomic fluorescence (TLAF), which utilises the strong fluorescence from an atomic tracer seeded in the flow [46]. This tracer is excited separately from the ground and first electronic energy levels to a common second electronic energy level using two wavelengths tuned to the respective transitions. Because both transitions are to the common excited level, the influence of quenching on the measured fluorescence emissions is reduced. The resultant emissions corresponding to the complementary relaxation transitions are measured (e.g., following excitation from state 0-2

the emissions from the relaxation transition 2-1 are measured), from which the temperature can be derived. A brief time delay between the excitation pulses (~ 100 ns) is used to prevent interference between the excitation and relaxation transitions. Similar to LIF, the fluorescence emissions are optically separable from elastic scattering and the results are independent of both tracer concentration and laser power because the two emission lines are measured, making this technique suitable for flows with strong elastic scattering [86]. However, the tracer species must be chosen such that the Boltzmann distribution at the flow temperature has two stable energy levels with sufficient population densities, which typically requires the measurements to be performed at high temperatures such as in a flame.

The multi-line method measures the emission intensity of a tracer molecule with a well-characterised absorption spectrum for a series of excitation wavelengths. The excitation spectra can then be compared to reference spectra to determine the temperature. This method has been applied for a wide range of temperatures (300-1900 K) using nitric oxide as the tracer [87], under conditions with strong background interference. However, because the scanning is not instantaneous the method is primarily suitable for time-resolved measurements with steady conditions.

The two-colour ratio method utilises the change in emission spectrum with temperature of certain species [88]. The ratio of fluorescence emission intensities measured in two optically separated wavelength bands is calculated, from which the temperature can be derived [89]. Because the emissions are recorded from the same location the local laser power and tracer concentration are identical, so that their respective influences on the individual signal intensities cancel when the ratio is calculated. This method is easily extended to planar imaging by expanding the laser beam into a thin sheet and using two cameras with optical filters for detection.

Thermometry using laser induced phosphorescence utilises solid thermographic phosphor particles, which have a temperature dependent emission spectrum and/or phosphorescence lifetime [90, 91]. This method has been widely used for surface temperature measurements, but has also previously been demonstrated using the particles as flow tracers. To infer the gas temperature from the phosphorescence, the particles are required to have a sufficiently fast thermal response (i.e., be sufficiently small) to closely approximate the gas phase temperature [24]. However, in flows with strong radiation the particles are being continually heated, meaning that the particle temperature is not a true representation of the gas temperature [25].

Of the available methods, two-colour LIF with a vapour tracer has good potential to provide accurate measurements of the gas-phase temperature in

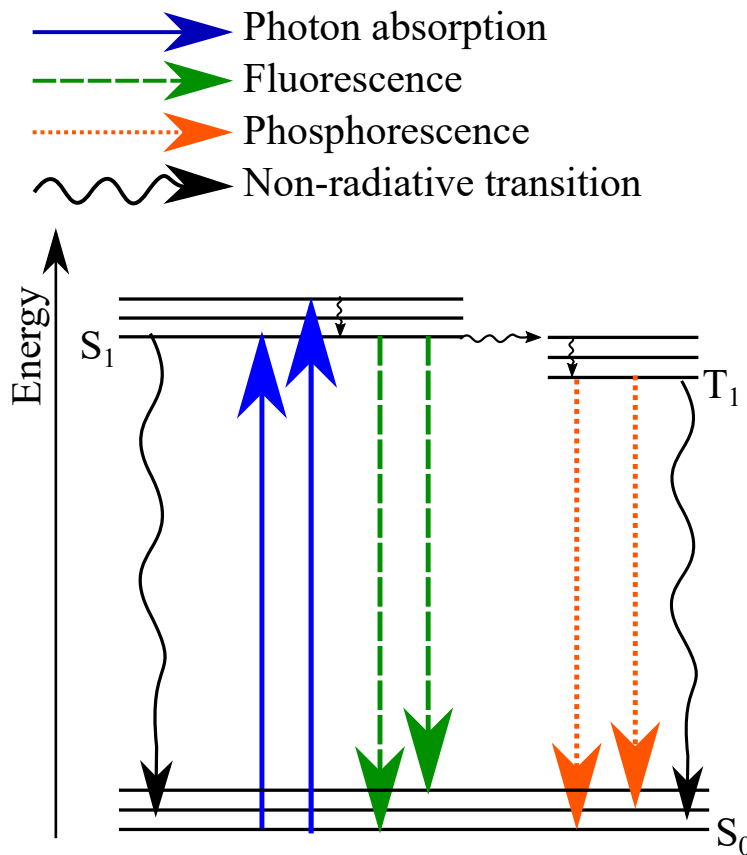


Figure 2.3: Simplified Jablonski diagram for an organic molecule, showing example relaxation mechanisms following electronic excitation. S_0 and S_1 denote the ground and first excited singlet states, respectively while T_1 denotes the first excited triplet state. Note that not all energy levels available for transitions are shown.

radiatively heated particle-laden flows relevant to industrial processes. To summarise, the advantages of this method are [92]:

- the capability to provide instantaneous planar measurements of the flow with good spatial resolution using a single pulse from a laser,
- the light sheet and detectors are both non-intrusive on the flow,
- the thermometry signal is optically separable from elastic scattering of the light sheet,
- the two-colour ratio that is used to determine the temperature is independent of variations in laser power and tracer concentration, and

- the tracer used is a vapour, so that it accurately reflects the gas temperature and exactly follows the fluid.

There are also limitations to this method, the most relevant being that:

- the use of the ratio from two detectors decreases the signal to noise ratio of the two-colour method compared to single detector methods,
- the accuracy of this method is yet to be assessed in a densely loaded particle-laden flow, and
- measurements using organic tracers are typically limited to temperatures < 600 °C due to the decrease in signal with temperature and pyrolysis of the molecules at elevated temperature [93, 94].

A further advantage of the two-colour LIF method is that it has the potential to be used in conjunction with previously demonstrated methods to non-intrusively measure other parameters within particle-laden flows, using optical filters to separate the required signal. These methods include the use of LIP for measurements of the particle temperature, number density, and velocity [24, 25].

Several fluorescent species have been utilised as the tracer for planar two-colour LIF thermometry, including toluene [89], anisole [95], 3-pentanone [96], and p-xylene [97]. Of these, toluene is a well-characterised tracer with good signal strength and sensitivity to temperature within the range of 20-400 °C [88, 94]. While other tracers such as anisole have a stronger signal than toluene and/or are less sensitive to detrimental oxygen- and self-quenching effects, toluene was chosen for the present experiments because it has been extensively investigated and demonstrated to be accurate in conditions with the potential for strong interference from scattering. Such measurements utilising two-colour toluene LIF thermometry include in optical engines [92, 98], near to reflective surfaces [93, 99], and in flows with oil droplets [100]. Two-colour toluene LIF has also been demonstrated to have a single shot precision of ± 8 °C at 100 °C, although the precision decreases with temperature because of the corresponding decrease in fluorescence signal strength with increasing temperature [93]. For these reasons, two-colour LIF with toluene as the tracer species was chosen to perform the gas-phase temperature measurements for the investigations included in the present thesis.

2.6 Summary and Research Gaps

Heat transfer in particle-laden flows is currently poorly understood, particularly for flows with strong thermal gradients, despite their widespread utilisation in industrial systems. This is primarily because of the complex, non-linear and mutually-interacting flow phenomena and heat transfer processes. The key research gaps identified in the present literature are:

1. there is a lack of available techniques that have been demonstrated for measurements of the gas-phase temperature with good spatial and temporal resolution in particle-laden flows within the two- and four-way coupling regimes;
2. neither the mean nor instantaneous temperature distribution within turbulent particle-laden flows subjected to high-flux radiation has been experimentally determined; and
3. the effect of flow parameters such as heating flux, particle diameter, and particle loading on these distributions are yet to be evaluated experimentally.

Chapter 3

Methods

Two main types of experiment were completed as part of the present thesis, both of which were designed to provide simultaneous measurements of the gas-phase temperature and particle number density.

1. Experiment type I consisted of a pre-heated particle-laden jet, with measurements performed for three different particle materials (Alumina, polymethyl methacrylate (PMMA), and zinc-activated zinc oxide) with median particle diameters spanning $1 < \bar{d}_p < 40 \mu\text{m}$.
2. Experiment type II consisted of a particle-laden jet heated using high-flux radiation, with measurements performed using a single particle material for series of peak heating fluxes ($0 \leq \dot{Q}_{peak}'' \leq 42.8 \text{ MW/m}^2$), time-averaged particle volumetric loadings ($0.625 \times 10^{-3} \leq \bar{\phi} \leq 1.4 \times 10^{-3}$), and median particle diameters ($173 \leq \bar{d}_p \leq 423 \mu\text{m}$).

A separate experimental arrangement was used for each experiment, although both arrangements utilised common sub-systems that were required to be designed and tested to meet the needs of the present investigation. These sub-systems were:

- the flow facility, consisting of a co-annular pipe jet within a well-characterised wind tunnel;
- the particle feeding system, which consisted of a screw feeder to provide a steady particle flow rate;
- a toluene seeding system; and
- the optical arrangement for laser diagnostics (i.e., the lasers, cameras, lenses, and filters used).

This chapter presents the details of each sub-system, measurement technique, experimental arrangement, and analytical method utilised in the present thesis.

3.1 Wind tunnel and jet

The wind tunnel presented in Figure 3.1 was designed to provide an optically accessible, well-defined particle-laden flow. The walls of the wind tunnel were made from acrylic with a 300×300 mm internal cross-section and test section length of 650 mm, which was designed to be oriented in either a vertically-upward or downwards configuration. Ambient air was driven through the wind tunnel using a variable-speed fan located downstream from the test section, with the spatially averaged flow velocity controllable in the range 0.5-4 m/s. Wire mesh screens and a honeycomb section upstream from the test section were used to reduce the influence of coherent fluid structures in the wind tunnel. Adjustable window sections positioned on each wall of the wind tunnel allowed optical access for each camera and laser used. Circular fused silica windows with a diameter of 50 mm were used in these sections, to efficiently transmit high-flux radiation in the wavelength range of 200-1000 nm with high optical quality.

The particle-laden flows investigated were of a jet issuing from a long, straight pipe that was centrally located within the wind tunnel. The central pipe was interchangeable, with pipes of diameter $D = 6.2$ and 12.6 mm of length up to 2080 mm utilised in the presented experiments. This pipe length is sufficiently long for the particle-laden flow to approach a fully developed condition [57]. An annular pipe co-axially located with the jet of diameter 69 mm and length 1100 mm was used to condition the flow and to allow toluene seeding throughout the entire measurement region. Both the central and annular pipes employed symmetrical inlets to reduce flow bias. The velocity profile throughout the wind tunnel and jet flow (without particles) was characterised using a hot-wire anemometer for a series of flow conditions, with these results presented in Appendix A.

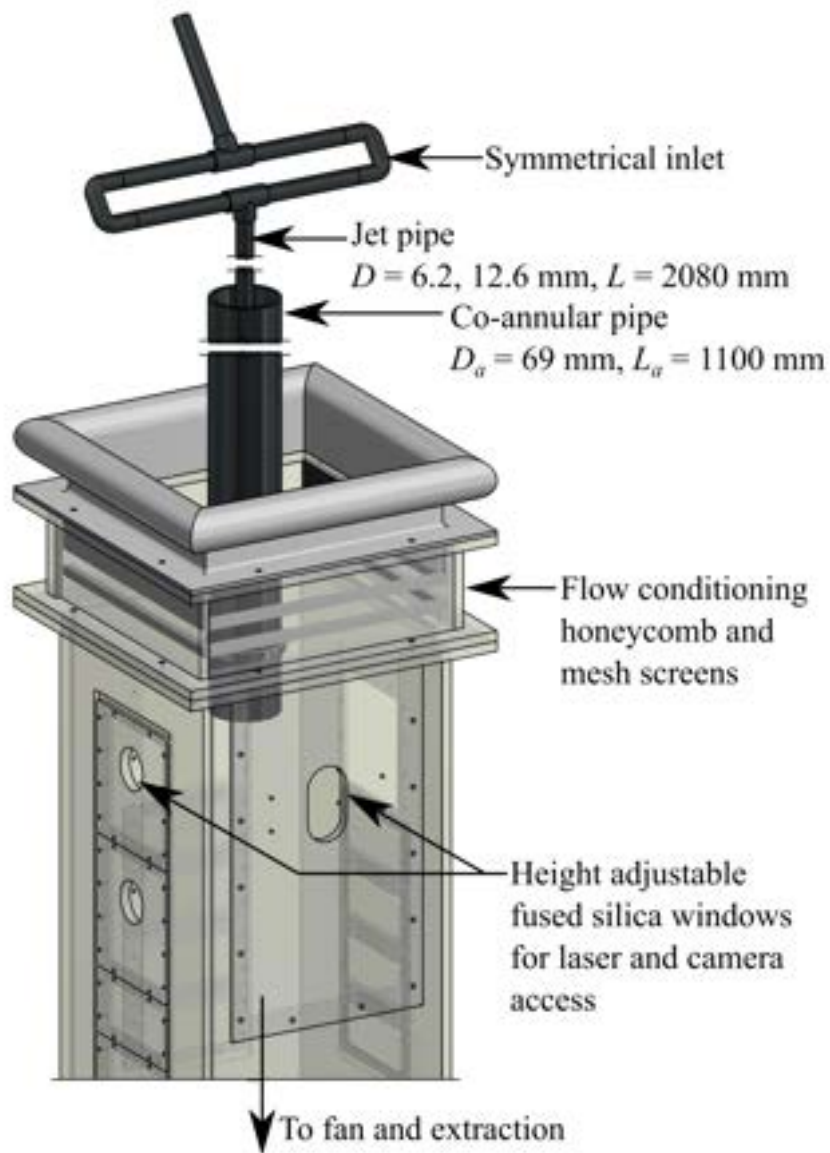


Figure 3.1: The wind tunnel that was designed to provide optically accessible measurements of a particle-laden jet flow.

3.2 Screw feeder

Several screw feeders were designed to introduce particles into the central jet flow for the range of volumetric loadings required for experiments ($\bar{\phi} = 0.1 - 1.5 \times 10^{-3}$), for the variety of particle materials used in Experiments I and II with bulk densities in the range $800 < \rho_b < 3,280 \text{ g/cm}^3$. Two hoppers were built to house the particles and screws: one of acrylic that was used with screws of outer diameter $D_o = 38 \text{ mm}$, for particle volumetric flow rates of $4 < \dot{V}_p < 28 \text{ cm}^3/\text{s}$; the other 3D printed using polylactic acid that was used with screws of $D_o = 17.5 \text{ mm}$, for $1.5 < \dot{V}_p < 10 \text{ cm}^3/\text{s}$. The screws were 3D printed to allow for a variety of complex designs to be manufactured efficiently. The screws were printed in two halves that were glued together and mounted to a stainless-steel shaft, to improve the screw rigidity and allow the shaft to be coupled to the motor.

For fundamental, well-characterised measurements of a particle-laden flow, the instantaneous particle loading is required to be temporally steady. This is not typically the case for standard screw designs, for which the output pulses at a frequency equal to the rotational speed of the screw. As such, the key design parameters of the manufactured screws were varied to determine which configurations reduce the influence of this pulsing. The volumetric flow rate and steadiness of material output from the designed screws is dependent on a series of parameters, most importantly the [101]:

- inner (D_i) and outer (D_o) screw diameters,
- screw pitch (P),
- number of screw flights (F),
- rotational speed (ω),
- screw flight thickness,
- clearance between screw and casing, and
- the internal friction angle (or the angle of repose) of the particles, with an increase in the internal friction angle typically corresponding to a decrease in the volumetric flow rate.

The key screw design parameters that were varied for the present measurements are illustrated for an example screw in Figure 3.2. The rotational speed of the screw was controlled in the range $0 \leq \omega \leq 200 \text{ rpm}$ using a stepper motor. The output mass flow rate for each screw was calibrated as a function

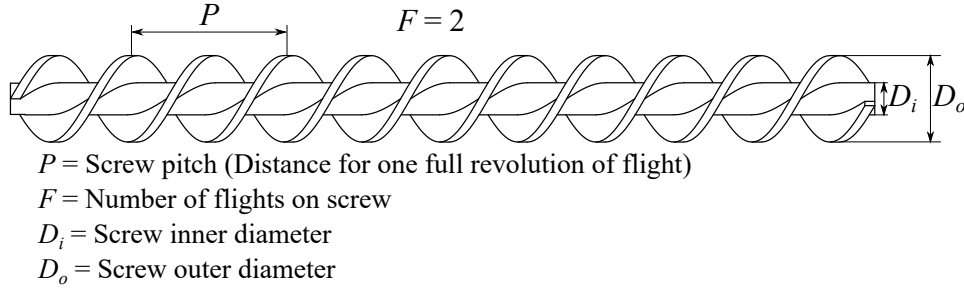


Figure 3.2: Diagram of design parameters for the screws used to analyse the particle volumetric flow rate and the steadiness of output from the screw feeder.

Table 3.1: Design parameters of the series of screws manufactured

Screw	D_o	D_i	P	F	c_p	c_i	c_{pe}
A	17.5	6.5	15.8	1	0.9	0.37	0.9
B	17.5	6.5	23.7	1	1.35	0.37	1.35
C	17.5	6.5	10.5	1	0.6	0.37	0.6
D	17.5	6.5	15.8	1	0.9	0.54	0.9
E	17.5	6.5	15.8	1	0.9	0.71	0.9
F	17.5	6.5	31.6	2	1.8	0.37	0.9
G	17.5	6.5	63.2	4	3.6	0.37	0.9

of ω for each particle used, by measuring the cumulative mass of particles expelled from the screw as a function of time using a collection container attached to a strain gauge recording data at 10 Hz. From this data the mass flow rate (\dot{m}), and hence also the volumetric flow rate, were calculated.

Seven separate screws were designed and manufactured to evaluate the relationship between the pitch, the core diameter, and the number of flights on the output volumetric flow rate and steadiness of the output. The outer diameter of the screws was kept constant at $D_o = 17.5$ mm, for use with the 3D printed hopper. The typical screw design guideline used in industry is for the pitch to diameter ratio $c_p = P/D_o \approx 1$ [101], so that screws were designed for a series of c_p around this value. The other dimensionless parameters varied in the screw design were the core to outside diameter ratio, $c_i = D_i/D_o$, and the effective pitch to diameter ratio, defined as $c_{pe} = c_p/F$. The design parameters of the resultant series of screws that were designed and manufactured are summarised in Table 3.1, with a diagram of each screw presented in Figure 3.3.

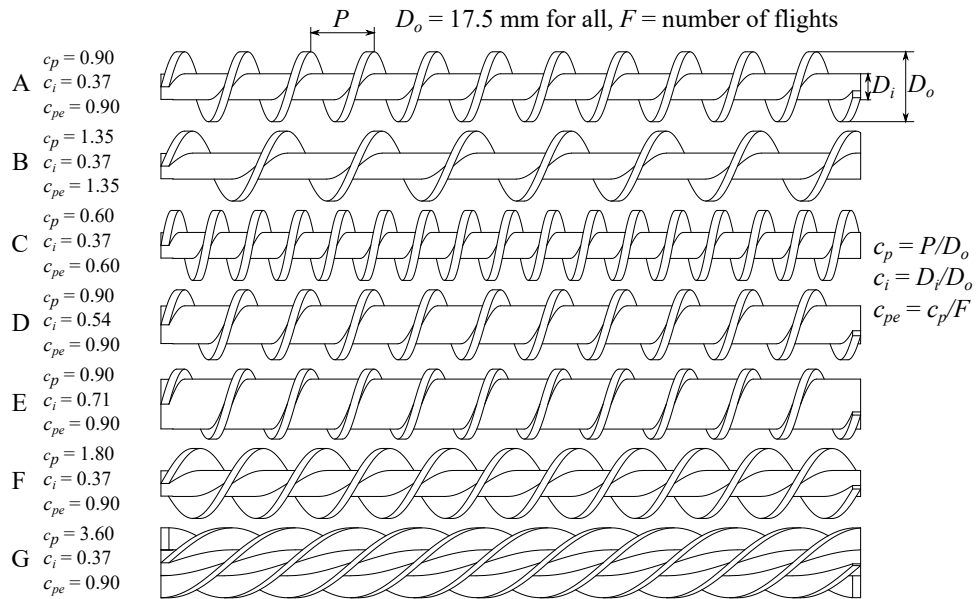


Figure 3.3: Screws that were manufactured to investigate the effect of pitch, core diameter and number of flights on the magnitude and steadiness of the particle mass flow rate.

3.2.1 Output flow rate

The output mass flow rate of $40 \mu\text{m}$ PMMA particles from the screws as a function of ω , together with \dot{m} as a function of c_p , c_i and F , are presented in detail in Appendix B. As such, these results are only briefly summarised here. The mass flow rate \dot{m} was found to increase linearly with an increase in ω for each screw, consistent with expectation. For the three parameters varied:

- \dot{m} increased with c_p for the three pitches investigated. The data points from the three screws used are insufficient to determine the optimal pitch, however it can be inferred that it is closer to $c_p = 1.35$ than $c_p = 0.9$ for the present arrangement;
- \dot{m} decreased with an increase in c_i , consistent with the decrease in volume of material within each screw pitch with an increase in c_i ;
- \dot{m} was similar for $F = 1$ and 2 ($c_p = 0.9$ and 1.8 , respectively), with a strong decrease for $F = 4$ ($c_p = 3.6$). This decrease for $F = 4$ is attributed to the relatively long pitch of each individual flight, for which the material is likely to be predominantly transferred axially around the screw axis rather than radially towards the outlet [101].

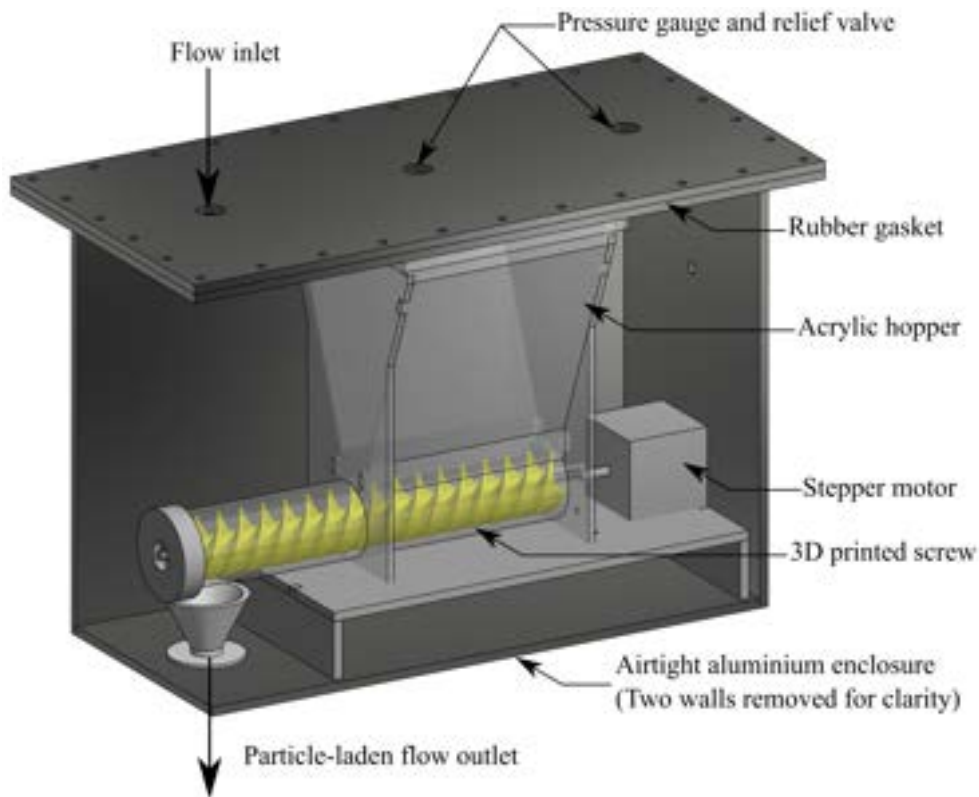


Figure 3.4: The acrylic screw feeder assembly and aluminium enclosure used to seed particles into the gas flow.

A sealed aluminium enclosure was also built to house the screw feeder during experiments, in which the particles were combined with a gas flow of known volumetric flow rate to allow control of the volumetric loading of particles. A diagram of this arrangement is presented in Figure 3.2. The lid of the enclosure is removable to allow access to the particle hopper, with a rubber gasket and regular evenly spaced bolts used to ensure an airtight seal is maintained while in operation. On the lid of the enclosure are three tapped holes for connection to the flow inlet, a pressure gauge, and a pressure relief valve, with the particle-laden flow exiting the enclosure through a funnel leading to tapped hole on the base.

3.2.2 Output steadiness

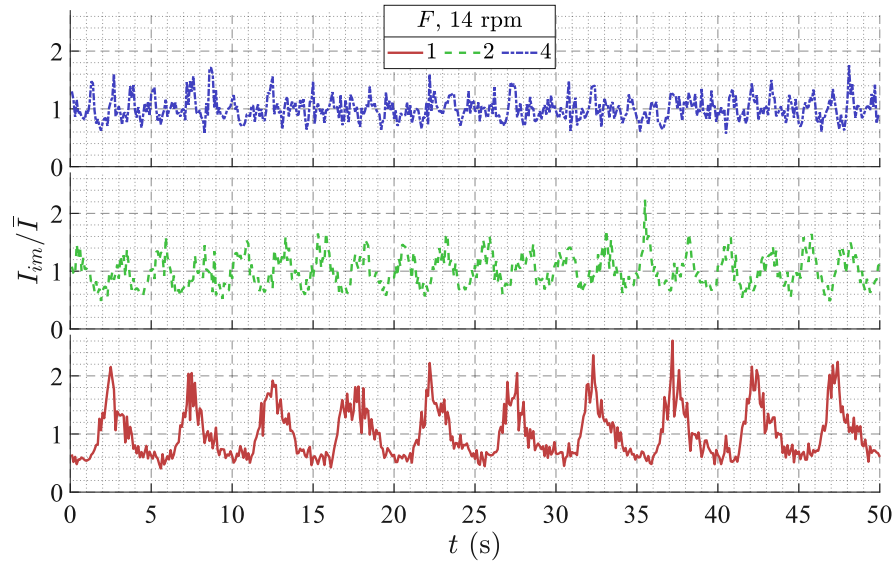
The steadiness of the particle flow rate was also evaluated for each screw at a series of rotational speeds by seeding the $40\ \mu\text{m}$ PMMA particles into the wind tunnel arrangement for Experiment II, as described in Section

3.4.2 and presented in Figure 3.10, although without heating. The jet flow was of particles seeded in air only, while the annular flow also consisted of air. Images of the scattering from the 532 nm light sheet by particles were recorded at 10 Hz for approximately 50 seconds, to ensure all time scales from the screw were covered. It is possible that the instantaneous particle volumetric changed from the screw outlet to the jet within the conveying pipes, although any such effects are expected to be minor and to affect the flow rate distribution measured for each screw equally. The instantaneous particle number density near to the jet outlet was derived from the mean value of the scattering intensity measured within the region bounded by $1 < x/D < 3$, $|r/D| < 0.35$ for each image. The steadiness of the particle flow rate was then analysed for each screw using the time series of the instantaneous scattering intensity. The fast Fourier transform (FFT) of each time series was also calculated to identify the frequency of the variations in particle loading.

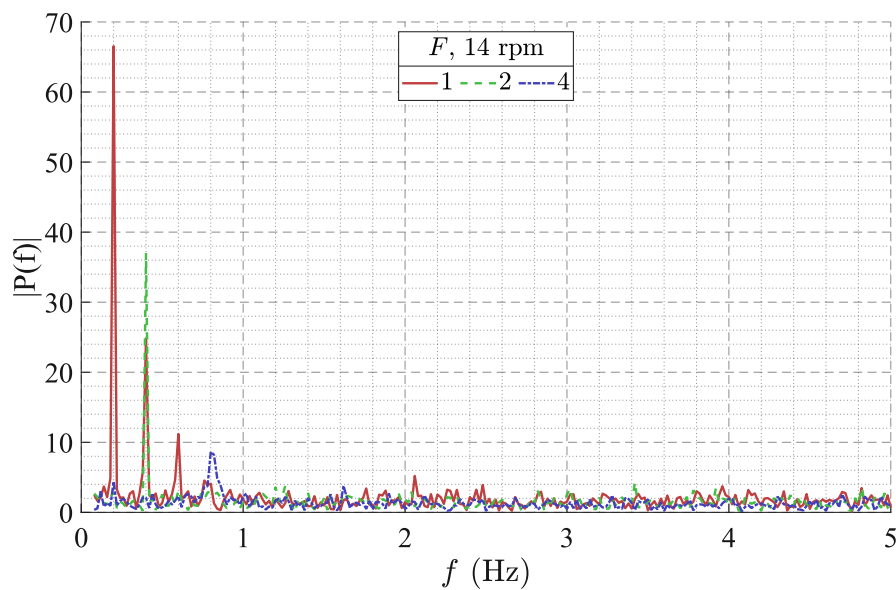
The results from these experiments are also presented in detail in Appendix B. Figure 3.5 presents the key results of the measured time series of scattering intensity, normalised by the mean value (I_{im}/\bar{I}), for the screws with 1, 2, and 4 flights with $c_{pe} = 0.9$ and $\omega = 14$ rpm (a), together with the corresponding FFT of the time series (b). The results show that there is a periodic dependence of I_{im}/\bar{I} with time, most significantly for the screw with $F = 1$. This is clearly illustrated in the FFT for the screw with $F = 1$, with a clear first peak at a frequency of $f \approx 0.2$ Hz and subsequent peaks of lower magnitude at integer multiples of this frequency. This frequency corresponds closely to the 14 rpm rotational speed of the screw, which is equivalent to 0.23 Hz. The temporal variation in the measured intensity can be seen to decrease with an increase in F . Additionally, the frequency at which the peaks of greatest magnitude in the FFT occur also increases proportional to F , with the peak location well described by $f = F\omega/60$. The magnitude of the peaks of the FFT also decrease significantly with an increase in F , which implies that the output from the screw with $F = 4$ is much steadier than for the typical design with $F = 1$.

The effect of the other varied parameters (c_p , c_i , and ω) on the steadiness of the particle flow rate output from the screw was relatively minor to that of changing the number of flights. To summarise the results presented in Appendix B, the steadiness of the flow was found to:

- increase slightly with an increase in c_p ,
- be independent of c_i , and



(a)



(b)

Figure 3.5: Time series of Mie scattering intensity from particles in the flow for screws with 1, 2, and 4 flights (a), together with the fast Fourier transform for the same screws (b), normalised by the time-averaged mean.

- increase slightly with ω .

3.2.3 Particle properties

Several particle materials with various sizes, luminescence properties, and radiation absorptivities were selected to be used in the experiments. For Experiment I, which aims to quantify the effect of particle luminescence and size on the interference to two-colour LIF, alumina, zinc activated zinc oxide (ZnO:Zn), and PMMA particles were used. The properties of each of these are presented in Table 3.2, with the results from a spectral analysis of the luminescence properties of each material discussed in detail in Paper I [32] and Chapter 4.1.

The primary reason for selecting three different particle materials was the different emissions from each following illumination with 266 nm light:

- alumina does not emit luminescence,
- ZnO:Zn emits strong phosphorescence [90, 102], and
- PMMA emits broadband fluorescence.

The PMMA particles are spherical with a standard deviation in the diameter of less than 5% [57]. Because of this, four different median diameters of these particles were selected to be used, to isolate the effects of particle diameter on the interference as well as for accurate discrimination of the particle Stokes number.

For Experiment II, it was desirable to use near-spherical particles with good radiation absorbance (to maximise the temperature increase of the particles), a narrow size distribution (to isolate the influence particle diameter), and a high melting point (for simplified heat transfer interactions).

Table 3.2: Particle properties. The value in the Emissions column are those recorded following 266 nm illumination

Material	\bar{d}_p (μm)	$d_{p,agg}$ (μm)	Sk_D	ρ_p (kg/m^3)	Shape	Emissions (nm)
Alumina	0.5	< 40	0.01	3,950	Crystalline	None
ZnO:Zn	1	< 200	0.03	5,600	Crystalline	350-600
PMMA	6	N/A	0.26	1,200	Spherical	270-400
PMMA	10	N/A	0.73	1,200	Spherical	270-400
PMMA	20	N/A	2.9	1,200	Spherical	270-400
PMMA	40	N/A	11.7	1,200	Spherical	270-400

The particles selected to meet these needs were Carbobead CP particles, which are comprised of aluminosilicate ceramic material. These particles are near-spherical and separated through sieving into a series of diameter distributions with median diameters of $\bar{d}_p = 173, 205, 238$ and $423 \mu\text{m}$. The absorbance of the Carbobead CP material was estimated to be $\alpha = 0.93$ based on previous measurements utilising a similar particle material [103].

3.3 Two-colour toluene LIF

Two-colour LIF has been developed as a robust technique for thermometry in challenging environments for optical measurements [88, 89]. This method utilises the temperature-dependent fluorescence emission spectrum from a tracer in the flow [85]. The intensity of fluorescence emissions from the tracer at a wavelength of λ following excitation by a monochromatic laser is proportional to the laser energy fluence (Q''), tracer concentration (n), tracer absorption cross-section (σ_{abs}), and tracer fluorescence quantum yield (Φ). These parameters are typically a function of spatial location (\mathbf{x}), temperature (T), or pressure (p) [104]. The emission intensity I_λ is well described by the equation:

$$I_\lambda \propto Q''(\mathbf{x})C(\mathbf{x})\sigma_{abs}(T(\mathbf{x}))\Phi_\lambda(T(\mathbf{x}), p). \quad (3.1)$$

If the distributions of radiative flux, pressure, and tracer concentration in the flow are uniform, of a known distribution, or measured separately, the temperature of the flow can be determined directly from the intensity of the fluorescence emission. However, this is typically not the case in particle-laden flows because attenuation leads to significant variations in the local radiative power. Additionally, particle-laden flows under conditions relevant to practical and industrial systems are typically turbulent with significant mixing, which in turn leads to significant variations in concentrations and pressures. To overcome similar challenges for flows in harsh measurement environments, the method of two-colour LIF was developed [88, 89].

Two-colour LIF measures the intensity of fluorescence emissions in two spectral channels (λ_1 and λ_2) from the same probe volume, with the signal for the two channels separated using optical filters. The ratio of emission intensity in these channels is then calculated, for which the influences of radiative flux, toluene concentration, and pressure cancel. The resultant ratio is proportional to temperature only, given by [89]:

$$\frac{I_{\lambda 1}}{I_{\lambda 2}} \propto \frac{\sigma_{abs}(T(\mathbf{x}))\Phi_{\lambda 1}(T(\mathbf{x}))}{\sigma_{abs}(T(\mathbf{x}))\Phi_{\lambda 2}(T(\mathbf{x}))}. \quad (3.2)$$

The effect of the absorption cross section also cancels out, meaning that the emission ratio remains a function of temperature only. The flow temperature can therefore be calculated from the equation:

$$T(\mathbf{x}) = F \left(\frac{I_{\lambda_1}(T, \mathbf{x})}{I_{\lambda_2}(T, \mathbf{x})} \right), \quad (3.3)$$

where F is a function determined through calibration.

Toluene was chosen as the fluorescent tracer to be used for temperature measurements in the presented experiments because it has previously been utilised in a range of challenging conditions, as discussed in Section 2.5. The absorption transition typically utilised for toluene LIF is that from the ground state to the first excited singlet state, $S_0 \rightarrow S_1(\pi, \pi^*)$ [88]. The absorption spectrum corresponding to this transition is strong in the range 240-270 nm at room temperature [105], with this range broadening with an increase in temperature [88]. Common wavelengths used for laser diagnostics within this range include at 248 nm, from a Krypton Fluoride (KrF) excimer laser, and at 266 nm, from the fourth harmonic of a neodymium-doped yttrium aluminium garnet (Nd:YAG) laser. The 266 nm beam from a pulsed Nd:YAG laser (Quantel Q-smart) was used to excite the toluene for both experiments performed for this thesis. The Nd:YAG laser was chosen because it is relatively efficient and low cost to provide the excitation wavelength at a flux sufficient to generate the required toluene fluorescence emissions, compared to dye lasers, while also being low-maintenance, which assists with effective and cost-efficient measurement.

The fluorescence emission spectrum of toluene following excitation at 266 nm for a series of flow temperatures, normalised by the peak value, is presented in Figure 3.6. The fluorescence emissions can be seen to be in the range 260-400 nm at 23 °C, with the peak intensity occurring at 280 nm. This emission spectrum shifts to longer wavelengths with an increase in the flow temperature, with the peak wavelength increasing at a rate of ~ 0.02 nm/K. Additionally, the intensity of the red-side (i.e., greater λ) tail of the emission increases relative to the peak with an increase in temperature. The approximate ranges that were used for the two-colour LIF thermometry channels (λ_1 and λ_2) in the present experiments are also marked on the graph by the blue and red shaded regions, respectively. The full details of the spectral channels used are described in Paper I and Paper II for Experiments I and II, respectively, with a summary presented in Section 3.4.1. It can be seen that the normalised emission in the band λ_1 typically encompasses the peak emission wavelength for all temperatures, while for the band λ_2 the total (integrated) emission intensity increases significantly relative to the

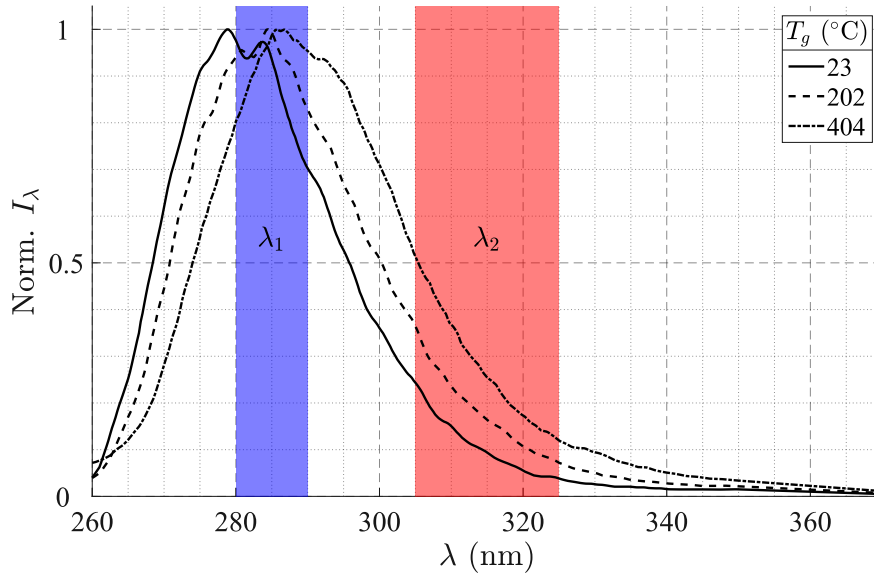


Figure 3.6: The normalised fluorescence emission spectra of toluene following 266 nm excitation for a series of temperatures together with example wavelength bands λ_1 and λ_2 used for two-colour LIF thermometry, denoted using the shaded regions (the emission spectra data are adapted from Faust et al. [107]).

peak with an increase in temperature. The temperature of the toluene tracer can therefore be inferred from this relative change in intensity recorded.

The magnitude of the fluorescence signal from toluene is strongly reduced in the presence of molecular oxygen due to collisional quenching (i.e., non-radiative de-excitation of the toluene molecule that occurs upon contact with an oxygen molecule [106]). In an environment with 20% oxygen by volume, such as for atmospheric air, the fluorescence quantum yield of toluene is more than an order of magnitude weaker than for pure nitrogen. Therefore, the present experiments utilised pure nitrogen as the carrier gas for both the jet and co-flow.

3.3.1 Toluene seeding

Two toluene bubblers were also designed and manufactured to selectively seed toluene vapour into the jet and annular flows. A dry flow of nitrogen was bubbled through a bath of liquid toluene, as shown in Figure 3.7, resulting in a toluene concentration of 2.75% by volume (corresponding to the saturation concentration at room temperature [108]) at the bubbler outlet. The final

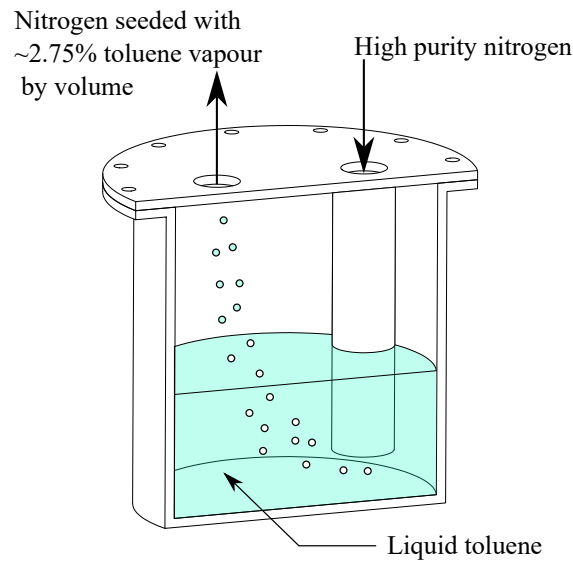


Figure 3.7: Schematic diagram of the bubbler manufactured to seed toluene in flows. The view is sectioned to show internal detail.

concentration of toluene in the jet and annular flows was controlled by combining the seeded flow with an unseeded bypass stream. The bubbler was manufactured from aluminium with a PTFE gasket, because these materials are resistant to reaction with toluene.

3.4 Experimental arrangements

In addition to the different wind tunnel arrangements, particles used, and flow conditions, each experiment also utilised separate optical and heating systems. The following sub-sections describe the complete arrangement used for each experiment in detail.

3.4.1 Arrangement for Experiment I

The primary aim for Experiment I was to assess the suitability of the planar two-colour LIF measurement for measurements of the gas-phase temperature in densely loaded ($\phi > 10^{-4}$) particle-laden flows. A schematic diagram of the arrangement used for these measurements is presented in Figure 3.8, with the key experimental parameters summarised in Table 3.3. The wind tunnel was oriented vertically upwards with the central jet pipe of diameter $D = 6.2$ mm employing nitrogen as the carrier gas. The bulk mean velocity of the flow at the jet exit was $U_{g,b} = 12.3$ m/s, with a resultant jet exit Reynolds

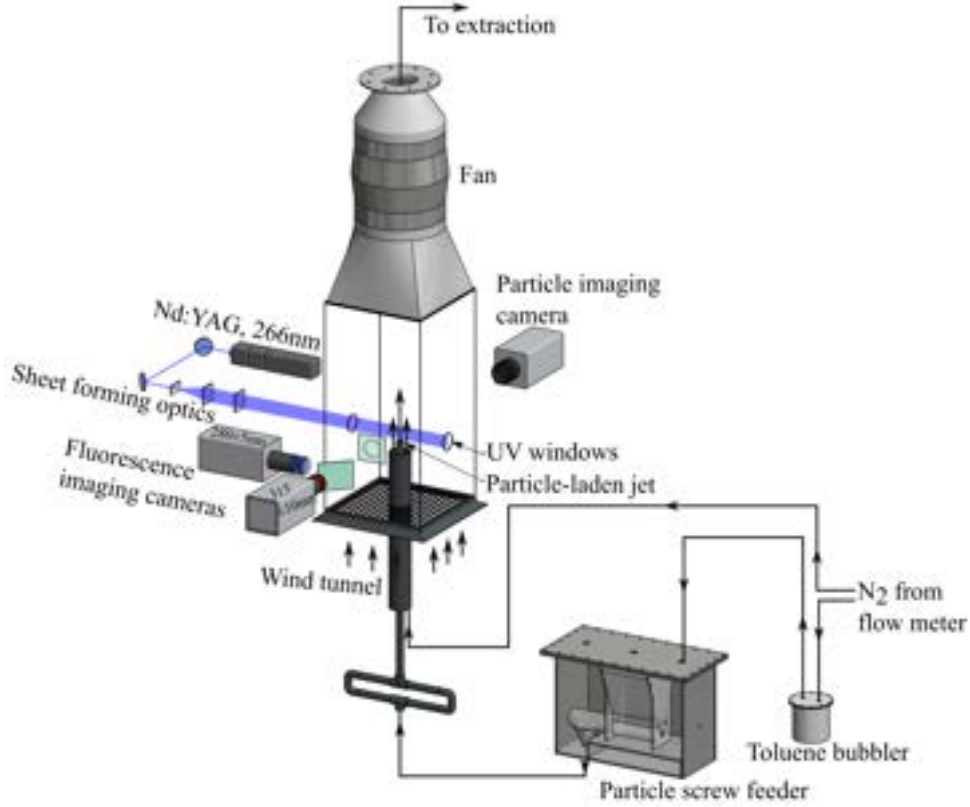


Figure 3.8: Experimental arrangement of the particle-laden jet system used for simultaneous measurements of gas temperature using two-colour LIF and particle number density from Mie scattering.

number of:

$$Re_D = \frac{\rho_f U_{g,b} D}{\mu} = 5,000. \quad (3.4)$$

Both toluene and particles were seeded into the jet flow, with an approximate toluene concentration of $C = 2.75\%$ by volume and an average particle volumetric loading of $\bar{\phi} = 4 \times 10^{-4}$. The temperature of the jet flow was controlled using a tape heater fitted to the outside of the jet pipe. The co-annular flow of unseeded nitrogen issued from a pipe of diameter $D_a = 69$ mm with an exit bulk mean velocity of $U_{g,a,b} = 1$ m/s. This jet-to-co-flow velocity ratio of $U_{g,b}/U_{g,a,b} \approx 12$ was chosen to match the previous pipe-jet experiments of Lau and Nathan [44].

Toluene vapour was used as the tracer for two-colour LIF with the excitation beam from the fourth harmonic of a Quantel Q-smart Nd:YAG laser.

The 266 nm beam was formed into a sheet 40 mm high and approximately 0.3 mm thick in the measurement region. The fluence of the light sheet in the measurement region was approximately 417 mJ/cm^2 . At this fluence the fluorescence response is highly non-linear [109], although the intensity ratio was verified to be independent of fluence within the range $14\text{--}654 \text{ mJ/cm}^2$ using a spectrometer (see Section 4.1.1). The channels used for two-colour LIF were recorded on separate PI-Max4 intensified CCD cameras, each focussed using a spherical $f = 100 \text{ mm}$ UV lens with an iris aperture (Thorlabs LB4821). Both cameras were positioned on the same side of the wind tunnel so that the optical path through the flow is identical for each channel. This is important to ensure that the effects of attenuation and signal trapping are the same for each channel, meaning the calculated intensity ratio is independent of these artifacts. Optical filters were used to suppress the detection of scattered light at 266 nm and a plate beam-splitter was used to separate the fluorescence emission into the two channels, centred at 280 and 315 nm. Additional filters were also used to suppress the light at wavelengths from fluorescence, scattering, and background noise that were outside of the chosen bands for each channel. The full details of these filters are presented in Paper I [32], with the resultant optical density of each channel, calculated from the manufacturers data, presented in Figure 3.9. The particle volume fraction distribution was measured simultaneously with the fluorescence images using the Mie scattering of the 266 nm sheet from particles, imaged using a PCO HSFC pro with a Nikon $f = 50 \text{ mm}$ F/1.4 lens. This camera was positioned diametrically opposite to the LIF channel cameras and was not configured with any optical filters. The imaging region was bounded by $0.5 < x/D < 6$, $|r/D| < 2.75$, where x is the axial co-ordinate parallel to the pipe axis and r is the radial co-ordinate parallel to the direction of laser light with the origin of these co-ordinates being the jet centreline at the exit plane.

The particles were introduced in the flow using the screw feeder system described in Section 3.2, with the particles in this experiment deliberately chosen to generate interference and introduce increased uncertainties to the temperature measurement from a range of sources. These include Mie scattering, signal trapping, attenuation of light from the laser, and luminescence emissions. The particles used are listed below, with the full details presented in Section 3.2.3:

- spherical PMMA particles of diameter $d_p = 6, 10, 20, 40 \text{ }\mu\text{m}$, with resultant jet exit Stokes numbers of $Sk_D = 0.26, 0.73, 2.9, 11.8$;
- alumina particles predominantly of $d_p \approx 1 \text{ }\mu\text{m}$ but forming aggregates up to $40 \text{ }\mu\text{m}$, with $0.02 < Sk_D < 38.5$; and

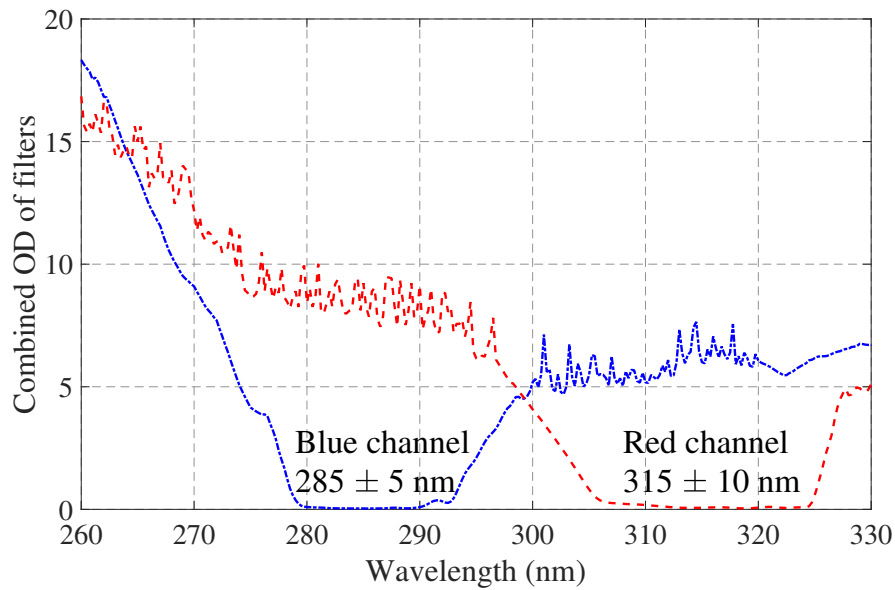


Figure 3.9: Combined optical density (OD) as a function of wavelength for all filters used to form each channel for two-colour LIF.

- zinc activated zinc oxide (ZnO:Zn) particles also predominantly of $d_p \approx 1 \mu\text{m}$ but with aggregates up to $200 \mu\text{m}$, with $0.03 < Sk_D < 1370$.

Both the alumina and ZnO:Zn particles were baked in an oven before being used in the experiments to remove moisture, which assisted to reduce the size and number of aggregates formed.

Table 3.3: Flow parameters used for Experiment I.

Parameter	Symbol	Value	Units
Jet pipe diameter	D	6.2	mm
Jet pipe length	L	1,100	mm
Annular pipe diameter	D_a	69	mm
Jet flow rate	\dot{V}_f	20.5	SLPM
Annular flow rate	$\dot{V}_{f,a}$	212	SLPM
Jet bulk mean velocity	$U_{g,b}$	12.3	m/s
Annular bulk mean velocity	$U_{g,a,b}$	1	m/s
Flow Reynolds number	Re_D	5,000	-
Average particle loading	$\bar{\phi}$	4×10^{-4}	-
Particle Stokes number	Sk_D	0.02-38.5 (Alumina)	-
		0.03-1,370 (ZnO:Zn)	-
		0.26, 0.73, 2.9, 11.8 (PMMA)	-
Jet toluene concentration	C	2.75	%v/v
Two-colour LIF channel	S_{285}	285 ± 5	nm
wavelengths	S_{315}	315 ± 10	nm
Imaging region	x	$0.5 < x/D < 6$	-
	r	$-2.75 < r/D < 2.75$	-

3.4.2 Arrangement for Experiment II

The primary objective of Experiment II was to assess the gas-phase temperature distributions in a radiatively heated particle-laden flow. The arrangement that was used for these measurements is presented in Figure 3.10, with the key flow parameters summarised in Table 3.4. The wind tunnel was oriented vertically downwards (opposite to that used for Experiment I) with a jet pipe of length $L = 2,080$ mm and diameter $D = 12.6$ mm, and with the co-annular pipe of diameter $D_a = 69$ mm. The jet flow was formed from the combination of two streams of nitrogen, one of 7 SLPM that was seeded with toluene and the other of 18 SLPM that conveyed the particles. The resultant toluene concentration of the combined pipe jet flow was approximately 0.75% by volume. The bulk mean velocity of the jet flow was $U_{g,b} = 3.6$ m/s, with a Reynolds number of $Re_D = 3,000$. Measurements of the temperature distribution were recorded for three time-averaged particle volumetric loadings of $\bar{\phi} = 6.25 \times 10^{-4}$, 1×10^{-3} and 1.4×10^{-3} . The annular flow of nitrogen had a bulk mean velocity of 0.3 m/s with a toluene concentration of approximately 0.25% at the outlet.

The toluene fluorescence was generated using a 266 nm beam from the fourth harmonic of a Quantel Q-smart Nd:YAG laser, with the particle loading

3.4 Experimental arrangements

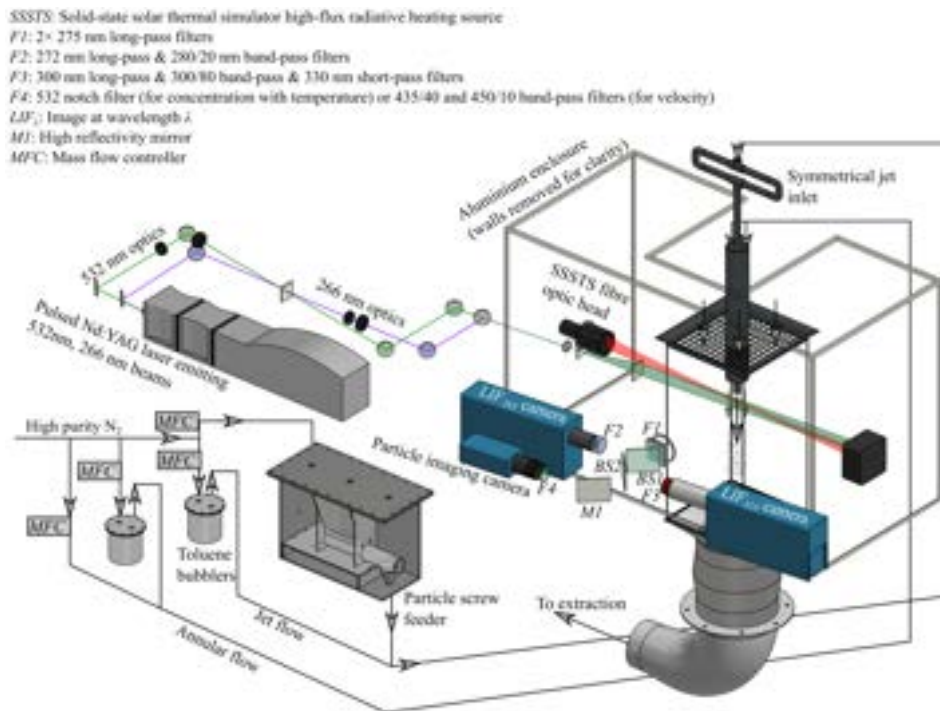


Figure 3.10: Experimental arrangement of the radiatively heated particle-laden jet used for simultaneous measurements of gas temperature, using two-colour LIF, and of particle number density, using Mie scattering.

imaged simultaneously using scattering from a beam of the second harmonic of the same laser (532 nm). Each beam was formed into a co-planar sheet for measurements in the region $0.3 < x/D < 3.7$, $|r/D| < 2$. The average fluences of the 266 nm and 532 nm sheets in the measurement region were 50 and 1.4 mJ/cm², respectively. Three cameras, two to image the LIF and one for Mie scattering, were used in this experiment. Each camera was positioned on same side of wind tunnel so that each channel shared a common optical path through the flow. In addition to the filters used for Experiment I, a second beam-splitter and additional filters were used to separate the fluorescence emissions and scattered light into the three channels required. The full details of the filters used are presented in Paper II [33], with the two LIF channels being centred at 285 and 315 while the channel to detect scattering used a narrow-band filter at 532 nm (termed S_{285} , S_{315} , and S_{532} , respectively). Two PCO Di-Cam intensified s-CMOS cameras were used to image S_{285} and S_{315} , focussed using a spherical $f = 100$ mm UV lens with iris aperture (Thorlabs LB4821) for S_{285} and a Soder UV 100 mm F/2.8 lens for S_{315} . The scattering channel S_{532} was imaged using a PCO.2000 CCD with a Tamron

macro 80-210 mm lens.

The velocity of the particles was also measured separately from the LIF measurements using the S_{532} camera in the same experimental arrangement as described above, except for a 4W 450 nm semiconductor laser (CivilLaser) with an adjustable, modulated power supply that was used in place of the Q-smart laser. That is, the particle velocities were measured under the same conditions as the temperature measurements, although not simultaneously. The power supply provided two pulses to the laser, with pulse widths of 30 and 40 μ s for the first and second pulses, respectively, and a delay of 270 μ s between pulses. The approximate pulse energies were 69 and 137 μ J for the first and second pulse, respectively. The particle velocities were determined from the two images of scattering from particles using an in-house particle tracking velocimetry (PTV) Matlab code.

The particle-laden flow was heated using a solid-state solar thermal simulator (SSSTS), which is formed from the combination of 41 mono-chromatic, infrared diode lasers emitted from a common fibre-optic head as described by Alwahabi et al. [110]. The axisymmetric beam of diameter ~ 12 mm on the focal plane emitted from the SSSTS is controllable up to powers $\dot{Q}_0 = 2,840$ W. The profile of the beam is near-Gaussian with a uniform intensity in the region near to the beam axis. The resultant peak flux of the beam, measured on the beam axis, was $\dot{Q}_{peak}'' = 42.8$ MW/m² for the peak power. The profile of the heating beam intensity, I , normalised by the peak value I_{peak} is presented in Figure 3.11a. Here, X is the co-ordinate of the heating beam parallel to the jet axial co-ordinate x , with the origin on the beam axis. The beam was aligned such that the axis intersected with the jet centreline 17.6 mm from the exit plane, as shown in Figure 3.11b together with the relative positions of the jet pipe and diagnostic laser sheets. The SSSTS beam was absorbed using a water-cooled power meter (Gentec model HP100A-4KW-HE) positioned down-beam from the wind tunnel, which also recorded the beam power at a sampling rate of 10 Hz. The entire experimental setup, including the fibre-optic head, wind tunnel, and power meter, was enclosed in an interlocked aluminium box for safe operation.

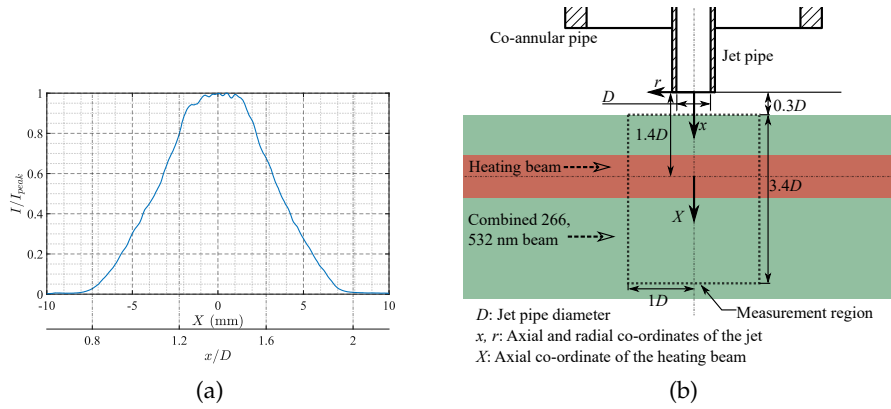


Figure 3.11: Schematic diagram of the measurement region with key co-ordinates and dimensions shown (a) and the axial profile of the heating laser intensity normalised by the peak intensity, I/I_{peak} (b).

A series of distributions of near spherical aluminosilicate particles (Carbobeard CP), with median diameters $\bar{d}_p = 173, 208, 238, 423 \mu\text{m}$, were used in this experiment. The particle size distribution of each of these was measured using a Malvern Mastersizer 2000, with the results presented in Figure 3.12. These particles were selected because they are non-luminescent (i.e., generate less interference to the two-colour LIF method) and have a high absorptivity. Additionally, these particles are similar to those that have previously been used for on-site testing of a particle-based CST receivers [30]. The resultant Stokes numbers of each of these particle distributions, calculated using the median diameter for the large eddy time scale, are $Sk_D = 86, 121, 163$ and 514, respectively.

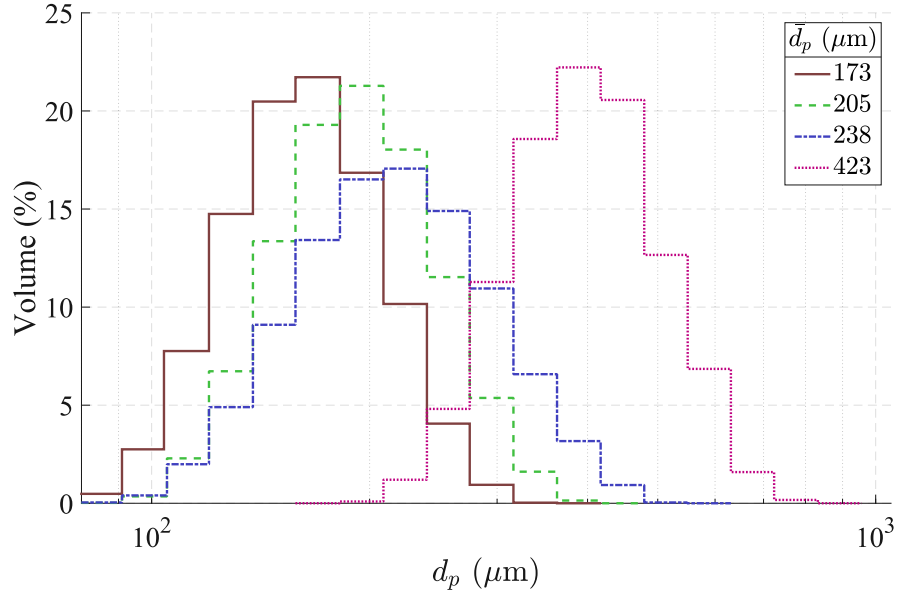


Figure 3.12: The measured volume-weighted particle diameter distribution of the particles used for Experiment II.

Table 3.4: Flow parameters used for Experiment II.

Parameter	Symbol	Value	Units
Jet pipe diameter	D	12.6	mm
Jet pipe length	L	2,080	mm
Annular pipe diameter	D_a	69	mm
Jet flow rate	\dot{V}_f	25	SLPM
Annular flow rate	$\dot{V}_{f,a}$	55	SLPM
Jet bulk mean velocity	$U_{g,b}$	3.6	m/s
Annular bulk mean velocity	$U_{g,a,b}$	0.3	m/s
Flow Reynolds number	Re_D	3,000	-
Average particle loading	$\bar{\phi} (\times 10^{-3})$	0.625, 1, 1.4	-
Particle Stokes number	Sk_D	86, 121, 163, 514	-
Jet toluene concentration	C	0.75	%v/v
Annular toluene concentration	C_a	0.25	%v/v
Two-colour LIF channel wavelengths	S_{285} S_{315}	285±5 315±10	nm
Imaging region	x r	0.3 < x/D < 3.7 -1 < r/D < 1	-
Heating laser powers	\dot{Q}_0	0, 910, 1,430, 1,950, 2,410, 2,840	W

3.4.3 Spectroscopic measurements

The spectral response of the toluene and particles to the 266 nm light was measured for two reasons: 1) to assess whether there is particle luminescence that interferes with the wavelength bands used for two-colour LIF and 2) to determine whether the toluene emission spectrum and particle luminescence emissions are independent of the laser power within the range investigated. Figure 3.13 presents the experimental arrangement used to assess particle luminescence following exposure to the 266 nm laser light. Steel plates were coated with each particle material used in Experiment I (PMMA, ZnO:Zn, alumina). The laser beam was then focussed onto these plates using a spherical lens, with a beam diameter of 2 mm at the surface. The resultant fluence of the beam was calculated to be 31.8 mJ/cm^2 . Emissions from the plate were collected using a spherical lens and fibre optic probe then transferred through an optical fibre bundle to a spectrometer (Princeton Instruments Acton Series Spectrograph) with a 150 groove/mm grating. The emission intensity was recorded for wavelengths in the range of 280-500 nm in intervals of 0.17 nm.

Measurements of the emission spectra of toluene were also recorded for a series of radiative fluences within the range $14\text{-}654 \text{ mJ/cm}^2$, using the same spectrometer and focussing lens. These measurements were conducted under ambient conditions in the same arrangement as for Experiment II, as presented in Section 3.4.2, with the fibre-optic probe positioned in place of the first beam-splitter. The results from this assessment are presented in Section 4.1.1.

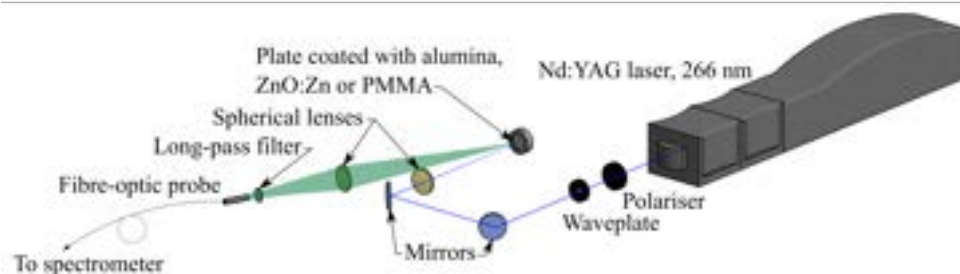


Figure 3.13: Arrangement used to measure the spectral response of the particle materials used (PMMA, ZnO:Zn, alumina) to the 266 nm light used for two-colour LIF.

3.5 Analytical heat transfer model

A simplified one-dimensional heat transfer model of the radiatively heated particle-laden flow was developed to estimate the particle- and gas-phase temperatures in Experiment II, adapted from the method presented by Kueh et al. [25]. The change in temperature with time of both a single, spherical particle and the surrounding volume of gas moving along the jet centreline was calculated using Equations 2.13 and 2.15, which consider the radiative heating of particles, the convection between particles and gas, and the radiation emitted from the heated particles. The incident radiation absorption was modelled to be a function of axial location to match the profile for the SSSTS beam presented in Figure 3.11.

In the model, the particle volumetric loading of the flow is assumed to be uniform and steady to match the jet exit values used in the experiments. A constant slip velocity ratio of $U_{slip} = 0.2U_f$ is used, approximated from the value measured by Gillandt et al. [43] for particles with $d_p = 110 \mu\text{m}$ and $\rho_p \approx 2,000 \text{ kg/m}^3$ at a loading of $\phi \approx 5 \times 10^{-4}$. Attenuation of the radiation up-beam from the particle is assumed to be negligible. The values for specific heat capacity (as a function of particle temperature), absorptivity, and emissivity are estimated from those measured for similar particles [22, 103, 111]. The carrier fluid is modelled as pure nitrogen with the density, viscosity, and specific heat calculated as a function of the fluid temperature [112]. The model input parameters are summarised in Table 3.5. The results of the model are compared to the experimental measurements of the temperature distribution in Section 4.2.

An example of the results from the heat transfer model of the axial evolution of the temperatures of both the particle- and gas-phases is presented in figure 3.14 (a), together with the corresponding values of the absolute power of each heat transfer process (b). The results presented are for the case with $\bar{d}_p = 173 \mu\text{m}$, $\bar{\phi} = 1.4 \times 10^{-3}$ and $\dot{Q}_0 = 2840 \text{ W}$ (note that data on the y-axis for the heat transfer powers are presented on a logarithmic scale), which are the conditions that the temperature increase is expected to be the greatest. It can be seen that the average particle temperature is expected to increase from the ambient by up to $315 \text{ }^\circ\text{C}$ within the heating region, while the average gas phase temperature continually increases within the heating region at a much lower rate than the particles. However, the temperature difference between the particles and gas means that the gas continues to be heated through convection with the particles to the downstream edge of the imaging region ($x/D < 4$), up to $110 \text{ }^\circ\text{C}$.

Table 3.5: Input parameters used for the analytical heat transfer model. The particle properties used were those previously measured for the Carbobead CP particles or similar [22, 30, 103]. The properties used for the gas were those of pure nitrogen. Temperature dependent parameters are indicated within the brackets in the Symbol column.

Input parameter	Symbol	Value
Peak heating flux	\dot{Q}''_{peak}	13.7, 29.4, 36.3, 42.8 MW/m ²
Particle diameter	d_p	173, 205, 238, 423 μm
Particle volumetric loading ($\times 10^{-3}$)	ϕ	0.625, 1, 1.4
Particle density	ρ_p	3,270 kg/m ³
Particle specific heat	$c_{p,p}(T_p)$	0.7-1.1 kJ/kgK
Particle absorptivity	α	0.89
Particle emissivity	ϵ	0.85
Particle velocity	U_p	2.9 m/s
Fluid velocity	U_f	3.6 m/s
Fluid density	$\rho_f(T_f)$	1.1-0.8 kg/m ³
Fluid viscosity	$\mu_f(T_f)$	$1.8\text{-}2.2 \times 10^{-5}$ Ns/m ²
Fluid specific heat	$c_{p,f}(T_f)$	1.04 kJ/kgK
Ambient temperature	T_a	20 °C

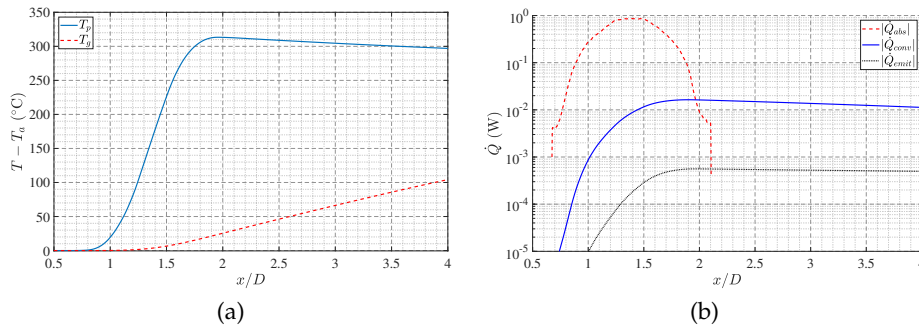


Figure 3.14: The simulated temperature from the one-dimensional model of both the particle and gas (a) together with the absolute powers of the modelled particle heat transfer components (b) as a function of axial distance, for the parameters listed in Table ?? with $\bar{d}_p = 173 \mu\text{m}$, $\bar{\phi} = 1.4 \times 10^{-3}$ and $\dot{Q}_0 = 2840 \text{ W}$.

3.6 Random particle distribution simulation

A simple simulation of particles in the jet flow with a Poisson distribution was generated using Matlab for two reasons:

1. to estimate the expected transmission of the radiative heating beam for each flow condition investigated in Experiment II, and
2. to compare the measured particle distribution with that of a Poisson distribution, which gives an indication of whether preferential concentration of the particles occurs in the flow.

The model generates a random distribution of particles in a cylindrical spatial domain with both a length and diameter of $1.5D$ positioned such that the centre of the domain coincided with the intersection of the jet axis and that of the SSSTS beam. The domain was discretised into pixels with sides of length $0.001D$, which was calculated to be sufficiently small for the results to converge. The particle locations were modelled using a weighted distribution such that the radial profiles of particle number density matched those measured for the case with $\bar{d}_p = 173 \mu\text{m}$ (see Section 4.2.1) with an average volumetric loading matching that of the experimental cases. The particles were modelled to be spherical with a diameter distribution equal to the measured distribution (see Figure 3.12). If there was spatial overlap between any of the generated particles in the 3-D space, they were removed and iteratively replaced until there was no overlap.

To estimate the absorption of the SSSTS beam, a 2-D binary mask of the particle locations projected in the direction of the laser was generated. The spatial distribution of heating laser flux in each resulting pixel was then calculated using the measured profile of the heating beam presented in Figure 3.11. The simulated transmission and attenuation of the heating beam through the flow was then calculated from the element-wise multiplication of the heating flux and the binary mask of projected particles, using the assumption of negligible particle transmissivity, forward scattering, and multiple scattering.

To compare the measured particle distribution with that of the Poisson distribution, only particles within the region corresponding to that of the laser sheet were retained. The particles within this simulated laser sheet were then analysed using the same Voronoi method as was used for the experiments (see Section 3.8.4).

3.7 Two-colour LIF calibration

The calibration to measure the two-colour LIF ratio as a function of temperature was completed separately for both Experiment I and II, because of the different filters, cameras and lenses used. The calibration measurements were performed in the same experimental arrangement as for the corresponding experiment, except with the flow pre-heated using the voltage-controlled tape heater fitted to the outside of the jet pipe. The method used was similar for both experiments, so that only the exact method used for Experiment II is described here. The LIF measurements were recorded for a series of temperatures in the range expected for experiments ($20 < T_g < 160$ °C, see Section 3.5), with the actual gas temperature measured using a thermocouple inserted into the flow near to the jet exit plane ($x/D < 0.5$). Once the temperature of the flow reached a steady state for each tape heater voltage setting, the thermocouple was removed to ensure that it does not interfere with the flow or laser sheet in the measurements. More than 100 two-colour LIF images were then recorded for each temperature, with the thermocouple then re-inserted into the flow to verify that the flow temperature remained constant throughout the measurements. The two-colour intensity ratio was then calculated for each flow temperature using the average value measured within the potential core region of the jet (i.e., region with uniform temperature equal to that at the outlet), bounded by $0.6 < x/D < 1$ and $|r/D| < 0.2$. The resultant calibration data, together with the intensity measured in each channel, are presented in Figure 3.15. The relationship between the intensity ratio and temperature was found to be well described by a linear relationship for each experiment. The decrease in fluorescence intensity with temperature was also demonstrated, with a decrease from $\sim 45,000$ counts to $\sim 8,000$ recorded for an increase in the temperature from $T_g = 20$ to 160 °C.

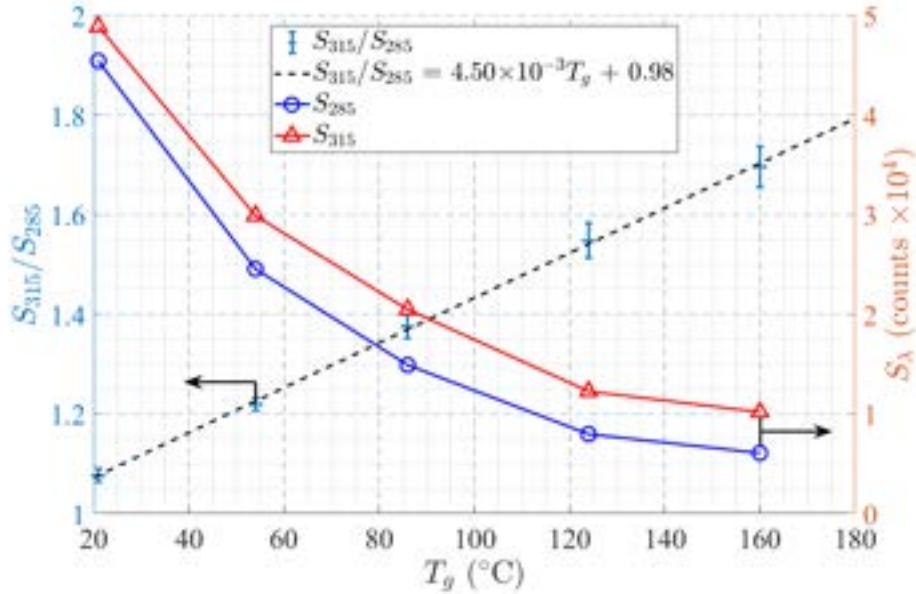


Figure 3.15: Calibration curve relating the two-colour LIF intensity ratio to temperature, together with the fluorescence intensity in each channel.

3.8 Image processing

3.8.1 LIF

The temperature was determined from the two-colour LIF images S_{285} and S_{315} using a series of stages, performed using in-house Matlab codes. The main processing steps were completed using the same methodology for both experiments, with only the detailed processing for Experiment II described here. Typical images from each camera, together with the derived temperature, are presented in Figure 3.16. Firstly, a background image, calculated from the average of ≥ 100 instantaneous images collected under experimental conditions but with flow switched off, was subtracted from each instantaneous image of the fluorescence emissions. The two channels were then aligned by imaging a target plate of holes and notches, which was illuminated from behind with a UV lamp. Matching points on each image were selected to transform S_{285} to match S_{315} using a least-squares fit. This aligned the images to within approximately 1 pixel.

A second image matching stage was performed by incrementing S_{285} in both the x and r directions over ± 1 pixel in intervals of 0.1 pixels, then calculating the intensity ratio S_{285}/S_{315} for each pixel in the region $0.5 < x/D < 0.8$ and $0.4 < |r/D| < 0.6$, where the temperature is uniform but

the fluorescence intensity gradients are strong. As shown in equations 3.2 and 3.3, the intensity ratio should be uniform in these regions because the temperature is uniform. Therefore, the alignment with the lowest variation in the measured ratio was used to correct each individual image. The change from the initial alignment following this second stage was typically < 0.3 pixels. It is particularly important for the alignment to be as exact as possible for the particle-laden flow because of the strong variations in fluorescence intensity from attenuation of the laser beam and signal trapping. Regions with a low fluorescence intensity were then removed to reduce the influence of measurement noise on the results, with the low intensity threshold defined separately for Experiments I and II. The details of the threshold calculation are provided in Paper I [32] and Paper II [33], respectively.

The fluorescence intensity ratio S_{285}/S_{315} was then calculated on a pixel-by-pixel basis for each instantaneous image pair. The images of S_{285}/S_{315} were then corrected for spatial variations in the camera collection efficiency and optical aberrations using images of the unheated flow, for which the intensity ratio is theoretically uniform. That is,

$$(\mathbf{S}_R)_{corr} = (\mathbf{S}_R) \circ \frac{(\mathbf{S}_R)_{amb}}{(\mathbf{S}_R)_{amb}} \quad (3.5)$$

where $S_R = S_{285}/S_{315}$, the bold notation indicates the image array, \circ indicates element-wise multiplication, and the subscripts *corr* and *amb* denote the corrected and room temperature intensity ratios, respectively. The intensity ratio in each corrected pixel was then converted to temperature using the calibration relationship, (presented in Paper I [32] for Experiment I and Figure 3.15 [33] for Experiment II). Each instantaneous temperature image was then smoothed using a median filter (5×5 pixels for Experiment II) to remove data from pixels that were outliers compared to their neighbours. This smoothing leads to a loss of spatial resolution, although the linear spatial dimension of the 5×5 kernel was still smaller than the laser sheet width in each experiment, which was $\geq 300 \mu\text{m}$. The resultant spatial resolutions of each camera for the two experimental arrangements are presented in Paper I and Paper II, respectively.

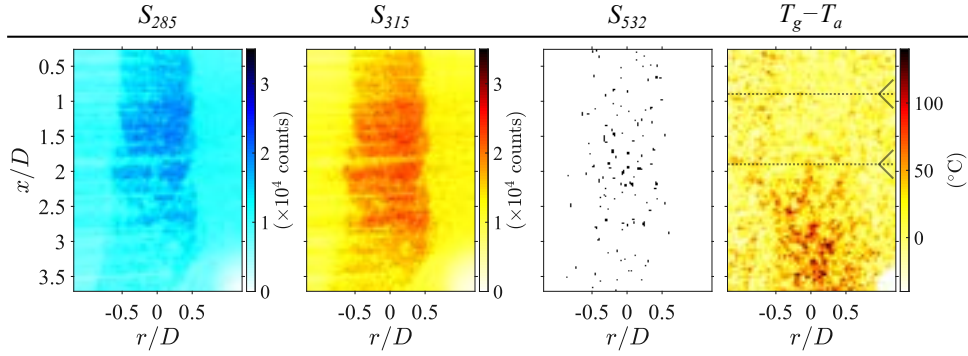


Figure 3.16: Simultaneous images from the three channels used in Experiment II, S_{285} , S_{315} and S_{532} , together with the resultant temperature calculated using the two-colour ratio method.

3.8.2 Hot and cold region determination

A new method was developed to determine the regions of the flow with a local, instantaneous temperature significantly higher or lower than the average (here named ‘hot regions’ and ‘cold regions’, respectively). This method uses quantitative criteria that can be varied systematically to define the hot and cold regions, which is similar to the method used previously to identify and classify particle clusters [113]. This method is illustrated using a typical instantaneous image from the case with $Sk_D = 86$, $\bar{\phi} = 1.4 \times 10^{-3}$ and $\dot{Q}_0 = 2840 \text{ W}$ in Figure 3.17. The spatial variations in the instantaneous image of gas-phase temperature above ambient, $T_g(x, r) - T_a$, within and downstream from the heating region ($0.9 < x/D < 1.9$) can be seen in Figure 3.17a. The hot and cold regions were determined from a comparison of this instantaneous temperature distribution with the time-averaged value using the following steps:

1. For the time-averaged temperature image $\bar{T}_g(x, r) - T_a$ (Figure 3.17b), the radially averaged temperature across $|r/D| < 0.3$ was computed. This results in a column vector with values corresponding to the jet temperature as a function of distance down-stream from the jet exit. This column vector was then replicated across the width of the original image to form the image $\bar{T}_{g,CL}(x) - T_a$, as shown in Figure 3.17c.
2. The normalised temperature was then calculated for the array using the equation:

$$\Theta(x, r) = \frac{T_g(x, r) - T_a}{\bar{T}_{g,CL}(x) - T_a}, \quad (3.6)$$

which was evaluated on an element-wise (i.e., pixel-by-pixel) basis. This normalisation was performed using $\bar{T}_{g,CL}(x)$, rather than $\bar{T}_g(x, r)$, because large errors can occur in regions with $\bar{T}_g(x, r) \approx 0$, such as near to the jet edge. Regions with $\bar{T}_{g,CL}(x) - T_a < 3$ °C (i.e., where the denominator term used to calculate $\Theta(x, r)$ is close to zero) were considered unreliable and hence were removed from further analysis.

- Each individual image of $\Theta(x, r)$ was then smoothed using a circular Gaussian filter kernel f with a characteristic smoothing length scale $L_S = 4\sigma$, where σ is the standard deviation of the Gaussian function, expressed as:

$$f_{m,n} = \exp \left[-8 \left(\frac{m^2 + n^2}{L_S^2} \right) \right], \quad (3.7)$$

where m and n are the array indices in the r and x directions with respect to the origin, respectively. Using this, the value of each pixel (i, j) of the smoothed temperature field $\Theta_S(x, r)$ is given by:

$$[\Theta_S]_{i,j} = \left(\sum_{m=-\delta}^{\delta} \sum_{n=-\delta}^{\delta} f_{m,n} [\Theta]_{i-m, j-n} \right) \times \left(\sum_{m=-\delta}^{\delta} \sum_{n=-\delta}^{\delta} f_{m,n} \right)^{-1}, \quad (3.8)$$

where $\delta = L_S/2$ is chosen for the bounds of the smoothing kernel size. Figure 3.17d presents the instantaneous, normalised temperature after smoothing with $L_S = 0.1D$.

- For each individual image, the reference temperature difference, Θ_{ref} , was calculated as the spatial average of $\Theta(x, r)$ in the region of $2.5 < x/D < 3$ and $|r/D| < 0.25$. The hot and cold regions were then identified as regions with $\Theta_S(x, r)$ that differed significantly from this reference.
- Threshold values were used to separate the hot and cold regions, with the thresholds for the hot and cold regions, ϵ_H and ϵ_C , respectively, calculated as a function of axial distance from the equations:

$$\epsilon_H(x, L_S) = \Theta_{ref} + \frac{k\sigma_T(x, L_S)}{\bar{T}_{g,CL}(x) - T_a} \quad (3.9)$$

and

$$\epsilon_C(x, L_S) = \Theta_{ref} - \frac{k\sigma_T(x, L_S)}{\bar{T}_{g,CL}(x) - T_a}, \quad (3.10)$$

where $\sigma_T(x, L_S)$ is the axial profile of the pixel-to-pixel standard deviation of $\Theta_S(x, r)$, calculated from all pixels with $|r/D| < 0.3$. The symbol k represents a multiplier to the standard deviation. The threshold

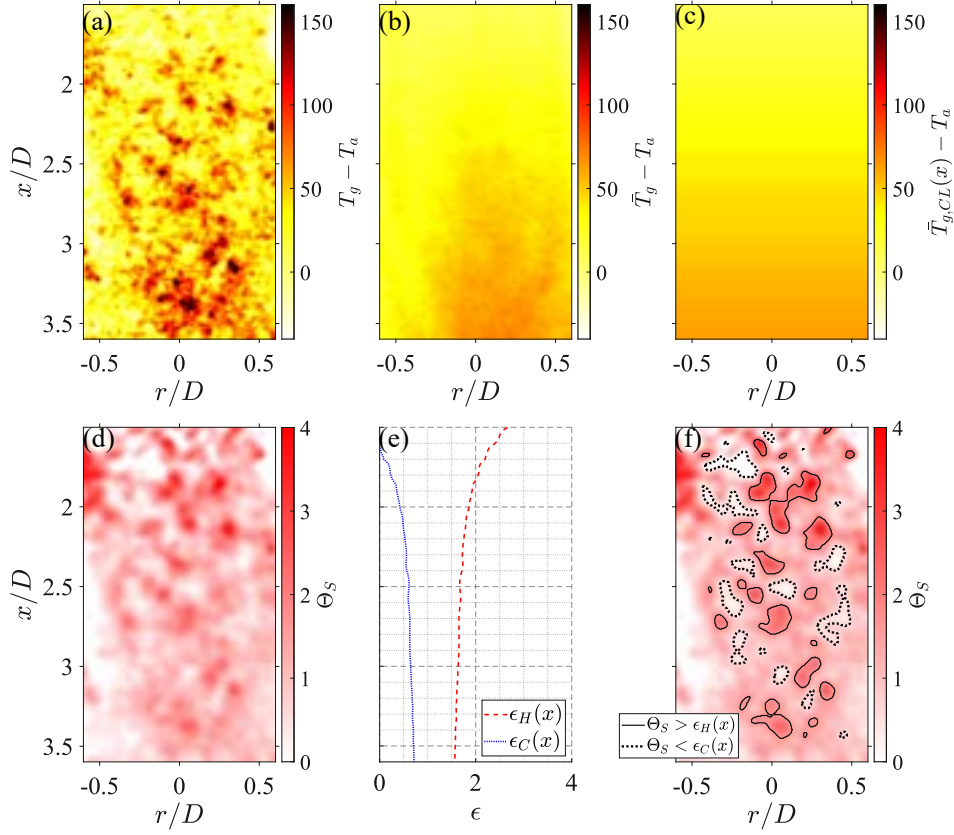


Figure 3.17: Images to illustrate the method used to determine local areas of relative high and low temperature: (a) the instantaneous gas-phase temperature, $T_g - T_a$, (b) the time-averaged temperature, $\bar{T}_g - T_a$, (c) the axial profile of the time- and radially-averaged temperature in the region $|r/D| < 0.3$ after replication into an array across the width of the original image, $\bar{T}_{g,CL}(x) - T_a$, (d) the smoothed normalised temperature increase from ambient, Θ_S , (e) the thresholds used to determine hot and cold regions, $\epsilon_H(x)$ and $\epsilon_C(x)$, respectively, and (f) Θ_S together with the boundaries of the determined hot and cold regions.

profile calculated for the example image with $L_S = 0.1D$ and $k = 1$ is presented in Figure 3.17e. The resultant hot and cold regions, overlaid on the image of $\Theta_S(x, r)$, are presented in Figure 3.17f.

6. The hot/cold regions with an area less than $0.008D^2$ (corresponding to the area of a circle with diameter $0.1D$) were considered to be too small for reliable measurement and thus removed from further analysis.

3.8.3 Particle loading

Similar to the LIF images, the background was first subtracted from the images of scattering by particles before alignment with S_{315} using images of the same target plate. Two separate methods were then used to calculate the instantaneous particle loading distribution in each experiment:

- In Experiment I, the chosen particles were typically smaller than or of a similar size to a pixel. In this case, the particle size parameter $\alpha_{sp} < 200$, which results in particle-light interactions being in the Mie scattering regime. For the PMMA particles, which are spherical with a mono-disperse size distribution, the local particle volume fraction is directly proportional to the measured intensity of the scattered light. However, this method was also used for the calculations of local volume fraction for the alumina and ZnO:Zn particles, because it was assumed that the statistical distribution of particle size in each image is constant. Volumetric loadings calculated using this assumption are denoted by ϕ^* in the results.
- In Experiment II, the chosen particles were typically much larger than a pixel. The radius of these particles is sufficiently larger than the 532 nm light for the scattering to be in the geometric optics regime. Since several pixels imaged each particle, individual particles were able to be identified and counted to determine the local particle number density, with the centre of each individual particle determined by calculating the intensity centroid of the region corresponding to each particle that was above the intensity threshold. Overlapping particles in each image (i.e., particles at similar locations within the measurement plane but at different depths within the laser sheet) were separated, where possible, using an in-house Matlab code. This was performed by identifying contiguous regions of intensity greater than the threshold that had an area significantly larger than the expected particle area. If this region contained two or more intensity peaks with the intensity distribution surrounding each peak well approximated by a 2D Gaussian distribution, the region was considered to contain multiple particles (corresponding to the number of peaks). The location of the individual particles was then calculated from the location where the Gaussian distribution was at its peak.

3.8.4 Particle cluster determination

For Experiment II, flow regions with a relatively high local particle loading (clusters), and those with no nearby particles (voids), were determined from the images of scattering using the well-established Voronoi method [114]. A typical instantaneous scattering image, following binarisation to identify the individual particles, is presented in Figure 3.18a. The Voronoi method involves partitioning the image into cells around each particle centroid, with the region belonging to each cell comprised of the ensemble of locations that are closer to the associated particle than any other [56]. The co-ordinates of the vertices around each cell were used to calculate the cross-sectional area of each individual Voronoi cell, A_{cell} . Cells with vertices outside of the measurement region, such as for particles near to the jet edge, were removed from further analysis. The Voronoi diagram for the example image is presented in Figure 3.18b.

In the present investigation, particles were defined to be within clusters if two or more adjacent Voronoi cells met the condition:

$$A_{cell}(x) < e_p \bar{A}_{cell}(x), \quad (3.11)$$

where e_p is a threshold value and \bar{A}_{cell} is the median cross-sectional area of the Voronoi cells, calculated as a function of axial location. A constant value of $e_p = 0.706$ was chosen for the threshold, because 1/3 of all Voronoi cells within a random particle distribution (i.e., Poisson distribution) would be expected to have an area below the threshold [115]. The constant threshold value is similar to that used in the method presented by Lau et al. [45]. This method was chosen for the present investigation instead of using an adaptive threshold, such as that presented by Monchaux et al. [114], because the adaptive threshold method requires the probability density function (PDF) of the cell areas to be calculated. This PDF calculation was considered to be unreliable for the cases in the present investigation due to the relatively low particle number density. The Voronoi cells that were considered to be clusters are also shown in Figure 3.18b with blue shading. While it is impossible to determine the 3-dimensional structure of the clusters from these images alone, the paper by Lau et al. [45] showed that these are typically rope-like in shape.

Using these definitions, both the gas-phase temperature and local number density were calculated within regions of the following size:

- the radius $< 0.1D$ from the centre of particles within clusters ($T_{g,Hi}$);
- the radius $< 0.1D$ from the centre of particles that are outside of clusters ($T_{g,Lo}$), and;

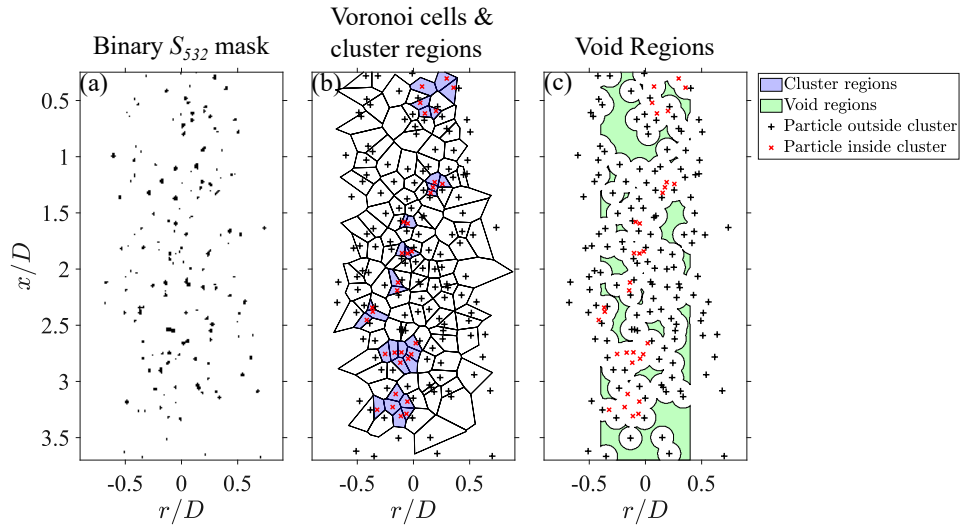


Figure 3.18: The binary particle mask from S_{532} (a), the resultant particle centroids together with the calculated Voronoi cells and determined clusters (b), and the void locations (c) for a single image from the case with $\bar{d}_p = 173 \mu\text{m}$ and $\phi = 1.4 \times 10^{-3}$.

- void regions ($T_{g,Vd}$), with the definition of these void regions described in detail below.

For the present investigation the voids were defined as regions that were further than $0.1D$ from the nearest particle, to match the length scale chosen to identify the hot and cold regions (Section 3.8.2). The void regions of the example image are presented in Figure 3.18c, together with the locations of particles both inside and outside of clusters. The calculation of the voids was limited to regions with $|r/D| < 0.4$, to avoid bias towards the jet edge regions with a low particle number density and low average local temperature rise. It should be noted that regions where $T_{g,Hi}$ and $T_{g,Lo}$ were measured can overlap for the case where two particle centroids, one of which was considered to be inside of a cluster and the other not, were within $0.2D$ of each other.

Chapter 4

Results

As outlined in Section 1.3, the main body of the present thesis consists of a summary of the key results from the journal articles produced, together with some previously un-published results. The published journal articles (Papers I [32], II [33], and III [34]) are presented in full in Appendices C, D, and E, respectively, while the journal article currently under review (Paper IV [35]) is presented in full in Appendix F.

The chapter is divided into three main sections, each summarising the key results from the following investigations:

1. a study of the interference modes in the method two-colour laser induced fluorescence (LIF) applied to particle-laden flows (Section 4.1), with the results distilled from Papers I and II [32, 33];
2. a study of the time-averaged temperature distributions measured in a particle-laden jet heated using high-flux radiation for a series of particle diameters, particle volumetric loadings, and heating fluxes, with the results distilled from Papers II and III [33, 34];
3. a study of the instantaneous temperature distributions for the same conditions investigated as for (2), with the results distilled from Papers II and IV [33, 35];

4.1 Interference to two-colour LIF in a particle-laden flow

This section summarises the results from the investigation assessing the suitability of the two-colour LIF technique for gas-phase temperature measurements in particle-laden flows. As described in Section 3.3, the technique

relies upon measurement of the fluorescence emissions from toluene in two separate spectral bands (285 ± 5 nm and 315 ± 10 nm for the present experiments). However, the scattering, fluorescence, and/or phosphorescence signal from particles may interfere with the toluene LIF signal, particularly if the spectral responses from the former overlap with the latter. An evaluation of the accuracy of the two-colour LIF thermometry method in a particle-laden flow is presented. The full details of the results are presented in Papers I and II, with the former presenting the results from Experiment I (described in Section 3.4.1) using PMMA, ZnO:Zn, and alumina particles in a uniformly pre-heated flow, and the latter from Experiment II (described in Section 3.4.2) using highly absorptive aluminosilicate particles in a radiatively heated flow.

4.1.1 Spectral emission measurements

The spectral response of toluene for a series of fluences of 266 nm light (Q''_{266}) is presented in Figure 4.1a, following subtraction of the average background noise and normalisation by the total measured response. The spectra collapse closely for all fluences investigated, which implies that the fluorescence emission spectrum of toluene following excitation at 266 nm is independent of the fluence within the range used in the present investigation. As such, the two-colour ratio will also be independent of laser power for the main experiments, consistent with the theory presented and previous measurements [88]. Figure 4.1b presents the measured fluorescence emission intensity for each of the two-colour LIF channels (I_{285} and I_{315}), together with the intensity ratio I_{315}/I_{285} , as a function of the toluene concentration in the jet for the range of concentrations used in Experiment II (0.25-0.75% by volume). These measurements were recorded within the potential core of the unheated jet with the toluene concentration controlled by varying the fractions of nitrogen flowing through the toluene bubbler and bypass streams, for a constant total flow rate of 25 SLPM. It can be seen that the fluorescence intensity recorded for both channels increases approximately linearly with the toluene concentration within the span of concentrations utilised. The results also show that the intensity ratio I_{315}/I_{285} is insensitive to concentration, with an average value of $I_{315}/I_{285} = 1.09 \pm 0.01$. This corresponds to a variation in the temperature of $T_g = 23.7 \pm 2.3$ °C for measurements of the unheated flow. Importantly, the trend of the change in intensity ratio with temperature is non-monotonic, which indicates that these variations are primarily a result of experimental scatter rather than a systematic bias due to self-quenching by the toluene molecules [109]. The standard deviation of the shot-to-shot intensity ratio also increases with a decrease in toluene concentration, corresponding to

4.1 Interference to two-colour LIF in a particle-laden flow

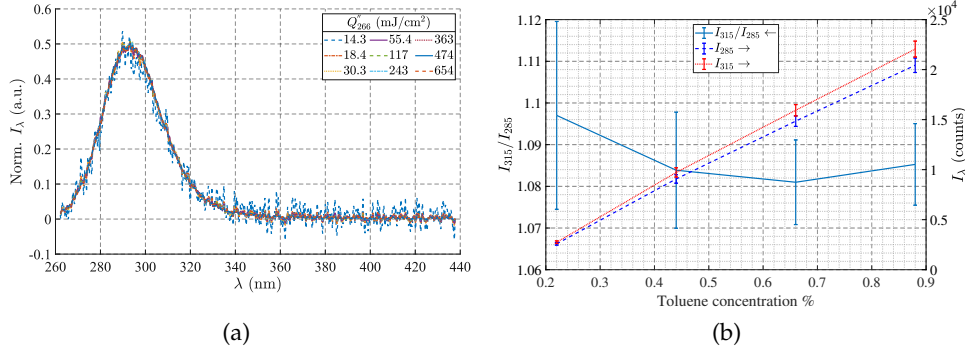


Figure 4.1: Normalised spectral response measured from toluene following illumination with 266 nm light for a series of fluences (a). The measured fluorescence intensity for each of the two-colour fluorescence channels together with the intensity ratio I_{315}/I_{285} as a function of toluene concentration (b). The errorbars represent one standard deviation for the measured shot-to-shot intensity and temperature.

an increase in the standard deviation of temperature from $\sigma_T = 2.2$ °C for a toluene concentration of 0.88% to $\sigma_T = 5.0$ °C for a concentration of 0.22%.

Figure 4.2 presents the measured spectral response from the particle materials (ZnO:Zn, alumina, and PMMA) that were used in Experiment I, following illumination with 266 nm light. The results show that the PMMA emits broadband fluorescence, with a peak intensity (I_λ) at $\lambda = 315$ nm. The emitted fluorescence encompasses the spectral regions in which measurements are recorded for two-colour toluene LIF thermometry in the present investigation (285 ± 5 nm and 315 ± 10 nm). As such, luminescence interference to the thermometry measurements is expected to be significant in flows with these particles. The phosphorescence emission from ZnO:Zn is strong ($> 10\times$ that of the PMMA at the peak) in the range 360-450 nm, with the emission spectrum closely matching that following excitation at 355 nm [116]. These emissions are at longer wavelengths than those used for toluene LIF, therefore it is expected that appropriate choice of optical filters will suppress the detection of both scattered light and luminescence interference from the ZnO:Zn particles. The results also show that any luminescence from alumina following excitation is negligible in the spectral range relevant to toluene LIF, with the measured intensity at least 3 orders of magnitude weaker than the peak intensity measured for the ZnO:Zn particles.

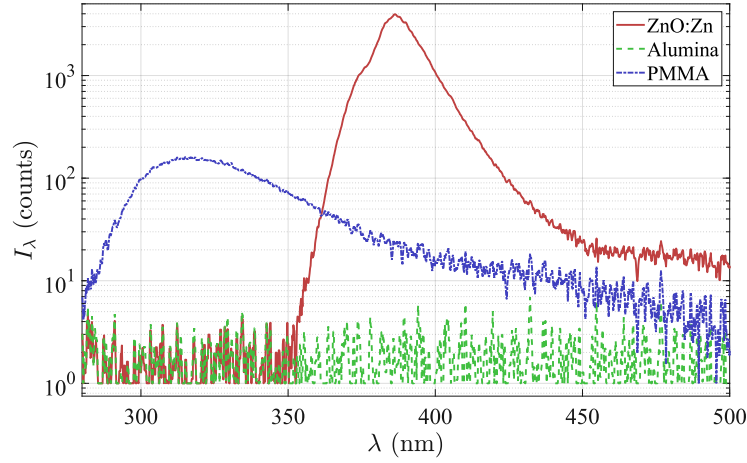


Figure 4.2: Spectral response measured from the three particle materials used in Experiment I to illumination with 266 nm light. The wavelengths used to detect the emissions for two-colour LIF thermometry in the presented investigations were in the range 280-325 nm.

4.1.2 Measurements of the pre-heated flow without particles

Figure 4.3 presents the gas-phase temperature above ambient ($\Delta T = T_g - T_a$, where T_g is the measured temperature and T_a is the ambient temperature) of the single-phase flow (i.e., with no particles seeded) measured on the jet centreline (ΔT_c), after normalisation by the value at the jet exit (ΔT_e). The value $\Delta T_c / \Delta T_e$ is known as the scalar mean of the jet, and is consistent for all scalar quantities (e.g., density, concentration, and temperature) [117, 118]. These measurements were performed in the arrangement used for Experiment I (described in Section 3.4.1), with the initial temperature of the flow controlled using the same pipe heater that was used for the calibration measurements. The results in Figure 4.3 are presented together with the scalar mean for a pipe jet measured by Papadopoulos and Pitts [118] (indicated by P&P hereafter) for two fluid density ratios (ρ_e / ρ_∞ , where ρ_e and ρ_∞ are the densities of the jet and surrounding flows at the exit plane, respectively). The axial distance presented is normalised by the effective diameter of the jet (D_ϵ), which accounts for the change in the fluid density and velocity with temperature [117]. The effective diameter is defined as:

$$D_\epsilon = \frac{2M_e}{\sqrt{\pi\rho_\infty J_e}} \quad (4.1)$$

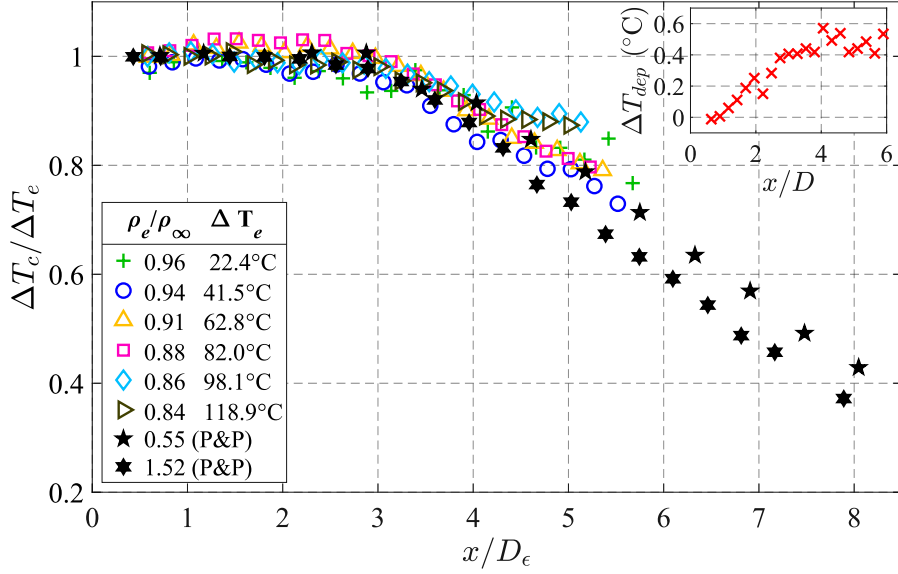


Figure 4.3: The axial profile of gas-phase temperatures above ambient ($\Delta T = (T_g - T_a)$) on the jet centreline measured using the two-colour LIF technique, normalised by the jet exit value, for a series of initial temperatures. Also presented are the scalar mixing values presented by Papadopoulos and Pitts [118] (denoted by P&P) for two initial density ratios ρ_e/ρ_∞ , where ρ_e is the density of the jet fluid and ρ_{inf} is the density of the surrounding flow. The inset presents the temperature above ambient measured for the case without heating, ΔT_{dep} .

where

$$M_e = \int_0^{D/2} 2\pi\rho_e U_{g,b} r dr \quad (4.2)$$

is the jet exit mass flux,

$$J_e = \int_0^{D/2} 2\pi\rho_e U_{g,b}^2 r dr \quad (4.3)$$

is the jet exit momentum flux and $U_{g,b}$ is the bulk mean velocity of the jet.

The results show that the scalar mean $\Delta T_c/\Delta T_e$ is close to uniform for $x/D_e < 3$, while $\Delta T_c/\Delta T_e$ decays towards zero with axial distance for $x/D_e > 3$. This is consistent with the length of the potential core identified from previous measurements of turbulent pipe jets [117, 119]. The data for each initial density ratio collapse closely for $x/D_e < 4$, with good agreement shown with the previous results of P&P [118]. The differences in values between the present and previous measurements for $x/D_e > 4$ are attributed

to the differing experimental conditions (e.g., the co-flow used in the present investigation).

Also presented in the inset of Figure 4.3 is the measured temperature difference from the ambient value (ΔT_{dep}) for the special case with the flow not heated. That is, for this case, any departure from 0 indicates a systematic error in the measurement. The measured temperature for this case was $|\Delta T_{dep}| < 0.6$ °C for $0.5 < x/D < 6$, which is a modest error relative to the range of temperatures investigated (0 °C $< \Delta T_e < 120$ °C). The combination of these results gives good confidence that the two-colour LIF technique is accurate for measurements in the pipe-jet conditions used in the present experiments.

4.1.3 Measurements for Experiment I

Sets of instantaneous images of the unheated particle-laden flow from Experiment I, for a series of instantaneous particle volumetric loadings (ϕ) of the 20 μm PMMA particles, are presented in Figure 4.4. Presented in columns (i) and (ii) are the simultaneous images of the intensity recorded by the two LIF channels S_{285} and S_{315} , respectively. The intensity scale for these channels is presented in terms of the signal-to-noise ratio (SNR), defined as the total signal measured divided by the average background signal (i.e., with the flow switched off and no toluene within the measurement region). Column (iv) presents the instantaneous local particle volume fraction distribution, imaged simultaneously with the LIF. The images in Column (iii) present the difference in temperature between that calculated from the two-colour LIF ratio and the ambient value, ΔT_{dep} . Because the flow is unheated, this temperature difference should theoretically be uniformly zero for each volumetric loading investigated. Therefore, the measured variations of ΔT_{dep} are attributed to errors in the measurement. Potential sources of systematic errors include:

- elastic scattering of the laser sheet by particles and
- luminescence of the particles,

while random error sources include:

- camera shot noise,
- background interference,
- signal trapping/attenuation, and
- spatial variations in particle loading.

It can be seen from the instantaneous distributions that these errors in the temperature measurement are present for each particle loading, with the range of ΔT_{dep} measured increasing with an increase in ϕ . These errors are particularly significant near to the jet edge, in regions with a relatively low toluene concentration and a correspondingly low fluorescence SNR. The greatest error in the measurement can be seen in image (*d – iii*) for $\phi = 8 \times 10^{-4}$ at $x/D = 1.8$ and $r/D = 0.1$, with a value of $\Delta T_{dep} = 189$ °C measured at this location. This can be seen to correspond to a region with a locally high particle volume fraction, so that this error is primarily attributed to direct interference from the particles (i.e., scattering or luminescence). The interference due to the particles is also evident in the images without toluene in the jet, as presented in row (*c*), although the signal measured in the LIF channels from the flow with particles only is typically more than an order of magnitude lower than that from the toluene fluorescence.

Figure 4.5 presents the probability density function (PDF) of ΔT_{dep} for a series of particle volumetric loadings, measured from each pixel in the region $|r/D| < 0.4$ and $0.55 < x/D < 3$ for 5 images with the labelled instantaneous particle loadings. The results show that the PDFs of temperature measured for each loading are approximately Gaussian in shape, with an increase in the modal value of ΔT_{dep} (i.e., the value at which the peak of the PDF occurs) increasing with an increase in $\bar{\phi}$ from $\Delta T_{dep} = 0$ °C for $\bar{\phi} < 0.5 \times 10^{-4}$ to $\Delta T_{dep} = 15.8$ °C for $\bar{\phi} = 8 \times 10^{-4}$. This implies that there is a systematic error introduced from the presence of particles in the measurement, which is consistent with what can be seen in the instantaneous images presented in Figure 4.4. However, this systematic error is close to zero for $\bar{\phi} = 5 \times 10^{-5}$ and less than 5 °C for $\bar{\phi} \leq 2 \times 10^{-4}$.

The presence of particles in the flow also increases the influence of random errors in the measurement, with the standard deviation of ΔT_{dep} increasing from $\sigma_T = 5.9$ °C for $\bar{\phi} = 0$ (i.e., the single phase flow) to $\sigma_T = 8.1$ °C for $\bar{\phi} = 8 \times 10^{-4}$. The results show that both the systematic and random errors in gas-phase temperature measurements using the two-colour LIF method are greater in particle-laden flows than single phase flows. However, the results presented here imply that the two-colour LIF method is suitable for use in flows laden with PMMA particles at volumetric loadings of $\bar{\phi} < 2 \times 10^{-4}$, which includes flows within the two-way coupling regime commonly used for practical applications.

Figure 4.6 presents ΔT_{dep} as a function of the local particle loading ϕ for each of the ZnO:Zn, 20 μm PMMA and alumina particles. The error bars for each measurement point represent one standard deviation of ΔT_{dep} (σ_T). The only PMMA particle diameter presented is the $\bar{d}_p = 20$ μm case, because the

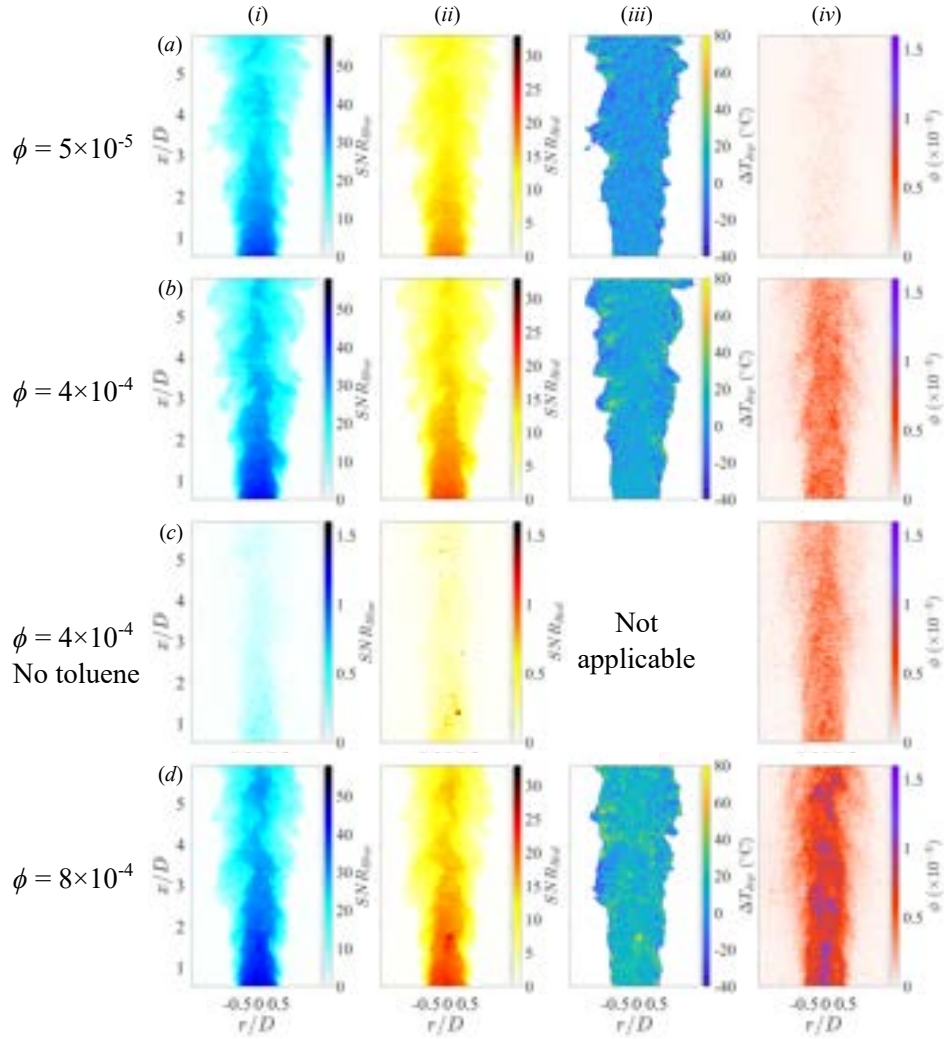


Figure 4.4: Single-shot images of the particle-laden flow at a series of instantaneous particle loadings for the $20\ \mu\text{m}$ PMMA particles in the unheated jet, for the (i) intensity measured in LIF channel S_{285} , (ii) intensity measured in LIF channel S_{315} , (iii) the temperature difference from the actual ambient value calculated using the LIF ratio (ΔT_{dep}) and (iv) the local particle volumetric loading. The images in row (c) were from the flow with particles but without toluene seeded; note the different colourbar scale for the fluorescence intensities for this case.

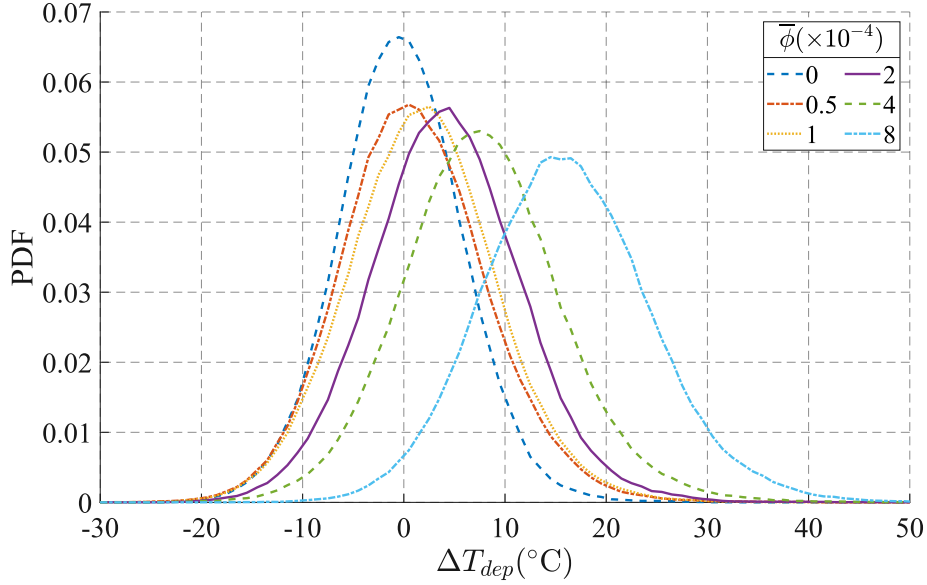


Figure 4.5: Probability density functions of the measured temperature difference from ambient for the unheated flow with $20 \mu\text{m}$ PMMA particles for a series of instantaneous particle volumetric loadings, calculated in the jet region $|r/D| < 0.4$ and $0.55 < x/D < 3$.

results were similar regardless of particle diameter. The results show that the trends observed from Figure 4.5 are consistent for each particle material used, with an increase in both ΔT_{dep} and σ_T measured for an increase in ϕ . The temperature difference ΔT_{dep} is greater for the PMMA particles than for the ZnO:Zn and alumina particles. This result, combined with the emission spectra presented in Figure 4.2, indicates that the fluorescence emissions from the PMMA particles lead to greater measurement errors than the elastic scattering from particles, which is expected to be of a similar magnitude for each material. The bias error of the measurement is $\Delta T_{dep} < 5 \text{ }^\circ\text{C}$ for the PMMA particles for local loadings of $\phi < 2 \times 10^{-4}$, while for the alumina and ZnO:Zn particles the measurements are accurate to this value for $\phi < 7 \times 10^{-4}$. This suggests that, while the fluorescence may be dominant, the interference from elastic scattering also becomes significant at sufficiently high ϕ . The effect of interference from scattering could be further suppressed using additional optical filters, which demonstrates that the two-colour LIF method shows good potential for accurate measurements of the gas-phase temperature even for flows in the four-way coupling regime ($\phi > 10^{-3}$).

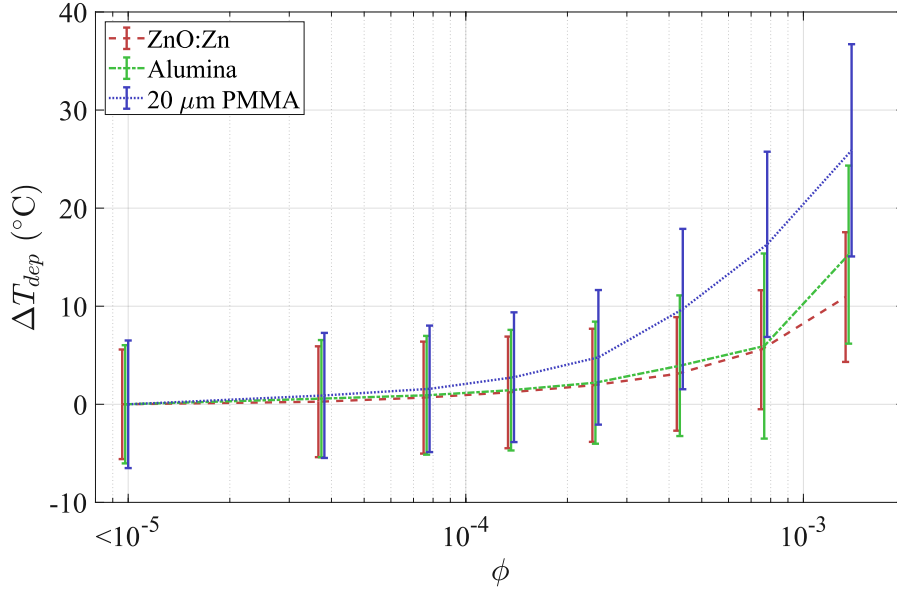


Figure 4.6: The difference between the measured temperature and ambient value (ΔT_{dep}) as a function of local particle loading (ϕ) in the unheated jet for the three particle materials investigated. The error bars represent one standard deviation.

4.1.4 Measurements for Experiment II

Experiment II differs from the Experiment I in that non-luminescent aluminosilicate particles were used because of their suitability as the absorbing medium for radiative heating, and additional filters to suppress interference to the two fluorescence channels were used. The particles used were of a different material and much larger ($\bar{d}_p \geq 173 \mu\text{m}$) than those used for Experiment I ($\bar{d}_p \leq 40 \mu\text{m}$). Since the scattering signal scales with d_p^2 , while the luminescence signals scale with d_p^3 , an additional assessment of the interference was required. Figure 4.7 presents typical single-shot images from the two fluorescence channels, S_{285} and S_{315} , and the corresponding image from scattering channel, S_{532} , together with the temperature distribution derived from the two-colour LIF ratio, T_g . The top row presents the jet flow without particles seeded and with the heating laser switched on at an output power of $\dot{Q}_0 = 2840 \text{ W}$, to assess the significance of absorption of the heating beam by the flow. The bottom row presents the flow laden with the $\bar{d}_p = 173 \mu\text{m}$ particles at a volumetric loading of $\phi = 1.4 \times 10^{-3}$ and the heating laser switched off, to determine the effect of elastic scattering, attenuation, and signal trapping on the measurement accuracy. Images were also recorded

of the particle-laden flow with the heating laser switched on but without toluene, but these are not presented because the elastic scattering of the heating laser to either fluorescence channel was indistinguishable from the camera noise.

For the flow without particles and the heating laser switched on, it can be seen that the measured temperature of the jet is close to uniform. This implies that absorption of the heating beam by the unladen flow is negligible. The variations in the temperature distribution for this case are due to the random errors in the measurements, as described in Section 4.1.3. Additionally, no clear change in the measured temperature distribution can be seen for the unheated case with particles, despite significant variations in the fluorescence intensity due to attenuation of the excitation laser and signal trapping of the fluorescence emissions by the particles. The reduction in LIF signal recorded due to the particles can be seen clearly in the zoomed inset image (note the different colourbar scale to highlight the gradients in the intensity). The median particle diameter for the presented images of \bar{d}_p is approximately 25% of the laser sheet width. As such, the fluence of the light sheet would be expected to decrease by approximately 25% in the flow down-beam from the centre of a single particle that is fully within the laser sheet. The local fluence could be further decreased if several particles shadow nearby regions. However, because the two fluorescence channels share an identical optical path through the flow, the effect of these variations in intensity on the measured fluorescence signal are similar for each channel. A slight misalignment between the two channels can cause significant errors, particularly in regions with strong gradients in toluene concentration (e.g., the shear layer between the jet and co-flow) or local fluence (e.g., in the streaks down-beam from particles). While the images were closely matched, regions with an erroneous high- and low-temperature may still be present, particularly near to the boundary between the jet and co-flow. The resultant systematic error of the average measured temperature for the ambient flow was $\Delta T_{dep} = 5.5 \text{ }^\circ\text{C}$ for the $\bar{d}_p = 173 \text{ }\mu\text{m}$ particles, which is estimated to increase to $\Delta T_{dep} = 8 \text{ }^\circ\text{C}$ for a flow temperature of $\bar{T}_g = 150 \text{ }^\circ\text{C}$ due to the decrease in fluorescence intensity with temperature. Additionally, the particles in the flow lead to a modest increase in the random errors for the entire image, with $\sigma_T = 21 \text{ }^\circ\text{C}$ for $\phi = 0$ increasing to $\sigma_T = 24 \text{ }^\circ\text{C}$ for $\phi = 1.4 \times 10^{-3}$. However, if only the regions with a relatively low intensity due to attenuation and signal trapping are considered, the pixel-to-pixel uncertainty in the measured temperature increases to $40 \text{ }^\circ\text{C}$.

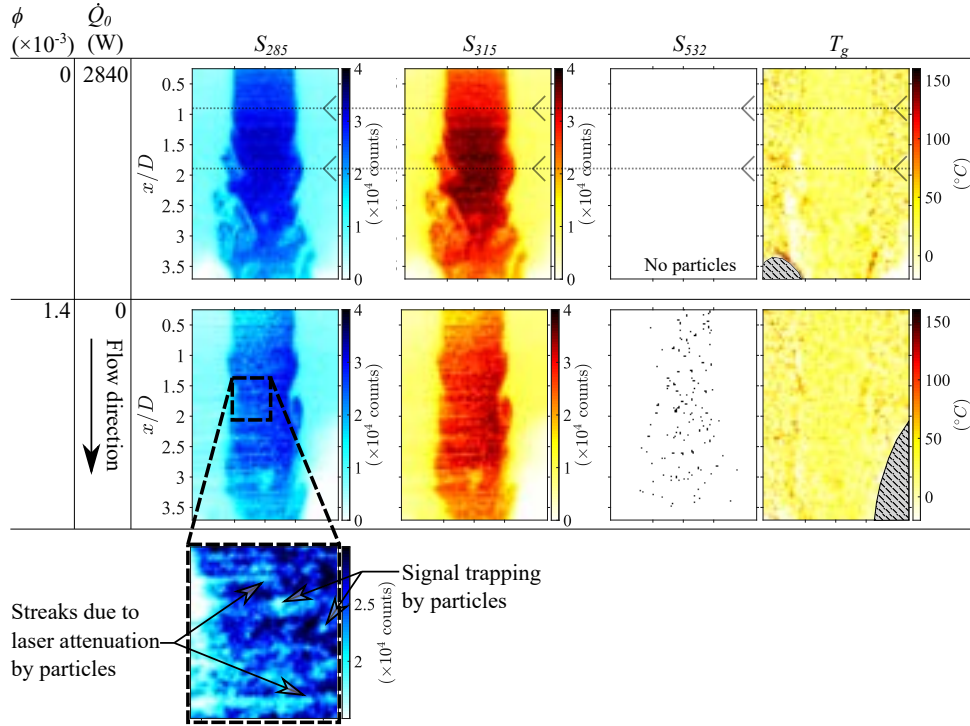


Figure 4.7: Typical instantaneous images from each camera, S_{285} , S_{315} , and S_{532} , together with the temperature calculated from the two-colour LIF ratio, T_g . The top row presents the case without particles and with the heating laser switched on with an output power of $\dot{Q}_0 = 2840$ W. The dotted lines and arrows represent the approximate boundary and direction of the heating laser, respectively. The bottom row presents the case with $\bar{\phi} = 1.4 \times 10^{-3}$ but with the heating laser switched off, with the inset showing the important features of attenuation of the light sheet and signal trapping by particles in greater detail.

4.2 Time-averaged measurements of a radiatively heated particle-laden flow

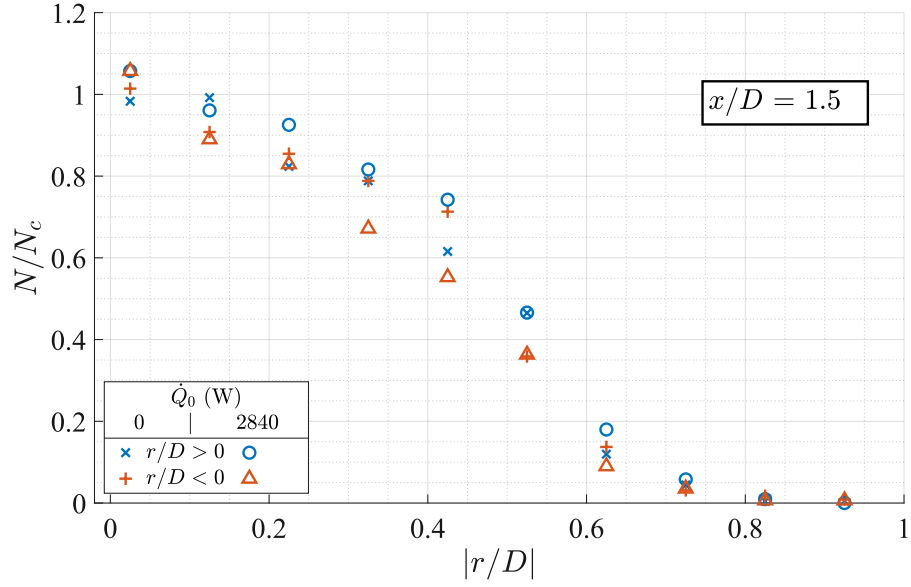
This section summarises the time-averaged gas-phase temperature and particle distributions measured of the radiatively heated particle-laden jet for Experiment II, evaluated for a series of heating powers (\dot{Q}_0), median particle diameters (\bar{d}_p), and average particle volumetric loadings ($\bar{\phi}$). The full details of the results from these measurements are presented in Papers II [33] and III [34].

4.2.1 Particle number density and velocity measurements

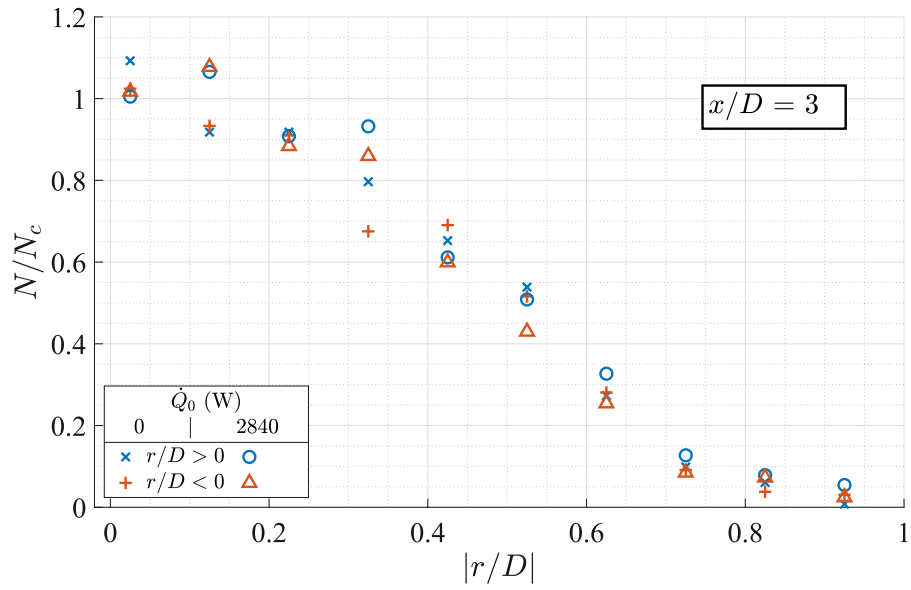
It should be noted that the particle number density was measured simultaneously with the temperature, while the velocity was measured separately for identical flow conditions.

Figure 4.8 presents the radial profiles of particle number density (N) normalised by the centreline value (N_c) for both $r/D > 0$ and $r/D < 0$ at $x/D = 1.5$ (a) and $x/D = 3$ (b), for the flow with $\dot{Q}_0 = 0$ and 2840 W, $\bar{d}_p = 173$ μm and $\bar{\phi} = 1.4 \times 10^{-3}$. The results presented are for the flow with $\bar{d}_p = 173$ μm only, because this case has the lowest Stokes number ($Sk_D = 86$) and hence is expected to be the most responsive to flow motions. Additionally, the results for the flows with $\bar{d}_p > 173$ μm display the same trends as reported for the presented case. It can be seen that the number density at each location and heating flux is consistent, with a peak in N/N_c on the centreline decreasing slightly to $N/N_c \approx 0.8$ at $|r/D| = 0.3$ for each axial location. These results are broadly consistent with those presented by Lau and Nathan [44] and Tsuji et al. [39] for particles with $Sk_D \gg 1$. Nearer to the jet edge, for $|r/D| > 0.3$, the number density further decreases with an increase in $|r/D|$, with N/N_c approaching zero at $|r/D| \approx 0.8$ for $x/D = 1.5$ and $|r/D| \approx 0.9$ for $x/D = 3$. This implies that the jet spread is relatively minor throughout the measurement region investigated, consistent with the well-known trends for the near-field of a jet [117]. The results also show that the number density profiles for $r/D < 0$ and $r/D > 0$ are similar (i.e., the particle number density is radially symmetrical about the jet axis). Importantly, the number density profiles do not change significantly between the flows with and without the heating laser, which implies that heating-induced flow motions such as buoyancy or turbulence do not affect the lateral migration of particles.

Figure 4.9 presents the radial profiles of the particle velocity in the axial direction (U_p), normalised by the centreline velocity at the jet exit (U_c), measured at the axial locations of $x/D = 1, 2$, and 3 for both the flows with $\dot{Q}_0 = 0$ and 2840 W. For both cases, $\bar{d}_p = 173$ μm and $\bar{\phi} = 1.4 \times 10^{-3}$. These axial locations comprise the regions near to both edges of the heating region, which is bounded by $0.9 < x/D < 1.9$, and one location downstream that is near to the edge of the measurement region. The results show that the particle velocity is close to uniform across the width of the jet for each x/D , with $0.9 < U_p/U_c < 1$ at $x/D = 1$. The results also show that the presence of high flux radiation does not significantly change the velocity profile at any axial location investigated, consistent with the results for the number density. The combination of these results give good confidence that any flow motions



(a)



(b)

Figure 4.8: Radial profiles of the particle number density normalised by the centreline value measured at $x/D = 1.5$ (a) and $x/D = 3$ (b) for both $r/D > 0$ and $r/D < 0$ for the flow with $\dot{Q}_0 = 0$ and 2840 W, $\bar{d}_p = 173$ μm and $\bar{\phi} = 1.4 \times 10^{-3}$.

4.2 Time-averaged measurements of a radiatively heated particle-laden flow

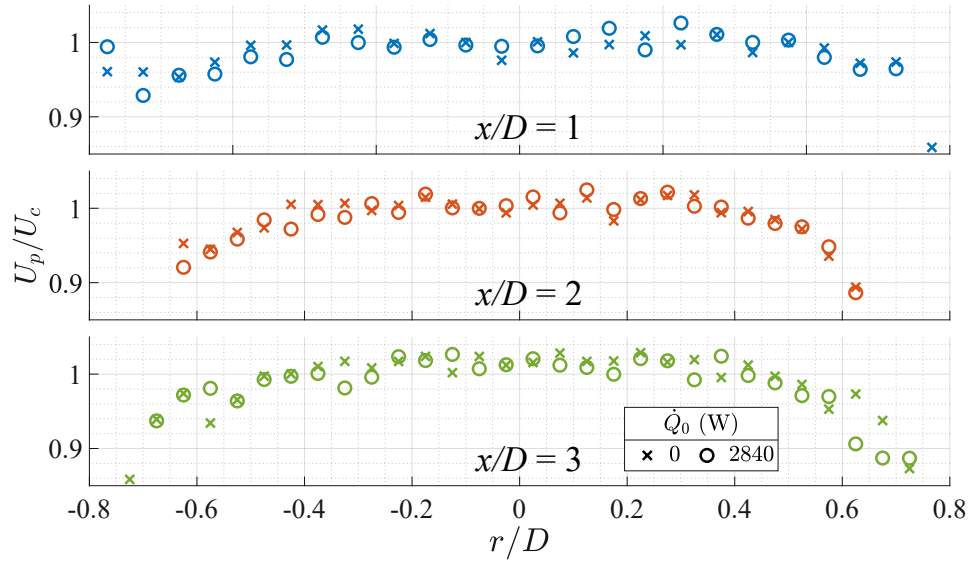


Figure 4.9: Radial profiles of the particle velocity normalised by the centreline value measured at $x/D = 1, 2$, and 3 for the unheated flow and with $\dot{Q}_0 = 2840$ W. For each case, $\bar{d}_p = 173$ μm and $\bar{\phi} = 1.4 \times 10^{-3}$.

generated by thermal gradients do not influence the particle phase for the relatively large, dense particles investigated here.

4.2.2 Gas-phase temperature measurements

Figure 4.10 presents the measured temperature distributions of the jet for a series of heating powers (\dot{Q}_0) with a median particle diameter of $\bar{d}_p = 173$ μm and average particle volumetric loading of $\bar{\phi} = 1.4 \times 10^{-3}$ (top), a series of \bar{d}_p with $\dot{Q}_0 = 2840$ W and $\bar{\phi} = 1.4 \times 10^{-3}$ (middle), and a series of $\bar{\phi}$ with $\dot{Q}_0 = 2840$ W and $\bar{d}_p = 205$ μm . For each case with heating, the temperature can be seen to increase from the beginning of the heating region to the downstream edge of the measurement region, which suggests the temperature will continue to rise beyond the measurement region investigated. This also indicates that the particles are considerably hotter than the gas throughout this region, with the convective heat transfer between the particles and gas significant. The majority of the temperature increase is constrained within the main jet for $|r/D| < 0.5$, consistent with the relatively minor spread of particles in the near-field of the jet (see Figure 4.8). At axial locations downstream from the heating region, the peak temperature measured can be seen to be near to the jet centreline. The decrease in the measured gas-phase temperature with radial distance from the jet centreline is attributed to the distribution

of particle loading in the jet, which is concentrated towards the jet axis (see Figure 4.8), together with the shear-driven mixing with the ambient co-flow that occurs in jets [117].

The temperature of the flow can be seen to increase with an increase in heating power, a decrease in particle diameter, and an increase in particle loading. These trends are consistent with the rate of particle temperature increase being proportional to both the radiative flux and total cross-sectional area of particles (see also equation 2.13), and the gas temperature increase being proportional to both the particle-gas temperature difference and the total surface area of particles (see also equation 2.15). In the experimental system, the radiative flux of the heating beam is proportional to the output power, while the particle cross-section and surface area both increase with either an increase in $\bar{\phi}$ (for a constant \bar{d}_p) or a decrease in \bar{d}_p (for a constant $\bar{\phi}$).

Attenuation of the heating beam can also be seen from the time-averaged temperature images, with the temperature measured on the up-beam side ($r/D > 0$) of the jet typically greater than that on the down-beam side. This attenuation is most significant for the cases with $\bar{\phi} = 1.4 \times 10^{-4}$ and $\bar{d}_p \leq 238 \mu\text{m}$. This implies that the significance of attenuation of the heating beam on non-uniformities in the temperature distribution is also dependent on the total cross-sectional area of particles in the flow, consistent with expectation.

4.2 Time-averaged measurements of a radiatively heated particle-laden flow

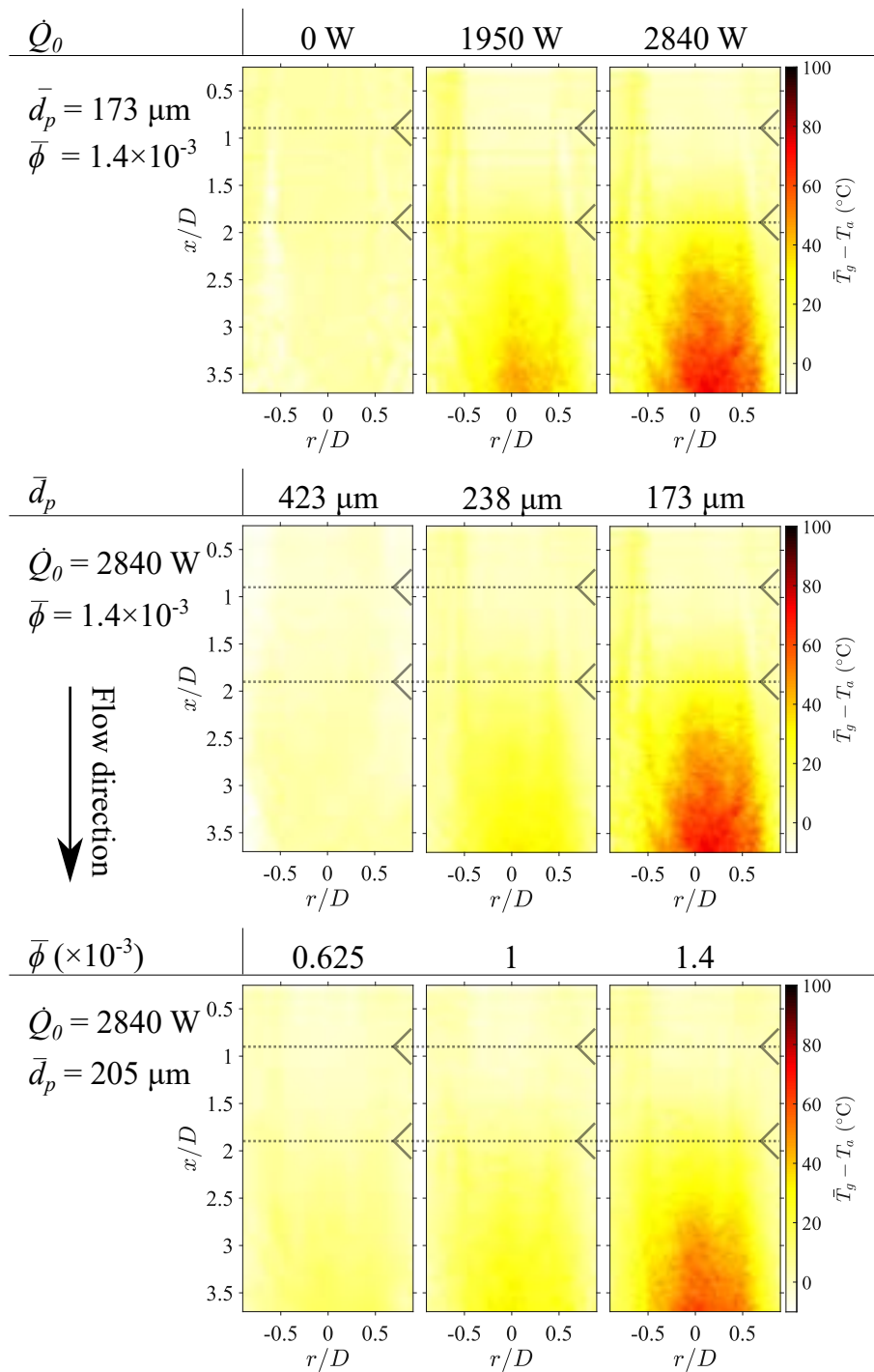


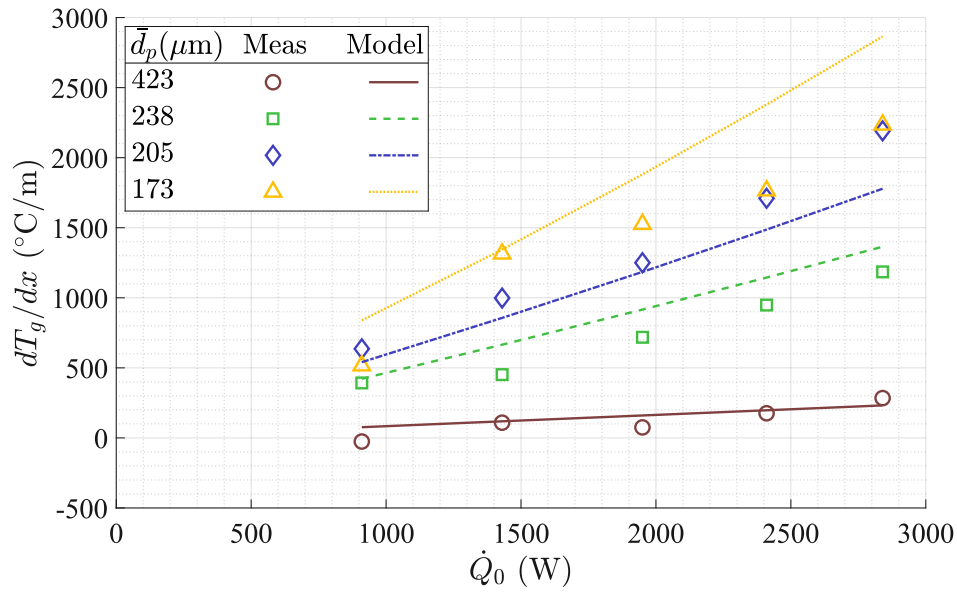
Figure 4.10: The time-averaged temperature distributions of the radiatively heated particle-laden jet for a series of heating powers (\dot{Q}_0) with a median particle diameter of $\bar{d}_p = 173 \mu\text{m}$ and average particle volumetric loading of $\bar{\phi} = 1.4 \times 10^{-3}$ (top), a series of \bar{d}_p with $\dot{Q}_0 = 2840 \text{ W}$ and $\bar{\phi} = 1.4 \times 10^{-3}$ (middle), and a series of $\bar{\phi}$ with $\dot{Q}_0 = 2840 \text{ W}$ and $\bar{d}_p = 205 \mu\text{m}$.

Figure 4.11 presents the average rate of gas-phase temperature increase with axial distance on the jet centreline (dT_g/dx), evaluated over the region $2 < x/D < 3$ for both the measurements and the one-dimensional heat transfer model, as a function of \dot{Q}_0 for each \bar{d}_p with $\bar{\phi} = 1.4 \times 10^{-3}$ (a) and as a function of $\bar{\phi}$ for each \bar{d}_p with $\dot{Q}_0 = 2840$ W (b). The gradient dT_g/dx increases approximately linearly with an increase of \dot{Q}_0 , while dT_g/dx increases monotonically for an increase of $\bar{\phi}$. The axial gradient dT_g/dx also typically increases with a decrease in \bar{d}_p , except for the particle distributions investigated with $\bar{d}_p \leq 238$ μm . These trends are consistent with those identified from the time-averaged temperature distributions presented in Figure 4.10. The greatest measured gradient of temperature increase was $dT_g/dx \approx 2,200$ $^\circ\text{C}/\text{m}$ for the flow with $\dot{Q}_0 = 2840$ W, $\bar{\phi} = 1.4 \times 10^{-3}$ and $\bar{d}_p = 173$ or 205 μm . This corresponds to a gas-phase temperature heating rate of approximately $8,000$ $^\circ\text{C}/\text{s}$, using the assumption that the gas velocity remains constant at the calculated jet exit bulk-mean value of 3.6 m/s.

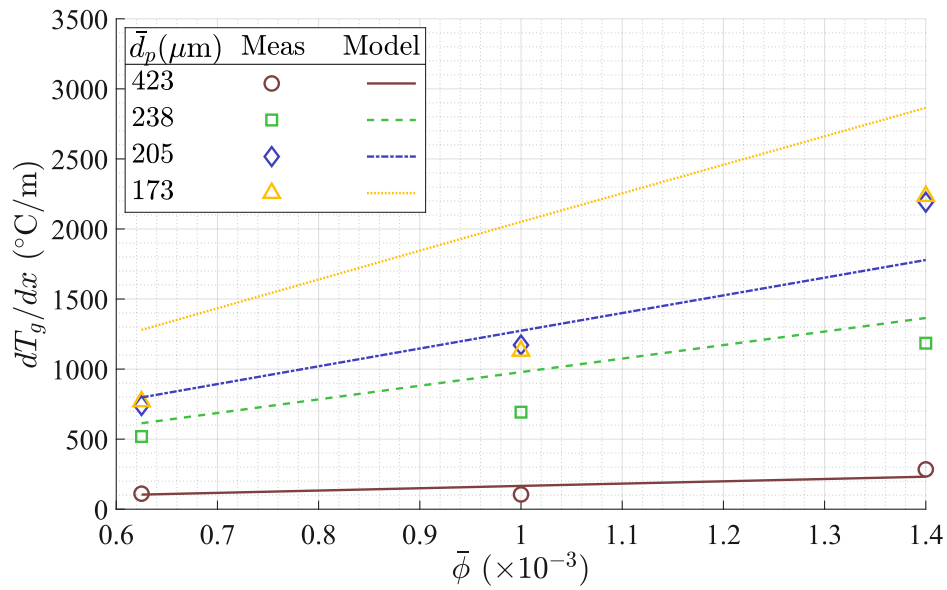
The model can be seen to generally overestimate the measured gradient, except for the case with $\bar{d}_p = 238$ μm . The difference between the value of dT_g/dx measured and calculated from the model also generally increases with an increase in \dot{Q}_0 , an increase in $\bar{\phi}$, and a decrease in \bar{d}_p , which suggests that the flow is better approximated by the simple model in situations with a relatively low heating flux and few particles in the flow. The differences between the measurements and model are attributed primarily to the estimated quantities in the model. These include the slip velocity, which was assumed to be constant but is actually highly variable in a turbulent two-phase flow. Additionally, particle clustering and attenuation of the heating beam occur in the real flow, but were not accounted for in the model. However, the generally close agreement between the model and measurements gives confidence that the results from simplified model are a reasonable estimate of the temperature and heat transfer processes in the flow.

Figure 4.12 presents the power from the SSSTS beam that was transmitted through the particle-laden flow, \dot{Q}_{tr} , normalised by the initial beam power, \dot{Q}_0 , as a function of particle diameter for a series of volumetric loadings with $\dot{Q}_0 = 2840$ W. Both the transmission from the power meter measurements and from the random particle simulation are presented. The results are consistent with those presented in Figures 4.10 and 4.11, with the transmission \dot{Q}_{tr}/\dot{Q}_0 decreasing with an increase in the total cross-sectional area of particles in the flow (i.e., an increase in ϕ for constant \bar{d}_p and a decrease in \bar{d}_p for constant ϕ). The lowest measured transmission of the SSSTS beam was $\dot{Q}_{tr}/\dot{Q}_0 = 0.79$ for the particles with $\bar{d}_p = 173$ μm at a volumetric loading of $\bar{\phi} = 1.4 \times 10^{-3}$. Using the previously measured absorptivity of these particles ($\alpha = 0.89$) [103],

4.2 Time-averaged measurements of a radiatively heated particle-laden flow



(a)



(b)

Figure 4.11: The average rate of gas-phase temperature increase with axial distance on the jet centreline over the region $2 < x/D < 3$ for both the measurements and the one-dimensional model, as a function of heat flux for a series of \bar{d}_p with $\bar{\phi} = 1.4 \times 10^{-3}$ (a) and as a function of volumetric loading for a series of \bar{d}_p with $\dot{Q}_0 = 2840$ W (b).

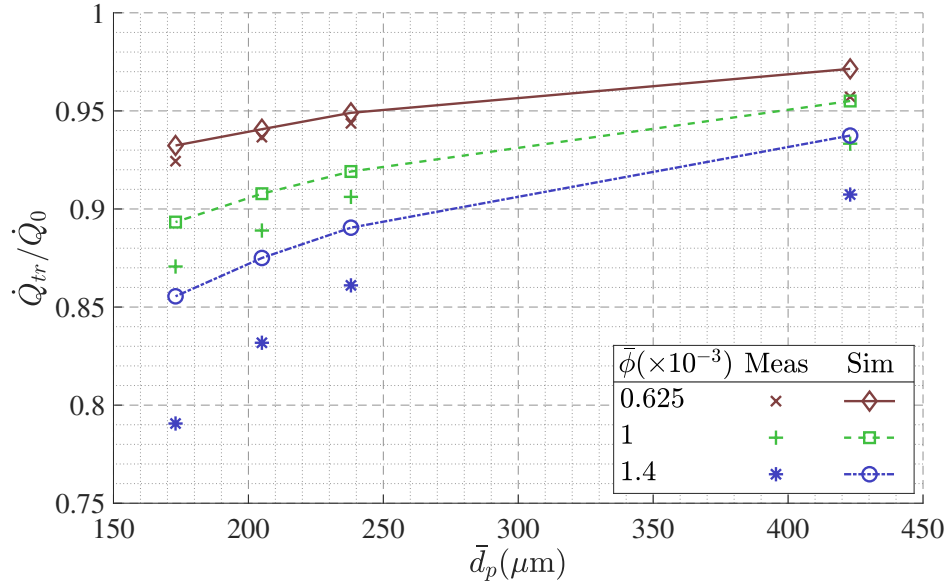


Figure 4.12: Comparison of the measured (Meas) and simulated (Sim) power of the SSSTS beam transmitted through the particle-laden flow, normalised by the total beam power, as a function of particle diameter for each volumetric loading investigated. The measured results presented are for the cases with $\dot{Q}_0 = 2840$ W.

this corresponds to an approximate absorption of the beam by particles of $\dot{Q}_{abs}/\dot{Q}_0 = 0.19$.

The results seen for the measured transmission match sufficiently well with the simulated values to have good confidence in the trends. For each case the measured transmission is lower than that calculated from the model, with the difference increasing with an increase in $\bar{\phi}$ for all cases of \bar{d}_p investigated. Possible reasons for this discrepancy include:

- the particles are simulated as spherical, whereas the specified sphericity of the particles by the manufacturer is 0.9, which would increase the area-to-volume ratio of the real particles compared to those modelled;
- fine particles may be generated from breakage or abrasion of the initial particles, leading to a greater projected area of particles for the same volumetric loading;
- any fine particles that occupy a very small total volume percent, but relatively larger number density, may not be detected during the measurement of the particle diameter distribution.

4.3 Instantaneous measurements of a radiatively heated particle-laden flow

While these complexities in the real system are not easily predicted or incorporated in models, their contribution is also expected to be modest.

and exhibits an angle-dependent intensity due to the summation of oscillations

4.3 Instantaneous measurements of a radiatively heated particle-laden flow

This section summarises the findings from the analysis of the instantaneous distributions of the temperature and particle volume fraction in the radiatively heated particle-laden jet, evaluated for a series of heating powers (\dot{Q}_0), median particle diameters (\bar{d}_p), and particle volumetric loadings ($\bar{\phi}$). These measurements were performed in Experiment II, with most of the results presented in detail in Papers II [33] and IV [35].

Figure 4.13 presents typical images from the particle-laden flow of the instantaneous temperature, the fluorescence intensity (presented for channel S_{285} only), and the detected scattering from particles, for each diameter distribution investigated with $\bar{\phi} = 1.4 \times 10^{-3}$ and $\dot{Q}_0 = 2840$ W. The dashed lines and arrowheads on the temperature images indicate the approximate boundaries and direction of the heating beam, respectively. A reference case with the heating laser switched off (i.e., $\dot{Q}_0 = 0$ W) is also presented for the $\bar{d}_p = 423$ μm particles, for which the reduction in fluorescence signal due to attenuation or signal trapping from a single particle (and therefore also the expected magnitude of random errors) is most significant.

The instantaneous temperature distribution of the radiatively heated particle-laden flow is highly non-uniform downstream from the region with radiative heating ($0.9 < x/D < 1.9$), with distinct, localised regions of high and low temperature that can be seen throughout the flow (here termed 'hot' and 'cold' regions, respectively). The magnitude of the temperature difference between the hot and cold regions increases with a decrease in \bar{d}_p , consistent with the increase of the average absolute temperature rise (see Figure 4.10). Additionally, these hot and cold regions remain distinct from the surrounding flow to the downstream edge of the measurement region investigated. This suggests that both the particles and surrounding gas flow remain coherent (i.e., have similar velocities) and/or that the particles remain sufficiently hot that particle-gas convection more significantly influences the instantaneous temperature field than mixing with the cold co-flow due to entrainment.

The generation of the hot and cold regions is attributed to the spatial and

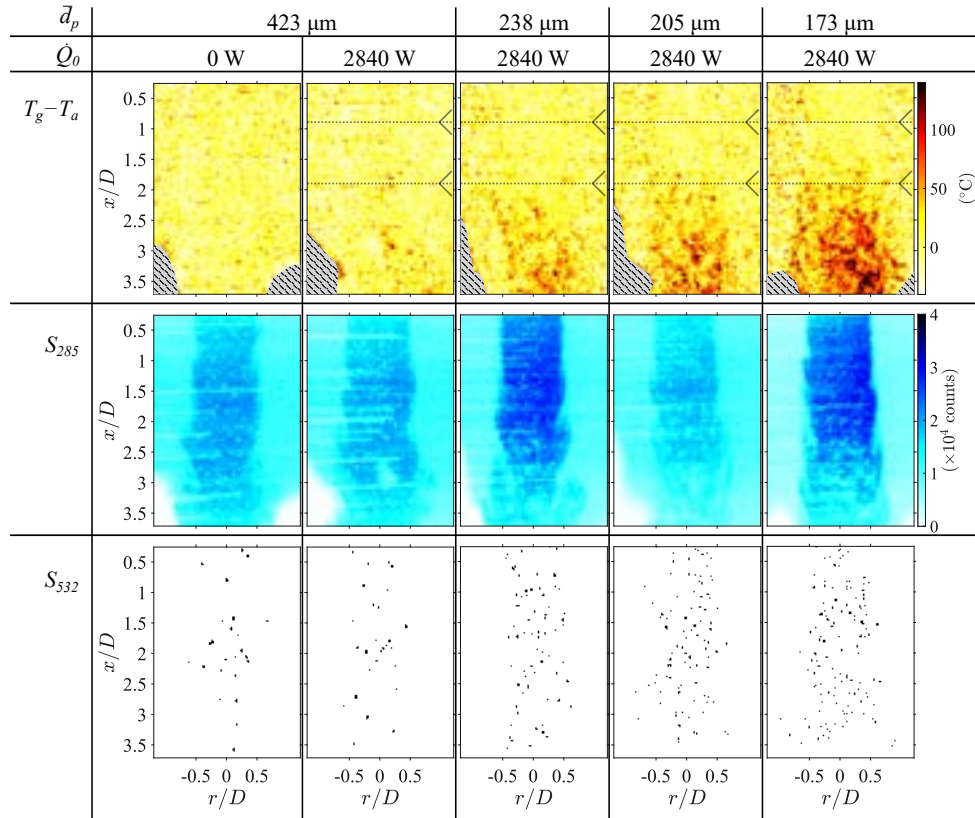


Figure 4.13: Typical instantaneous images of the temperature calculated from the two-colour LIF ratio, the fluorescence intensity in the channel S_{285} and the binary particle mask for each particle size investigated with $\phi = 1.4 \times 10^{-3}$ and $\dot{Q}_0 = 2840$ W. Also presented is a reference case with the heating laser switched off, for the $\bar{d}_p = 406$ μm particles. The dotted lines represent the upper and lower extent of the heating laser, where used, while the arrowheads indicate its direction. The regions with hatching correspond to where the fluorescence signal from either S_{285} or S_{315} is below the threshold for reliable measurements.

4.3 Instantaneous measurements of a radiatively heated particle-laden flow

temporal variations in the particle distribution, with local regions with a high particle loading ('clusters') and regions without particles ('voids') forming in the flow. The non-uniform particle distribution can be seen visually from the images of scattering by particles, with the variations in local particle volume fraction particularly evident for the cases with a relatively high particle number density (i.e., for $\bar{d}_p \leq 238 \mu\text{m}$). Because the Stokes numbers of these particles is $Sk_D \gg 1$, the generated clusters and voids are most likely the result of random particle motions [54]. Therefore, it is reasonable to assume that such variations in the local particle volume fraction, and therefore also the temperature for flows with strong radiative heating, occur in all particle-laden flows with initial volumetric loadings of magnitude similar to the present experiments ($\bar{\phi} \sim 10^{-3}$) regardless of the particle Stokes number.

Separate from these hot and cold regions, the measured temperature of individual pixels can occasionally vary significantly from that of its neighbours. These are likely to be errors in the measurement and attributed to several possible causes: 1) noise/natural variation of the fluorescence intensity measurements; 2) slight misalignment of the fluorescence images, which can lead to significant errors in regions with strong intensity gradients (e.g., the shear layer), and 3) interference from the particles. Additionally, it can be seen that the temperature within the hot regions is occasionally greater than the peak temperature measured during the calibration (160 °C). The temperature calculated within these regions using the calibration curve presented in Figure 3.15 was predominantly < 200 °C. Previously conducted calibration measurements (not presented in this thesis) indicated that the linear relationship between intensity ratio and temperature for the present experimental arrangement continued to hold for the temperature range of $20 \text{ °C} < T_g < 230 \text{ °C}$, although the uncertainty continued to increase with increasing temperature due to the decrease in fluorescence intensity. As such, the random errors within these high-temperature regions are expected to be similar to those calculated for the regions with relatively low fluorescence intensity due to laser sheet attenuation and signal trapping by particles (i.e., $\sigma_T \approx 40 \text{ °C}$). Therefore, while the temperature in these regions can be accurately measured to be greater than the calibration peak temperature, individual peaks may also occur due to errors of the measurement.

The instantaneous distribution of fluorescence intensity can also be seen to be highly variable for each \bar{d}_p , with these signal variations arising due to the combination of several factors:

- the differing initial concentrations of toluene in the jet and co-flow,
- the mixing of each of these flows with the unseeded surroundings,

- the non-uniform laser sheet profile,
- signal trapping by particles, and
- attenuation of the excitation laser by particles and toluene.

The attenuation and signal trapping by particles lead to particularly strong gradients in intensity, with the resultant intensity distribution displaying circular regions of low fluorescence intensity and streaks that are aligned with the beam direction (right to left in the image). The size of these regions and total reduction in intensity can be seen to increase with an increase in \bar{d}_p , with a reduction of up to 45% in the streaks down-beam from the $\bar{d}_p = 423 \mu\text{m}$ particles. Despite this, the pixel-to-pixel standard deviation within a single image of the unheated particle-laden flow was in the range $17.8 < \sigma_T < 18.8 \text{ }^\circ\text{C}$ for each \bar{d}_p , which implies that the reduction in intensity due to particles is the same for both S_{285} and S_{315} (see also Figure 3.16), such that the intensity ratio remains approximately the same. Resultantly, the errors to the two-colour LIF method due to particles are minor compared to those already present for the single phase flow.

Figure 4.14 presents instantaneous images of the gas-phase temperature for the flow with $\bar{d}_p = 238$ and $173 \mu\text{m}$, $\dot{Q}_0 = 2840 \text{ W}$ and $\bar{\phi} = 1.4 \times 10^{-3}$, together with the corresponding normalised, smoothed temperature Θ_S labelled with the boundaries of the hot and cold regions (see Section 3.8.2 for the method used to determine the hot and cold regions), and the locations of the individual particles and void regions. The presented images of the flow are limited to the regions that typically exhibit a significant temperature rise, for $1.4 < x/D < 3.6$ and $|r/D| < 0.5$. It can be seen that the hot and cold regions are interspersed throughout the flow, with each region typically appearing as an irregular ellipse-like shape whose primary axes are aligned at an angle of $\sim 45^\circ$ to the jet centreline. This shares some similarity with the oblique angles seen for particle clusters in a particle-laden jet, for a flow with $Sk_D \approx 1.4$ [113]. Additionally, the hot regions can be seen to be more prevalent near to the jet axis, while the cold regions are more common near to the jet edge. This is consistent with the combination of the heated particles being concentrated toward the jet axis (see Figure 4.8) and the influence of convection/mixing with the cold co-flow near to the jet edges.

No clear patterns in the location of clusters or voids can be seen from the particle images, consistent with the expectation that they are formed as the result of random variations in the particle motions. This was confirmed by comparing the results from the Voronoi analysis of the experimental particle locations with the random particle simulation (see Paper IV for this analysis).

4.3 Instantaneous measurements of a radiatively heated particle-laden flow

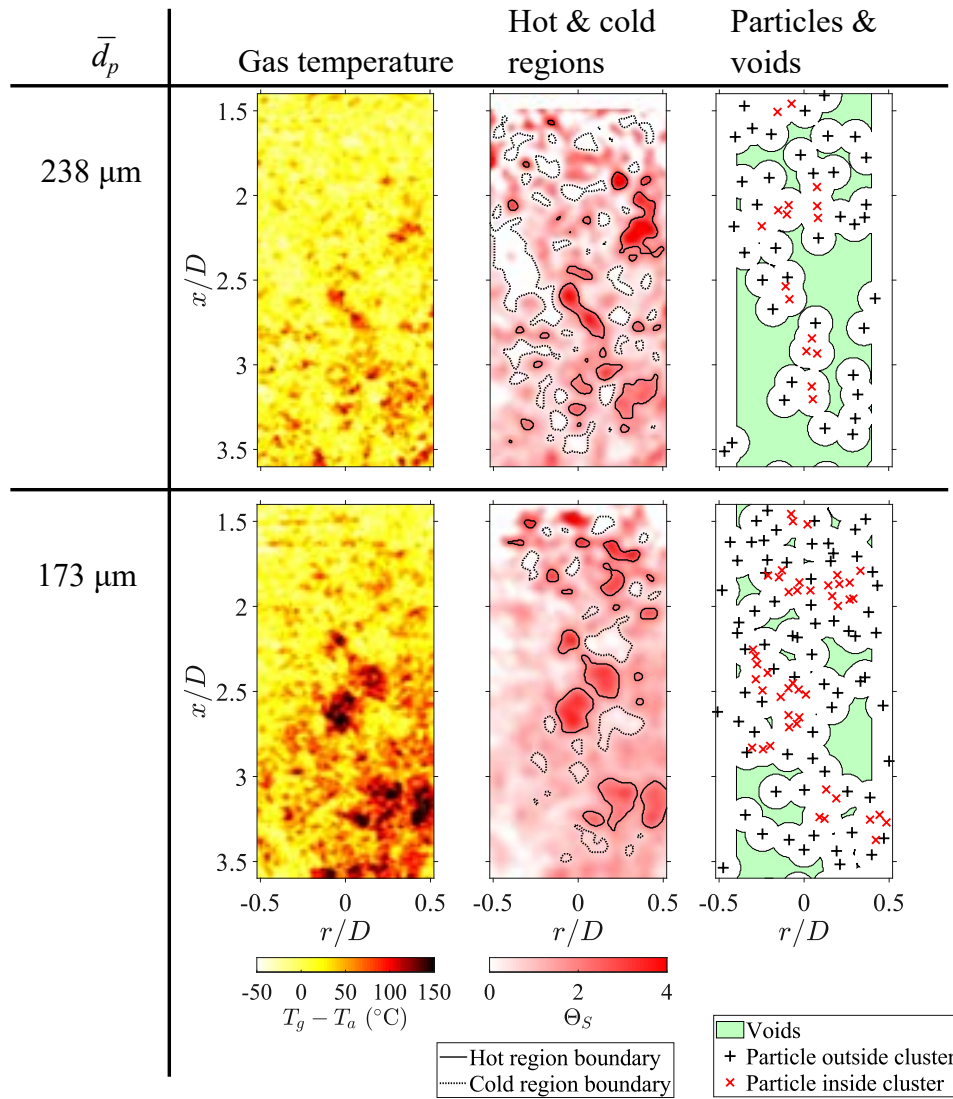


Figure 4.14: Selected instantaneous images of the gas-phase temperature for two particle diameters, the corresponding normalised, smoothed temperature Θ_s with the detected hot and cold region boundaries and the simultaneous particle locations, both inside and outside of clusters, and the void regions.

The flow regions with a locally high local volumetric fraction also correspond well visually with the location of the hot regions, particularly for those with particles identified to be within clusters. This visual agreement is consistent to the downstream edge of the measurement region, implying that the flow structures such as clusters are persistent (i.e., long lived) in the flow.

It can also be seen that the proportion of the flow determined to be within the void regions (defined as being further than $0.1D$ from the nearest particle) increases with an increase in \bar{d}_p , due to the corresponding decrease in particle number density. The average proportion of the flow within the void regions for a constant particle loading of $\bar{\phi} = 1.4 \times 10^{-3}$ was 24, 33, 47, 79% for $\bar{d}_p = 173, 205, 238, 423 \mu\text{m}$, respectively, which have corresponding particle number densities of $n_p = 0.39, 0.24, 0.18$ and 0.04 particles/ mm^{-3} , respectively. This implies that the regions of the flow that remain unheated, or with a relatively minor temperature rise compared to that of the flow near to particles, become increasingly significant with a decrease in particle number density.

Figure 4.15 presents the particle volume fraction measured within the boundaries of the hot and cold regions, ϕ_{reg} , normalised by the time-averaged volume fraction evaluated at the region centroid, $\bar{\phi}(x)$, as a function of axial distance for a series of \bar{d}_p with $\bar{\phi} = 1.4 \times 10^{-3}$ and $\dot{Q}_0 = 2410$ W. The results are presented as the ensemble average of all regions within equally spaced bins of length $0.25D$, with the ensemble averaging procedure represented by the angled brackets ($\langle \rangle$). The results show that the local particle volume fraction within the hot regions is significantly greater than both the mean and that in the cold regions, with $\langle \phi_{reg} / \bar{\phi}(x) \rangle > 1.5$ in the hot regions for each particle diameter distribution. Conversely, typical values of $\langle \phi_{reg} / \bar{\phi}(x) \rangle < 1$ are measured within the cold regions. This implies that, within the region $1.5 < x/D < 3.5$, both phases of the flow remain coherent (i.e., the particles and gas move together with little slip) and/or that the particles remain sufficiently hot to continually generate strong thermal gradients through convective heat transfer. The measured correlation between the local volume fraction and the hot/cold regions decreases slightly with axial distance (i.e., $\langle \phi_{reg} / \bar{\phi}(x) \rangle$ approaches 1 with an increase in x/D), suggesting that the entrainment of the cold surrounding gas through mixing and convection within the gas phase becomes increasingly significant relative to the particle-gas convection with distance downstream from the heating region. While the present measurements are limited to the near field, this correlation is expected to continue to weaken for measurements further downstream.

Figure 4.16 presents the measured temperature $T_g - T_a$ as a function of the local particle volumetric fraction (ϕ_{loc}), normalised by the time-averaged

4.3 Instantaneous measurements of a radiatively heated particle-laden flow

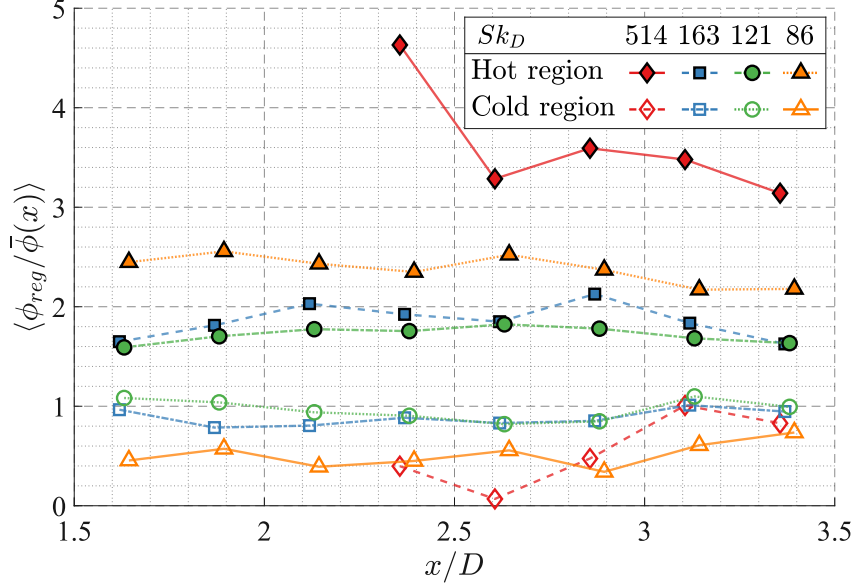


Figure 4.15: Ensemble average of the measured particle volumetric loading within the detected hot and cold regions, ϕ_{reg} , normalised by the time-averaged loading at the same location, $\bar{\phi}(x)$, as a function of axial location for a series of Sk_D with $\bar{\phi} = 1.4 \times 10^{-3}$ and $\dot{Q}_0 = 2410$ W.

volumetric fraction ($\bar{\phi}$), for a series of Sk_D with $\bar{\phi} = 1.4 \times 10^{-3}$ and $\dot{Q}_0 = 2410$ W (a) and for a series of axial distances with $Sk_D = 86$, $\bar{\phi} = 1.4 \times 10^{-3}$ and $\dot{Q}_0 = 2410$ W (b). The temperature is presented for the three flow conditions of $T_{g,Hi}$, $T_{g,Lo}$, and $T_{g,Vd}$ (defined in Section 3.8.4). It should also be noted that, by the definition used, the particle loading within the voids is $\phi_{loc} = 0$.

The presented data used for Figure 4.16a is limited to the region of $2 < x/D < 2.25$, $|r/D| < 0.3$, which is immediately downstream from the heating beam. This region was chosen to be analysed because of the large temperature difference between the particles and gas, and subsequent strong temperature gradients in the flow. Additionally, within this region the time-averaged radial profiles of the temperature and particle volumetric fraction are close to uniform for each case, with \bar{T}_g varying by less than 15 °C and $\bar{\phi}/\bar{\phi}_{CL} > 0.8$ (see Figure 4.8). As such, the non-uniformities in the particle volume fraction due to the radial distribution in the pipe flow are small for the presented results. This means that the primary driver for any variations in the gas-phase temperature are expected to be the random fluctuations of particle motions.

The temperature around particles can be seen to be greater than that in

the voids for each \bar{d}_p and each axial location downstream from the beginning of the heating beam. The local temperature measured around particles can be seen to increase with an increase in $\phi_{loc}/\bar{\phi}$, consistent with the time-averaged results. Additionally, $T_{g,Hi}$ is typically greater than $T_{g,Lo}$ for a given $\phi_{loc}/\bar{\phi}$, although this difference is relatively modest with $T_{g,Hi} - T_{g,Lo} < 3$ °C for each case. The results also show that the absolute value of the temperature difference $T_g - T_a$ is more strongly dependent on \bar{d}_p than ϕ_{loc} . For example, for $Sk_D = 121$, $T_{g,Hi} - T_a$ increases from 20 °C to 29 °C for a four-fold increase in the local volume fraction from $\phi_{loc}/\bar{\phi} = 1$ to $\phi_{loc}/\bar{\phi} = 4$. However, for a decrease of the particle diameter by approximately half, from 423 μm to 205 μm (corresponding to an $\sim 8\times$ increase in particle number density), at a fixed volume fraction of $\phi_{loc}/\bar{\phi} = 3$, $T_{g,Hi} - T_a$ increases from 8 °C to 24 °C.

The gradient of the temperature rise with volume fraction (i.e., the slope of the lines) can be seen to increase with a decrease in the particle diameter. This gradient also increases with an increase in $\phi_{loc}/\bar{\phi}$ for the cases with $Sk_D \leq 121$ and $\phi_{loc}/\bar{\phi} > 2.5$. Taken together, these results imply that both the particle loading and diameter will significantly influence the instantaneous temperature distribution for sufficiently small particles. This suggests that the variations in temperature will be particularly significant in flows that generate local particle loadings much higher than the mean, such as those with aerodynamic particle clustering where regions with $\phi_{loc}/\bar{\phi} > 10$ have been measured [113].

For the results measured upstream from the heating laser at $x/D = 0.75$, the temperature for each case is approximately zero regardless of the local particle volume fraction. This is consistent with expectation because the particles are yet to be heated directly at this point, although multiple scattering of the heating laser by particles may lead to an effective broadening of the heating region. Downstream from the heating region, not only does the average temperature increase with an increase in axial distance but for $x/D < 2.5$ the correlation between temperature and loading also becomes stronger. The increase in temperature with $\phi_{loc}/\bar{\phi}$ downstream from the region with radiative heating means that the flow is being continually heated by the particles, implying that the particles remain significantly hotter than the gas to the downstream edge of the measurement region.

4.3 Instantaneous measurements of a radiatively heated particle-laden flow

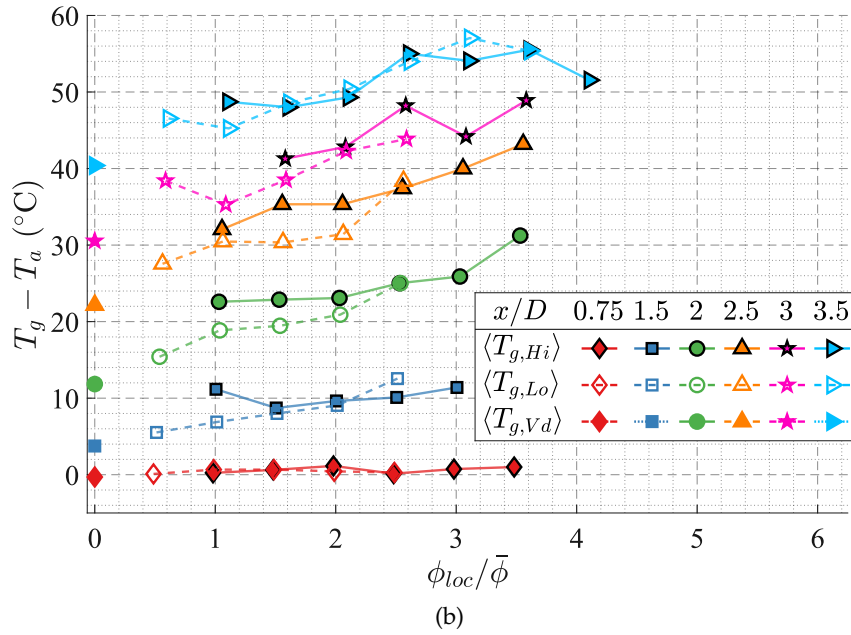
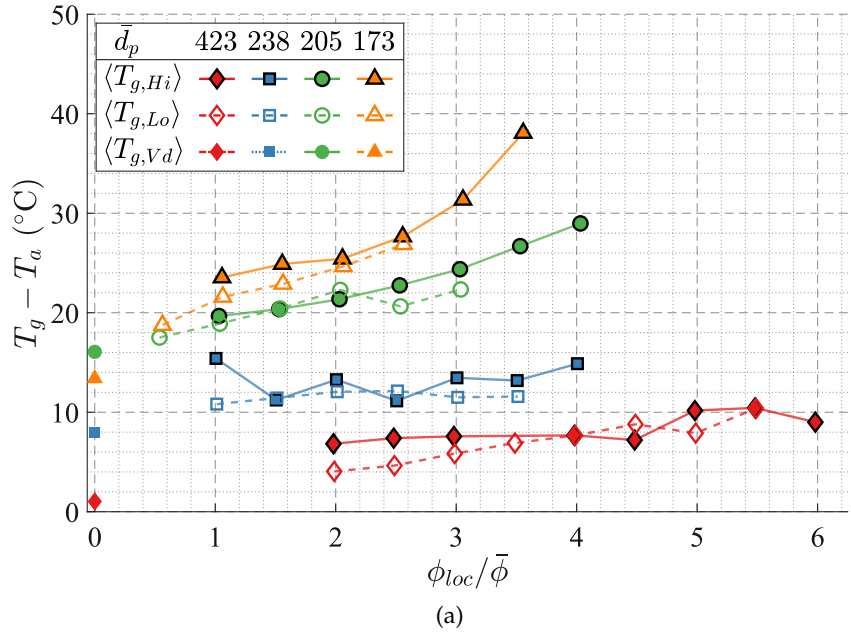


Figure 4.16: The ensemble average of the temperature above ambient as a function of the local particle volumetric loading, for the regions around particles inside clusters, outside clusters and in voids, for a series of Sk_D with $\bar{\phi} = 1.4 \times 10^{-3}$ and $\dot{Q}_0 = 2410$ W measured in the region immediately downstream from the heating laser of $2 < x/D < 2.25$ (a) and for a series of axial locations with $Sk_D = 86$, $\bar{\phi} = 1.4 \times 10^{-3}$ and $\dot{Q}_0 = 2410$ W (b).

Chapter 5

Conclusions and recommendation for future work

5.1 Conclusions

Optical filtering was used to isolate the fluorescence emissions from toluene LIF and suppress interference from elastically scattered light to allow spatially resolved gas-phase temperature measurements in particle-laden flows, at volumetric loadings in the two- and four-way coupling regimes relevant to industrial systems. The particle volumetric loading for which measurements were suitable was found to be primarily dependent on the particle material. The measurement error was found to increase with an increase in the local particle volumetric loading, ϕ , for each of the PMMA, ZnO:Zn, and alumina particles investigated. The PMMA particles, which emit broadband fluorescence at the wavelengths used for two-colour LIF in the present investigation, were found to generate greater interference for the same local volumetric loading than both the zinc-activated zinc oxide (ZnO:Zn), which emits phosphorescence at wavelengths longer than used for two-colour LIF, and alumina particles, which did not exhibit luminescence. For the present optical arrangement (Experiment I, see 3.8), the combined interference from the particle fluorescence and elastic scattering of laser light led to a systematic error in the measurement of 5 °C at a volumetric loading of $\phi = 2 \times 10^{-4}$ for the PMMA particles, while for the alumina and ZnO:Zn particles the temperature measurement was accurate to within 5 °C for $\phi < 7 \times 10^{-4}$. The method was also identified to be potentially suitable for measurements of flows in the four-way coupling regime, for $\phi > 10^{-3}$, with additional optical filtering and appropriate particle materials. Additionally, the measurement accuracy for the flow with PMMA particles was found to be independent of

the particle size (and hence number density for a constant volume fraction), implying that the fluorescence emitted from the particles was the primary source of interference for this material.

The two-colour LIF method was also demonstrated to be suitable for measurements of the gas-phase temperature distribution in a particle-laden jet heated using infra-red radiation at fluxes up to a peak of 42.8 MW/m^2 , for a flow with highly absorptive, aluminosilicate ceramic particles of median diameter $173 \leq \bar{d}_p \leq 423 \text{ }\mu\text{m}$ and average particle volumetric loadings in the range $6.25 \times 10^{-4} \leq \bar{\phi} \leq 1.4 \times 10^{-3}$. Additional optical filters were utilised for this investigation (Experiment II, see 3.10) to allow the assessment of higher loadings than used for Experiment I. The instantaneous radial distribution of gas-phase temperature, measured downstream from the start of the heating region, was found to be highly variable, both spatially and temporally. Regions of locally high temperature were identified to remain coherent to the downstream edge of the measurement region investigated ($x/D = 3.7$). The average temperature rise of the gas flow was measured to increase at rates up to $2,200 \text{ }^\circ\text{C/m}$ on the jet centreline, in the region downstream from where the particles are heated rapidly following the absorption of high-flux radiation. This increase in temperature with axial distance was close to linear, indicating that there was a significant temperature difference between the particles and gas to the downstream edge of the measurement region.

In the region downstream from the heating beam ($0.9 < x/D < 3.7$), the time-averaged temperature rise of the gas from the ambient value was found to be proportional to the heating beam power. This is consistent with the linear dependences of both the particle temperature on the radiative flux and of the convective heat transfer on the particle-gas temperature difference. Similarly, this temperature rise was found to be proportional to the particle volumetric loading. This is consistent with the total radiation absorption being proportional to the total cross-sectional area of particles and the particle-gas convection being proportional to the particle surface area, both of which are linearly dependent on $\bar{\phi}$. The temperature rise was found to decrease significantly for an increase in the particle diameter \bar{d}_p . This is due to the non-linear relationships for \bar{d}_p with both the radiation absorption and convective heat transfer (from both the Nusselt number calculation and particle surface area).

The trends identified from a simplified one-dimensional heat transfer model tracking a single particle on the jet centreline were found to closely match those from the time-averaged measurements of the gas-phase temperature, both within and immediately downstream from the heating region. Such simplified models are suitable to give an indication of the effect of

the particle diameter and volumetric loading on the average heat transfer in the system, particularly for flows with relatively few particles and low heating flux. However, they do not account for the random fluctuations of particle distributions or local heating fluxes, which were found to be highly non-uniform in the real flow leading to strong instantaneous temperature gradients. The difference between the model and measurements was found to typically increase with an increase in the heating power and a decrease in the particle diameter. These differences are primarily attributed to the estimated quantities in the model, such as the particle-fluid slip velocity, together with the influence of particle clustering and heating beam attenuation that occur in the real flow but are not accounted for in the model.

Neither the time-averaged particle distribution nor the particle velocity field were measured to change with an increase in the radiative heating flux. This implies that any motions induced by thermal gradients in the gas-phase, such as from buoyancy, turbulence, or thermophoresis, do not significantly affect the particle phase in the jet flow investigated, for the relatively large, dense particles used in the present thesis.

The local, instantaneous gas-phase temperature was found to be well correlated with the local particle volume fraction. The temperature difference between the regions around particles within clusters, around particles outside of clusters, and within void regions was measured to increase significantly with a decrease in particle diameter. Similarly, localised regions that were identified to have a relatively high temperature compared to the surrounding flow ('hot' regions) were found to typically have a higher particle volume fraction than the mean, while a low local volume fraction was measured within the boundaries of the identified 'cold' regions. This trend was seen at each axial location to the edge of the measurement region investigated ($x/D < 3.7$), indicating that the gas and particles closely follow each other through the flow (i.e., both phases have similar velocities) and/or that the convective heat transfer between the particles and gas is more significant than entrainment of the cold co-flow through mixing and convection.

5.2 Recommendation for future work

Numerous opportunities are available to capitalise on the advances reported in the present thesis, to improve the current understanding of non-isothermal particle-laden flows that exhibit highly complex, mutually interacting, non-linear flow motions. Despite the advances of the present work in demonstrating a method for instantaneous, spatially-resolved gas-phase temperature measurements of particle-laden flows and analysing the effect of particle

diameter and volumetric loading in such flows, further work is required for complete characterisation of particle-laden flows.

Further understanding of the fundamental processes within non-isothermal particle-laden flows requires not only measurements of gas-phase temperature and particle loading, as performed in the present experiments, but also of the gas-phase velocity, particle velocity, and particle temperature. Ideally, these measurements should be conducted simultaneously under identical conditions. Such measurements are also required for a wider range of particle Stokes numbers (i.e., $Sk_D \sim 1$ and $Sk_D \ll 1$) and flow conditions (i.e., $Re_D > 10,000$) to assess the effect of the particle response, particle clustering, and flow turbulence on the fundamental heat transfer processes. The influence of both gas- and particle-phase motions induced from thermal gradients in the system, such as buoyancy, turbulence and thermophoresis, are also required to be assessed for $Sk_D \sim 1$ and $Sk_D \ll 1$.

Either time-resolved measurements of the radiatively heated flow or additional, detailed analysis of spatially-resolved measurements are required to assess the coherence of the heated regions identified in the present thesis. This coherence is also required to be analysed in regions further downstream than were investigated for the present thesis ($x/D < 3.7$) to improve understanding of the interactions that may only become significant in the far-field, such as gas-phase mixing and buoyancy. Furthermore, spatially resolved measurements of the gas-phase temperature and velocity in the region around individual particles are required, to provide deeper understanding of particle-fluid interactions.

Measurements of these key parameters in the more complex flow configurations used for industrial particle-laden flow systems would also be useful for system-specific knowledge, together with improved insight into the fundamental flow processes. Such measurements are also needed for the development and validation of reliable, predictive numerical models, which can then be used to optimise the efficiency of particle-laden flow systems.

Appendix A

Wind tunnel characterisation

The radial velocity profile of the pipe-jet, co-annular flow and wind tunnel that was used for the experiments, described in Section 3.1, was measured using hot-wire anemometry. The velocity was determined from the output voltage of a TSI IFA 300 constant temperature anemometer using a National Instruments data acquisition system (PXI-4462). A TSI single-wire tungsten probe was used, with measurements sampled at 10 kHz. Measurements were recorded at each point for 2 minutes to ensure that all time scales of flow structures were identified. The output voltage from the probe was calibrated to velocity using a custom-made jet connected to a mass flow controller with a smooth contraction that generates a near-uniform velocity field at the exit plane. During the calibration, both the hot-wire probe and a pitot-static probe, used to determine the actual flow velocity from the pressure, were positioned at the jet exit plane near to the axis. The pressure was determined from the pitot-static tube using a Baratron 1000. Measurements of the output voltage and flow pressure were then performed for a series of flow velocities. The probe was left switched on overnight before recording the calibration and measurements to ensure the outlet voltage was stable. The position of the probe was controlled using a 3-axis traverse, which was accurate to within 0.25 mm for each spatial dimension. The radial profile of the flow velocity within the wind tunnel was measured for a series of axial distances and jet Reynolds numbers. The distance between data points was varied depending on the local velocity gradients, such that the data points are more closely spaced within the jet and shear layers than in the relatively uniform wind tunnel flow.

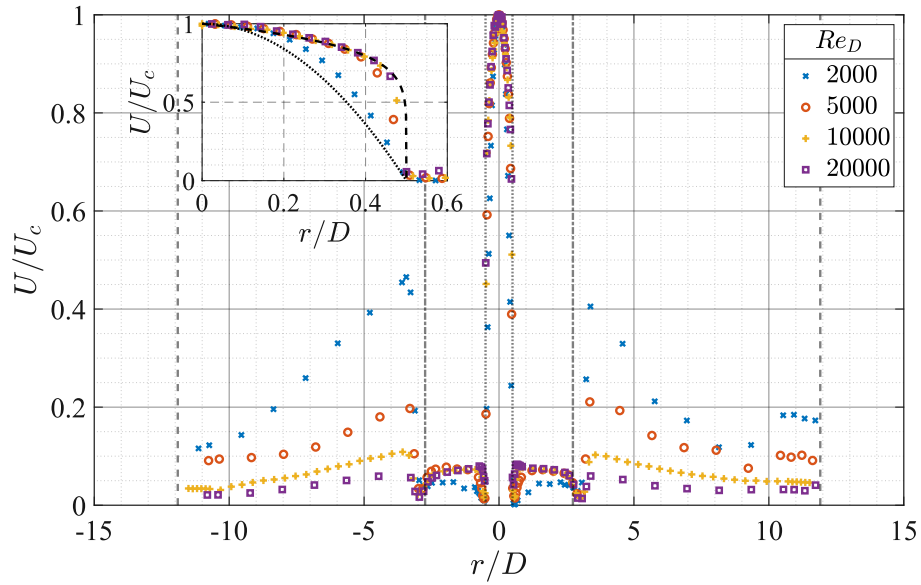
Figure A.1 presents the radial profile of axial velocity (U) within the wind tunnel (a), the radial profile normalised by the centreline value U/U_c (b), while Figure A.2 presents the normalised standard deviation of measured

velocity u'/U for $|r/D| < 0.6$, each measured near to the jet exit plane ($x/D = 0.5$) for a series of pipe Reynolds numbers of $Re_D = 2,000, 5,000, 10,000$ and $20,000$. The vertical lines in each figure indicate the position of the jet pipe, annular pipe, and wind tunnel walls. The annular flow rate was set such that the volumetric flow rate was 1/12th of the jet to match the previous measurements by Lau and Nathan [44]. The fan drawing air through the wind tunnel was set to the lowest available power. The inset axes for figure A.1 present the detailed profile of velocity measured near to the jet axis with $0 < r/D < 0.6$. The results show that the jet velocity is greatest on the centreline and decreases with r/D to the pipe wall, consistent with well-known pipe jet trends. The centreline exit velocity of the jet was $U_c = 25.2, 13.8, 6.6$ and 3.6 m/s for the flows with $Re_D = 20,000, 10,000, 5,000$ and $2,000$ respectively. The velocity measured in the shear layer region of $0.5 < r/D < 0.6$ was close to zero because of the finite thickness of the pipe wall. The peak velocity within the annular flow was at $r/D = 0.7$ with a near-uniform velocity measured in the region $0.7 < r/D < 2$. The annular pipe exit is slightly upstream (~ 10 mm) of the jet exit, so that the velocity downstream from the annular pipe wall is greater than for the central pipe. The velocity in the wind tunnel co-flow closely matches for each Re_D , with a velocity of $U = 1.7$ m/s near to the annular pipe wall at $r/D = 3.5$ decreasing to $U = 0.5$ m/s near the tunnel wall.

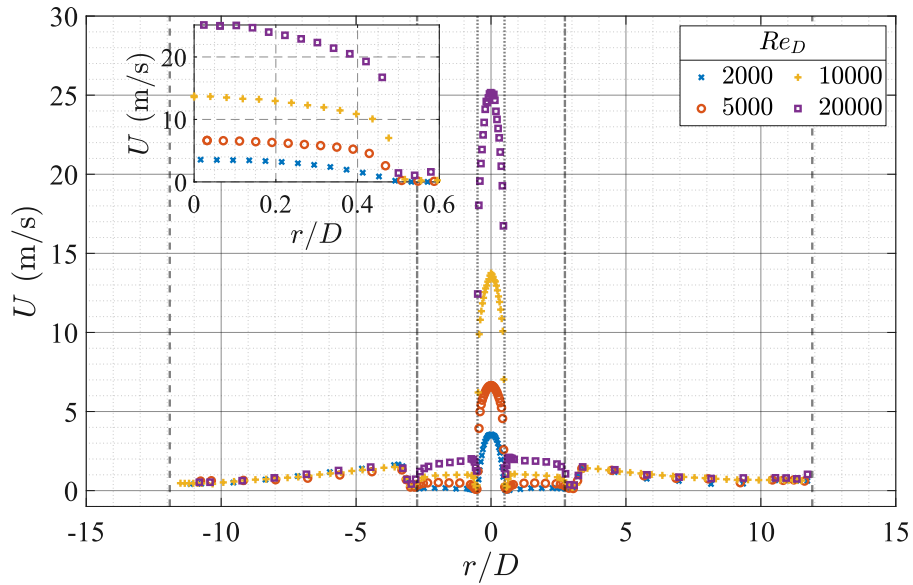
The normalised velocity profiles U/U_c collapse closely for $Re_D \geq 5,000$, while the decay from the centreline to the jet edge is greater for the flow with $Re_D = 2,000$. This is due to the turbulence of the flow, which is characterised by the Reynolds number. For the investigated jet flows:

- $Re_D = 2,000$ is expected to be in the laminar regime,
- $Re_D = 5,000$ is expected to be in the transitional regime, and
- $Re_D \geq 10,000$ are expected to be fully turbulent [120].

The laminar flow in a pipe jet is expected to have a parabolic velocity profile of the form $U/U_c = 1 - (2r/D)^2$. The turbulent velocity is generally well approximated by a 1/7th power law profile of the form $U/U_c = (1 - 2r/D)^{1/7}$. These velocity profiles are presented together with the measured results in Figure A.1b. The results show that the measured velocity profile closely matches the 1/7th power law for $Re_D \geq 10,000$. For the $Re_D = 5,000$ case the velocity profile closely matches the 1/7th power law for $r/D < 0.4$ while it is lower for $r/D > 0.4$, indicating that the flow is not fully turbulent. For the flow with $Re_D = 2,000$, U/U_c closely matches the parabolic profile expected for laminar flows.



(a)



(b)

Figure A.1: Radial profiles of axial velocity of the jet and co-flow for a series of jet Reynolds numbers measured near to the jet exit plane at $x/D = 0.5$ (a), the velocity normalised by the centreline value (b). The insets present the detail of the velocity in the jet flow for $|r/D| < 0.6$, with the analytical profiles for both laminar and turbulent pipe jets also presented for the middle sub-figure. The vertical dashed lines indicate the jet diameter ($\cdot\cdot$), annular pipe diameter ($\cdot-$) and the wind tunnel walls ($--$).

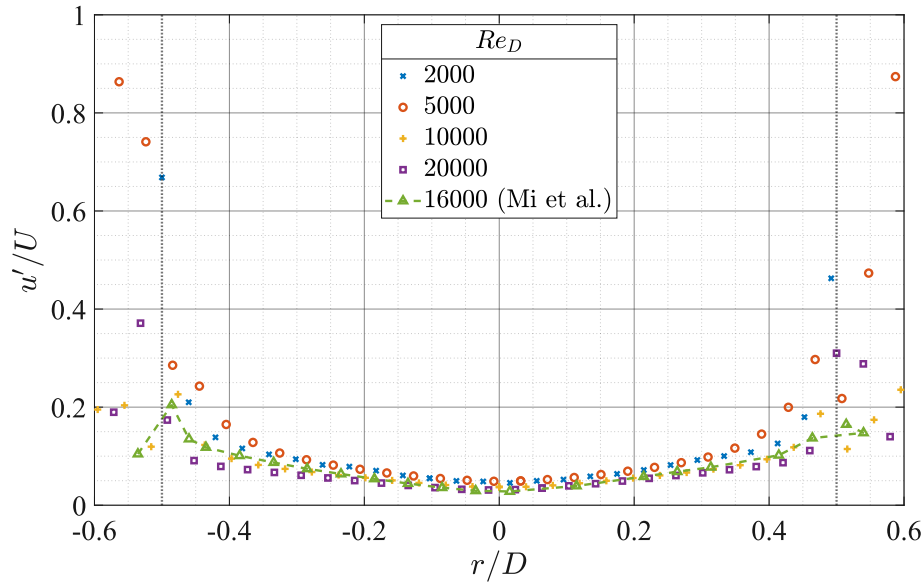


Figure A.2: Radial profile of the standard deviation of velocity fluctuations for a series of jet Reynolds numbers measured near to the jet exit plane at $x/D = 0.5$

The root mean square (RMS) of fluctuations in the velocity was measured to be $u'/U \approx 0.35$ at $r/D = 0$ for each Re_D , while near to the pipe edge u'/U typically increases with a decrease in Re_D . The velocity fluctuation data reported by Mi et al. [117] is also presented for Figure ??, for measurements of a turbulent pipe jet with a Reynolds number of $Re_D = 16,000$. The measured values match closely to this data for the fully turbulent cases with $Re_D \geq 10,000$, giving confidence that the jet flow is fully developed.

Figure A.3 presents the radial profiles of velocity in the wind tunnel, measured at a series of axial locations $x/D = 0.5, 12.6, 19.1$ and 22.2 , for the flow with $Re_D = 20,000$. The inset presents the velocity profiles normalised by the centreline velocity measured at $x/D = 0.5, U/U_e$. The results show that the velocity of the jet flow with $|r/D| < 0.5$ decreases with axial distance, due to entrainment of the surrounding flow. The entrainment of the co-flow also results in an increase of velocity measured within the co-flow in the region $(0.5 < |r/D| < 5)$ with axial distance. The magnitude of the velocity difference between the jet and co-flow decreases with x/D as the flow approaches a well-mixed condition.

Figure A.4 presents the velocity of the wind-tunnel co-flow (U_{cf}) measured at $r/D = 3.5$, normalised by the peak value, as a function of the fan

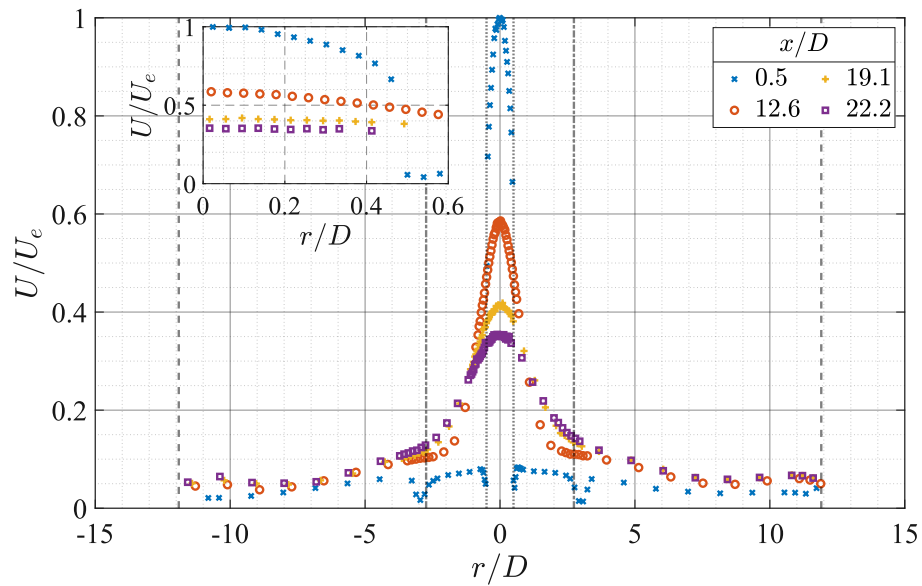


Figure A.3: Velocity measurements from hot-wire anemometry of the jet and co-flow at a series axial distances for $Re_D = 20,000$, normalised by the jet exit velocity. The inset shows the detail of the velocity in the jet flow, for $|r/D| < 0.6$. The vertical dashed lines indicate the jet diameter ($\cdot\cdot$), annular pipe diameter ($\cdot-$) and the wind tunnel walls ($- -$).

controller setting. The co-flow velocity can be controlled to be down to 40% of the maximum value, with an approximately linear relationship between the fan setting and flow velocity for settings in the range of 30-70%. The measured values correspond to co-flow velocities the range of $1.7 < U_{cf} < 4.1$ m/s at this radial location.

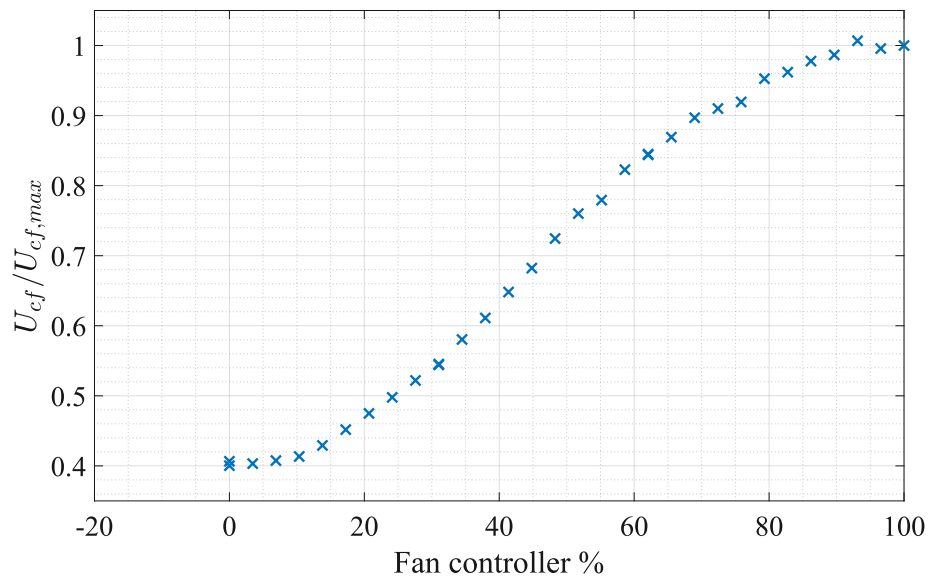


Figure A.4: Measured velocity in the co-flow for a series of fan controller positions, normalised by the velocity at the maximum speed.

Appendix B

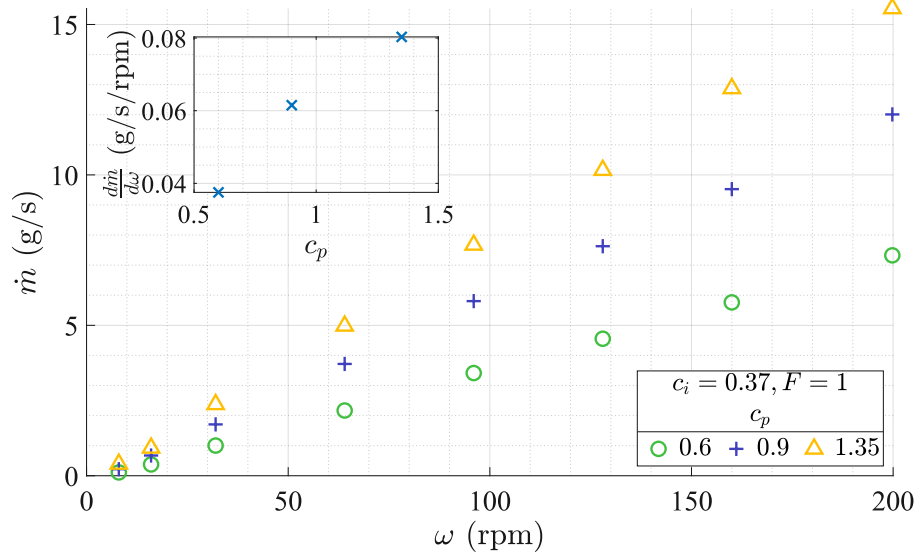
Screw feeder

Appendix B presents the evaluation of the series of screws designed for particle seeding that are described in Section 3.2. Both the mass flow rate of particles output from the screw, as a function of the screw rotational speed, and the steadiness of the mass flow rate with time were measured for free-flowing, mono-disperse spherical PMMA particles of diameter $40\ \mu\text{m}$ and absolute density $1200\ \text{kg}/\text{m}^3$. The three parameters varied in the screw designs were the pitch, P , the inner diameter, D_i , and the number of flights, F . From these, three non-dimensional parameters were calculated for each screw:

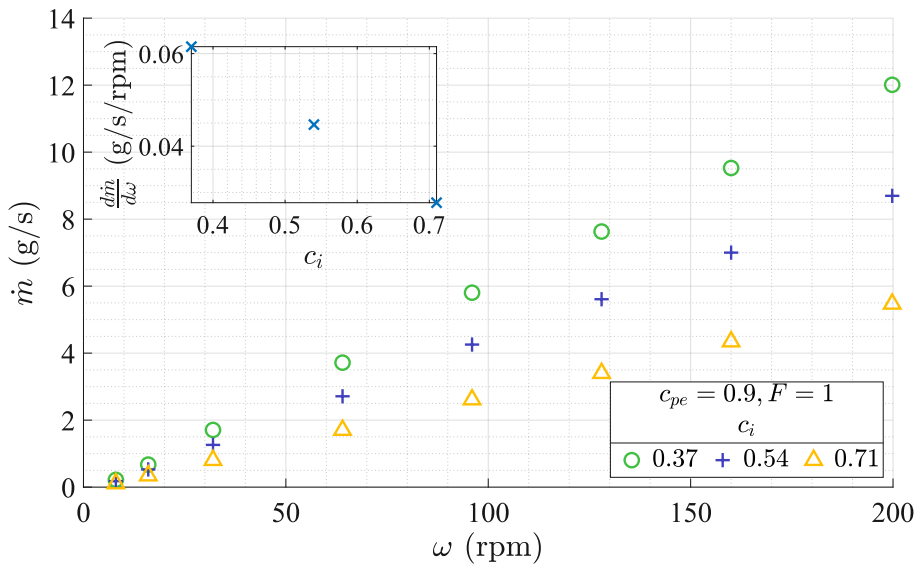
- the pitch to outer diameter ratio, $c_p = P/D_o$;
- the inner to outer diameter ratio, $c_i = D_i/D_o$;
- and the effective pitch of the screw, calculated from $c_{pe} = c_p/F$.

Seven separate screws were manufactured to isolate the effect of each of these on the particle flow, with the design parameters presented in Table 3.1 and Figure 3.3.

Figure B.1 presents the mass flow rate (\dot{m}) of particles output from the screw feeder as a function of screw rotational speed ω for screws designed with a series of c_p with $c_i = 0.37$ and $F = 1$ (a), a series of c_i with $c_p = 0.9$ and $F = 1$ (b), and a series of F with $c_{pe} = 0.9$ and $c_i = 0.37$ (c). The inset in each sub-figure presents the slope of a linear fit to the data, $d\dot{m}/d\omega$, as a function of c_p , c_i , and F , respectively. The results show that \dot{m} increases linearly with ω for $\omega < 200$ rpm for each screw investigated. This is consistent with expectation for a free-flowing material because the particles uniformly fill the volume between flights (i.e., without ‘bridging’ of the material between surfaces that forms voids), such that a constant volume of material is emitted

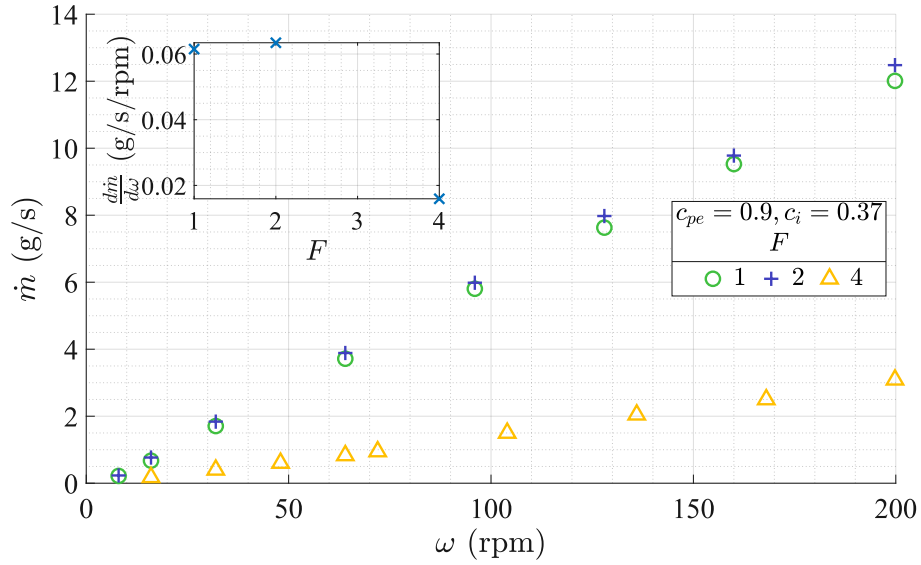


(a)



(b)

Figure B.1: (Continued next page)



(c)

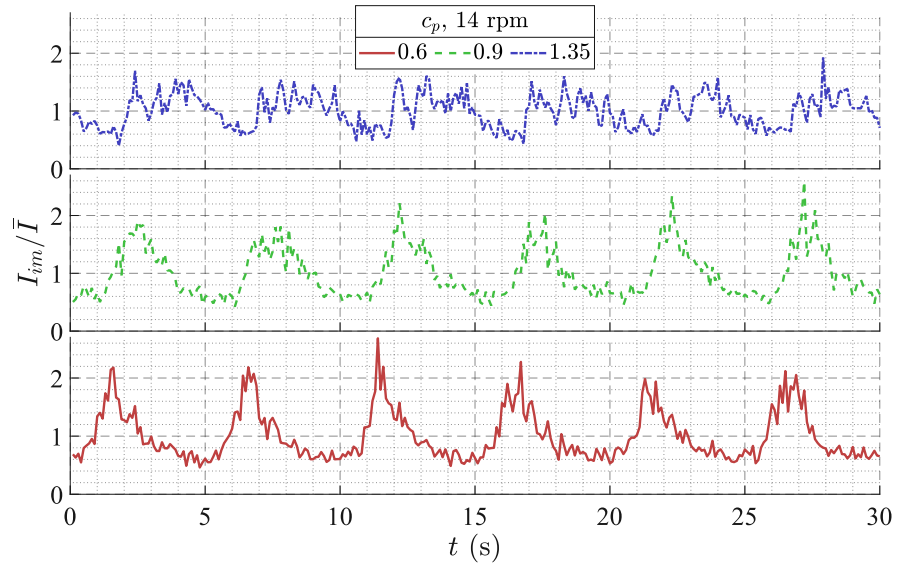
Figure B.1: Particle mass flow rate from screw feeder as a function of rotational speed for screws with varying pitch (c_p , a), core diameter (c_i , b), and number of flights (F , c), for 40 μm diameter spherical PMMA particles. The inset in each sub-figure presents the linear fit to the data, $d\dot{m}/d\omega$, as a function of c_p , c_i and F , respectively.

for each rotation of the screw. The value of $d\dot{m}/d\omega$ can be seen to increase with c_p within the range investigated here. Previous measurements indicate that there is an optimal c_p in terms of volumetric efficiency of the screw, with short-pitch screws conveying little material per rotation and long-pitch screws tending to transfer the material radially rather than axially [121, 122]. Additional screw designs with $c_p > 0.9$ would be required to be investigated to determine the optimal c_p for this system.

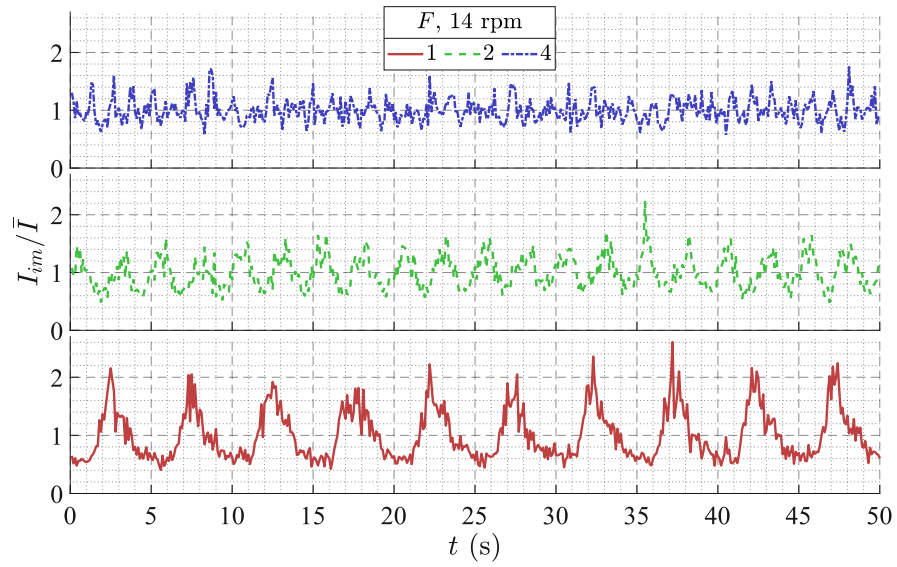
The results also show that \dot{m} decreases approximately linearly with increasing c_i , which is consistent with expectation because the volume contained within each pitch is proportional to $D_o^2 - D_i^2$, which is equivalent to $D_o^2(1 - c_i^2)$. No clear relationship can be seen between \dot{m} and F for the conditions investigated here, with measured gradients of $d\dot{m}/d\omega = 0.062$, 0.063, and 0.016 for $F = 1, 2$, and 4, respectively. This is potentially because of the relatively long pitch of each individual screw flight for the screw with $F = 4$ ($c_p = 3.6$) that results in significant radial transport of the material rather than axially towards the outlet, while for $F = 1$ and 2 (i.e., $c_p = 0.9$ and 1.8, respectively) the efficiency of axial transport is similar.

The steadiness of the mass flow rate of particles output from the screw feeder was investigated for each screw design by seeding the particles into the pipe jet arrangement described in Section 3.4.2, except without toluene in the flow and with the 266 nm laser switched off. The intensity of the Mie scattering of the 532 nm laser sheet from 40 μm PMMA particles, which is directly proportional to the particle number density for mono-disperse, spherical particles, was measured at 10 Hz for a series of mass flow rates for each screw. Each measurement was recorded for 50 seconds, to ensure that all time scales from the screw were covered. The instantaneous particle distribution may vary in the flow from the screw outlet to the jet exit. However, this flow configuration is the same as for the main experiments, so that these distributions are expected to be representative of the measurements in the main experiments. The instantaneous particle loading was derived from the spatial average of scattering intensity measured within the region $1 < x/D < 3$, $|r/D| < 0.35$. Potential sources of error and interference to this measurement include attenuation of the probe laser sheet, multiple scattering by particles, and signal trapping. However, each of these are expected to be minor for the particles and loadings investigated in the present experiments. The scattering signal is also proportional to the laser pulse energy, which was measured to vary by less than 10% from shot-to-shot. As such, any resultant temporal variations in the measured intensity are primarily attributed to fluctuations of the instantaneous particle volume fraction.

Figure B.2 presents the time-series of intensity measured in each individual image, normalised by the mean intensity for each case (I_{im}/\bar{I}), for the series of screws with varying pitch (a) and number of flights (b) with $\omega = 14$ rpm, together with I_{im}/\bar{I} for a series of rotational speeds with $F = 1$ and $c_p = 0.9$ (c). The results show that there is a periodic dependence of the average measured intensity with time for each c_p investigated, most significantly for the screw with the smallest pitch of $c_p = 0.6$. A screw with rotational speed of $\omega = 14$ rpm completes a full revolution every 4.3 seconds, which corresponds well to the time between the peaks in intensity. The magnitude of the periodic fluctuations in the intensity signal can be seen to decrease significantly with an increase in F , suggesting that the output from the 4-flighted screw is significantly more steady than from the standard single flight design. However, the compromise between the increase in steadiness and decrease in flow rate must also be considered. The results also show that the magnitude of fluctuations in intensity is greatest at $\omega = 14$ rpm, decreasing for $\omega = 32$ and 50 rpm then increasing again for $\omega = 68$. This increase for the $\omega = 68$ case is likely due to increased vibrations that were observed in the system for this rotational speed, which was attributed to ω

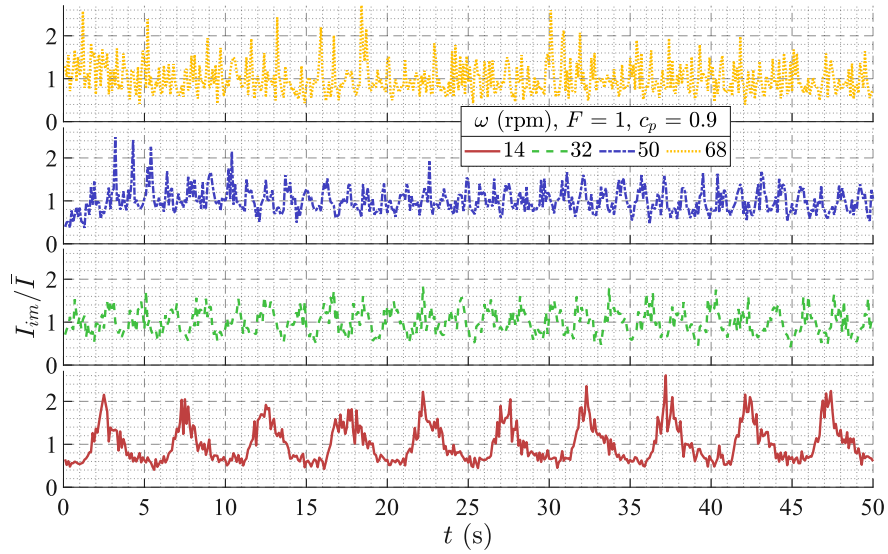


(a)



(b)

Figure B.2: (Continued next page)



(c)

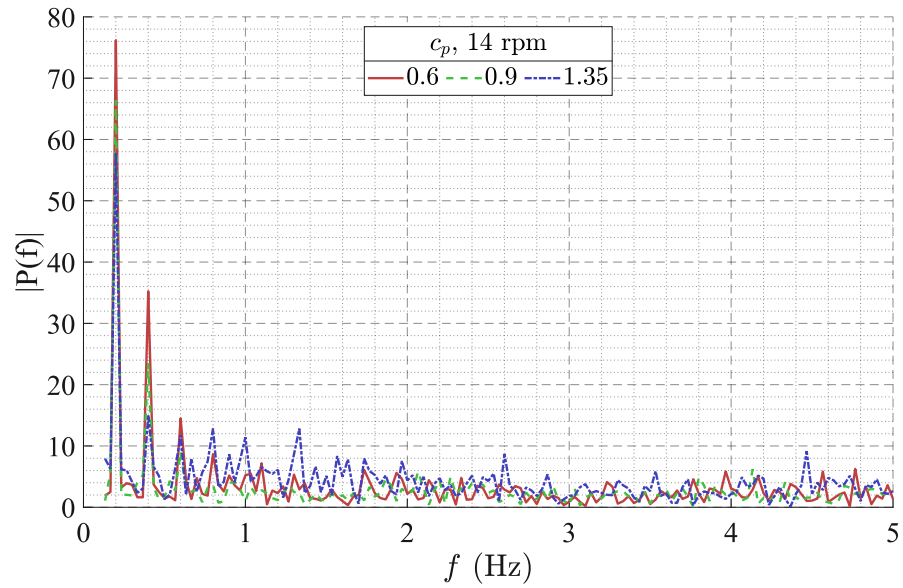
Figure B.2: Time series of intensity from particle scattering for screws with varying pitch (a) and number of flights (b), together with that for one screw at a series of rotational speeds (c), normalised by the time-averaged mean.

being close to a natural frequency in the system. Care should be taken to avoid these speeds for reliable output from the screw.

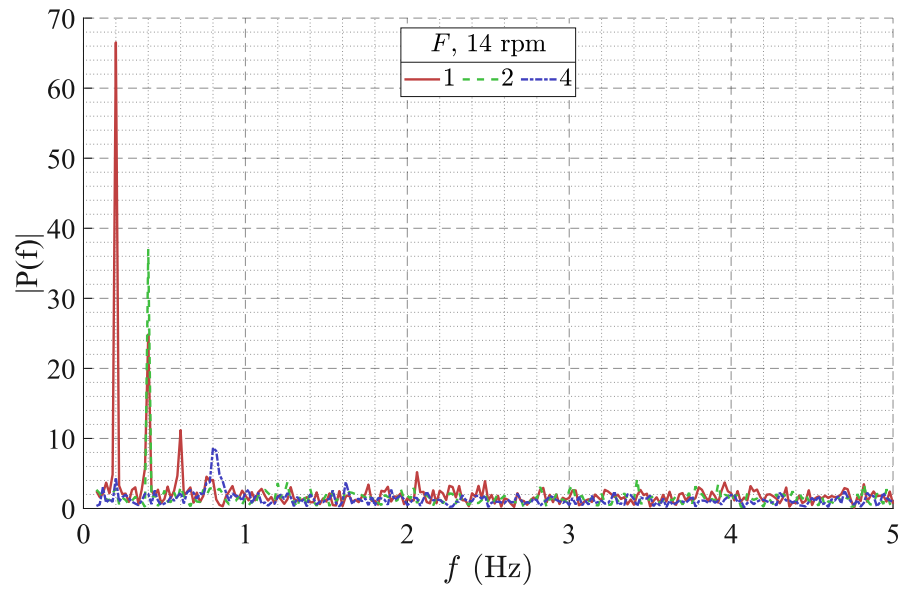
Figure B.3 presents the fast Fourier transform (FFT) of the time series of the intensity of elastically scattered light for the flow with particles introduced using screws with varying c_p at constant ω (a), with varying F at constant ω (b), and for a single screw at a series of rotational speeds with the frequency normalised by the rotational speed (c). Distinct peaks can be seen in the FFT for all c_p at the same frequency (f), with the first peak at 0.2 Hz and subsequent peaks at integer multiples of this frequency. This corresponds well to the rotational speed of 14 rpm, which is equivalent to 0.23 Hz. The amplitude of the peak is greatest for $c_p = 0.6$, with the amplitude decreasing with an increase in c_p . The frequency of the peaks in the FFT also increases proportional to F , with the peak occurring at frequencies that are $\sim F\omega/60$ for all F investigated here. The amplitude of the primary peak decreases significantly with F , which is consistent with the previous results implying that the particle flow rate becomes more steady with increasing F . For the series of rotational speeds, the strongest peak of the FFT is close to 1 for each ω . The amplitude of this peak, relative to the other peaks at higher

frequencies, decreases with an increase in ω . This indicates that while the flow is more steady at higher speeds, there is still a distinct periodic variation for the screw with one flight at all speeds.

In summary, the results show that screws with a longer pitch, more flights and operating at higher speeds seed particles in the flow more steadily, within the range of conditions investigated in the present study.

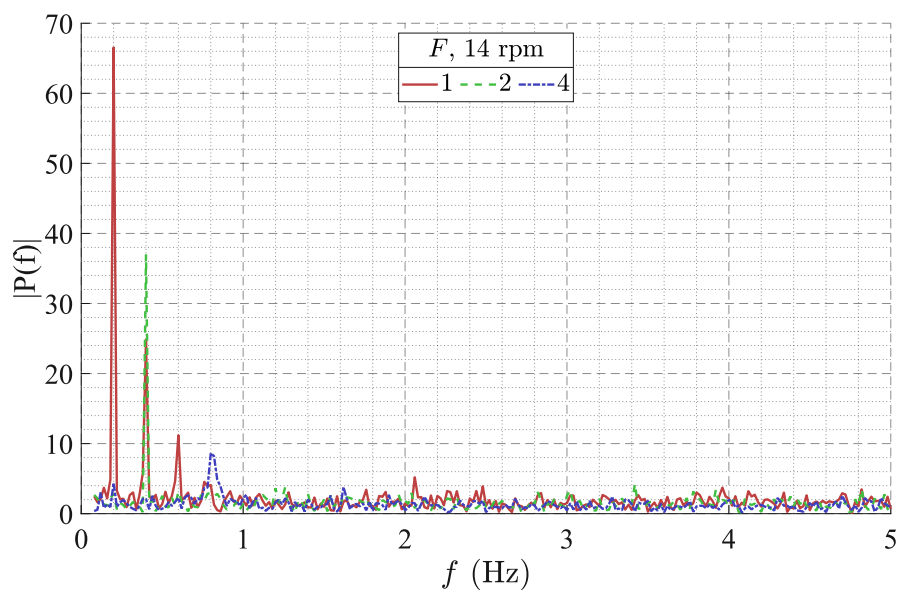


(a)



(b)

Figure B.3: (Continued next page)



(c)

Figure B.3: The fast Fourier transform of the time series of scattering intensity for screws at constant speed with varying pitch (a) and number of flights (b), along with for one screw at rotational various speeds (c), with the frequency normalised by the rotational speed.

Appendix C

Paper I - Luminescence interference to two-colour toluene laser-induced fluorescence thermometry in a particle-laden flow

This chapter presents the published journal article:

Lewis, E. W., Lau, T. C. W., Sun, Z., Alwahabi, Z. T. and Nathan, G. J. (2020), "Luminescence interference to two-colour toluene laser-induced fluorescence thermometry in a particle-laden flow." *Experiments in Fluids* 61(4): 101.

The article in its published format is available at:
<https://doi.org/10.1007/s00348-020-2942-8>.

The content of this chapter is identical to that of the published article, with the following exceptions:

1. The typesetting and referencing style may have been altered for consistency within the thesis.
2. The position and sizing of the figures and tables may differ.

Statement of Authorship

Title of Paper	Luminescence interference to two-colour toluene laser-induced fluorescence thermometry in a particle-laden flow
Publication Status	<input checked="" type="checkbox"/> Published <input type="checkbox"/> Accepted for Publication <input type="checkbox"/> Submitted for Publication <input type="checkbox"/> Unpublished and Unsubmitted work written in manuscript style
Publication Details	Lewis, E. W., Lau, T. C. W., Sun, Z., Alwahabi, Z. T. and Nathan, G. J. (2020), "Luminescence interference to two-colour toluene laser-induced fluorescence thermometry in a particle-laden flow." <i>Experiments in Fluids</i> 61(4): 101.

Principal Author

Name of Principal Author (Candidate)	Elliott W. Lewis		
Contribution to the Paper	Designed experimental arrangement and undertook experiments, developed data processing methods, interpreted data, wrote manuscript.		
Overall percentage (%)	70		
Certification:	This paper reports on original research I conducted during the period of my Higher Degree by Research candidature and is not subject to any obligations or contractual agreements with a third party that would constrain its inclusion in this thesis. I am the primary author of this paper.		
Signature		Date	1/11/2021

Co-Author Contributions

By signing the Statement of Authorship, each author certifies that:

- i. the candidate's stated contribution to the publication is accurate (as detailed above);
- ii. permission is granted for the candidate to include the publication in the thesis; and
- iii. the sum of all co-author contributions is equal to 100% less the candidate's stated contribution.

Name of Co-Author	Timothy C. W. Lau		
Contribution to the Paper	Co-supervised experimental design, assisted with data analysis, edited the manuscript.		
Signature		Date	1/11/2021

Name of Co-Author	Zhiwei Sun		
Contribution to the Paper	Supervised the experiments, assisted with interpretation of data.		
Signature		Date	1/11/2021

Name of Co-Author	Zeyad T. Alwahabi		
Contribution to the Paper	Designed research concept, co-supervised experimental work and data interpretation.		
Signature		Date	

Name of Co-Author	Graham J. Nathan		
Contribution to the Paper	Co-supervised experimental design, assisted with the interpretation of results and edited the manuscript.		
Signature		Date	9/11/2021

Luminescence interference to two-colour toluene laser-induced fluorescence thermometry in a particle-laden flow

Elliott W. Lewis^{1,3}, Timothy C. W. Lau^{1,3}, Zhiwei Sun^{1,3},
Zeyad T. Alwahabi^{2,3}, and Graham J. Nathan^{1,3}

¹*School of Mechanical Engineering, University of Adelaide, Australia*

²*School of Chemical Engineering and Advanced Materials, University of
Adelaide, Australia*

³*Centre for Energy Technology, University of Adelaide, Australia*

Abstract

We present the use of two-colour toluene planar laser induced fluorescence (LIF) to obtain spatially resolved measurements of the gas temperature (T_g) in a particle-laden turbulent flow under sufficiently dense particle loading that the interference from laser interactions with the particles is significant. The effect of the ratio of volumetric flow rates of the particle-phase to the gas-phase (ϕ) on the accuracy and precision of two-colour toluene LIF thermometry was systematically investigated for three particle materials, alumina, zinc activated zinc oxide (ZnO:Zn) and polymethyl methacrylate (PMMA), each of which have differing interactions with the excitation laser. The PMMA particles were spherical and mono-disperse with diameters of 6 to 40 μm , while the alumina and ZnO:Zn particles had diameters in the range 1-40 μm and 2-200 μm respectively. The results show that the accuracy of the gas temperature measurement is insensitive to particle size for the PMMA particles, but dependent on the instantaneous particle loading. Importantly, reliable measurements can be performed in the dense two-way coupling regime, with the measurement being accurate to within 5 °C for $\phi < 2.5 \times 10^{-4}$ for the PMMA particles and for $\phi < 7.6 \times 10^{-4}$ for the alumina and ZnO:Zn particles.

1 Introduction

Particle-laden turbulent flows within environments with strong temperature gradients are employed in, or being developed for, a wide range of industrial systems such as concentrated solar thermal (CST) receivers [1], pulverised fuel flames [2] and flash calciners in alumina and cement production [3]. The heat and mass transport processes that control the performance of these systems are highly complex, with mutually interacting and non-linear phenomena such as turbulence, particle-fluid interaction, particle-particle collisions, particle clustering, multi-mode heat transfer and chemical reactions [4–7]. Importantly, the mean and instantaneous distributions of particle number density and temperature can ultimately affect process efficiencies, emissions, safety and overall system performance. However, the lack of experimental data of these distributions prevents the development of the detailed understanding and predictive models that are needed to optimise them. Hence, there is an important need for high quality, reliable and spatially-resolved measurements of the temperature of both phases in these complex particle-laden flows.

The vast majority of industrial systems operate with particle concentrations that are sufficiently dense to be in the two- or four-way coupling regime. Flows in the two-way coupling regime have particle volumetric loadings in the range $10^{-6} < \phi < 10^{-3}$, where $\phi = \dot{V}_p/\dot{V}_f$ is the ratio of the volumetric flow rates of particles to the fluid. At these loadings both the surface area and/or momentum of the particle phase influences the gas flow field sufficiently for it to differ substantially from its single-phase counterpart [5]. In the four-way coupling regime, $\phi > 10^{-3}$, the particle loading is sufficiently high such that particle-to-particle interactions also become significant. Additionally, in concentrated solar systems and most conventional combustion systems, both the convective and radiative heat transfer modes are also significant [7, 8], with particle radiation absorption complicated by shadowing, attenuation and re-radiation effects from other particles. These flows are typically turbulent, such that fluctuations in the instantaneous velocity difference between individual particles and the surrounding gas may substantially affect local convection, and hence local gas temperatures. Particle-laden flows typically also involve the generation of clusters, which are localised regions with instantaneous particle loadings much greater than the mean [4, 9]. The presence of these clusters can significantly affect individual particle radiation absorption and emission [10]. The complexities of resolving all the parameters in turbulent, particle-laden flows with multi-mode heat transfer makes modelling these systems challenging while direct numerical simulations are computationally expensive [6, 8, 11]. Therefore,

both qualitative and quantitative experimental measurements in well-defined flows are required to improve the fundamental understanding of heat transfer processes in non-isothermal particle-laden flows as well as to provide data for the development and validation of models.

A thorough understanding of non-reacting particle-laden flows typically requires access to simultaneous and spatially resolved measurements of velocity, concentration and temperature. While there have been recent strides in the measurement of particle velocity and temperature [12, 13], there is a paucity of in-situ, well resolved experimental measurements of temperature distributions in particle laden flows. This is particularly true for multi-dimensional data provided by planar imaging, which can measure both gradients and information of spatial distributions. Previous planar measurements have either been limited to the particle-phase temperature [14], or to flows in which the particle diameter and temperature gradients are sufficiently small to allow the assumption that the particles are in thermal equilibrium with the surrounding gas [13, 15, 16]. Hence, to date no direct measurements of the gas-phase temperature in radiatively heated particle-laden flows are available. This gap is significant because the heat transport to gases in strongly irradiated particle-laden flows, such as those in solar receivers, is dominated by an energy balance between radiative heating to the particles and convective cooling to the gas. Furthermore, with sufficiently strong heat fluxes, these processes can be expected to be strongly coupled because they will generate large temperature gradients around small particles and may lead to strong buoyancy effects in some circumstances [17]. However, no data are presently available with which to assess the reliability of various potential techniques for planar measurement of the gas-phase temperature in the presence of particles.

Techniques such as Rayleigh scattering, coherent anti-Stokes Raman scattering (CARS) and laser induced fluorescence (LIF) have been widely used to measure spatially resolved gas temperature in single-phase flows [18–22]. However, large uncertainties are introduced when applying these laser-based methods to particle-laden flows, because the intensity of elastically scattered laser light from particles is typically significantly stronger than the thermometry signal. Filtered Rayleigh scattering is one potential approach to suppress the elastically scattered light using a narrowband filter [23], although previous applications of this method have found it to be sensitive to stray light. Other methods to suppress this scattered light include structured illumination [24], however it is less well established than LIF, which has the advantage that emissions from the thermometry signal are at longer wavelengths than the excitation laser. This allows interference from elastic scattering to be reduced by optical filtering, as shown by previous works

imaging near surfaces [25] and with droplets [26]. By selection of a suitable fluorescent vapour as a tracer, the LIF signal can be derived directly from the gas-phase, without the need to assume thermal equilibrium with a particle tracer. The underlying principle of LIF thermometry is the dependence of the fluorescence emission intensity on the tracer temperature, as represented by the following equation [21],

$$I_{LIF,\lambda} \propto I_{laser}(x, r)\eta_{\lambda}n(x, r)FQY_{\lambda}(T(x, r)), \quad (1)$$

where I_{LIF} is the fluorescence emission intensity, λ is the emission wavelength, I_{laser} is the laser intensity, x is the axial co-ordinate, r is the radial co-ordinate, η is the detection efficiency of the camera, n is the concentration of the tracer, T is the tracer temperature and FQY is the fluorescence quantum yield of the tracer. To accurately measure the gas-phase temperature from the fluorescence intensity, the tracer concentration and laser power must either be measured and/or kept uniform in the measurement region. This is challenging to achieve in practical systems, especially in turbulent flows with significant mixing and a discrete (i.e. particle) phase. However, a useful option to mitigate these challenges is to use two-colour LIF, whereby temperature is measured using the ratio of emission intensity in two wavelength bands, which cancels all spatial effects [27]. This leaves the ratio as a function of temperature only, as shown by the equation,

$$\frac{I_{red}}{I_{blue}} \propto \frac{\eta_{red}FQY_{red}(T(x, r))}{\eta_{blue}FQY_{blue}(T(x, r))}, \quad \therefore T(x, r) = f\left(\frac{I_{red}}{I_{blue}}\right), \quad (2)$$

where the two wavelength bands are called the blue and red channel respectively, and the function f is determined through calibration. The main limitation of this method is that the overall measurement uncertainty is increased by the use of two cameras, each of which is constrained by the signal to noise ratio. There is therefore a need to quantify these effects in particle-laden flows.

The presence of particles in the imaging region increases the errors in the intensity measured relative to in a single-phase medium, with the interference originating from several sources. These include: a) attenuation, which reduces light intensity as a function of path distance through the attenuating medium thereby also reducing the signal [28]; b) multiple scattering of light from particles, which can introduce false signals in the measurement region; and c) luminescence of particles after absorption of the excitation light, resulting in processes such as fluorescence and phosphorescence.

While the two-colour LIF provides a viable method to measure temperature, it has not previously been demonstrated to have a useful accuracy in

particle-laden turbulent flows, which will generate large interferences. Therefore, the aim of the present investigation is to demonstrate a method to spatially measure the gas-phase temperature in a particle-laden turbulent flow, and to quantify the effect of the presence of particles on the accuracy of the temperature measurement. The environment chosen for this assessment is a turbulent jet laden with solid particles, which allows systematic variation of particle diameter, volumetric loading and the optical properties of the particles.

2 Methodology

2.1 Experimental arrangement

The experiment, as shown in Figure 1, consisted of a vertically upward particle-laden jet issuing from a long, round pipe of internal diameter $D = 6.23$ mm. The pipe length was 1100 mm, resulting in a length to diameter ratio of 176, so that the particle-laden flow approached a fully developed state at the jet exit [29]. The jet pipe and a 69 mm coaxial annular flow were centrally located in a 300 mm square wind tunnel. A honeycomb section and a series of mesh screens were placed upstream of the tunnel inlet to condition the flow, which was driven with a fan downstream from the test section. The jet and annular flows had respective bulk velocities of 12.3 m/s and 1 m/s, resulting in a jet to co-flow velocity ratio of 12.3, matching the previous work of Lau and Nathan [30]. The wind tunnel co-flow consisted of air flowing at 1 m/s to match the annular flow. The resultant Reynolds number of the jet flow, defined as $Re_D = \rho V D / \mu$, where ρ is the fluid density, V is the flow bulk velocity, μ is the dynamic viscosity of the fluid, was 5000, resulting in a turbulent flow at the pipe exit.

Both the jet and annular flows employed nitrogen (purity > 99.99%) as the carrier gas, while the jet was also seeded with toluene vapour and particles. The toluene vapour was seeded into the jet flow by bubbling the nitrogen through a reservoir of liquid toluene, resulting in a concentration of approximately 2.75% by volume, corresponding to saturation at room temperature [31]. Toluene was selected as the tracer because it is a well-established species for two-colour thermometry with high relative signal strength and sensitivity to temperature compared to other tracers used for LIF [32]. Nitrogen was used in both the jet and annulus to avoid quenching by oxygen of the fluorescence signal in the measurement region [33]. The source of the excitation beam was the fourth harmonic of a Quantel Q-smart Nd:YAG laser operating at 10 Hz, a wavelength of 266 nm and an output

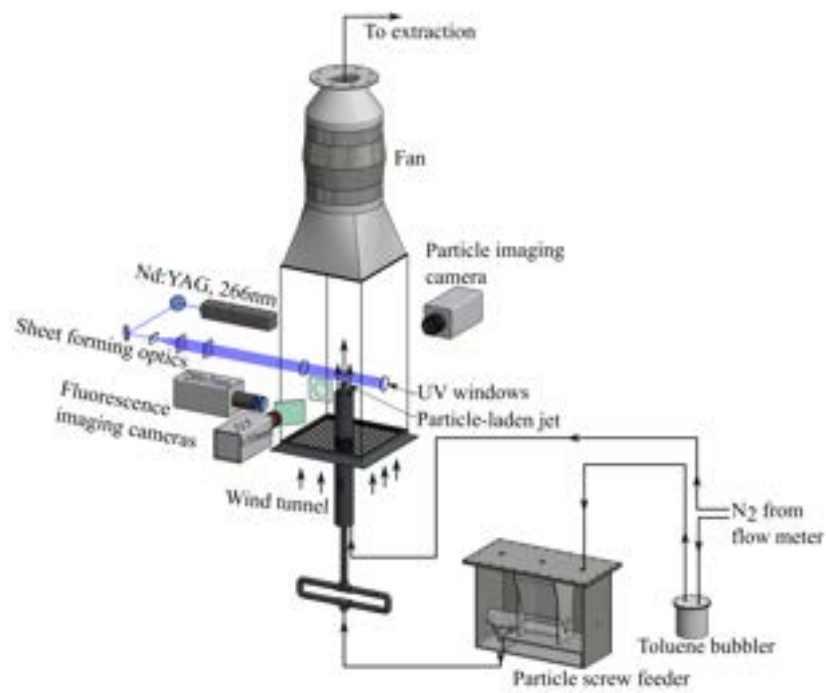


Figure 1: Schematic diagram of the experimental arrangement for simultaneous two-colour LIF gas-phase temperature measurements and particle imaging in a turbulent, particle-laden jet.

laser energy of 100 mJ/pulse. The edges of the beam were trimmed using an iris aperture before the beam was formed into a sheet 40 mm high and 0.3 mm wide at the jet centreline using three cylindrical lenses with an approximate resultant fluence of 417 mJ/cm² in the measurement region. At this fluence the relationship between emission intensity and laser power is non-linear [34]. Hence, the emission spectrum of toluene was measured using a spectrometer (Princeton Instruments Acton Series Spectrograph) for fluences from 14-654 mJ/cm². The normalised emission spectrum, and resultant ratio of intensities in two spectral bands, was measured to be constant over the range of fluences investigated. As such the two-colour ratio method was found to be suitable for temperature measurements for the current experimental conditions.

The two colours of the LIF emission were recorded separately using two PI-Max4 intensified CCD cameras with the image focussed using separate 50.8 mm diameter spherical lenses with an iris aperture ($f = 100$ mm, Thorlabs LB4821) for each channel. Both cameras imaging fluorescence emissions were positioned on the same side of wind tunnel and imaged the same region in the flow, so that the effects of laser beam attenuation and signal trapping by particles were identical for both images. The cameras have a bit depth of 16, a 1024×1024 pixel array with a pixel size of 32.7 μm . Both cameras recorded images simultaneously at 1 Hz, imaging the full width of the jet near the pipe exit, from $-2.75 < r/D < 2.75$, and $0.5 < x/D < 6$. The camera gates were opened 50 ns before the laser was triggered and remained open for 350 ns to image the strongest part of the fluorescence emissions while minimising exposure to background light [35].

The colours to the two detection channels were separated from the fluorescence emissions using optical filters. The total emission first passed through two 275 nm long-pass filters (Asahi spectra) arranged in series. The filtered emission was then split into two channels using a 310 nm dichroic beam-splitter (Semrock FF310-Di01). Additional optical filters were also used separately for each channel, namely a 272 nm long-pass (Semrock FF01-272/LP) together with a 280 nm band-pass filter (Semrock FF01-280/20) in series for the blue channel, and a 300 nm long-pass (Semrock FF01-300/LP) together with a 330 nm short-pass filter (Semrock FF01-330/SP) in series for the red channel. The resulting spectral bands of the two fluorescence channels, I_{blue} and I_{red} , have a high transmission at the wavelengths of 285 ± 5 nm and 315 ± 10 nm respectively, as shown by the combined optical density (OD) of all filters used to form each channel in Figure 2. It should also be noted that each channel has an OD ≈ 15 at 266 nm to block the elastic scattering of the laser beam. The spectral bands for these two channels were chosen such that the resultant intensity ratio is sensitive to temperature in the range expected

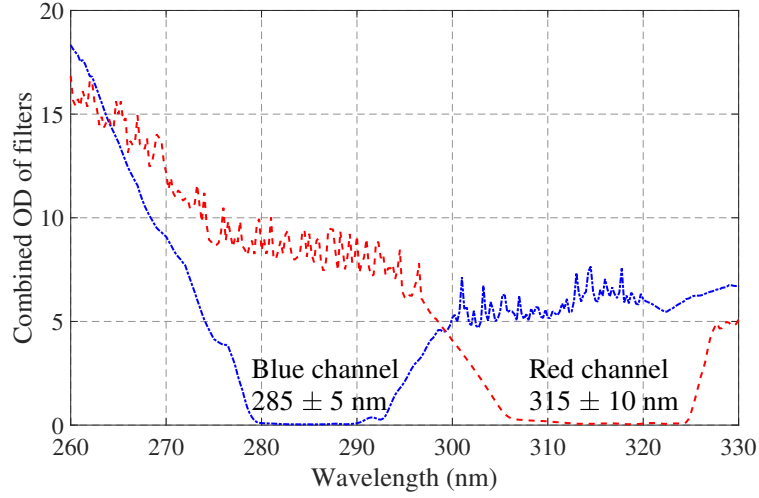


Figure 2: Combined optical density (OD) of all optical filters and beam-splitter used to form the two detection channels for two-colour thermometry, as calculated from the manufacturers data [36, 37].

in the current experiment, i.e. $15 < T < 160$ °C [38]. More specifically, the blue channel is expected to measure the peak fluorescence emission of toluene, which occurs approximately at 280 nm in the expected temperature range, while the red channel measures the spectral region that is highly sensitive to temperature [39].

Particles were introduced into the jet using a screw feeder located within a sealed, pressurised enclosure. The average volumetric loading was controlled by setting the screw rotation speed to achieve a time-averaged loading of $\phi_{bulk} = 4 \times 10^{-4}$ for all experimental cases. Three types of particles previously used in two-phase flow measurements [12, 30], namely polymethyl methacrylate (PMMA), zinc activated zinc oxide (ZnO:Zn) and alumina, were chosen for the study. Each of these materials exhibits a different spectral response to UV light, with PMMA emitting broadband fluorescence and ZnO:Zn emitting fluorescence and phosphorescence. Alumina is not expected to emit luminescence after interaction with UV light. The PMMA particles were spherical with diameters of 6, 10, 20, 40 μm (to within 10% for each size) [30]. Due to their mono-disperse size distribution they were used to compare the effect of particle size on interference. The alumina particles had a nominal diameter of approximately 1 μm , although they tended to form aggregates up to 40 μm diameter in the feeding system. The ZnO:Zn particles had a size distribution of 2-200 μm . The alumina and ZnO:Zn particles were baked in an oven overnight before each measurement day to minimise the

potential for particle aggregation. LIF images were also recorded under the same flow and imaging conditions without particles to ascertain the accuracy of the method without interference from particles.

The Mie scattering from the particles was imaged simultaneously with the fluorescence emissions using a third intensified CCD camera (PCO HSFC pro, 12 bit) fitted with a Nikon lens ($f = 50$ mm, F/1.4). These images were collected unfiltered with the camera positioned diametrically opposite to the optically filtered cameras (see Figure 1). The signal from the scattered light was used to infer the instantaneous spatial distribution of the particle volumetric loading on a pixel-by-pixel basis, i.e. $\phi(x, y, t) = \phi_{bulk} \frac{I(x, y, t)}{I_{mean}}$, where $I(x, y, t)$ is the instantaneous intensity measured, and I_{mean} is the time-averaged intensity in the region of $-0.1 < r/D < 0.1$, $0.5 < x/D < 3$ (i.e. the region where particle number density is approximately uniform). It should be noted the relationship above is exact only for the mono-disperse PMMA particles, since the scattered signal is proportional to both the particle diameter and number density. For the alumina and ZnO:Zn particles, which have a wide size distribution, the local volumetric loading was estimated by assuming that the statistical distribution of particle sizes in each instantaneous image is constant. With this assumption, the mean scattering intensity from each instantaneous image is directly proportional to the mean particle volumetric loading. The particle loading inferred using this assumption is denoted the pseudo particle volumetric loading, ϕ^* . To ensure that the particle concentration imaging was not influenced by the fluorescence emissions of toluene, images of a flow of nitrogen seeded with toluene were compared with those from a flow of nitrogen only. It was found that there was no significant increase in the signal measured when toluene is added to the flow, which implies that the fluorescence signal from toluene was below the noise level of this camera.

2.2 Image processing

The instantaneous images from all three cameras were processed separately using a series of stages. Firstly a background image was subtracted from each instantaneous image. The background image was averaged from 500 images taken under experimental conditions without the jet flow, after all the toluene and particles had been flushed from the imaging region. A separate set of background images were recorded for each experimental day. Next, the images from all three cameras were spatially aligned by matching points on a target image consisting of a grid of holes illuminated by a diffuse UV lamp. For each instantaneous image, pixels with intensity values below

10% of the mean intensity in the potential core region ($-0.1 < r/D < 0.1$, $0.5 < x/D < 3$) of the time-averaged room temperature image taken without particles were discarded from further analysis. The fluorescence intensity ratio was then calculated using the remaining pixels on a pixel-by-pixel basis. The instantaneous intensity ratio images were then normalised by the time-averaged intensity ratio of the room temperature case. This corrects for spatial inhomogeneity in the collection efficiency of both cameras capturing fluorescence emissions and was done on the basis that the time-averaged intensity ratio at room temperature should be uniform. The intensity ratio was converted to temperature using the calibration curve shown in Figure 5. The temperature images were then smoothed using a 9×9 mean filter to decrease the influence of noise on the measured results. The result is that each pixel corresponds to a measurement width and height that is approximately the same size as the light sheet thickness, i.e. each pixel measures a volume with dimensions $294 \times 294 \times 300 \mu\text{m}$.

2.3 Calibration

Prior to the main experiment, calibration measurements were conducted by imaging the toluene-seeded jet flow at 13 gas temperatures between $15 \text{ }^\circ\text{C}$ and $160 \text{ }^\circ\text{C}$. The temperature of the gas was controlled using an electrical tape heater wrapped around the jet pipe (Briskheat BWH052100LD) set to provide a constant heating voltage. The actual gas temperature was measured at $x/D = 0.5$ using a thermocouple inserted in the flow. A total of 250 images were captured at each temperature, with the imaging and illumination configuration matching that of the main experiment. The intensity ratio was averaged over a 240×45 pixel region near the jet exit ($-0.3 < r/D < 0$, $0.65 < x/D < 2$), where the temperature was spatially and temporally uniform and there was no interference from the thermocouple probe.

2.4 Spectroscopic arrangement

Measurements of the spectral emissions at room temperature of $17 \text{ }^\circ\text{C}$ were conducted for all three types of particles after illumination with the 266 nm laser light. This was done by directing a 266 nm laser beam onto steel plates coated with the three types of particles and recording the emissions using a spectrometer (Princeton Instruments Acton Series Spectrograph) with a 150 groove/mm grating, as shown in Figure 3. The laser excitation energy was 1 mJ/pulse, with the beam focussed onto a 2 mm circular area of the particle-coated plates using a spherical lens, resulting in a laser fluence of 31.8 mJ/cm^2 . The emission signal from the particles was focussed

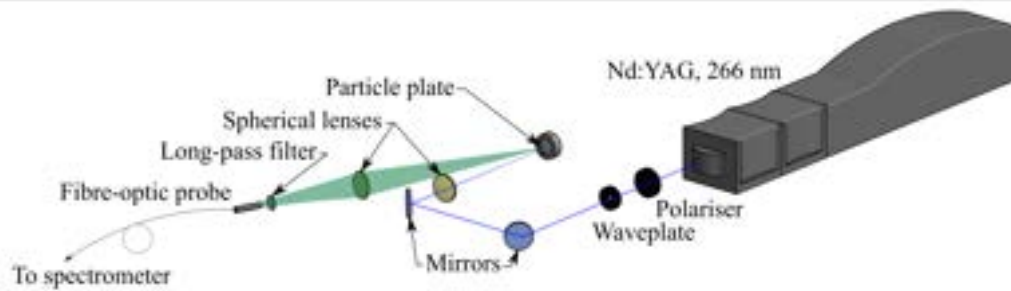


Figure 3: Optical arrangement for the spectroscopic measurement of the response of each particle type to excitation by 266 nm light. The particles were mounted to a plate as shown.

with another spherical lens onto a fibre optic probe that transferred the collected light to the spectrometer through an optical fibre bundle (Thorlabs BFL200HS02). A long-pass filter (Semrock 272 nm) was placed between the lens and probe to separate reflected laser light. Spectral emissions were measured for wavelengths between 280-500 nm in intervals of 0.17 nm. The spectrometer camera gate width was 200 ns, opening 20 ns before the laser pulse to maximise signal collected and minimise noise. The signal intensities were averaged over 200 exposures, with the camera gain fixed at unity so that the emission intensities for all particle types could be compared under identical operating conditions.

3 Results

3.1 Spectroscopy measurements

The emission spectrum from each type of particle during exposure to 266 nm radiation is presented in Figure 4, with the data smoothed using a three-element moving-mean filter to improve clarity. The phosphorescent emissions from ZnO:Zn particles are in the range from 350-420 nm, which is similar to the phosphorescence emission spectrum after excitation at 355 nm [14, 16]. The signal in the spectral range captured in the main experiments (280-325 nm) is low, indicating that the phosphorescence will provide little interference to temperature measurements. The signal from alumina particles is very low, more than 3 orders of magnitude less than the peak emission from ZnO:Zn across the entire spectral range measured. This implies that there will be negligible interference from the alumina particles in the spectral channels used for the current two-colour LIF thermometry measurements.

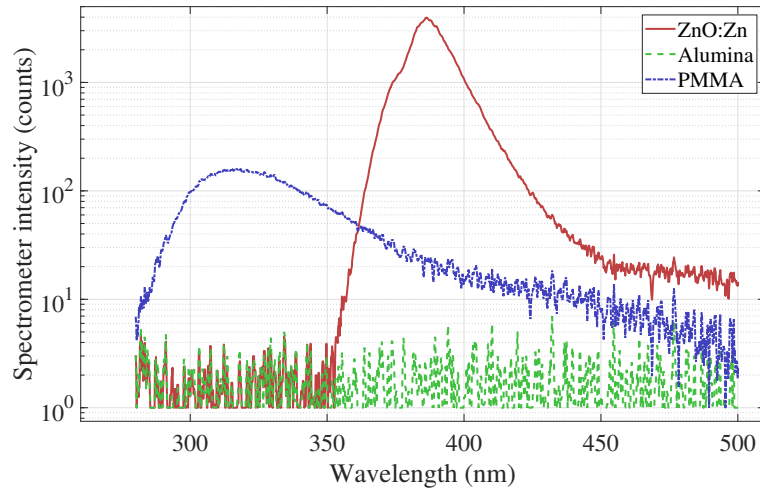


Figure 4: The measured spectroscopic response of the three types of particle to illumination with 266 nm laser light. For reference, the two spectral bands toluene fluorescence detected were at 285 ± 5 nm for the blue channel and 315 ± 10 nm for the red channel.

However, the PMMA particles exhibit a broadband emission (280-500 nm), which constitutes an interference to the wavelengths measured in the main experiments, with a peak at 315 nm. The measurements were verified to be insensitive to laser fluence, up to the fluence used in the main experiment. These results highlight the importance of particle material selection in experiments utilising the two-colour planar LIF thermometry method.

3.2 Calibration

Figure 5 presents the dependence on temperature of the fluorescence intensities of both the red and blue channels, in terms of signal to noise ratio (SNR), together with the subsequent ratio. The SNR is defined as the ratio of toluene fluorescence signal for each channel to the noise in the background for that channel. The noise measured by each pixel varied by less than 1% from the mean across the entire array, so that mean value was used for all pixels. The SNR during the calibration was 14.2 and 25.2 at room temperature for the red and blue channels respectively, decreasing to 6.0 and 6.9 at 160 °C. This decrease in SNR with temperature is due to the decrease in fluorescence quantum yield of toluene with temperature [27]. The intensity ratio was found to increase linearly with temperature in the range of $15 \text{ °C} < T < 160 \text{ °C}$, which allowed a linear function to be used, reducing uncertainty and

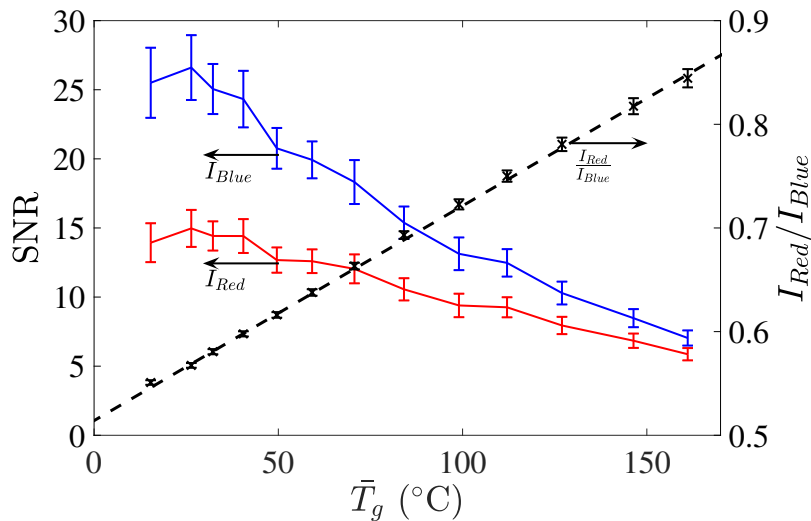


Figure 5: Calibration curve of the dependence on gas temperature of the signal to noise ratio (SNR) for both channels (red and blue lines), together with the resultant intensity ratio (black markers), as measured in a heated jet without particles. The dashed black line is a linear curve fit of the intensity ratio data.

simplifying the image processing. The resultant curve fit was found to be $T = 482.6 \frac{I_{Red}}{I_{Blue}} - 248.1$ (with a R-squared goodness of fit, $R^2 = 0.9997$), where T is in $^{\circ}\text{C}$, although it should be emphasised that this equation is only applicable to the current imaging conditions. Multiple runs of the calibration measurements taken before and after the main experiments showed an average difference in the intensity ratio of 3.17%, with a maximum difference of 4.85% occurring at 145 $^{\circ}\text{C}$. The uncertainty in the calculated temperature is shown as error bars in Figure 5, which presents the standard deviation of the spatially-averaged intensity ratio measured within single images. This increases from ± 0.0027 (corresponding to a temperature error of ± 1.3 $^{\circ}\text{C}$) at 15 $^{\circ}\text{C}$ to ± 0.0089 (± 4.3 $^{\circ}\text{C}$) at 160 $^{\circ}\text{C}$. The error in intensity ratio is less than 5 $^{\circ}\text{C}$ at each temperature despite standard deviations of up to 10% in fluorescence intensity. This highlights the advantage of using the two-colour method for temperature measurement as it is significantly less sensitive to fluctuations in the toluene concentration and laser power than the raw intensity.

3.3 Single-phase temperature measurements

The gas temperature was measured in a flow without particles, i.e. $\phi = 0$, to assess the accuracy of the method at a reference case. The jet centreline fluorescence intensity, I_c , and the scalar mean, Θ_c , normalised by the exit values, I_e and Θ_e respectively, are presented in Figure 6 and Figure 7. Here, $\Theta(x, r) = T(x, r) - T_a$ is the mean scalar field, where T_a is the ambient temperature, while the exit values were measured on the jet centreline at $x/D = 0.5$. In these figures, the axial co-ordinate is normalised by the effective diameter D_e , which accounts for the variations in the initial fluid density and the mean bulk velocity of the jet at the different temperature conditions [18, 40–42]. The effective diameter for a single-phase pipe jet is defined as

$$D_e = \frac{2M_e}{\sqrt{\pi\rho_\infty J_e}} \quad (3)$$

where

$$M_e = \int_0^{\frac{D}{2}} 2\pi\rho_e U_e r dr \quad (4)$$

is the jet exit mass flux,

$$J_e = \int_0^{\frac{D}{2}} 2\pi\rho_e U_e^2 r dr \quad (5)$$

is the jet exit momentum flux, ρ_e is the density of the jet at the exit plane, ρ_∞ is the density of the surrounding fluid and U_e is the mean axial velocity at the jet exit.

The results in Figure 6 show that there is a decay in the signal intensity of both the red and blue channels as the flow moves downstream, primarily due to the mixing of the seeded jet with the unseeded annular flow of nitrogen. Further downstream, any additional mixing with the co-flow of air will introduce quenching of the toluene signal by oxygen. The resultant scalar mean, presented in Figure 7, is approximately uniform for $x/D_e < 3$ for all cases in which the jet is heated, before decaying with axial distance in the manner expected for a pipe jet [42–44].

Importantly, the data for $x/D_e < 4$ collapses for all measured temperatures, which provides evidence for the robustness of the current technique. Also shown in Figure 7 is the centreline decay in the near field as measured previously by Papadopoulos and Pitts [43] (P&P), at similar Reynolds numbers of 6,000 and 8,100 with respective density ratios of $\rho_e/\rho_\infty = 0.55$ and 1.52. Only data from other cases in the near field at similar Reynolds number are compared as the centreline scalar mean profile is dependent on

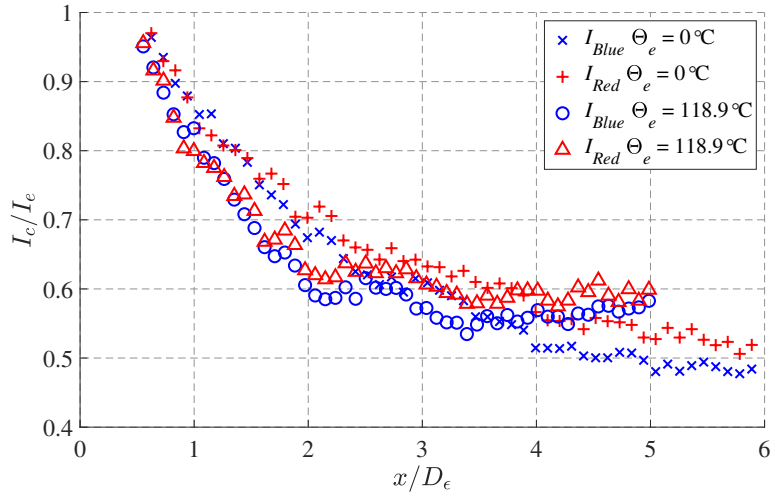


Figure 6: The fluorescence intensity at the jet centreline, normalised by the exit value I_e , for both the red and blue channels for the heated unladen pipe jet. Only every 20th data point is shown for clarity.

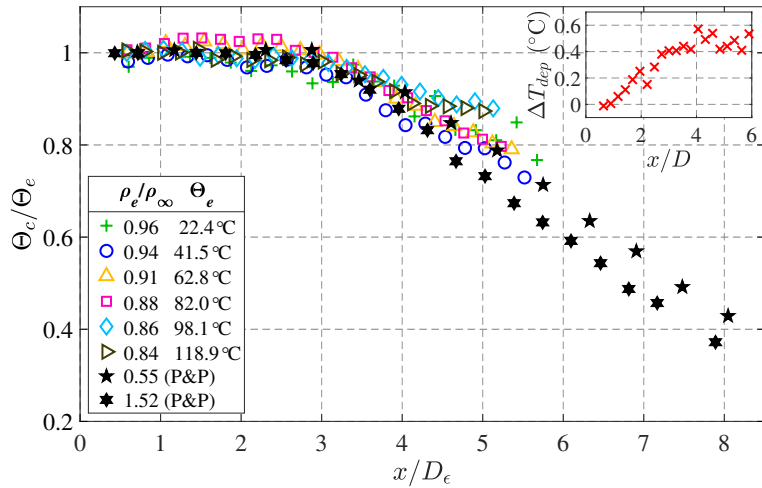


Figure 7: The axial evolution on the centreline of the normalised scalar mean, $\Theta = T(x, r) - T_a$, where $T(x, r)$ is the measured gas-phase temperature and $T_a = 17^\circ\text{C}$ is the ambient temperature. The inset shows the measured temperature on the centreline for the ambient case. Only every 50th data point is shown for clarity. Also shown are the previous measurements of [43], denoted as P&P.

Reynolds number [19]. The current results of Θ_c/Θ_e match well with that of P&P's $Re_D = 6000$ case through the measurement region for $\Theta_e < 82.0$, with the scalar being uniform for $x/D_e < 3$ before decaying to $\Theta_c/\Theta_e = 0.8$ at $x/D_e = 5$. At higher temperatures, $\Theta_e > 82.0$, the current data matches well with P&P's results only for $x/D_e < 4$. The differences in results for $x/D_e > 4$ are attributed to the differences in experimental conditions, in particular the use of a co-flow which was not used in P&P's measurements. Hence, the agreement in the results is sufficiently good to give confidence in the present measurements. For the room temperature case, the use of the normalised scalar mean Θ_c/Θ_e is not appropriate as the normalisation terms become zero. Hence the non-normalised values are used for this case. This is presented as a difference between the temperature measured by the two-colour ratio and the ambient temperature, $\Delta T_{dep} = T_{IR} - T_a$. The results, presented in the inset of Figure 7 shows that the measured temperature is accurate to within $0.1\text{ }^\circ\text{C} < \Delta T_{dep} < 0.5\text{ }^\circ\text{C}$ over the range $0.5 < x/D < 6$.

Figure 8 presents the radial distribution of fluorescence intensities normalised by the centreline intensity I_c for both channels, together with the resultant scalar mean normalised by the centreline value, Θ/Θ_c , at $x/D = 0.5$. The toluene fluorescence intensities are uniform to within 15% in the central region of the jet, $|r/D| < 0.4$. This results in a value of Θ that is uniform to within 2% of the centreline value. Near to the jet edge, the normalised intensities decrease to < 0.1 at $|r/D| = 0.6$, due to a dilution of the toluene from mixing with the annular flow. Within this region, Θ/Θ_c tends to decrease with $|r/D|$ over the range $0.4 < |r/D| < 0.5$, albeit with some scatter. Similar measurements of the radial temperature scalar profile of a jet emerging from a long pipe at $x/D = 0.1$ by Mi et al. [42] matches well with the present data in the range of $|r/D| < 0.4$. However, there are differences in the two measurements in the region of $0.45 < |r/D| < 0.55$. This can be attributed to the low fluorescence signal strength of the present measurements in this region. Nevertheless, the mean measured temperature at $|r/D| = 0.5$ is still accurate to within $1\text{ }^\circ\text{C}$ of the actual temperature for the unheated jet (inset of Figure 8) despite a 50% drop in fluorescence signal strength.

Figure 9 presents the standard deviation of the measured temperature calculated from the ensemble of values measured at every pixel in every image, σ_T , as a function of the signal to noise ratio for both fluorescence channels at two jet exit temperatures, $\Theta_e = 0\text{ }^\circ\text{C}$ and $118.9\text{ }^\circ\text{C}$. It can be seen that σ_T decreases with increasing SNR for both channels under most conditions as expected. For both channels, σ_T increases with temperature, indicating that the fluctuations in temperature are not only due to noise, but partly due to actual temperature variations in the flow. Nevertheless, for the room temperature case, the minimum standard deviation is $\sigma_T = 5.7\text{ }^\circ\text{C}$ at a

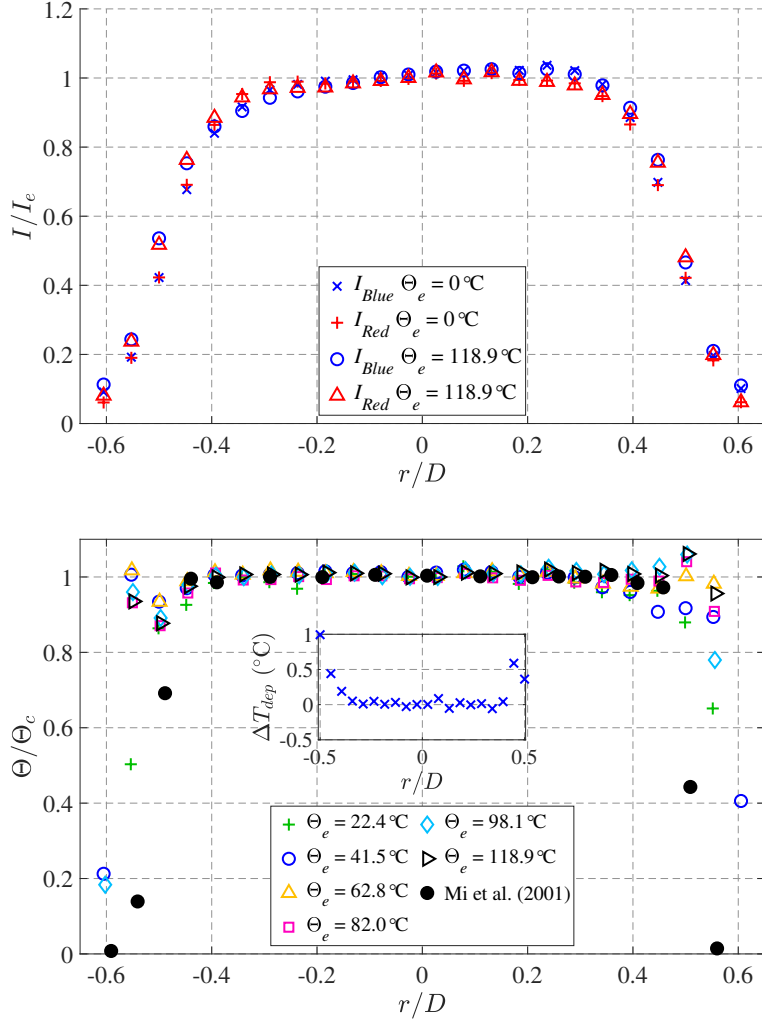


Figure 8: Radial distributions of (top) normalised fluorescence intensities for both channels at the minimum and maximum temperatures measured and (bottom) mean scalar field normalised by the centreline value at $x/D = 0.5$ for the single-phase flow and for all measured temperatures in the heated jet. Only every 10th data point is shown for clarity. The inset in the bottom sub-figure presents the difference between the measured and ambient temperatures at $x/D = 0.5$ for the room temperature case. Also presented is the mean profile measured by Mi et al. [42] at $x/D = 0.1$.

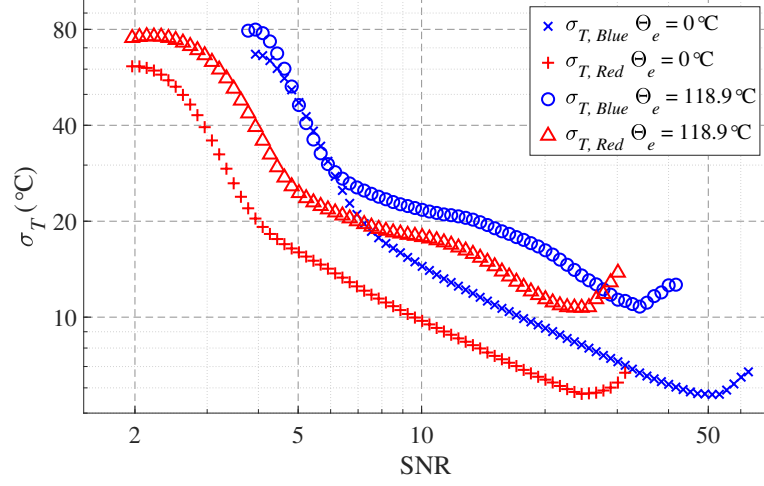


Figure 9: Standard deviations of temperature measurements as a function of signal to noise ratio, calculated from the entire array of pixels for all the individual fluorescence images from both channels.

corresponding SNR of 51 and 25 for the blue and red channels respectively, which provides an estimate to the minimum uncertainty of the current measurements. For $\Theta_e = 118.9$ °C the minimum standard deviation increases to $\sigma_T = 10.7$ °C at a SNR of 34 and 24.5 for the blue and red channels, respectively. However, it should be noted that the minimum SNR measured here is dependent on the threshold values used; higher threshold values will decrease σ_T at the expense of discarding more data. In any case, this highlights the value of achieving a high SNR for both fluorescence channels.

3.4 Two-phase temperature measurements

A series of sets of single shot images are presented in Figure 10 for various spatially averaged volumetric loadings ($\bar{\phi}$) of 20 μm PMMA particles, over the range of $5 \times 10^{-5} < \bar{\phi} < 8 \times 10^{-4}$ for the case of the unheated jet. Each set of images comprises the signal from the two fluorescence channels, the corresponding temperature presented as ΔT_{dep} and the distribution of particle volumetric loading. These results are consistent with those for other sizes of PMMA particles, not presented for conciseness. Since the jet is unheated at the room temperature of 17 °C, any deviations in the measured temperature distribution are due to a combination of the base measurement uncertainty of the method (see section 3.3) and interference due to the presence of particles. Uncertainty in the measured temperature can be particularly significant close

to the jet edge, where the low concentration of the toluene tracer leads to a weak fluorescence signal. However, these errors are restricted to the extremities of the jet, and are not expected to affect the measurements near the centreline of the jet where the toluene concentration is relatively high.

For low particle loadings, $\bar{\phi} < 2 \times 10^{-4}$, the interference due to the presence of particles on the temperature measurements can be seen to be small, with little correlation between the particle concentration and the derived temperature. However, for $\bar{\phi} > 2 \times 10^{-4}$, particle interference starts to become more prominent. As an extreme example, for $\bar{\phi} = 8 \times 10^{-4}$ at $x/D = 1.8$ and $r/D = 0.1$ (Figure 10*f-iii*), the derived gas temperature was 189 °C greater than the actual gas temperature. A comparison with the particle distribution reveals that this region corresponds to a localised area of high particle concentration. Interference is also evident in the images without toluene, where a local region of high particle concentration ($\phi = 7.9 \times 10^{-4}$) can be seen in the red channel, although this intensity is significantly lower than from the toluene fluorescence.

Such interference from particles could be due to attenuation, signal trapping, multiple scattering and/or particle emission. Attenuation from particles is estimated to be small, with a maximum attenuation of 26% across the measurement region calculated for the alumina particles [28]. Signal trapping between the measurement region and imaging plane is also expected to be negligible as the pipe diameter is small ($D = 6.23$ mm). Furthermore, the effect of both attenuation and signal trapping is expected to reduce the signal in both channels equally, such that the ratio will remain unchanged. The effect of multiple elastic scatterings was assessed by inserting a 0.5 mm diameter wire in the laser sheet to generate a dark line in the images along the beam direction, and subsequently comparing the intensity measured in each channel of flows with and without particles, for the same laser fluence. The intensity profile measured by the filtered cameras in the region around the wire was the same for instantaneous particle loadings from 0 – 8×10^{-4} , showing that the effect of multiple scattering is also negligible. Therefore, the increase in derived temperature in these regions is attributed primarily to the emission from the PMMA particles interfering with the fluorescence signal from the toluene tracers (see also Section 3.1). The large errors in measured temperature in the flow with a volumetric loading of $\bar{\phi} > 4 \times 10^{-4}$ for these PMMA particles suggests that this is a useful threshold in accuracy of the gas temperature measurement with this type of particle.

Figure 11 presents the probability density function (PDF) of measured temperature for a series of volumetric loadings of 20 μm PMMA particles, representing different levels of interference corresponding to the images shown in Figure 10 and ensemble averaged over 5 images for each loading. The

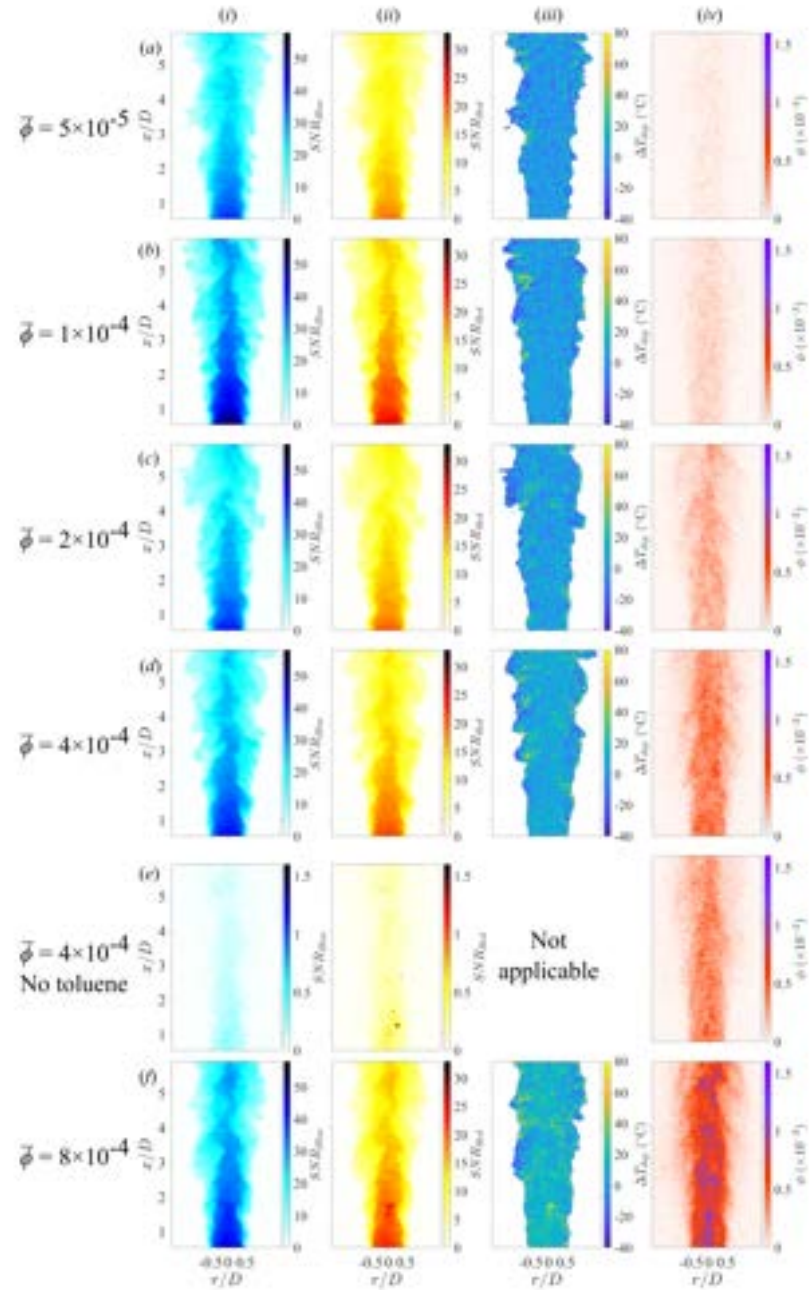


Figure 10: Selected simultaneous single shot images for various spatially averaged volumetric loadings of $20 \mu\text{m}$ PMMA particles in an unheated jet of (i) the blue channel intensity, (ii) the red channel intensity, (iii) the corresponding error in the temperature and (iv) local particle volumetric loading. The images in row (e) were collected without toluene in the flow, note that the colourbar scale is different for this case

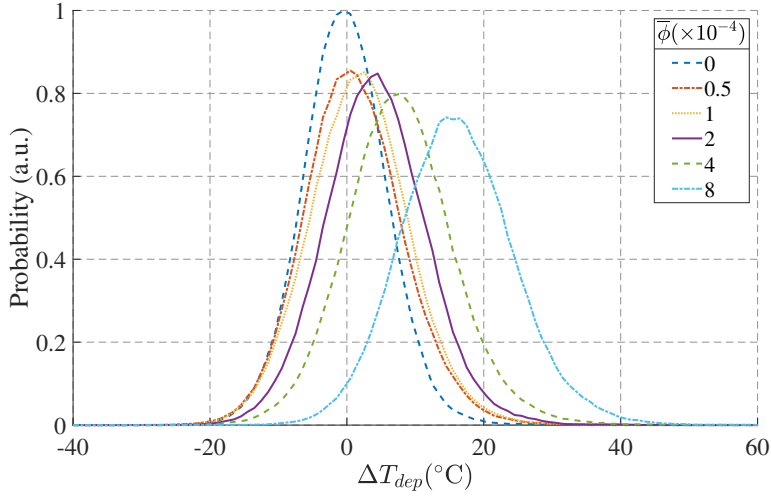


Figure 11: PDFs of the difference between the measured and actual gas temperatures obtained in the unheated jet laden with $20 \mu\text{m}$ PMMA particles. These PDFs were calculated for data in the region of $|r/D| < 0.4$, $0.55 < x/D < 3$.

results show that the PDFs have a Gaussian-like profile, with a standard deviation of approximately $5.9 \text{ }^\circ\text{C}$ for $\bar{\phi} = 0$, increasing slightly to a standard deviation of $8.1 \text{ }^\circ\text{C}$ for $\bar{\phi} = 8 \times 10^{-4}$. The peak of the PDF occurs for $\Delta T_{dep} \approx 0$ at $\bar{\phi} < 1 \times 10^{-4}$, implying a negligible bias error at these low loadings. However, this bias error increases significantly for $\bar{\phi} > 2 \times 10^{-4}$, with the peak of the PDF for $\bar{\phi} = 8 \times 10^{-4}$ occurring at $\Delta T_{dep} = 15.8 \text{ }^\circ\text{C}$. That is, the bias error from PMMA particles increases with particle loading. The increase in the standard deviation of measurements with higher particle loading indicates that the random error is also more significant when particles are present in the flow. The combination of these errors indicate that the local particle loading is a major factor in determining the accuracy of LIF thermometry in practical cases. Nevertheless, these errors represent the worst-case scenario, since they were obtained with the spectrally active PMMA particles.

Figure 12 presents the influence of particle volumetric loading on ΔT_{dep} for 4 different PMMA particle sizes measured on the jet centreline near the exit plane, in the region of $|r/D| < 0.25$, $0.85 < x/D < 1.15$ (i.e. where the fluorescence SNR is strong). The results show that ΔT_{dep} increases with ϕ , as previously discussed. For example the mean ΔT_{dep} for the $20 \mu\text{m}$ particles is $2.7 \text{ }^\circ\text{C}$, $9.7 \text{ }^\circ\text{C}$ and $25.9 \text{ }^\circ\text{C}$ at $\phi = 1.4 \times 10^{-4}$, 4.4×10^{-4} and 1.4×10^{-3} respectively. This trend is consistent for all particle sizes, implying

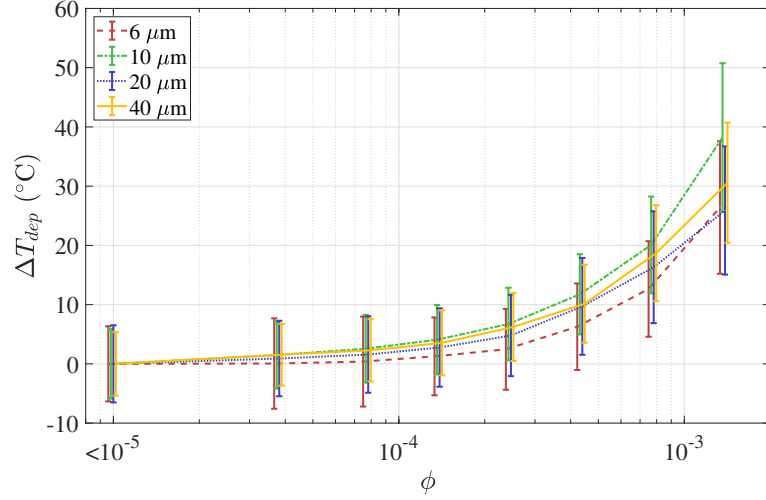


Figure 12: Effect of particle loading on the difference between the measured and actual gas temperature for four different PMMA particle sizes in the unheated jet. Here the measurements were limited to the centreline at $x/D = 1$. The error-bars denote ± 1 standard deviation.

that particle diameter does not have a significant impact on the temperature measurement. As the number of particles increase with decreasing particle diameter for any given particle loading, the results also show that it is particle volumetric loading, rather than particle number density, which impacts the measurement accuracy. For $\phi < 1.4 \times 10^{-4}$, $\Delta T_{dep} + \sigma_T < 10^\circ\text{C}$ for all particle diameters. The standard deviation in the temperature error, σ_T , also increases with ϕ , from $\sigma_T = 5.7^\circ\text{C}$ for $\phi = 0$ to $\sigma_T = 8.1^\circ\text{C}$ for $\phi = 4.4 \times 10^{-4}$ and $\sigma_T = 10.8^\circ\text{C}$ for $\phi = 1.4 \times 10^{-3}$, for the $20\ \mu\text{m}$ particles. These results are consistent with the results in Figure 11 showing that both the random and bias errors in the gas temperature measurement increase with particle loading, with the most significant increase occurring for $\phi > 2 \times 10^{-4}$ regardless of particle size.

Figure 13 shows effect of particle volumetric loading on the fluorescent intensity measured at room temperature in both channels, normalised by the time-averaged intensity of the flow without particles. The results show that neither the mean or standard deviation of the normalised intensities are strongly influenced by particle size, which implies that the error in gas temperature measurement is independent of particle size, at least for the particles investigated in the present study. This is consistent with the derived temperature data presented in Figure 12. However, Figure 13 also shows that the normalised intensities are influenced by particle loading, particularly at

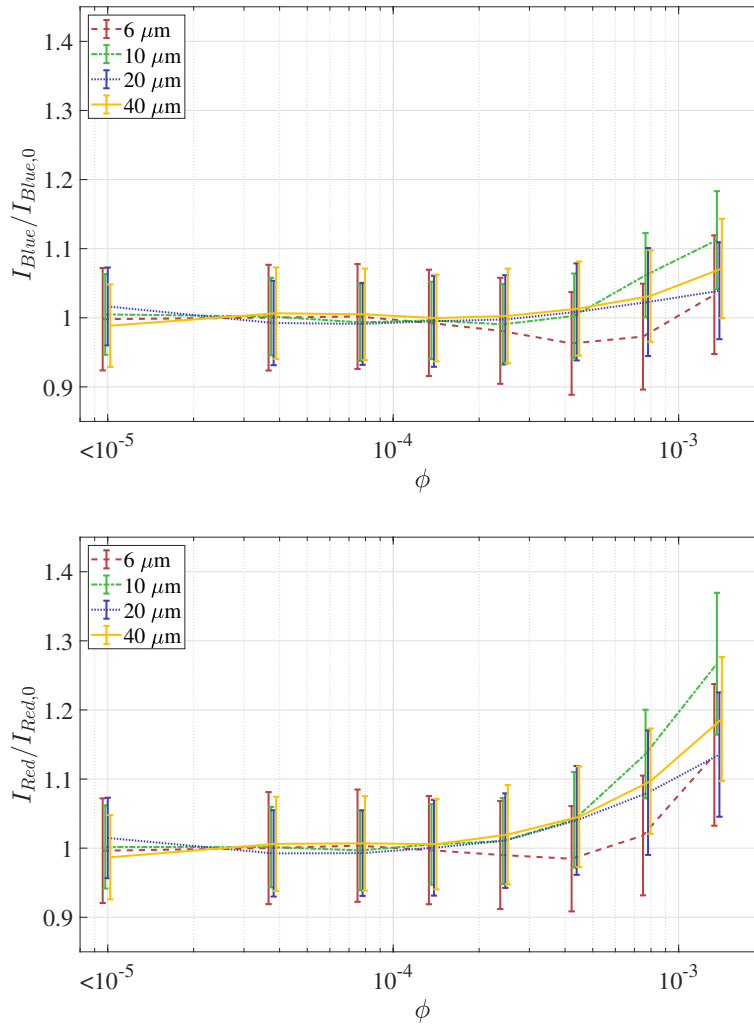


Figure 13: Effect of particle loading on the intensity measured in both the blue and red channels normalised by the intensity without particles, for four different particle sizes in the unheated jet, measured on the centreline at $x/D = 1$. The error-bars denote ± 1 standard deviation.

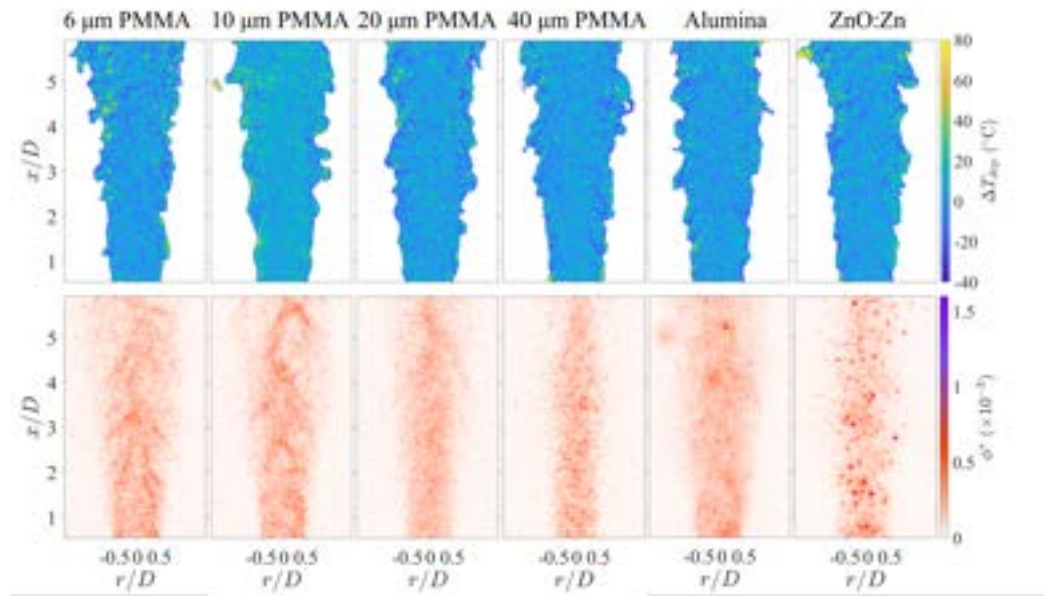


Figure 14: Selected single shot images of the difference between the measured and actual gas temperature (top row) and particle volumetric loading (bottom row) for all particles investigated in the unheated jet. Note that the pseudo-loading is used in lieu of the actual particle loading for the alumina and ZnO:Zn particles. The spatially averaged volumetric loading is $\bar{\phi}^* = 2 \times 10^{-4}$.

high values of ϕ . At loadings of $\phi > 10^{-3}$ the average normalised intensity of the red and blue channels are 10% and 5% greater, respectively, than in the flow without particles. The greater increase in the red channel relative to the blue channel results in an increase in the two-colour ratio, and subsequently the measured temperature, as seen in Figure 12. This greater increase in red channel intensity could be due either to the toluene fluorescence signal strength being lower in the red band (see Figure 5), which would lead to a greater relative influence from broadband interference, or to interference from PMMA fluorescence, which is stronger in the red channel than the blue (see Figure 4).

Instantaneous images of the gas temperature and particle volumetric loading for four different PMMA particle sizes, together with the alumina and ZnO:Zn particles, are presented in Figure 14 for a spatially averaged particle loading of $\bar{\phi}^* = 2 \times 10^{-4}$. From the images with the 6 μm and 10 μm particles (bottom row of Figure 14), it can be seen that coherent clusters of particles develop with the jet, consistent with previous measurements [45]. The local particle loading can be much higher than the average loading ($\phi^* > 8 \times 10^{-4}$) within these clusters, which in turn increases local particle interference and subsequently the uncertainty in the gas temperature measurement. By contrast, the alumina particles are approximately uniformly distributed throughout the flow, with $\Delta T_{dep} < 15$ °C throughout 82.7% of the pixels in the image with intensities above the threshold value. However, in some regions particle agglomerates cause interference to the temperature measurement. This can be seen, for example, for the alumina at $r/D = 0.1$ and $x/D = 5.2$, where the presence of a particle agglomerate results in a $\Delta T_{dep} = 53.8$ °C. As alumina does not fluoresce or phosphoresce (see Figure 4), the source of interference in this case is attributed to Mie scattering of laser light. For the ZnO:Zn particles, particle agglomeration is prominent, with many particle aggregates visible in the particle image. A high degree of particle agglomeration has also been reported in previous studies [14]. However, while there appears to be significant particle agglomeration, this does not significantly interfere with the gas temperature measurements, indicating that scattering from the ZnO:Zn particles is less significant than from the alumina.

Figure 15 presents the relationship between the particle pseudo-loading, ϕ^* , and ΔT_{dep} for the three particle types tested. As can be seen, the trends for the three particle types are similar, i.e. both ΔT_{dep} and σ_T increase with ϕ^* . For a loading of $\phi^* = 4.4 \times 10^{-4}$, ΔT_{dep} is 3.1 °C and 3.9 °C for the ZnO:Zn and alumina particles, respectively, with a corresponding σ_T of 5.8 °C and 7.1 °C. These are substantially lower than the corresponding errors for the PMMA particles ($\Delta T_{dep} = 9.7$ °C, $\sigma_T = 8.1$ °C). That is, for the same particle loading, the ZnO:Zn particles have the smallest errors,

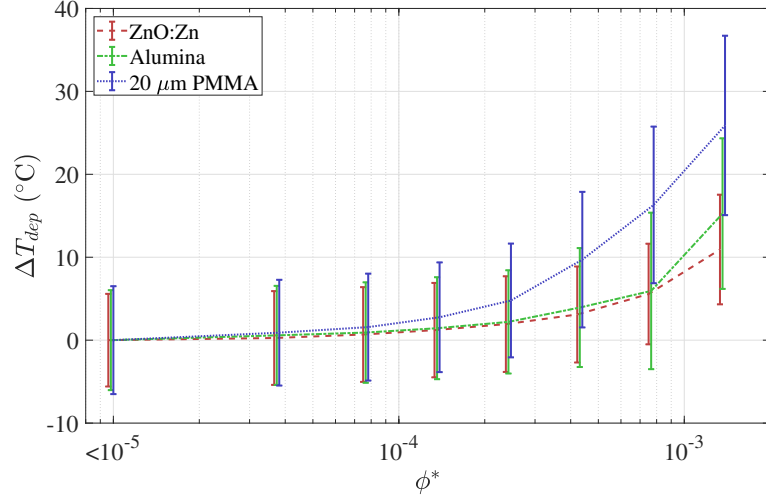


Figure 15: Effect of local particle pseudo-loading (ϕ^* , measured as described in section 2.1) on the temperature measured for ZnO:Zn, alumina and PMMA particles, for the unheated particle-laden jet. Note that the data for the 20 μm PMMA particles are replicated from Figure 12 for reference.

while the PMMA particles have the greatest. This is despite the ZnO:Zn particles emitting significant phosphorescence, because the majority of the phosphorescence is emitted at wavelengths outside the spectral bands used for toluene LIF in the current measurement, resulting in a weaker impact on the temperature measurement. The alumina particles exhibit a similar response to the ZnO:Zn particles for ΔT_{dep} , because there is no inelastic emission from the alumina particles. In comparison, the emission from the PMMA particles is significant within both of the spectral bands utilised for toluene LIF in the current measurements (see section 3.1).

Taken together, these results show that all forms of particle interference investigated here (Mie scattering, fluorescence and phosphorescence) can lead to an increase in both random (larger σ_T) and bias errors (larger ΔT_{dep}) in the gas phase temperature measurement with increasing ϕ . For the present imaging configuration, particle fluorescence is the most significant source of error, limiting the particle loading of PMMA particles to $\phi < 2.5 \times 10^{-4}$ to ensure $\Delta T_{dep} < 5^\circ\text{C}$. For the ZnO:Zn and alumina particles the corresponding particle loading range for the same ΔT_{dep} is $\phi^* < 7.6 \times 10^{-4}$. Importantly, for all cases, the SNR is sufficiently strong for the measurement to provide useful measurements for a particle-laden flow in the two-way coupling regime, demonstrating that the current method is capable of accurately measuring gas-phase temperatures in conditions relevant to a wide range of industrial

and natural particle-laden flows.

4 Conclusions

The range of conditions in which two-colour LIF thermometry can be used in particle-laden flows with a known level of accuracy has been identified for three types of particle with differing levels of spectral interference. This extends understanding of the applicability of two-colour LIF thermometry from previous work, which was limited to low loadings in particle-laden flows. In particular, it has been shown that interference due to the interaction of particles with light is typically negligible for particle volumetric loadings within the lower end of the two-way coupling regime and can extend to the bottom of the four-way coupling regime for particles without any significant spectral interference. Hence it can be used within the regimes of interest to many industrial applications.

The extent to which the interference from the particles influences the intensity measured in the filtered spectral bands was found to depend on the particle type. This increase in intensity of the interference with particle loading is not the same in the blue and red channels, leading to an error in the derived temperature. The luminescence of particles after UV excitation is the most significant source of interference for PMMA particles. However, spectral interference was not significant for the ZnO:Zn particles, which phosphoresce at wavelengths outside the detected spectral bands, or for the alumina particles, for which the main source of interference is Mie scattering. The derived temperature was accurate to within 10 °C up to particle loadings of $\phi^* < 7.6 \times 10^{-4}$ for the ZnO:Zn and alumina particles, with a corresponding standard deviation $\sigma_T = 5.8$ °C and 7.1 °C respectively, a slight increase from $\sigma_T = 5.6$ °C in the flow without particles. The interference from particles on the derived temperature was found to be independent of particle size for the PMMA particles, with an error of less than 10 °C up to $\phi = 2 \times 10^{-4}$ for all particle diameters tested, with a corresponding $\sigma_T = 8.1$ °C at this loading for the 20 μm particles.

The interference from particles provides greater uncertainty in areas of low toluene concentration, due to a lower fluorescence signal strength. Use of ZnO:Zn or non-emitting particles may allow LIF measurement to be extended into the denser end of the four-way coupling regime. However this can only be confirmed with a reliable method of measuring particle loading for these particles.

5 Appendix

The accuracy of the two-colour thermometry is significantly influenced by the strength of the fluorescence signals relative to the noise, as shown in Figure 9. In particular, because the temperature is inferred from the fluorescence intensity ratio rather than directly from the individual fluorescence intensities, the errors in temperature measurement can be particularly significant where the signal strength of the denominator term, in the present case the blue channel, is on the order of the noise strength. To reduce this effect, we employ two commonly used post-processing techniques – thresholding and smoothing. Here, we investigate the effect of these two techniques on the prevalence of errors in the temperature measurement for a single image. To quantify the errors, we first calculate the difference between the measured and actual temperature, ΔT_{dep} , on a pixel-by-pixel basis for the entire region of the image that is above the specified threshold. The mean ($\overline{\Delta T_{dep}}$) and standard deviation ($\sigma_{\Delta T}$) of this ensemble were then calculated for the case where the jet is unheated, because the actual gas temperature is uniform and known for this case.

Figure 16 presents the effect of the threshold value, ϵ , on both $\overline{\Delta T_{dep}}$ and $\sigma_{\Delta T}$. The threshold is normalised by I_{base} , which is the temporally and spatially averaged fluorescence intensity, within the region $-0.1 < r/D < 0.1$, $0.5 < x/D < 3$, where the toluene tracer is not mixed with the co-flow. The thresholding procedure was performed separately for each channel, such that the temperature at each pixel was only calculated if the intensity in both channels satisfy their respective threshold requirements. The values of I_{base} correspond to $SNR = 38.4$ and 19.6 for the blue and red channels respectively. The results show that $\overline{\Delta T_{dep}} < 0.1^\circ\text{C}$ for $\epsilon/I_{base} > 7\%$, while $\sigma_{\Delta T}$ reduces monotonically as ϵ/I_{base} increases. While the errors in the measured temperature can be further reduced at larger ϵ , this also reduces the number of usable data points in each image, particularly near to the jet edges (see Figure 8 and Figure 10). Therefore, as a compromise, a threshold value of ϵ/I_{base} of 10% was used for the present investigation. This resulted in pixels with $SNR \leq 3.84$ or 1.96 for the blue and red channels, respectively, being excluded from the temperature measurement.

Figure 17 presents the influence of smoothing kernel size, N , on $\overline{\Delta T_{dep}}$ and $\sigma_{\Delta T}$. Here, the smoothing kernel applied to the instantaneous temperature measurements is a $N \times N$ pixel mean filter. Pixels below the ϵ/I_{base} threshold were excluded from the smoothing procedure. Each pixel measures a region of cross-section $32.7 \times 32.7 \mu\text{m}$, so that the minimum spatial resolution of the filtered images is $32.7 \times N \mu\text{m}$. A threshold value of 10% was applied to the images before filtering. It can be seen that both $|\overline{\Delta T_{dep}}|$ and

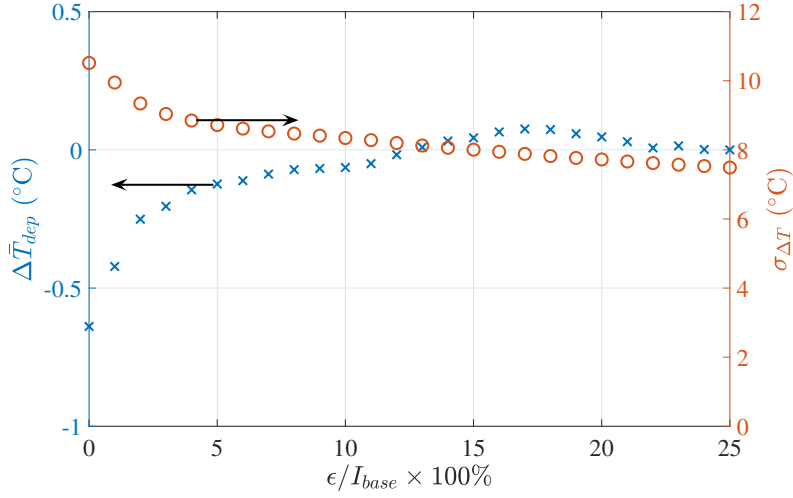


Figure 16: Effect of threshold magnitude (ϵ) as a percentage of I_{base} on the mean temperature error and corresponding standard deviation ($\overline{\Delta T_{dep}}$ and $\sigma_{\Delta T}$) for two-colour LIF measurements in an unheated jet without particles.

$\sigma_{\Delta T}$ decrease as the filter size is increased. Without filtering (i.e. $N = 1$), $\overline{\Delta T_{dep}} = -1.7$ °C, with a standard deviation of 25.7 °C. For all values of $N \geq 9$, $\overline{\Delta T_{dep}} < 0.025$ °C, with the corresponding $\sigma_{\Delta T}$ for $N = 9$ and 15 being 8.3 °C and 5.7 °C respectively. While a larger smoothing kernel decreases both $|\overline{\Delta T_{dep}}|$ and $\sigma_{\Delta T}$, this comes at the expense of spatial resolution. Hence, a kernel size of 9×9 pixels was chosen because it has a near zero mean error with a relatively low standard deviation, while still preserving a reasonable spatial resolution of 294 μm . As the light sheet thickness for the current experiments is ≈ 300 μm , this results in a roughly cubic measurement volume of $294 \times 294 \times 300$ μm for each pixel.

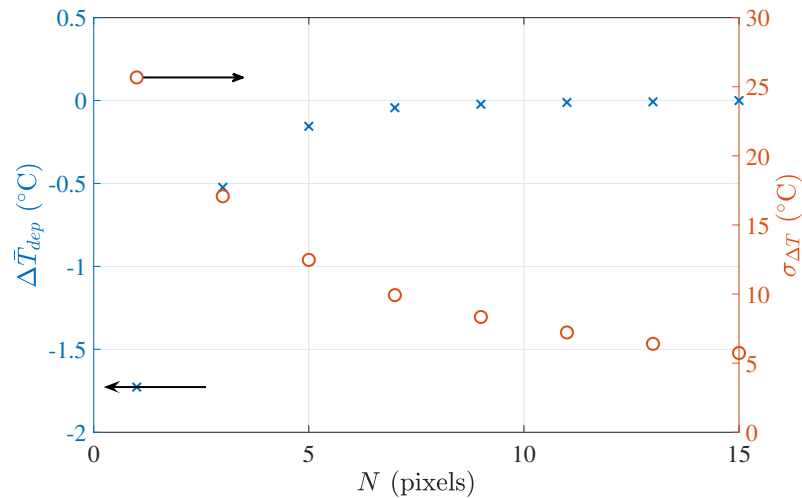


Figure 17: Effect of square filter kernel size (N) on the mean temperature error and corresponding standard deviation ($(\overline{\Delta T_{dep}})$ and $\sigma_{\Delta T}$) for two-colour LIF thermometry of a single image in an unheated jet without particles.

References

- [1] C. K. Ho and B. D. Iverson. “Review of high-temperature central receiver designs for concentrating solar power”. In: *Renewable and Sustainable Energy Reviews* 29 (2014), pp. 835–846.
- [2] A. Williams, M. Pourkashanian and J. M. Jones. “Combustion of pulverised coal and biomass”. In: *Progress in Energy and Combustion Science* 27.6 (2001), pp. 587–610.
- [3] W. M. Fish. “Alumina calcination in the fluid-flash calciner”. In: *Essential Readings in Light Metals*. Vol. 1. Switzerland: Springer International Publishers, 2016, pp. 648–652.
- [4] E. K. Longmire and J. K. Eaton. “Structure of a particle-laden round jet”. In: *Journal of Fluid Mechanics* 236 (1992), pp. 217–257.
- [5] S. Elgobashi. “An Updated Classification Map of Particle-Laden Turbulent Flows”. In: *IUTAM Symposium on Computational Approaches to Multiphase Flow: Proceedings of an IUTAM Symposium held at Argonne National Laboratory, October 4-7, 2004*. Ed. by S. Balachandar and A. Prosperetti. Dordrecht: Springer Netherlands, 2006, pp. 3–10.
- [6] R. Grena. “Thermal simulation of a single particle in a falling-particle solar receiver”. In: *Solar Energy* 83.8 (2009), pp. 1186–1199.

- [7] G. J. Nathan, P. A. M. Kalt, Z. T. Alwahabi, B. B. Dally, P. R. Medwell and Q. N. Chan. “Recent advances in the measurement of strongly radiating, turbulent reacting flows”. In: *Progress in Energy and Combustion Science* 38.1 (2011).
- [8] F. Miller and R. Koenigsdorff. “Theoretical analysis of a high-temperature small-particle solar receiver”. In: *Solar Energy Materials* 24.1 (1991), pp. 210–221.
- [9] T. C. W. Lau, J. H. Frank and G. J. Nathan. “Resolving the three-dimensional structure of particles that are aerodynamically clustered by a turbulent flow”. In: *Physics of Fluids* 31.7 (2019), p. 071702.
- [10] H. Pouransari and A. Mani. “Effects of Preferential Concentration on Heat Transfer in Particle-Based Solar Receivers”. In: *Journal of Solar Energy Engineering* 139.2 (2016), pp. 021008–021008–11.
- [11] N. Siegel, C. Ho, S. Khalsa and G. Kolb. “Development and Evaluation of a Prototype Solid Particle Receiver: On-Sun Testing and Model Validation”. English. In: *Journal Of Solar Energy Engineering-Transactions Of The Asme* 132.2 (2010).
- [12] M. Aldén, A. Omrane, M. Richter and G. Särner. “Thermographic phosphors for thermometry: A survey of combustion applications”. In: *Progress in Energy and Combustion Science* 37.4 (2011), pp. 422–461.
- [13] B. Fond, C. Abram, A. L. Heyes, A. M. Kempf and F. Beyrau. “Simultaneous temperature, mixture fraction and velocity imaging in turbulent flows using thermographic phosphor tracer particles”. In: *Optics Express* 20.20 (2012), pp. 22118–22133.
- [14] K. C. Y. Kueh, T. C. W. Lau, G. J. Nathan and Z. T. Alwahabi. “Non-intrusive temperature measurement of particles in a fluidised bed heated by well-characterised radiation”. In: *International Journal of Multiphase Flow* 100 (2018), pp. 186–195.
- [15] C. Abram, B. Fond, A. L. Heyes and F. Beyrau. “High-speed planar thermometry and velocimetry using thermographic phosphor particles”. In: *Applied Physics B* 111.2 (2013), pp. 155–160.
- [16] C. Abram, B. Fond and F. Beyrau. “High-precision flow temperature imaging using ZnO thermographic phosphor tracer particles”. In: *Optics Express* 23.15 (2015), pp. 19453–19468.
- [17] A. Frankel, H. Pouransari, F. Coletti and A. Mani. “Settling of heated particles in homogeneous turbulence”. In: *Journal of Fluid Mechanics* 792 (2016), pp. 869–893.

- [18] D. R. Dowling and P. E. Dimotakis. “Similarity of the concentration field of gas-phase turbulent jets”. In: *Journal of Fluid Mechanics* 218 (1990), pp. 109–141.
- [19] W. M. Pitts. “Reynolds number effects on the mixing behavior of axisymmetric turbulent jets”. In: *Experiments in Fluids* 11.2 (1991b), pp. 135–141.
- [20] C. Schulz and V. Sick. “Tracer-LIF diagnostics: quantitative measurement of fuel concentration, temperature and fuel/air ratio in practical combustion systems”. In: *Progress in Energy and Combustion Science* 31.1 (2005), pp. 75–121.
- [21] M. Luong, W. Koban and C. Schulz. “Novel strategies for imaging temperature distribution using Toluene LIF”. In: *Journal of Physics: Conference Series* 45.1 (2006), p. 133.
- [22] J. D. Miller, M. N. Slipchenko, J. G. Mance, S. Roy and J. R. Gord. “1-kHz two-dimensional coherent anti-Stokes Raman scattering (2D-CARS) for gas-phase thermometry”. In: *Optics Express* 24.22 (2016), pp. 24971–24979.
- [23] A. P. Yalin and R. B. Miles. “Ultraviolet filtered Rayleigh scattering temperature measurements with a mercury filter”. eng. In: *Optics letters* 24.9 (1999), p. 590.
- [24] E. Kristensson, A. Ehn, J. Bood and M. Aldén. “Advancements in Rayleigh scattering thermometry by means of structured illumination”. In: *Proceedings of the Combustion Institute* 35.3 (2015), pp. 3689–3696.
- [25] M. Cundy, P. Trunk, A. Dreizler and V. Sick. “Gas-phase toluene LIF temperature imaging near surfaces at 10kHz”. In: *Experiments in Fluids* 51.5 (2011), pp. 1169–1176.
- [26] C. Jainski, L. Lu, V. Sick and A. Dreizler. “Laser imaging investigation of transient heat transfer processes in turbulent nitrogen jets impinging on a heated wall”. eng. In: *International Journal of Heat and Mass Transfer* 74 (2014), pp. 101–112.
- [27] W. Koban, J. D. Koch, R. K. Hanson and C. Schulz. “Absorption and fluorescence of toluene vapor at elevated temperatures”. In: *Physical Chemistry Chemical Physics* 6.11 (2004), pp. 2940–2945.
- [28] P. A. M. Kalt, C. H. Birzer and G. J. Nathan. “Corrections to facilitate planar imaging of particle concentration in particle-laden flows using Mie scattering, part 1: collimated laser sheets”. eng. In: *Applied optics* 46.23 (2007), p. 5823.

- [29] T. C. W. Lau and G. J. Nathan. “Influence of Stokes number on the velocity and concentration distributions in particle-laden jets”. In: *Journal of Fluid Mechanics* 757 (2014), pp. 432–457.
- [30] T. C. W. Lau and G. J. Nathan. “The effect of Stokes number on particle velocity and concentration distributions in a well-characterised, turbulent, co-flowing two-phase jet”. In: *Journal of Fluid Mechanics* 809 (2016), pp. 72–110.
- [31] C. L. Yaws. *Handbook of vapor pressure / Carl L. Yaws*. eng. Library of physico-chemical property data. Houston: Gulf Pub. Co., 1994.
- [32] S. Faust, M. Goschütz, S. A. Kaiser, T. Dreier and C. Schulz. “A comparison of selected organic tracers for quantitative scalar imaging in the gas phase via laser-induced fluorescence”. In: *Applied Physics B* 117.1 (2014), pp. 183–194.
- [33] W. Koban, J. D. Koch, R. K. Hanson and C. Schulz. “Oxygen quenching of toluene fluorescence at elevated temperatures”. In: *Applied Physics B* 80.6 (2005), pp. 777–784.
- [34] D Fuhrmann et al. “Self-quenching in toluene LIF”. eng. In: *Proceedings of the Combustion Institute* 36.3 (2017), pp. 4505–4514.
- [35] S. Faust, T. Dreier and C. Schulz. “Temperature and bath gas composition dependence of effective fluorescence lifetimes of toluene excited at 266nm”. In: *Chemical Physics* 383.1 (2011), pp. 6–11.
- [36] Asahi Spectra USA Inc. Web Page. 2018.
- [37] Semrock. Web Page. 2018.
- [38] V. A. Miller, M. Gamba, M. G. Mungal and R. K. Hanson. “Single- and dual-band collection toluene PLIF thermometry in supersonic flows”. In: *Experiments in Fluids* 54.6 (2013), p. 1539.
- [39] S. Faust, G. Tea, T. Dreier and C. Schulz. “Temperature, pressure, and bath gas composition dependence of fluorescence spectra and fluorescence lifetimes of toluene and naphthalene”. eng. In: *Applied Physics B* 110.1 (2013), pp. 81–93.
- [40] M. W. Thring and M. P. Newby. “Combustion length of enclosed turbulent jet flames”. In: *Symposium (International) on Combustion* 4.1 (1953), pp. 789–796.
- [41] W. M. Pitts. “Effects of global density ratio on the centerline mixing behavior of axisymmetric turbulent jets”. In: *Experiments in Fluids* 11.2 (1991a), pp. 125–134.

- [42] J. Mi, D. S. Nobes and G. J. Nathan. “Influence of jet exit conditions on the passive scalar field of an axisymmetric free jet”. In: *Journal of Fluid Mechanics* 432 (2001), pp. 91–125.
- [43] G. Papadopoulos and W. M. Pitts. “Scaling the Near-Field Centerline Mixing Behavior of Axisymmetric Turbulent Jets”. In: *AIAA Journal* 36.9 (1998), pp. 1635–1642.
- [44] R. W. Schefer and R. W. Dibble. “Mixture Fraction Field in a Turbulent Nonreacting Propane Jet”. In: *AIAA Journal* 39.1 (2001), p. 64.
- [45] T. C. W. Lau and G. J. Nathan. “A method for identifying and characterising particle clusters in a two-phase turbulent jet”. In: *International Journal of Multiphase Flow* 88 (2017), pp. 191–204.

Appendix D

Paper II - Insights from a new method providing single-shot, planar measurement of gas-phase temperature in particle-laden flows under high-flux radiation

This chapter presents the published journal article:

Lewis, E. W., Lau, T. C. W., Sun, Z., Alwahabi, Z. T. and Nathan, G. J. (2021), "Insights from a new method providing single-shot, planar measurement of gas-phase temperature in particle-laden flows under high-flux radiation", *Experiments in Fluids* 62(4).

The article in its published format is available at:

<https://doi.org/10.1007/s00348-021-03183-x>.

The content of this chapter is identical to that of the published article, with the following exceptions:

1. The typesetting and referencing style may have been altered for consistency within the thesis.
2. The position and sizing of the figures and tables may differ.

Statement of Authorship

Title of Paper	Insights from a new method providing single-shot, planar measurement of gas-phase temperature in particle-laden flows under high-flux radiation
Publication Status	<input checked="" type="checkbox"/> Published <input type="checkbox"/> Accepted for Publication <input type="checkbox"/> Submitted for Publication <input type="checkbox"/> Unpublished and Unsubmitted work written in manuscript style
Publication Details	Lewis, E. W., Lau, T. C. W., Sun, Z., Alwahabi, Z. T. and Nathan, G. J. (2021), "Insights from a new method providing single-shot, planar measurement of gas-phase temperature in particle-laden flows under high-flux radiation", Experiments in Fluids 62(4).

Principal Author


Name of Principal Author (Candidate)	Elliott W. Lewis		
Contribution to the Paper	Designed experimental arrangement and undertook experiments, developed data processing methods, interpreted data, wrote manuscript.		
Overall percentage (%)	70		
Certification:	This paper reports on original research I conducted during the period of my Higher Degree by Research candidature and is not subject to any obligations or contractual agreements with a third party that would constrain its inclusion in this thesis. I am the primary author of this paper.		
Signature		Date	1/11/2021

Co-Author Contributions

By signing the Statement of Authorship, each author certifies that:

- i. the candidate's stated contribution to the publication is accurate (as detailed above);
- ii. permission is granted for the candidate to include the publication in the thesis; and
- iii. the sum of all co-author contributions is equal to 100% less the candidate's stated contribution.

Name of Co-Author	Timothy C. W. Lau		
Contribution to the Paper	Co-supervised experimental design, assisted with data analysis, edited the manuscript.		
Signature		Date	1/11/2021

Name of Co-Author	Zhiwei Sun		
Contribution to the Paper	Supervised the experimental setup and data collection, assisted with interpretation of data, and edited the manuscript.		
Signature		Date	1/11/2021

Name of Co-Author	Zeyad T. Alwahabi		
Contribution to the Paper	Designed research concept, co-supervised experimental work and data interpretation.		
Signature		Date	

Name of Co-Author	Graham J. Nathan		
Contribution to the Paper	Co-supervised experimental design, assisted with the interpretation of results and edited the manuscript.		
Signature		Date	9/11/2021

Insights from a new method providing single-shot, planar measurement of gas-phase temperature in particle-laden flows under high-flux radiation

Elliott W. Lewis^{1,3}, Timothy C. W. Lau^{1,3,4}, Zhiwei Sun^{1,3},
Zeyad T. Alwahabi^{2,3}, and Graham J. Nathan^{1,3}

¹*School of Mechanical Engineering, University of Adelaide, Australia*

²*School of Chemical Engineering and Advanced Materials, University of Adelaide, Australia*

³*Centre for Energy Technology, University of Adelaide, Australia*

⁴*UniSA STEM, University of South Australia, Australia*

Abstract

Two-colour laser induced fluorescence (LIF) of toluene has been demonstrated to provide in-situ, spatially resolved, planar measurements of the gas-phase temperature in a particle-laden flow with strong radiative heating at fluxes up to 42.8 MW/m². Toluene was seeded in trace quantities into the gas flow laden with particles of mean diameter 173 μm at a volumetric loading sufficiently high for particle-fluid and particle-particle interactions to be significant. The particle number density was also measured simultaneously using Mie scattering. The two-colour LIF method was found to resolve temperature with a pixel-to-pixel standard deviation of 17.8 °C for unheated measurements in this system despite significant attenuation of the probe laser and signal trapping of the fluorescence emissions from the densely loaded particles. Following heating of the particles using high flux radiation, the increase in the gas-phase temperature from convection was found to be spatially non-uniform with highly localised regions of temperature spanning from ambient to 150 °C. This gas-phase heating continued well downstream from the limits of the region with radiative heating, with the time-averaged gas temperature increasing with distance at up to 2,200 °C/m on the jet centreline. The temperature

of the flow was non-symmetrical in the direction of the heating beam, because the particles attenuate the radiation through absorption and scattering. The addition of radiation at fluxes up to 42.8 MW/m^2 did not significantly change the particle number density distribution within the region investigated here.

1 Introduction

Particle-laden flows with strong radiative heat transfer are present in a range of systems including particle-based concentrated solar thermal (CST) receivers, flash calciners for alumina and cement production, and combustion of particulate fuels. The particles in these systems are typically heated rapidly following the absorption of high-flux radiation from a flame, concentrated sunlight, or from a chemical reaction such as combustion. The resulting strong thermal gradients lead to complex and non-linear heat transfer from both convective and radiative processes between the heat source, particles, fluid and the surroundings [1, 2]. These processes are further complicated by non-linear and mutually interacting phenomena in particle-laden flows such as turbulence, particle clustering [3], and particle-fluid coupling [4]. These phenomena can affect the mean and instantaneous velocity and particle number density distributions [5], which in turn affect both the radiative and convective heat transfer. Detailed understanding of these complex, coupled phenomena requires accurate, spatially-resolved, multi-dimensional and simultaneous measurements of the temperature and velocity of both phases, together with the local particle concentration (number density). However, such measurements of all of these parameters are not presently available, partially due to the challenging experimental arrangement required and lack of suitable techniques. Recent experiments have begun to address this gap [6–8]. However, there are currently no reports of in-situ and well-resolved measurements of the gas-phase temperature in particle-laden flows with strong radiative heating.

Previous numerical models of particles heated with high-flux radiation in particle receivers have shown that heat transfer between the radiation source and the particles, together with that between the particles and fluid, is strongly dependent on both the particle size and number density [9, 10]. Furthermore, it has been demonstrated that particle clustering, whereby particles are preferentially concentrated in highly localised regions, impacts heat transfer processes and local temperature distributions [11], which in turn affect the efficiency of the system. Additionally, the heating of particles in suspension by radiation at sufficiently high fluxes can induce turbulence

in the flow [12] and reduce the particle settling velocity [13] from the generation of buoyant plumes around the heated particles. The complexity of particle-fluid interactions in these systems also increases with particle volumetric loading ($\phi = \dot{V}_p/\dot{V}_f$, where \dot{V}_p and \dot{V}_f are the volumetric flow rates of the particles and fluid respectively). Additional particle-gas interactions occur for flows in the two-way coupling regime (for $10^{-6} < \phi < 10^{-3}$) and particle-particle interactions also occur in the four-way coupling regime (for $\phi > 10^{-3}$), as defined by Elgobashi [4]. These mutually-interacting, complex phenomena result in particle-laden flows being difficult to model reliably without both new understanding and computationally-expensive direct numerical simulations. Therefore, detailed experimental measurements of both the flow temperature and particle concentration are required to enable the development and validation of reliable, simplified models of these flows.

The use of experimental techniques with high spatial and temporal resolution in multiple dimensions are needed to provide measurements of spatial and temporal gradients in turbulent flows. Laser based techniques are a suitable choice, as these have the potential to provide spatially resolved two-dimensional measurements from a nanosecond scale laser pulse. However, utilising laser-based methods in particle-laden flows is difficult due to the challenges of laser attenuation, signal trapping [14], multiple scattering [15], and particle luminescence [16]. These challenges are particularly significant in flows with the high particle loadings ($\phi > 10^{-3}$) that are used in most practical systems, resulting in a paucity of detailed experimental measurements in such environments. Previous thermometry measurements of particle-laden flows with radiative heating include point measurements of the gas and walls using thermocouples in a CST particle receiver [17], a vortex particle receiver [18] and square duct [19], as well as planar particle temperature measurements in a jet [20]. However, there are currently no in-situ planar measurements of the gas temperature in densely loaded particle-laden flows heated by high-flux radiation that are spatially and temporally resolved. As such there is a need for experimental measurements of parameters including gas temperature to improve the current understanding of these flows.

Several techniques have been implemented to measure the instantaneous, planar gas temperature in a variety of flows, including laser Rayleigh scattering (LRS) [21], laser induced phosphorescence (LIP) [6] and laser induced fluorescence (LIF) [22]. In LRS, the thermometry signal is at the same wavelength as the excitation source (i.e. the laser), which results in significant interference from Mie scattering in flows with particles. Filtered LRS is a technique that has been used to suppress scattered laser light and stray light from other sources. However, the Mie scattering from particles is several orders of magnitude stronger than the Rayleigh signal leading to

difficulties isolating the Rayleigh signal from the Mie scattering. Additionally, the LRS signal is proportional to the local laser flux, which is highly non-uniform in a densely loaded particle-laden flow due to attenuation and multiple scattering. The LIF and LIP methods both have thermometry signals that are separable from scattered light using optical filtering and thus are well suited for measurements in particle-laden flows. However, LIP for gas-phase thermometry typically utilises small tracer particles in the flow together with the assumption that the two phases are in thermal equilibrium. In a flow subject to high-flux radiation this assumption does not hold because of absorption of the high-flux radiation by the particles, which results in a temperature difference between the particles and gas. In contrast, LIF thermometry typically utilises gas tracers that give a direct measurement of the gas-phase temperature. While LIF thermometry is a mature technique, its accuracy particle-laden flows has only begun to be assessed recently in an isothermal flow [16]. LIF thermometry has yet to be applied to measure gas-phase temperatures with high spatial resolution in industrially relevant particle-laden flows with strong thermal gradients.

Therefore, the objective of the present investigation is to determine the spatially resolved gas-phase temperature distribution in a particle-laden flow with a volumetric loading sufficiently high to be in the four-way coupling regime and with high-flux radiative heating. This measurement is a step towards improving understanding of heat transfer in particle-laden flows, in particular particle-laden flows with significant particle-fluid and particle-particle interactions. More specifically, we aim to experimentally determine the mean and instantaneous gas-phase temperature distributions in a well-characterised particle-laden flow heated at a systematically varied series of radiative fluxes up to 42.8 MW/m^2 . We also aim to provide some new insights from these measurements.

2 Methodology

2.1 Two-colour LIF thermometry

Toluene was chosen as the fluorescing species for LIF thermometry measurements because it has been previously demonstrated in flows with a range of challenging conditions including in a particle-laden jet [16], in flows with droplets [7, 23], near to surfaces at kHz rates [24] and in shock tubes [25]. Toluene is a well-characterised fluorescent tracer suitable for measurements at temperatures of $280\text{K} < T_g < 600\text{K}$ with an emission spectrum that is highly sensitive to temperature [26]. Toluene LIF thermometry using the two-colour

ratio method utilises the shift of the emission spectrum to longer wavelengths with increasing temperature [27]. The intensity of fluorescence emissions (I) at each wavelength (λ) after excitation by a suitable light source is dependent on the local toluene concentration (n), laser pulse energy (Q_{laser}), the absorption cross-section (σ_{abs}) and fluorescence quantum yield (Φ_F). Importantly, both σ_{abs} and Φ_F , and subsequently the absorption and fluorescence emission, of toluene are temperature (T) dependent [22]. The spatially resolved emission intensity of a dispersed fluorescent tracer in a flow, following excitation at a single wavelength using a laser formed into a sheet, is described by the following equation:

$$I_\lambda \propto Q_{laser}(x, r)n(x, r)\sigma_{abs}(T(x, r))\Phi_{F,\lambda}(T(x, r)), \quad (1)$$

where x and r are two relevant spatial co-ordinates of the flow. The influence of the spatially dependent parameters can be removed by taking the ratio of emissions in two spectral bands formed using optical filtering. The resultant ratio of signals measured by two cameras aligned to view along the same optical path through the flow, each measuring the intensity of fluorescence emissions in a filtered spectral band (S_λ), is shown to reduce to a function of temperature only by the equation:

$$\frac{S_{\lambda 1}}{S_{\lambda 2}} = \frac{\eta_{\lambda 1}\Phi_{F,\lambda 1}(T)}{\eta_{\lambda 2}\Phi_{F,\lambda 2}(T)} = f(T) \quad (2)$$

where η is the camera collection efficiency at the filtered wavelengths and f is a function that can be determined through calibration. Importantly, the intensity ratio is not dependent on the local laser fluence, Q_{laser} , or the toluene concentration, n , removing the necessity to correct the measured fluorescence emission for laser sheet attenuation, beam profile and mixing of the toluene seeded flow with the ambient gas.

2.2 Experimental arrangement

The experiment consisted of a system to provide simultaneous gas-phase thermometry and particle number density measurements in a particle-laden flow heated with high-flux radiation, as presented in Figure 1. The central flow issues from a long pipe with diameter $D = 12.6$ mm to generate a jet, with a development length of $165D$ that is sufficiently long to approach a fully developed particle-laden pipe flow [5]. The central pipe is aligned within a co-annular pipe of diameter 69 mm, which is used to generate a co-flow. The co-ordinate systems for the flow and optical system, together with the size of the measurement region, are presented in Figure 2. The jet pipe was

positioned centrally within a vertically oriented, downward directed wind tunnel of 300 mm square cross section. This arrangement was designed such that the pipe jet matches that investigated by [28]. The central pipe had a bulk velocity of $U_{g,b} = 3.6$ m/s, which was chosen because it was the lowest velocity at which the particles were effectively carried by the flow. A low velocity was desired to increase the residence time, and therefore the temperature rise, of the particles in the heating region. The resultant Reynolds number of the jet is $Re_D = \rho U_{g,b} D / \mu = 3000$, where ρ and μ are the density and dynamic viscosity of the flow respectively. The velocity of the annular co-flow and wind tunnel co-flow were both less than 0.5 m/s. Both the jet and annular flows employed high purity nitrogen as the carrier gas. Toluene and particles were seeded separately into two streams and then combined to form the jet flow, with the particles introduced into one stream with a volumetric flow rate of 18 SLPM using a screw feeder in a sealed container. The second stream, with a volumetric flow rate of 7 SLPM, was bubbled through liquid toluene held at ambient temperature, resulting in a toluene concentration of approximately 0.75% by volume for the combined jet flow. This concentration was estimated using the assumption that the outlet flow from the toluene bubbler is saturated. For the annular flow a 50 SLPM stream of nitrogen was combined with a toluene seeded stream of 5 SLPM, with a resultant toluene concentration in the annular flow of approximately 0.25% by volume. The toluene concentration in the annulus differed from that of the jet to allow for clear identification of the jet edges. The volumetric flow rates of each of these four flows were controlled by separate mass flow controllers (MFCs). Nitrogen was used as the carrier gas for both the jet and annular flow because the presence of oxygen strongly quenches the fluorescence emissions from toluene [29].

Aluminosilicate ceramic (Carbobeat CP 70/140) particles with an absolute density of 3.27 g/cm³ and an average sphericity of 0.9 were seeded in the jet flow using a screw feeder. The time-averaged volumetric loading of particles was chosen to be $\bar{\phi} = 1.4 \times 10^{-3}$, resulting in a particle-laden flow within the four-way coupling regime. The physical design of a screw feeder introduces a sinusoidal variation in the particle loading with time, which is particularly significant at low screw speeds. This effect was reduced using a screw with 4 flights operating at rotational speeds > 30 rpm. The resultant standard deviation in particle loading with time was 14.8% of the time-averaged mean. The particle diameter (d_p) distribution of the Carbobeat CP 70/140 particles, as measured using a Malvern Mastersizer 2000, is presented in Figure 3. The measured mean diameter by volume was $\bar{d}_p = 173$ μ m, with 80% of particles in the range of $125 < d_p < 235$ μ m. The resultant particle Stokes number, which is the ratio of the particle to flow time

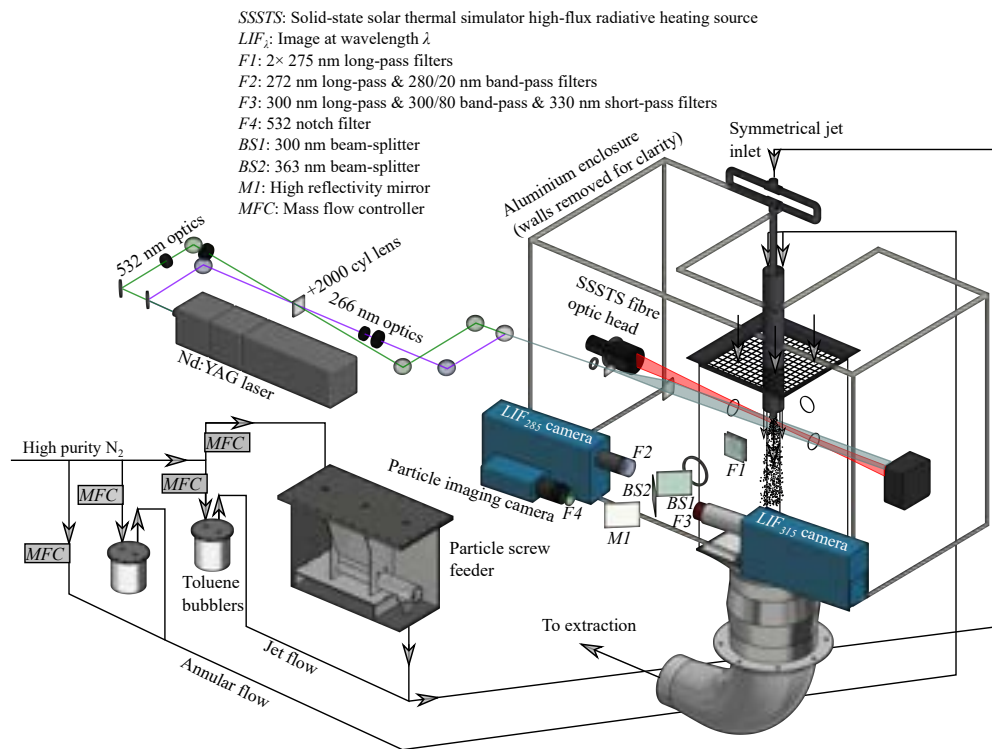


Figure 1: Experimental arrangement for simultaneous two-colour LIF thermometry and particle number density measurements of a particle-laden flow heated with high-flux radiation.

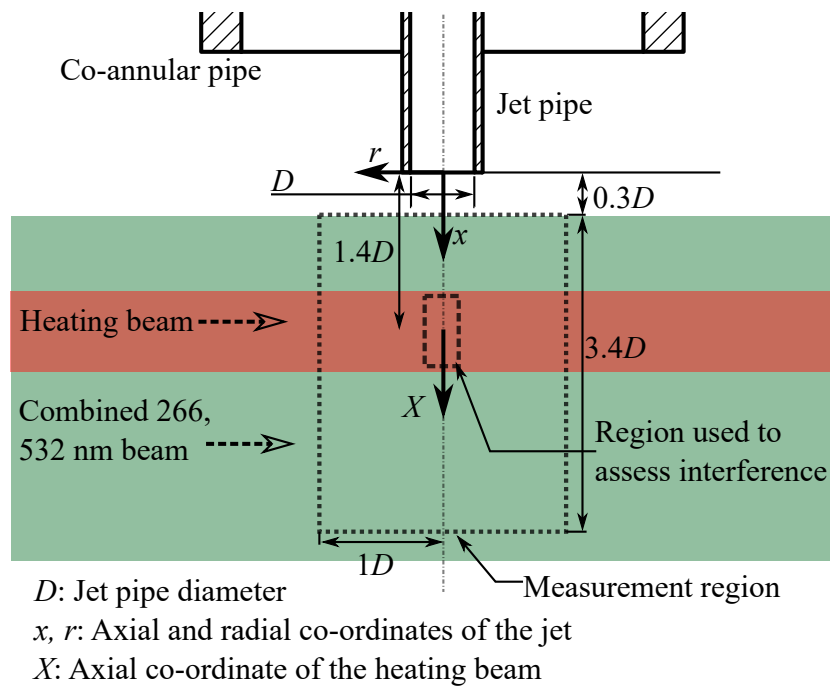


Figure 2: Schematic diagram of the region of interest showing key dimensions and the co-ordinate system (not to scale).

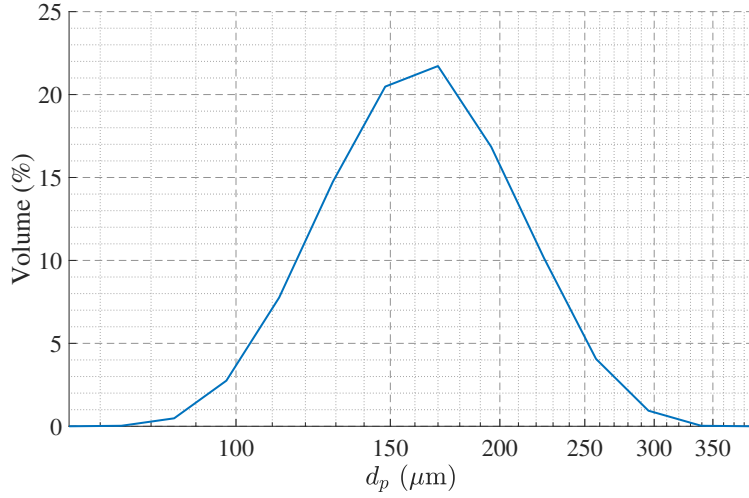


Figure 3: The measured size distribution for the Carbobead CP 70/140 particles.

response [30], for the large-scale motions in the jet was $Sk_D = \frac{\rho_p \bar{d}_p^2 U_{(g,b)}}{18\mu D} = 77$.

2.3 Optical arrangement

A Quantel Q-smart laser operating at 10Hz with two frequency doublers was used to generate second- and fourth-harmonic beams with respective wavelengths of 532 nm and 266 nm. Both beams were formed into co-planar sheets 60 mm high and approximately 0.6 mm thick in the measurement region of $|r/D| < 2$ and $0.3 < x/D < 3.7$, where x and r are the respective axial and radial co-ordinates of the jet. The combined laser sheet was aligned to pass through the jet centreline, as can be seen from Figure 1. The pulse energies of each wavelength, controlled using separate wave-plates and polarisers, were 18 and 0.5 mJ/pulse for the 266 and 532 nm beams respectively. The resultant fluences in the measurement region of the laser sheets were 50 and 1.4 mJ/cm² respectively. The radiative heating source was a solid-state solar thermal simulator (SSSTS), which is a diode laser bundle with a fibre optic head emitting a collimated, monochromatic infra-red (910 nm) beam with a full-width half maximum diameter of 7.34 mm as described by Alwahabi et al. [31]. The SSSTS beam was centred on the jet centreline 17.5 mm downstream from the jet exit plane. The intensity profile of the SSSTS beam, I , on the jet centreline, normalised by the peak intensity I_{peak} , is presented in Figure 4. Here X is the co-ordinate of the SSSTS beam co-linear with x , with the origin situated at the intersection of the SSSTS beam centre and

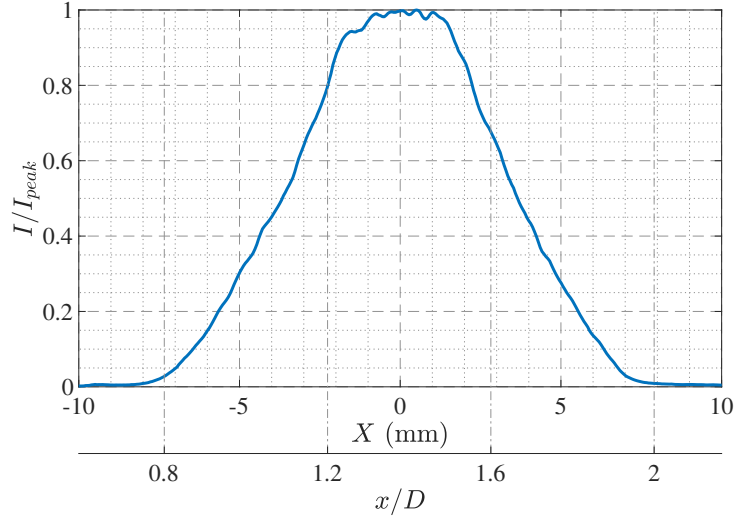


Figure 4: Solid-state solar thermal simulator (SSSTS) intensity profile normalised by the peak intensity, measured on the jet centreline in the axial direction. The profile is presented for the axial co-ordinate of both the jet flow (x) and heating beam (X), which are described in Figure 2.

the jet centreline. This profile was measured by imaging the reflection of the SSSTS beam from a diffuse glass plate angled at 45° to the beam direction. The SSSTS beam was absorbed by a water-cooled power meter (Gentec model HP100A-4KWHE) that measured the instantaneous SSSTS power at 10 Hz, located in the path of the beam after passing through the wind tunnel. For safety, the SSSTS fibre optic head, power meter and wind tunnel were all positioned inside an interlocked brick-lined aluminium enclosure during operation. During the experiments the flux of the SSSTS beam was varied in the range of $0 < \dot{Q}''_{peak} < 42.8 \text{ MW/m}^2$, where \dot{Q}''_{peak} is the peak heating flux of the SSSTS calculated using time-averaged power measured with the power meter and the profile in Figure 4.

Optical filtering was firstly used to separate the fluorescence emissions of the toluene (which are in the spectral region of 270-340 nm) from the elastically scattered light at 266 and 532 nm, and secondly used to separate the fluorescence emissions into two spectral bands centred at 285 and 315 nm (S_{285} and S_{315} respectively). To achieve this, the scattered and emitted light was initially passed through two 275 nm long-pass filters (Asahi Spectra ZUL0275), each with an optical density of 2.5 at 266 nm, to suppress the majority of elastically scattered 266 nm laser light. Two dichroic beam-splitters (Semrock FF310-Di01, Di01-R355) were then used to separate S_{285} and S_{315} from the Mie scattered light at 532 nm. The fluorescence channels

S_{285} and S_{315} were then refined using a series of optical filters and captured using two separate PCO Di-Cam intensified s-CMOS camera. The S_{285} channel was formed using a 272 nm long-pass (Semrock FF01-272LP) and 280 nm band-pass filter (Semrock BP280/20), with the resultant transmission band of 285 ± 5 nm being focussed using a spherical UV lens ($f = 100$ mm, Thorlabs LB4821). The S_{315} channel was formed using a 300 nm long-pass (Semrock FF01-300/LP), 330 nm short-pass (Semrock FF01-330/SP) and a 300 nm band-pass filter (Semrock FF01-300/80), with a resultant transmission band of 315 ± 10 nm being focussed using a Sodern UV 100 mm F/2.8 lens. The transmission efficiency of each channel is presented in Figure 5, and the filter combinations are summarised in Table 1. These filter combinations were chosen to form the two-colour fluorescence bands at 285 ± 5 nm and 315 ± 10 nm because a strong signal is expected for both these bands, and because the resultant two-colour ratio is sensitive to changes in temperature within the gas temperature (T_g) ranges expected in the current experiments of $20 \text{ }^\circ\text{C} < T_g < 200 \text{ }^\circ\text{C}$ [25]. The filters used to form both of the channels used for two-colour LIF also effectively suppress elastically scattered laser light at 266 nm, 532 nm and 910 nm, with a calculated optical density > 6 at these wavelengths.

The particles were imaged using the Mie scattering from the 532 nm laser that was transmitted through the two beam-splitters described earlier. The scattered light was then reflected by a mirror (Thorlabs PFSQ20-03-F01) and filtered using a 532 nm notch filter to form the particle detection channel (S_{532}). This channel was imaged using a PCO.2000 CCD with a Tamron macro 80-210 mm lens.

Each of the three cameras had a gate width of $1 \mu\text{s}$ that opened approximately 100 ns before the laser pulse, with images recorded at the laser pulse frequency of 10Hz. The spatial resolution for S_{285} , S_{315} and S_{532} was 17.8, 15.5 and 27.3 px/mm respectively. The resolution for the two fluorescence cameras were matched as closely as possible within the limitations of the available space and lenses. The three cameras were located on the same side of the wind tunnel so that all attenuation and signal trapping effects interfering with the signal were the same for each camera.

The Carbohead ceramic particles used here were found, from measurements using a spectrometer (Princeton Instruments Acton Series Spectrograph), to have no significant luminescence after exposure to any of 266, 532 or 910 nm light. Hence, scattering and signal trapping were deduced to be the primary sources of interference. Measurements of the intensity in each channel were conducted with and without the presence of particles and/or toluene, to quantify the effect of these sources of interference on the collected signal. The results of these measurements are presented in section 3.1.

Table 1: Optical filters used to form the two fluorescence channels, S_{285} and S_{315} , and one scattering channel, S_{532} . Abbreviations: LP = long-pass filter, SP = short-pass filter, BP = band-pass filter, BS = beam-splitter.

S_{285}	S_{315}	S_{532}
2×275 nm LP	2×275 nm LP	2×275 nm LP
310 nm BS (reflected)	310 nm BS (transmitted)	310 nm BS (transmitted)
272 nm LP	355 nm BS (reflected)	355 nm BS (transmitted)
280 nm BP (20 nm width)	300 nm LP	532 nm BP
	300 nm BP (80 nm width)	
	330 nm SP	

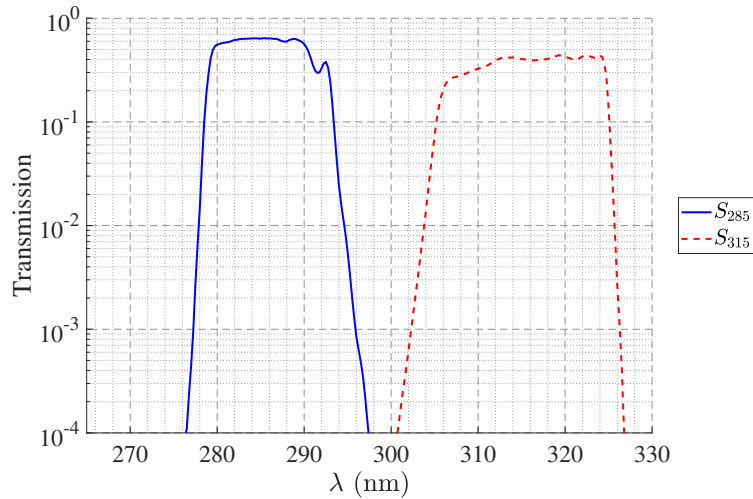


Figure 5: Spectral transmission efficiency of filter combinations used to form the two channels, S_{285} and S_{315} , for two-colour LIF thermometry. The combined filter transmission for each channel is calculated from data provided by the manufacturers [32, 33].

2.4 Image processing and analysis

Each experimental run comprised of a series of raw images collected simultaneously from the two fluorescence emission channels, S_{315} and S_{285} , and from the scattering channel, S_{532} , which were processed to determine the temperature and particle number density using in-house Matlab codes. A background image was measured for each channel from the time-average of 100 images collected under experimental conditions, except with the flow off and after all of the toluene and particles had been flushed from the imaging region. This background image was subtracted from the raw images. Spatial matching of the cameras was done on a pixel-by-pixel basis utilising a two-stage approach. In the first stage, a target image was taken of a thin metal plate with an evenly spaced grid of small (2 mm) holes and notches. This was aligned such that the face was co-planar with the laser sheet. A UV lamp (Spectroline EB-160C) illuminated the plate from behind, with the transmitted light being imaged in S_{285} and S_{315} with the filters in place (the use of the filtered spectral bands for the target imaging was chosen to be identical to the actual experiment to prevent errors from chromatic aberrations). For S_{532} the same target was imaged using ambient lighting of the room. The channels S_{285} and S_{532} were spatially aligned to S_{315} by matching a series of corresponding points on each of the target images. The target images were recorded once per day with the same transformation matrices used for all images recorded on the same day. It is estimated that the resultant images after this stage were matched to within ± 1 pixel. A second stage image processing algorithm was utilised to further improve the spatial matching to sub-pixel accuracy. This was achieved for each image series using the time-averaged images of the toluene-seeded jet in which the averaged image from S_{285} was offset systematically in both the x and y directions in increments of 0.1 pixels using bi-linear interpolation. At each increment, the intensity ratio was calculated on a per-pixel basis using the offset image, and the standard deviation of an ensemble of pixels within the region $0.5 < x/D < 0.9$, $|r/D| < 1$ was calculated. This region was chosen because it is upstream of the heating laser (so the flow temperature is uniform) and includes the shear layer near to the jet exit plane where there were strong toluene concentration gradients (such that any alignment error significantly changes the ratio). The offset that resulted in the lowest standard deviation was selected to be used for all instantaneous images. This method was completed for each case with a resulting variance between all cases recorded in any single day of < 0.3 pixels. Over the course of a day there was no clear trend in the changes to the value of the calculated offset, which suggests the variance is likely due to random error. For this reason, the mean of the offset

calculated from all cases on one day was used to correct all images taken on that particular day.

The ratio S_{315}/S_{285} of each instantaneous image was then calculated for each spatially matched pixel. Data from S_{285} and S_{315} with an intensity below a threshold value of $15\times$ the dark charge were removed from further analysis. This value was chosen for the threshold because previous work found that images for two-colour LIF with a signal to noise ratio of 15 were accurate to within 20°C at a range of temperatures [16]. The resultant two-colour ratio image of S_{315}/S_{285} was corrected for systematic errors in the intensity ratio, such as can arise from spatial inhomogeneity in camera response or spatial dependencies in the collection optics, using images taken under experimental conditions without particles or heating. This correction is based on the assumption that, without heating, the temperature in the measurement region is uniform at the ambient value. As such, the ratio calculated is expected to also be uniform, and any non-uniformity in the ratio is due to these systematic errors. This is similar to the correction performed by [7]. The temperature was calculated from S_{315}/S_{285} using a linear curve fit of the calibration data (as presented in the Calibration section). The single-shot temperature images were smoothed using a 5×5 pixel median filter to reduce influence of noise on results, with a resultant decrease spatial resolution. The filter kernel size (5×5 pixels) was chosen to be close to the laser sheet thickness, giving an approximately cubic measurement volume. The median filter was selected (rather than other filters such as a mean filter) because it is less sensitive to the large fluctuations of values that may occur in the intensity ratio when the denominator term is small. The ambient temperature for each image set was calculated from the time-averaged temperature measured upstream of the heating laser.

The images of the Mie scattered signal (S_{532}) were used to determine the particle locations. After background correction and spatial matching, the images were corrected for variations of the laser sheet profile. The profile was estimated using the particle scattering intensity measured by the camera, averaged along the beam path. The images were then binarised using a threshold of $10\times$ the standard deviation of the dark charge to ensure the signal from the particles was well separated from noise. The particle locations were then calculated from the intensity-weighted centroid of each particle in the binary mask. The instantaneous local particle number density was calculated by dividing each instantaneous image into an array of 21×21 pixel bins (corresponding to roughly $0.1D$), and then counting the number of particles within each bin.

2.5 Calibration

Calibration data was obtained by measuring the relationship between the gas temperature and the two-colour ratio S_{315}/S_{285} in the experimental system described above, except without the SSSTS beam or particles. Instead, the gas temperature was systematically varied over the range of $20\text{ }^\circ\text{C} < T_g < 160\text{ }^\circ\text{C}$ using an electric tape heater (Briskheat BWH052100LD) fitted to the outside of the central pipe. Thermocouples mounted to the central pipe and in the centre of the jet flow at $x/D < 0.5$ were used to measure the outlet temperature of the gas and ensure the system had reached a steady state before the LIF measurements were recorded. The thermocouple in the jet was removed prior to measurements to prevent interference and flow disturbances, and replaced after the measurement was completed to ensure there was no change in the flow temperature during the measurement. The time- and spatially-averaged two-colour ratio measured at each flow temperature in the region of $0.6 < x/D < 1$, $|r/D| < 0.2$, where the temperature of the flow was spatially uniform, was used to calibrate the two-colour ratio to the thermocouple measured temperature.

The resultant calibration curve relating gas temperature to S_{315}/S_{285} is presented in Figure 6, for gas temperatures in the range $20\text{ }^\circ\text{C} < T_g < 160\text{ }^\circ\text{C}$. The relationship between the intensity ratio of the two colours and the gas temperature is well described by a linear function of the form $S_{315}/S_{285} = 4.50 \times 10^{-3}T_g + 0.98$ ($R^2 = .9989$), for T_g in $^\circ\text{C}$. We emphasise here that the constants in this relationship is valid only for the particular optical system employed here, because the ratio depends on the combination of cameras, filters and collection optics. However, the form of the relationship is expected to be general. The signal intensity measured in the channel S_{315} can be seen to decrease from 4.89×10^4 to 1.02×10^4 counts for $T_g = 21$ and $160\text{ }^\circ\text{C}$ respectively, while the intensity of S_{285} decreases from 4.54×10^4 to 6.07×10^3 over the same range. This decrease in intensity is due to the decrease in fluorescence quantum yield of toluene with temperature [27], which leads to an increase in the uncertainty of the measurements with temperature. Nevertheless, for all temperatures recorded here, the fluorescence emission intensity measured in both channels remains significantly (> 65 times) larger than the background. Although the flow temperature in the measurement region is uniform, there is a small variation in the spatially averaged measurement of S_{315}/S_{285} as a result of camera shot noise, background scatter, electronic noise and sub-pixel misalignment of the two fluorescence images. The combined influence of these uncertainties leads to an image-to-image standard deviation of S_{315}/S_{285} of 1.2% at $21\text{ }^\circ\text{C}$ increasing to 2.4% at $160\text{ }^\circ\text{C}$, with the latter due to the strong decrease in fluorescence signal with

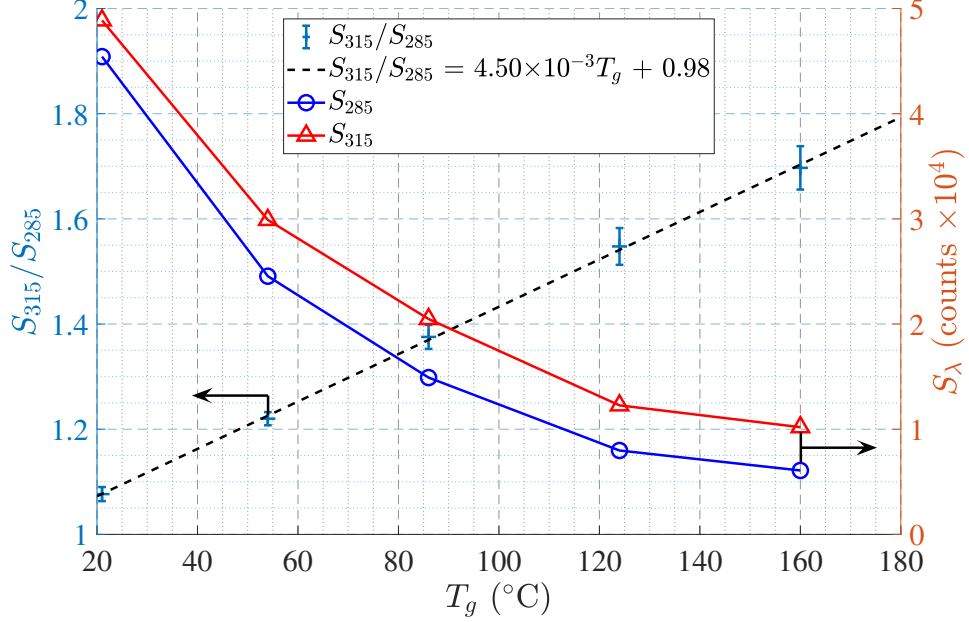


Figure 6: The relationship between gas temperature and S_{315}/S_{285} (×), together with a linear fit of the measured data (black dashed line). The error bars correspond to the image-to-image standard deviation in the measured ratio at each temperature. The dependence on temperature of the fluorescence intensity of S_{315} (Δ) and S_{285} (\circ) is also presented. For reference, the time- and spatially averaged dark charge signals measured in S_{285} and S_{315} were 90 and 92 counts, respectively.

temperature. This variation corresponds to an uncertainty of the spatially averaged measured temperature of 3 °C and 9 °C at flow temperatures of 21 °C and 160 °C respectively.

3 Results

3.1 Uncertainty analysis

3.1.1 Systematic errors

The accuracy of the current two-colour LIF measurements was estimated using images of the mean and instantaneous images of the unheated flow (i.e. a flow at uniform ambient temperature). Table 3 1 presents the results of a systematic study of the intensity recorded with each camera for a range

of cases with and without the presence of toluene, particles and laser beams in the measurement region. These measurements consist of the time- and spatially averaged intensity count, S_λ , in a 195×117 pixel region intersected by all lasers, i.e. the region $|r/D| < 0.3$ and $1 < x/D < 2$ (see also Figure 2), for the cases with and without the various lasers switched on. Cases 1-3 (rows 1-3) are for the flow without toluene with the conditions chosen to identify if scattering from particles or stray light is detected in any of the channels. Cases 4 and 5 have toluene seeded in the flow with the conditions chosen to identify whether or not the presence of the 532 and 910 nm lasers, with or without particles, affect the fluorescence signals, and also whether or not the fluorescence emissions generate significant interference to the S_{532} measurement. Case 1 presents the dark charge signal, here denoted as $S_{\lambda,DC}$. The signals measured with each camera for Cases 2 to 5 are normalised by $S_{\lambda,DC}$. The signal measured with S_{532} for the cases where the flow contains particles and with the 532 nm beam on (Cases 3 and 5) are not presented because the measurement is the spatial average of the scattering signal from disperse particles, which does not provide an accurate indication of the signal from individual particles. The results for each case are summarised below.

- The dark charge signals for each camera, presented in case 1 (row 1 in Table 2), were $S_{285,DC} = 90.1$ counts, $S_{315,DC} = 92.2$ counts and $S_{532,DC} = 398.9$ counts. Both S_{285} and S_{315} were recorded using 16-bit cameras, while S_{532} was recorded using a 14-bit camera.
- Case 2 presents the background noise, which is the measured signal with the lens uncapped and the diagnostic laser beams on with pulse energies identical to the main experiments but with no flow. It can be seen that this results in a 5% increase in S_{315} relative to the dark charge, but no significant increase for the other channels. This small increase in S_{315} is insignificant compared to the toluene signal (rows 4 and 5), which shows that ambient light and background laser light were effectively suppressed.
- For case 3 the diagnostic lasers and SSSTS beam were switched on with the particles seeded into the flow. It can be seen that no measurable increase is recorded for S_{285} or S_{315} , which shows that the elastic scattering of all laser wavelengths from particles was effectively suppressed by the optical filters used to form the LIF channels.
- For case 4 toluene was seeded in the flow with only the 266 nm laser switched on. It can be seen that the fluorescence emissions of toluene in this region were 349 and 378 times stronger than the dark charge

for S_{285} and S_{315} respectively. There was no increase in the signal for S_{532} , which demonstrates that the fluorescence emissions were effectively suppressed in this channel.

- Case 5 presents the signal from the flow with both toluene and particles seeded while the 266 nm and 532 nm lasers were switched on. The reduction in both S_{285} and S_{315} compared to case 4 is similar so that the resultant ratio $S_{315}/S_{285} = 1.133$ for case 5, which is only 2.2% greater than for case 4, with $S_{315}/S_{285} = 1.108$. This increase is a systematic error due to the interference of particles, through the combined effects of signal trapping, attenuation and multiple scattering. The resultant error in the temperature measurement is +5.5 °C at 28 °C and, assuming that this error is not strongly influenced by temperature, a +8 °C error at 150 °C.

Table 2: The conditions under which a series of experiments were performed to assess interference, measured by each camera in the imaged region aligned with the all lasers (S_λ). For the dark charge (row 1) the average intensity in counts (cts) is presented. The intensity is normalised by that of the dark charge for each other case. The 910 nm laser is the heating beam from the SSSTS. The data for S_{532} for the cases with both particles and the 532 nm laser are not presented (N.P.) because this method does not give a useful indication of the signal from individual particles.

Case	Toluene	Particles	266	Laser (nm)		910	S_{285} (cts)	S_{315} (cts)	S_{532} (cts)
				532	910				
1	No	No	No	No	No	No	90.1	92.2	398.9
2	No	No	Yes	Yes	No	No	$S_{285}/S_{285,DC}$ 1.01	$S_{315}/S_{315,DC}$ 1.05	$S_{532}/S_{532,DC}$ 1.00
3	No	Yes	Yes	Yes	Yes	Yes	1.00	1.00	N.P.
4	Yes	No	Yes	No	No	No	349	378	1.00
5	Yes	Yes	Yes	Yes	No	No	326	361	N.P.

3.1.2 Random errors

The random error in the intensity ratio S_{315}/S_{285} was estimated using the standard deviation of S_{315}/S_{285} (σ_R) in the ensemble of pixels within the region near to the jet exit of $0.5 < x/D < 0.7$ and $|r/D| < 0.1$. This region was chosen because the toluene concentration here is the highest in the flow and close to uniform, with the time-averaged fluorescence signal here $> 25,000$ counts for both S_{315} and S_{285} . For the unheated flow without particles (case 4 of Table 2) the standard deviation of the intensity ratio in this region was $\sigma_R = 0.088$, which corresponds to a standard deviation in the derived temperature of $\sigma_T = 21$ °C for a flow temperature of $T_g = 25$ °C. The standard deviation of the fluorescence signals measured in this region for S_{285} and S_{315} were $\sigma_{285} = 1,790$ counts and $\sigma_{315} = 1,970$ counts respectively. While these variations in the fluorescence signal are expected to decrease with the signal S_λ i.e. in regions with lower toluene concentration or at higher temperature, here we conservatively assume that σ_{285} and σ_{315} are constant for all fluorescence intensities. The lowest fluorescence signal measured for any heating flux in the region of $0.5 < x/D < 3.7$ and $|r/D| < 0.5$ is $S_{285} \approx 10,000$ counts, therefore the maximum relative standard deviations for the fluorescence channels are estimated to be $\sigma_{285}/S_{285} \approx 0.179$ and $\sigma_{315}/S_{315} \approx 0.197$. If the random noise is modelled a Gaussian distribution with standard deviation σ_λ for each channel, the maximum standard deviation of the temperature measurement can be numerically calculated to be $\sigma_T \approx 48$ °C for $T_g = 25$ °C and $\sigma_T \approx 94$ °C for $T_g = 150$ °C.

For the unheated flow with particles (case 5 of Table 2), the results show that the standard deviation of the measured intensity ratio in the region of $0.5 < x/D < 0.7$ and $|r/D| < 0.1$ increases slightly to $\sigma_R = 0.110$ ($\sigma_T = 24$ °C). The estimated maximum uncertainty, for the particle-laden flow with $S_{285} \approx 10,000$ counts, is $\sigma_T = 60$ °C for $T_g = 25$ °C and $\sigma_T = 118$ °C for $T_g = 150$ °C. While the uncertainties in the instantaneous pixel-to-pixel temperatures are relatively high, they are reduced significantly through time averaging. In the present experiments the time averaged data uses greater than 100 images for each case, and hence the uncertainty in the temperature reduces to $\sigma_{\bar{T}}/\sqrt{100} = 11.8$ °C.

3.2 Instantaneous temperature measurements

Figure 7 presents typical single-shot images of S_{285} and S_{315} , together with the temperature image and the binary particle mask from S_{532} , for three flow cases. One case without particles but with radiant heating (top row) and two cases with particles, one without (middle row) and the other with radiant

heating (bottom row). The heating flux was $\dot{Q}''_{peak} = 42.8 \text{ MW/m}^2$ for the cases with radiant heating while for the latter two cases the instantaneous particle volumetric loading was $\phi = 1.4 \times 10^{-3}$, which is sufficiently high for the particle-laden flow to be in the four-way coupling regime [4]. In this and subsequent figures the location and direction of the incident SSSTS beam are indicated by the dotted lines and arrowheads, with the SSSTS beam direction from the right to the left of the image (positive to negative r/D).

The fluorescence signal measured with the channels S_{285} and S_{315} is highly variable over the imaging region, due to the combined influences of variations in toluene concentration, laser fluence and temperature. The initial toluene concentration differs for the jet (0.75%) and the co-flow (0.25%), with inhomogeneity further increased downstream due to mixing in the shear layer and jet spreading. The local fluence of the 266 nm laser varies by approximately 25% in the axial direction due to the non-uniform laser sheet intensity profile. The fluence also decreases by approximately 20% across the jet along the excitation beam path length due to attenuation by the particles and absorption by the toluene. However, the spatial variations in the fluorescence signal due to the variations in toluene concentration and laser fluence are equal in both channels and are cancelled out in the two-colour ratio used to derive the temperature. This demonstrates the advantages of using the two-colour ratio method over seeking to deduce the temperature from a single wavelength. The emission intensity also decreases with increasing temperature, which can be seen in the images of S_{285} and S_{315} downstream from the heating region ($x/D > 0.9$). The intensity in this region is much lower for $\dot{Q}''_{peak} = 42.8 \text{ MW/m}^2$ than for $\dot{Q}''_{peak} = 0 \text{ MW/m}^2$ despite exhibiting a similar signal strength for $x/D < 0.9$.

The effect of attenuation of the excitation laser sheet by particles can be seen by comparing the fluorescence emission images in the top row of Figure 7, for which there are no particles in the flow, with the other two rows. The attenuation by the particles in the laser sheet can be seen to be significant from the horizontal streaks of low intensity (shadows), which occur down-beam from particles. The particles have a mean diameter of $173 \mu\text{m}$, which is about one quarter of the thickness of the laser sheet (approximately $600 \mu\text{m}$). This implies that the shadow down-beam from a single particle within the beam typically attenuates up to 25% of the laser excitation. However, even greater attenuation may be generated by the largest particles ($d_p \sim 300 \mu\text{m}$), agglomerated particles or by clusters of particles in close proximity. Circular regions of lower signal can also be seen, without a corresponding streak. These regions can be attributed to signal trapping by particles between the laser sheet and the collection optics, some of which result in strong attenuation of the fluorescence signal. These issues highlight

the importance of the present optical arrangement in which the use of the beam-splitter to separate the two channels means that both cameras collect signals from an identical optical path through the flow. In this way, effects such as signal trapping are the same in both channels and the temperature can still be measured. Nevertheless, the measurement uncertainty in these regions with attenuation is increased because of the reduction in the signal to noise ratio. Locations of both attenuation and signal trapping by the particles are identified in the bottom-left zoomed image of S_{285} in Figure 7.

For the case with particles in the flow and the heating laser operating at a flux of $\dot{Q}_{peak}'' = 42.8 \text{ MW/m}^2$, T_g can be seen to increase significantly with axial distance for $x/D > 1.5$. Most of the temperature rise can be seen to occur downstream from the region $0.9 < x/D < 1.9$ where the radiative heating is applied. No temperature gradients can be seen for the case with the heating laser on but without particles. This result is consistent with expectation, given that there is no significant absorption of the heating beam by the toluene or nitrogen. Instantaneous local temperatures of up to $150 \text{ }^\circ\text{C}$ are prevalent in the heated case, with these regions of high temperature corresponding to locations with high local particle number density. Importantly, significant inhomogeneity in the temperature immediately downstream from the heating region can be seen in the zoomed image with regions of T_g spanning the entire range from ambient to $150 \text{ }^\circ\text{C}$. This demonstrates that the time scale for the particles to transfer heat to the gas phase by convection is significantly longer than that required to heat the particles by radiation, as expected. Significant inhomogeneity in the gas-phase temperature persists even to the downstream edge of the image, $x/D = 3.5$, although it is somewhat reduced due to the influence of gas-phase mixing. These localised regions of high temperature remaining coherent downstream of the heating region indicates that the gas-phase heat transfer and/or mixing across the large flow length scales in the jet is relatively minor.

Random errors in the measurement can be seen in the temperature image for the case without heating, for which the flow is at uniform temperature. These measurement errors are most significant outside of the central jet flow ($|r/D| > 0.5$) because of the low fluorescence signal in the weakly seeded annular flow. The measured temperature is of less interest in this region than for the central jet flow because there are few, if any, particles present. In the central jet flow for the case without heating but with particles, the standard deviation of the measured temperature in the ensemble of pixels bounded by the region of $0.5 < x/D < 3.7$ and $|r/D| < 0.5$ was $\sigma_T = 17.8 \text{ }^\circ\text{C}$.

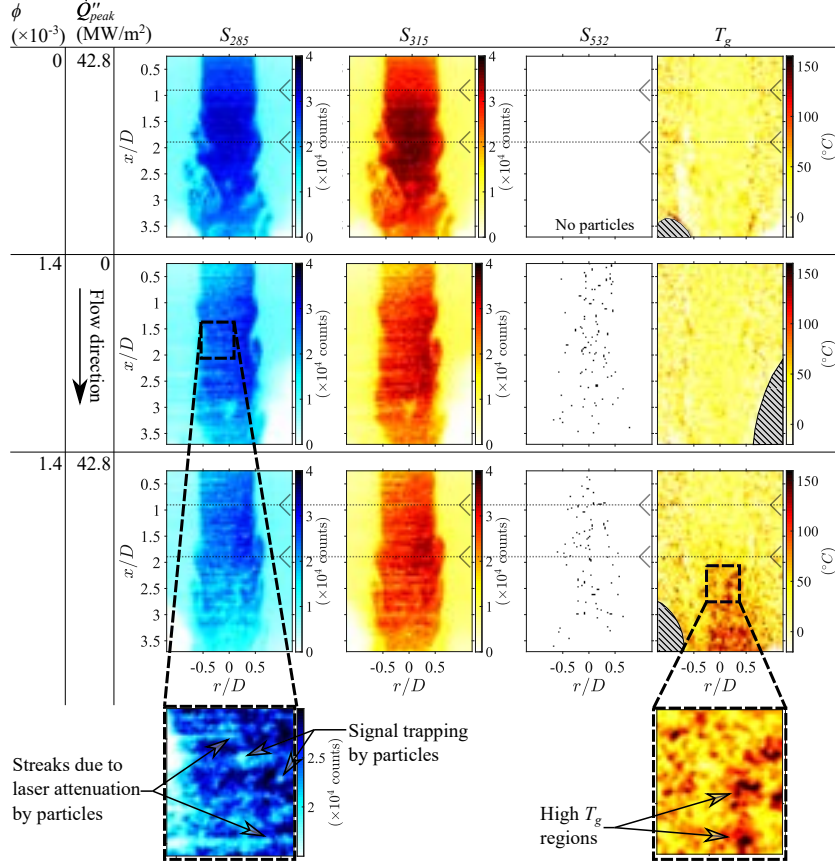


Figure 7: Typical single-shot images from each camera and the resultant temperature calculated from S_{315}/S_{285} . The top row has an instantaneous particle loading of $\phi = 0$ and a heating flux of $\dot{Q}''_{peak} = 42.8 \text{ MW/m}^2$. The middle and bottom rows have an instantaneous loading of $\phi = 1.4 \times 10^{-3}$ with $\dot{Q}''_{peak} = 0$ and 42.8 MW/m^2 respectively. The dotted lines indicate the location and direction of the SSSTS beam. The zoomed insets show interesting features of laser attenuation and signal trapping due to particles in the fluorescence channels (left, noting the colour scale is different to the main figure to improve the clarity of the features), as well as highly localised regions of high temperature that are present for $\dot{Q}''_{peak} = 42.8 \text{ MW/m}^2$ (right). The cross-hatched areas correspond to regions where the signal from one or both of S_{285} and S_{315} are below the minimum threshold for reliable measurements.

3.3 Time averaged results

Figure 8 presents the time-averaged images of gas-phase temperature above ambient $\bar{T}_g - T_a$, where the overbar denotes time-averaged values, for a series of cases with the particle-laden jet heated by the SSSTS at fluxes of $\dot{Q}_{peak}'' = 0, 13.7, 29.4, 36.3$ and 42.8 MW/m². The time-averaged particle volumetric loading for each case presented was $\bar{\phi} = 1.4 \times 10^{-3}$. It can be seen that the gas temperature is uniform across the jet in the region upstream of the SSSTS beam, i.e. for $x/D < 0.9$, in all cases. The temperature rise within the zone of irradiation is small, but becomes significant and continues to increase both with axial distance and heating flux. This lag can be attributed to the combination of two time constants, firstly, of the particles to reach their peak temperature whilst being heated by the SSSTS and, secondly, the convective heat transfer between the particles and gas. The gas temperature can be seen to increase with axial distance to the edge of the measurement region, which indicates that the particles are significantly hotter than the gas all the way to $x/D = 3.7$. Indeed, this also suggests that the gas temperature continues to rise beyond the measurement region investigated here.

The gas temperature is found to be non-uniform in the radial direction, with a maximum near to the centreline and with a higher average temperature measured for $r/D > 0$ than for $r/D < 0$. The gradients away from the axis can be attributed to shear-driven mixing with the ambient co-flow surrounding the jet, which is consistent with well-known trends in scalar mixing in jets [34]. However, radial gradients in particle concentration may also play a role [28]. The trend of lower temperatures on the down-beam side of the SSSTS can be attributed to shadowing effects, where the particles nearer the radiation source are subject to a higher flux than those behind. The greatest value of $\bar{T}_g - T_a$ was 86.1 °C, which occurs for the peak flux of $\dot{Q}_{peak}'' = 42.8$ MW/m², at the location $x/D = 3.69$, $r/D = 0.11$. The off-axis location of the peak temperature (i.e. $r/D = 0.11$) found here is consistent with the influence of particle attenuation that can be seen in Figure 7. The temperatures for the other heating fluxes at $x/D = 3.69$ and $r/D = 0.11$ were measured to be $\bar{T}_g - T_a = 62.1, 50.8$ and 25.8 °C for $\dot{Q}_{peak}'' = 36.3, 29.4$ and 13.7 MW/m² respectively.

Figure 9 presents the change in power from the SSSTS due to attenuation by the particles $\Delta\dot{Q} = \dot{Q}_0 - \dot{Q}_p$, where \dot{Q}_0 and \dot{Q}_p are the time-averaged powers recorded using the power meter down-beam of the wind tunnel for $\bar{\phi} = 0$ and 1.4×10^{-3} respectively. It can be seen that $\Delta\dot{Q}$ increases linearly with \dot{Q}_0 , as expected. The presented values of $\dot{Q}_0 = 910, 1950, 2410$ and 2840 W correspond to peak heating fluxes of $\dot{Q}_{peak}'' = 13.7, 29.4, 36.3$ and 42.8 MW/m² respectively. The fraction of the beam power attenuated by the

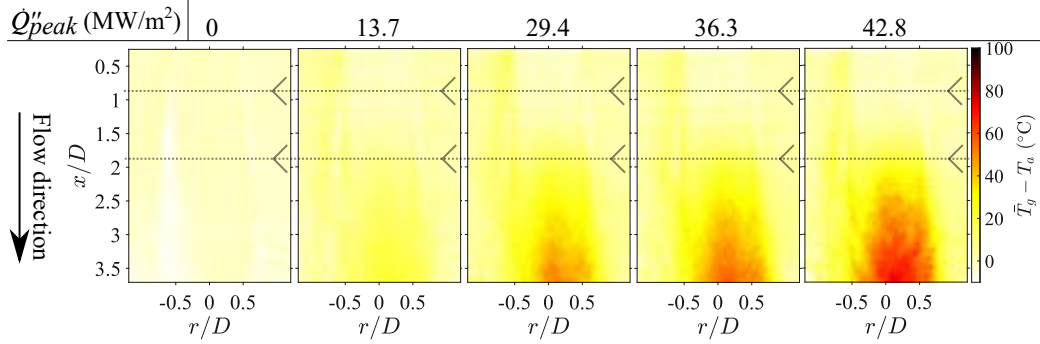


Figure 8: Time-averaged images of gas temperature above ambient, $\bar{T}_g - T_a$, for a mean particle loading of $\bar{\phi} = 1.4 \times 10^{-3}$ at a series of heating fluxes, \dot{Q}_{peak}'' . The dotted lines indicate the location and direction of the SSSTS beam.

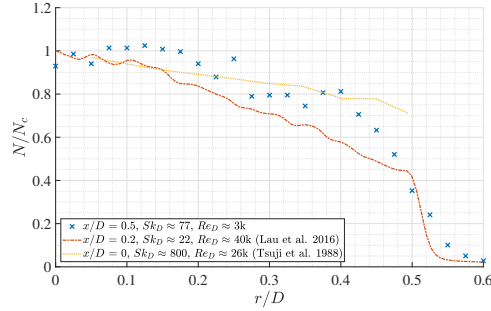
particles, $\Delta\dot{Q}/\dot{Q}_0$, is presented in the inset of Figure 9. It can be seen that $\Delta\dot{Q}/\dot{Q}_0$ increases from 0.17 to 0.21 as \dot{Q}_0 is increased from 910 W to 2840 W. A possible reason for this is the influence of temperature on the absorption cross section of the particles, which has been previously demonstrated by Zhao et al. [35] albeit with different particle materials.

The predicted attenuation of a beam through a particle-laden flow can be estimated using the Beer-Lambert law, given by $\Delta\dot{Q}/\dot{Q}_0 = 1 - \exp\left(-\frac{A_{p,1}l\bar{\phi}}{V_{p,1}}\right)$, where $A_{p,1}$ and $V_{p,1}$ are the projected area and volume of a single particle, respectively, and l is the path length of the beam through the flow [14]. For a path length corresponding to the inner diameter of the pipe, $l = D = 12.6$ mm, a particle volumetric loading of $\bar{\phi} = 1.4 \times 10^{-3}$ and assuming the particles are spherical with a diameter distribution corresponding to that presented in Figure 3, the attenuation is estimated to be $\Delta\dot{Q}/\dot{Q}_0 = 0.156$. This is slightly lower than the measured $\Delta\dot{Q}/\dot{Q}_0$, although this simplified prediction does not take into account the non-uniform heating laser profile. Despite these assumptions the calculated value is sufficiently close to the measurement to provide further confidence in the measured values of $\Delta\dot{Q}/\dot{Q}_0$.

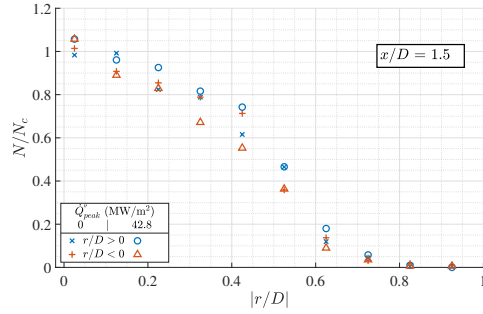
also observed at $x/D = 1.5$ (which is near to the centre of the heating region) although the jet has spread slightly such that N/N_c approaches zero at $r/D \approx 0.8$. The particles being predominantly concentrated near to the jet axis is consistent with the temperature measurements (Figure 8), which also shows that the gas temperature approaches a local maximum near to the jet axis. The radial profiles of N/N_c are similar for both $r/D < 0$ and $r/D > 0$, demonstrating that the particle number density is symmetrical about the jet axis despite the radial asymmetry that can be seen in the temperature images (Figure 8). This shows that the radial bias for the temperature measurements is not due to a similar bias in the particle concentrations. The results also show that the radial particle number density profile is broader at $x/D = 3$ than for $x/D = 1.5$, and that the profile transitions toward shallower gradients consistent with well-known jet spreading trends in single- and two-phase jets. Importantly, the radial number density profiles do not change significantly with heating flux within the axial range investigated here, which implies that neither heating-induced buoyancy nor heating-induced turbulence have any significant influence on lateral migration for these particles within this region.

The profiles of the measured temperature above ambient, $\bar{T}_g - T_a$, on the jet centreline for $0 < \dot{Q}''_{peak} < 42.8 \text{ MW/m}^2$, with a fixed particle loading of $\bar{\phi} = 1.4 \times 10^{-3}$, are presented in Figure 11. Also presented is the temperature change normalised by the heating flux, $(\bar{T}_g - T_a)/\dot{Q}''_{peak}$. The shaded area of the figure indicates the location and intensity of the heating beam. The results show that the gas temperature remains close to the ambient ($\bar{T}_g - T_a \approx 0$) both upstream from and within the beginning of the region with the heating laser, i.e. for $x/D < 1.1$, for all heat fluxes. Downstream from this, \bar{T}_g increases monotonically within the measurement region for all $\dot{Q}''_{peak} > 0 \text{ MW/m}^2$, due to the heat transfer from the heated particles to the gas. It should also be noted that the high-flux radiation from the SSSTS is in the region $0.9 < x/D < 1.9$, with the peak flux at $1.24 < x/D < 1.56$ (see also the profile presented in Figure 4). Thus there is a slight lag of approximately $0.2D$ between the initial radiation absorption and an observable increase of \bar{T}_g . Importantly, the normalised data, presented in the inset, show excellent collapse giving strong confidence in the measured results.

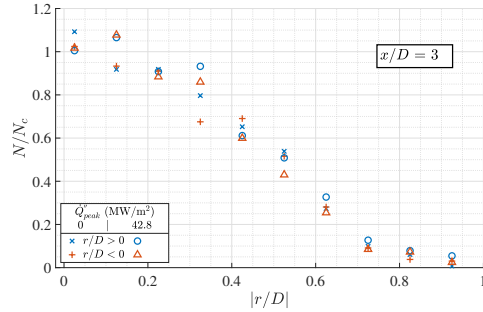
Figure 11 also shows that the rate of temperature rise increases with \dot{Q}''_{peak} , as expected, and that the temperature continues to increase near-linearly with axial distance downstream of the heating beam to the edge of the measurement region ($1.9 < x/D < 3.7$). This suggests that the gas temperature will continue to increase for some distance downstream since the temperature gradient will approach zero when its temperature equilib-



(a)



(b)



(c)

Figure 10: Radial particle number density, N , normalised by the centreline value, N_c , measured from particle scattering images recorded simultaneously with the fluorescence images. The top sub-figure presents the radial profile near to the jet exit for the current experiments along with the particle concentration measured by Tsuji et al. [36] and Lau and Nathan [28] in a particle-laden pipe jet. The bottom two sub-figures present the radial profiles measured at $x/D = 1.5$ (middle) and $x/D = 3$ (bottom), $r/D < 0$ and $r/D > 0$, for a mean particle loading of $\bar{\phi} = 1.4 \times 10^{-3}$, and for $\dot{Q}_{peak}'' = 0$ and 42.8 MW/m^2 .

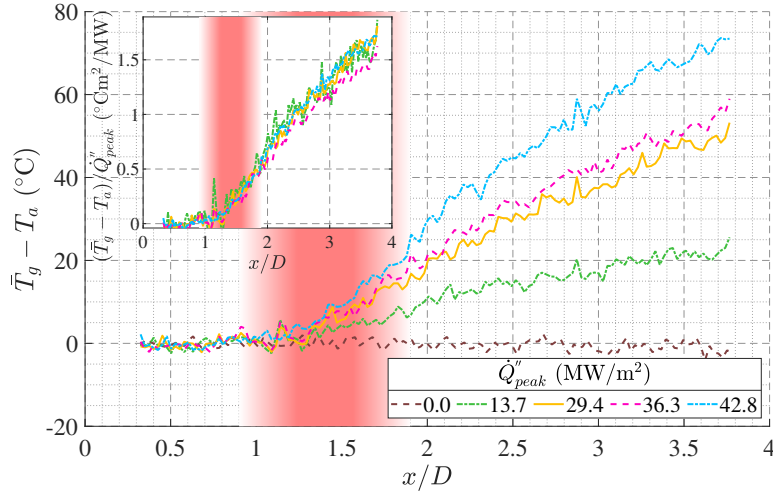


Figure 11: The measured gas temperature above ambient against axial distance on the jet centreline for a series of heating fluxes, with a mean volumetric loading of $\bar{\phi} = 1.4 \times 10^{-3}$ along with the centreline temperature normalised by the heating flux in the inset figure. The shaded areas indicate the SSSTS beam location and intensity.

rates that of the particles. These measurements are also consistent with the expectation that the particles have a higher temperature than the average gas temperature throughout the region for all heating fluxes, owing to the radiation being absorbed by the particles and transferred to the gas.

Near to the downstream end of the measurement region, at $x/D = 3.5$ (which is 32.8 mm from the upstream edge of the heating region), $\bar{T}_g - T_a = 67.7$ °C for $\dot{Q}''_{peak} = 42.8$ MW/m². At this axial location, $\bar{T}_g - T_a = 57.0$, 48.7 and 22.4 °C for $\dot{Q}''_{peak} = 36.3$, 29.4 and 13.7 MW/m² respectively. The normalised temperature curves presented in the inset of Figure 11 confirm the linear relationship between gas temperature rise and the heat gain of the particle phase by radiation absorption (i.e. $\Delta T_g \propto T_p - T_g$, where T_p is the particle temperature), since $T_p - T_a \propto \dot{Q}''_{peak}$. This is consistent with convection being the dominant mode of heat transfer between the heated particles and the gas and also implies that radiant cooling of the particles is negligible. That is, particle temperatures are not sufficiently high for radiation to be significant, consistent with the maximum value of $\bar{T}_g - T_a$ being 67.7 °C.

The rate of change of the centreline temperature with axial distance ($d\bar{T}_g/dx$), averaged over two separate regions of $1 < x/D < 2$ and $2 < x/D < 3$, are presented in Figure 12 for all fluxes. The region centred at

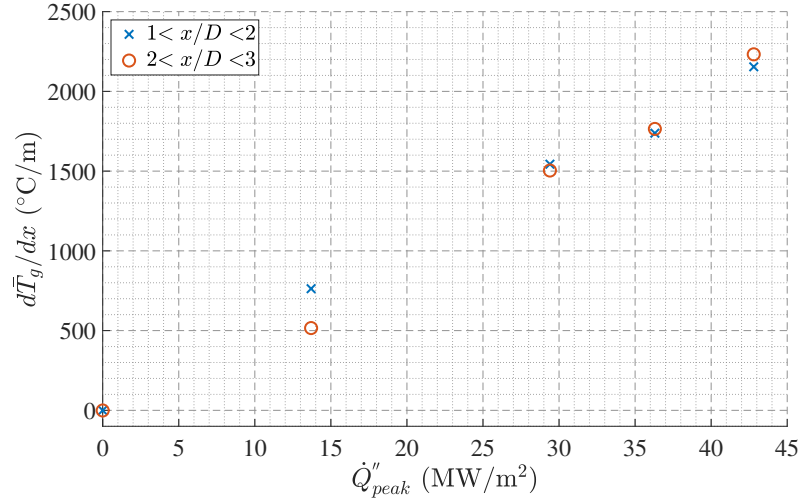
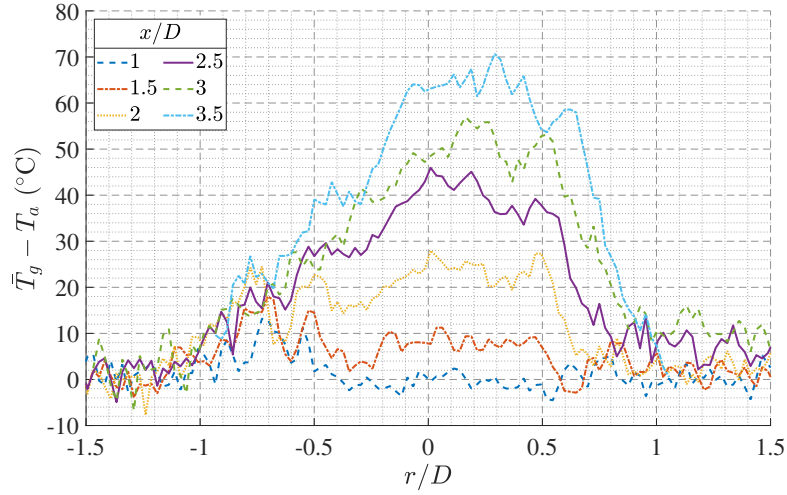


Figure 12: The measured axial temperature gradient as a function of radiation heat flux within two axial regions of the flow, $1 < x/D < 2$ and $2 < x/D < 3$.

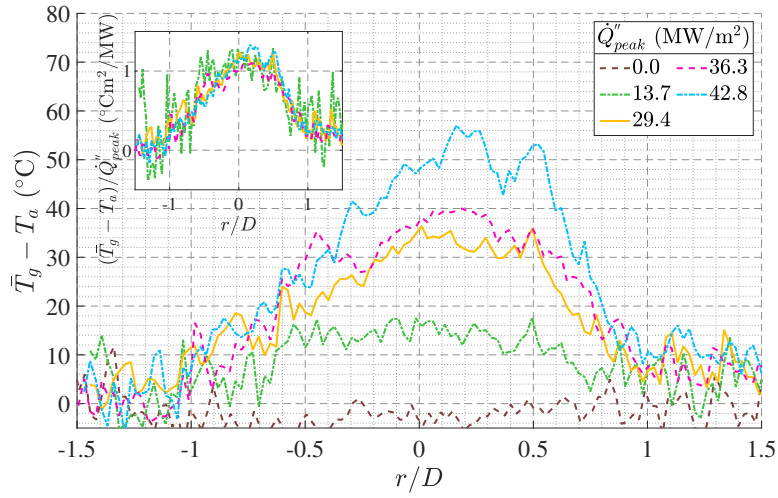
$x/D = 1.5$ is mostly comprised of the heating region, while the region centred at $x/D = 2.5$ has no radiative heat input. The rate $d\bar{T}_g/dx$ increases monotonically with \dot{Q}''_{peak} and is similar for both axial locations. The greatest measured rate of temperature increase was $d\bar{T}_g/dx = 2,200$ °C/m for $\dot{Q}''_{peak} = 42.8$ MW/m². Assuming a constant gas velocity in this region of 3.6 m/s (from the bulk velocity), the corresponding rate of gas temperature increase at this flux is approximately 8,000 °C/s. This is comparable to the particle temperature gain, for a different particle material and diameter, measured under similar conditions of 23,000 °C/s [8].

The radial profiles of mean (time-averaged) temperature above ambient, $\bar{T}_g - T_a$, at a series of axial distances for $\dot{Q}''_{peak} = 42.8$ MW/m² (top) and for a series of heating fluxes at $x/D = 3$ (bottom) are presented in Figure 13. The inset of the bottom sub-figure presents the temperature above ambient normalised by the heating flux. From both sub-figures it can be seen that the radial bias in temperature is consistent with the direction of the incident SSSTS beam, which is from positive r/D to negative (right to left in the figure). This confirms the significant role of attenuation of the SSSTS beam at the particle loading used in the current experiment ($\bar{\phi} = 1.4 \times 10^{-3}$). The resultant temperature is significantly different for $r/D = 0.4$ and $r/D = -0.4$, with $\bar{T}_g - T_a = 70.7$ °C and 38.0 °C respectively at $x/D = 3.5$ for $\dot{Q}''_{peak} = 42.8$ MW/m². The temperature for $r/D > 0$ continues to increase with x/D throughout the measurement region, while for $r/D < -0.3$ there

is little change from $x/D = 3$ to $x/D = 3.5$. The radial temperature profiles normalised by heating flux also collapse well here, which is consistent with the centreline temperature profiles in Figure 11.



(a)



(b)

Figure 13: Measured time-averaged radial profiles of gas temperature above ambient for a range of axial distances with $\dot{Q}''_{peak} = 42.8 \text{ MW/m}^2$ (top) and for all heat fluxes analysed at $x/D = 3$ (bottom). The inset of the bottom sub-figure presents the temperature above ambient normalised by the heating flux for the same conditions in the bottom sub-figure.

4 Conclusions

A spatially resolved, planar measurement of the instantaneous gas-phase temperature, together with the particle number density, has been demonstrated using two-colour laser induced fluorescence and Mie scattering within a particle-laden jet flow heated using high-flux radiation, for a series of heating fluxes up to $\dot{Q}''_{peak} = 42.8 \text{ MW/m}^2$. The elastically scattered laser light from the particles, which were seeded at a sufficiently high loading for the flow to be in the four-way coupling regime, was shown to be effectively suppressed by the optical filters for each of the two-colour LIF channels. The signal-to-noise ratio of the fluorescence emissions for the flow without particles was measured to be ≥ 349 for both channels, giving confidence in the method. For the case with particles in the flow and radiative heating the fluorescence signal could be seen to decrease by $< 7\%$, which was attributed to a combination of the decrease in fluorescence quantum yield of toluene with temperature, the attenuation of the excitation laser and signal trapping by particles. For a typical instantaneous image the two-colour LIF method was found to have a pixel-to-pixel standard deviation, for an isothermal flow with the particles seeded at $\bar{\phi} = 1.4 \times 10^{-3}$, of $17.8 \text{ }^\circ\text{C}$, despite the significant fluctuations in the fluorescence signal due to mixing of the flow, laser attenuation and signal trapping. This demonstrates the advantage of the two-colour method for such applications in that the dependence of temperature on the ratio of two wavelengths results in the effects of attenuation being cancelled out, provided that the two wavelengths are collected from a common optical path.

For the present system, with particles of mean diameter $173 \text{ } \mu\text{m}$ and a bulk flow velocity of 3.6 m/s , instantaneous gas temperatures of up to $125 \text{ }^\circ\text{C}$ above ambient were measured locally for a peak heating flux of $\dot{Q}''_{peak} = 42.8 \text{ MW/m}^2$ irradiating a transverse region of approximately 11 mm in diameter. These peak temperatures were found to occur in highly localised regions where the local particle volumetric loading was also simultaneously high. The time-averaged temperature was found to increase linearly with both heating flux and distance downstream from the heating region, with the gas temperature continuing to increase to the end of the measurement domain. A mean temperature increase of $67.7 \text{ }^\circ\text{C}$ above ambient was measured on the jet centreline at $x/D = 3.5$ (which is 32.8 mm downstream from the start of the heating region), also for $\dot{Q}''_{peak} = 42.8 \text{ MW/m}^2$. This corresponds to an average heating rate of approximately $2,200 \text{ }^\circ\text{C/m}$ for the gas.

The derived temperature images were found to provide several new insights into the heat transfer processes that occur in particle-laden flows subjected to high-flux radiation. The localised regions of high temperature could

be seen to remain coherent well downstream of the heating region, indicating that there is relatively little gas-phase heat transfer and mixing across length scales within the measurement region associated with large-scale turbulence. The temperature of the gas was also found to be higher on the side of the jet closest to the radiative heating source, which can be attributed to the heating beam being absorbed and/or scattered by the particles, consistent with expectation. It was also found that the particle number density was not significantly influenced by the presence of high flux radiative heating, within the measurement region investigated for heat fluxes up to $\dot{Q}_{peak}'' = 42.8 \text{ MW/m}^2$. This suggests that any effects of buoyancy-induced acceleration are small for the conditions investigated here.

References

- [1] F. Miller and R. Koenigsdorff. “Theoretical analysis of a high-temperature small-particle solar receiver”. In: *Solar Energy Materials* 24.1 (1991), pp. 210–221.
- [2] H. Watanabe, R. Kurose, S. Komori and H. Pitsch. “Effects of radiation on spray flame characteristics and soot formation”. In: *Combustion and Flame* 152.1 (2008), pp. 2–13.
- [3] T. C. W. Lau, J. H. Frank and G. J. Nathan. “Resolving the three-dimensional structure of particles that are aerodynamically clustered by a turbulent flow”. In: *Physics of Fluids* 31.7 (2019), p. 071702.
- [4] S. Elgobashi. “An Updated Classification Map of Particle-Laden Turbulent Flows”. In: *IUTAM Symposium on Computational Approaches to Multiphase Flow: Proceedings of an IUTAM Symposium held at Argonne National Laboratory, October 4–7, 2004*. Ed. by S. Balachandar and A. Prosperetti. Dordrecht: Springer Netherlands, 2006, pp. 3–10.
- [5] T. C. W. Lau and G. J. Nathan. “Influence of Stokes number on the velocity and concentration distributions in particle-laden jets”. In: *Journal of Fluid Mechanics* 757 (2014), pp. 432–457.
- [6] C. Abram, B. Fond and F. Beyrau. “Temperature measurement techniques for gas and liquid flows using thermographic phosphor tracer particles”. In: *Progress in Energy and Combustion Science* 64 (2017), pp. 93–156.

- [7] C. Jainski, L. Lu, V. Sick and A. Dreizler. “Laser imaging investigation of transient heat transfer processes in turbulent nitrogen jets impinging on a heated wall”. In: *International Journal of Heat and Mass Transfer* 74.Supplement C (2014), pp. 101–112.
- [8] K. C. Y. Kueh, T. C. W. Lau, G. J. Nathan and Z. T. Alwahabi. “Single-shot planar temperature imaging of radiatively heated fluidized particles”. In: *Optics Express* 25.23 (2017), pp. 28764–28775.
- [9] H. Chen, Y. Chen, H.-T. Hsieh and N. Siegel. “Computational Fluid Dynamics Modeling of Gas-Particle Flow Within a Solid-Particle Solar Receiver”. In: *Journal of Solar Energy Engineering* 129.2 (2006), pp. 160–170.
- [10] G. Evans, W. Houf, R. Greif and C. Crowe. “Gas-Particle Flow Within a High Temperature Solar Cavity Receiver Including Radiation Heat Transfer”. In: *Journal of Solar Energy Engineering* 109.2 (1987), pp. 134–142.
- [11] H. Pouransari and A. Mani. “Effects of Preferential Concentration on Heat Transfer in Particle-Based Solar Receivers”. In: *Journal of Solar Energy Engineering* 139.2 (2016), pp. 021008–021008–11.
- [12] R. Zamansky, F. Coletti, M. Massot and A. Mani. “Radiation induces turbulence in particle-laden fluids”. In: *Physics of Fluids* 26.7 (2014), p. 071701.
- [13] A. Frankel, H. Pouransari, F. Coletti and A. Mani. “Settling of heated particles in homogeneous turbulence”. In: *Journal of Fluid Mechanics* 792 (2016), pp. 869–893.
- [14] P. A. M. Kalt, C. H. Birzer and G. J. Nathan. “Corrections to facilitate planar imaging of particle concentration in particle-laden flows using Mie scattering, Part 1: Collimated laser sheets”. In: *Applied Optics* 46.23 (2007), pp. 5823–5834.
- [15] E. Berrocal, E. Kristensson, M. Richter, M. Linne and M. Aldén. “Application of structured illumination for multiple scattering suppression in planar laser imaging of dense sprays”. In: *Optics Express* 16.22 (2008), pp. 17870–17881.
- [16] E. W. Lewis, T. C. W. Lau, Z. Sun, Z. T. Alwahabi and G. J. Nathan. “Luminescence interference to two-colour toluene laser-induced fluorescence thermometry in a particle-laden flow”. In: *Experiments in Fluids* 61.4 (2020), p. 101.

- [17] N. Siegel, C. Ho, S. S. Khalsa and G. Kolb. “Development and Evaluation of a Prototype Solid Particle Receiver: On-Sun Testing and Model Validation”. In: *Journal Of Solar Energy Engineering-Transactions Of The Asme* 132.2 (2010).
- [18] D. Davis, F. Muller, W. Saw, A. Steinfeld and G. Nathan. “Solar-driven alumina calcination for CO₂ mitigation and improved product quality”. In: *Green Chem.* 19.13 (2017), pp. 2992–3005.
- [19] A. J. Banko, L. Villafaña, J. H. Kim and J. K. Eaton. “Temperature statistics in a radiatively heated particle-laden turbulent square duct flow”. In: *International Journal of Heat and Fluid Flow* 84 (2020), p. 108618.
- [20] K. C. Y. Kueh, T. C. W. Lau, G. J. Nathan and Z. T. Alwahabi. “Non-intrusive temperature measurement of particles in a fluidised bed heated by well-characterised radiation”. In: *International Journal of Multiphase Flow* 100 (2018), pp. 186–195.
- [21] R. B. Miles, W. R. Lempert and J. N. Forkey. “Laser Rayleigh scattering”. In: *Measurement Science and Technology* 12.5 (2001), R33–R51.
- [22] C. Schulz and V. Sick. “Tracer-LIF diagnostics: quantitative measurement of fuel concentration, temperature and fuel/air ratio in practical combustion systems”. In: *Progress in Energy and Combustion Science* 31.1 (2005), pp. 75–121.
- [23] G. Tea, G. Bruneaux, J. T. Kashdan and C. Schulz. “Unburned gas temperature measurements in a surrogate Diesel jet via two-color toluene-LIF imaging”. In: *Proceedings of the Combustion Institute* 33.1 (2011), pp. 783–790.
- [24] M. Cundy, P. Trunk, A. Dreizler and V. Sick. “Gas-phase toluene LIF temperature imaging near surfaces at 10 kHz”. In: *Experiments in Fluids* 51.5 (2011), pp. 1169–1176.
- [25] V. A. Miller, M. Gamba, M. G. Mungal and R. K. Hanson. “Single- and dual-band collection toluene PLIF thermometry in supersonic flows”. In: *Experiments in Fluids* 54.6 (2013), p. 1539.
- [26] S. Faust, M. Goschütz, S. A. Kaiser, T. Dreier and C. Schulz. “A comparison of selected organic tracers for quantitative scalar imaging in the gas phase via laser-induced fluorescence”. In: *Applied Physics B* 117.1 (2014), pp. 183–194.

- [27] W. Koban, J. D. Koch, R. K. Hanson and C. Schulz. “Absorption and fluorescence of toluene vapor at elevated temperatures”. In: *Physical Chemistry Chemical Physics* 6.11 (2004), pp. 2940–2945.
- [28] T. C. W. Lau and G. J. Nathan. “The effect of Stokes number on particle velocity and concentration distributions in a well-characterised, turbulent, co-flowing two-phase jet”. In: *Journal of Fluid Mechanics* 809 (2016), pp. 72–110.
- [29] W. Koban, J. D. Koch, R. K. Hanson and C. Schulz. “Oxygen quenching of toluene fluorescence at elevated temperatures”. In: *Applied Physics B* 80.6 (2005), pp. 777–784.
- [30] J. K. Eaton and J. R. Fessler. “Preferential concentration of particles by turbulence”. In: *International Journal of Multiphase Flow* 20 (1994), pp. 169–209.
- [31] Z. T. Alwahabi, K. C. Y. Kueh, G. J. Nathan and S. Cannon. “Novel solid-state solar thermal simulator supplying 30,000 suns by a fibre optical probe”. In: *Optics Express* 24.22 (2016), A1444–A1453.
- [32] Asahi Spectra USA Inc. Web Page. 2018.
- [33] Semrock. Web Page. 2018.
- [34] J. Mi, D. S. Nobes and G. J. Nathan. “Influence of jet exit conditions on the passive scalar field of an axisymmetric free jet”. In: *Journal of Fluid Mechanics* 432 (2001), pp. 91–125.
- [35] W. Zhao, Z. Sun and Z. T. Alwahabi. “Emissivity and absorption function measurements of Al₂O₃ and SiC particles at elevated temperature for the utilization in concentrated solar receivers”. In: *Solar Energy* 207 (2020), pp. 183–191.
- [36] Y. Tsuji, Y. Morikawa, T. Tanaka, K. Karimine and S. Nishida. “Measurement of an axisymmetric jet laden with coarse particles”. In: *International Journal of Multiphase Flow* 14.5 (1988), pp. 565–574.

Appendix E

Paper III - The effect of particle size and volumetric loading on the gas temperature distributions in a particle-laden flow heated with high-flux radiation

This chapter presents the published journal article:

Lewis, E. W., Lau, T. C. W., Sun, Z., Alwahabi, Z. T. and Nathan, G. J., (2022), "The effect of particle size and volumetric loading on the gas temperature distributions in a particle-laden flow heated with high-flux radiation", *International Journal of Heat and Mass Transfer* 182.

The article in its published format is available at:

<https://doi.org/10.1016/j.ijheatmasstransfer.2021.122041>.

The content of this chapter is identical to that of the published article, with the following exceptions:

1. The typesetting and referencing style may have been altered for consistency within the thesis.
2. The position and sizing of the figures and tables may differ.

Statement of Authorship

Title of Paper	Insights from a new method providing single-shot, planar measurement of gas-phase temperature in particle-laden flows under high-flux radiation
Publication Status	<input checked="" type="checkbox"/> Published <input type="checkbox"/> Accepted for Publication <input type="checkbox"/> Submitted for Publication <input type="checkbox"/> Unpublished and Unsubmitted work written in manuscript style
Publication Details	Lewis, E. W., Lau, T. C. W., Sun, Z., Alwahabi, Z. T. and Nathan, G. J. (2022), "The effect of particle size and volumetric loading on the gas temperature distributions in a particle-laden flow heated with high-flux radiation", International Journal of Heat and Mass Transfer 182.

Principal Author

Name of Principal Author (Candidate)	Elliott W. Lewis		
Contribution to the Paper	Designed experimental arrangement and undertook experiments, developed data processing methods, interpreted data, wrote manuscript.		
Overall percentage (%)	70		
Certification:	This paper reports on original research I conducted during the period of my Higher Degree by Research candidature and is not subject to any obligations or contractual agreements with a third party that would constrain its inclusion in this thesis. I am the primary author of this paper.		
Signature		Date	1/11/2021

Co-Author Contributions

By signing the Statement of Authorship, each author certifies that:

- i. the candidate's stated contribution to the publication is accurate (as detailed above);
- ii. permission is granted for the candidate to include the publication in the thesis; and
- iii. the sum of all co-author contributions is equal to 100% less the candidate's stated contribution.

Name of Co-Author	Timothy C. W. Lau		
Contribution to the Paper	Co-supervised experimental design, assisted with data analysis, edited the manuscript.		
Signature		Date	1/11/2021

Name of Co-Author	Zhiwei Sun		
Contribution to the Paper	Supervised the experimental setup and data collection, assisted with interpretation of data, and edited the manuscript.		
Signature		Date	1/11/2021

Name of Co-Author	Zeyad T. Alwahabi		
Contribution to the Paper	Designed research concept, co-supervised experimental work and data interpretation.		
Signature		Date	

Name of Co-Author	Graham J. Nathan		
Contribution to the Paper	Co-supervised experimental design, assisted with the interpretation of results and edited the manuscript.		
Signature		Date	9/11/2021

The effect of particle size and volumetric loading on the gas temperature distributions in a particle-laden flow heated with high-flux radiation

Elliott W. Lewis^{1,3}, Timothy C. W. Lau^{1,3,4}, Zhiwei Sun^{1,3},
Zeyad T. Alwahabi^{2,3}, and Graham J. Nathan^{1,3}

¹*School of Mechanical Engineering, University of Adelaide, Australia*

²*School of Chemical Engineering and Advanced Materials, University of Adelaide, Australia*

³*Centre for Energy Technology, University of Adelaide, Australia*

⁴*UniSA STEM, University of South Australia, Australia*

Abstract

The instantaneous, spatially resolved gas-phase temperature distribution within a particle-laden flow heated using high-flux radiation has been measured for a series of heating fluxes, particle volumetric loadings and particle diameters using two-colour laser induced fluorescence of toluene. The temperature of the gas downstream from the start of the heating region was found to increase with an increase in heat flux, an increase in particle loading and a decrease in particle diameter. Coherent regions of high and low temperature in the instantaneous flow associated with spatial variations in the particle distribution were identified for all particle diameters investigated. The time-averaged gas-phase temperature on the jet axis was found to increase approximately linearly with distance in the region downstream from the heating beam to the edge of the measurement region investigated, indicating near-constant convective heat transfer due to the large temperature difference between the gas and radiatively heated particles throughout this region. The axial gradient of gas-phase temperature with distance was also calculated using a simplified, one-dimensional heat transfer model. The difference between the model and measurements was, on average, less than 20%, with the magnitude of this difference found

to increase with a decrease in particle diameter and an increase in particle loading.

1 Introduction

Non-isothermal, high temperature particle-laden flows with strong radiative heat transfer remain poorly understood despite being widely utilised in industrial processes, such as the calcination of alumina in fluid-flash calciners [1] and the decomposition of calcium carbonate in kilns [2]. These processes often require temperatures in excess of 1000 °C for efficient operation, with the flow historically heated by the combustion of fossil fuels. Low-carbon energy sources that have been identified as potential alternatives include hydrogen, electricity and concentrated sunlight [3], with particle-based concentrated solar thermal (CST) receivers showing great potential for long-term operation at the required temperatures [4]. Laboratory-scale CST receivers have also been demonstrated to be functional and technically feasible for the processing of a range of minerals [5–7]. However, there is currently a lack of understanding of the heat transfer processes and particle-fluid interactions within these particle-laden flows. This hinders the rate of development of both new mineral processing and particle-based solar technologies. Therefore, systematic measurements of the key controlling parameters within these systems are required to optimise efficiencies and lower the risk of uptake for industrial applications.

The volumetric distributions of particles and the flow fields of both phases within a particle-laden flow are determined by complex and non-linear phenomena such as turbulence, particle clustering (whereby particles preferentially concentrate in highly localised regions of the flow [8, 9]) and particle-fluid coupling [10]. In systems employing heated particles, these phenomena are further complicated by the significant density gradients and buoyancy-induced motions generated from thermal gradients in the gas-phase [11]. The resultant heat transfer in the system is coupled to the fluid motions through the mutually interacting processes of particle-fluid momentum transport, convection, and buoyancy [12]. Additionally, the radiation absorbed by individual particles, and the subsequent particle temperature change, is highly non-uniform on an instantaneous basis due to the impact of turbulent flow motions on the particle distributions. This, in turn, influences both the local, instantaneous distributions of radiation attenuation and the multiple scattering of incident radiation [13]. This non-uniform radiation absorption is particularly significant for the densely seeded flows typically used in industrial processes, in which particle volumetric loadings of $\phi > 10^{-3}$ are

common, where $\phi = \dot{V}_p/\dot{V}_f$ is the ratio of the volumetric flow rate of the particles to that of the fluid. Furthermore, in turbulent particle-laden channel flows heated with radiation, particle clustering has been shown to lead to spatially and temporally non-uniform gas-phase temperatures [14, 15]. The combination of these complex, mutually interacting phenomena lead to significant challenges in modelling the system without resorting to computationally cost-prohibitive direct numerical simulations. Therefore, in-situ and well-resolved experimental measurements are required to provide both the insights into the heat transfer processes in particle based receivers and the datasets needed for the development and validation of numerical models.

The diameter and volumetric loading of particles are two key parameters that significantly affect the particle-fluid interactions and heat transfer in particle-laden flows. Previous simulations of particle-based CST receivers have shown that both the solar receiver efficiency, defined as the proportion of the total solar heat entering the system that is absorbed by particles, and the average particle temperature at the outlet decrease with an increase in particle diameter [16, 17]. The solar receiver efficiency was also found to increase with particle volumetric loading, because a greater proportion of the incident radiation is absorbed by the particles [18]. Conversely, the average particle temperature at the outlet decreases with increasing loading because individual particles are increasingly likely to be in the shadow of those closer to the radiative source. However, these results are limited to spatially averaged data or point-wise measurements, which are unable to resolve the instantaneous gradients in the flow. As such, in-situ spatially resolved measurements are required to further improve the understanding of heat transfer in these systems. Despite the availability of data from simultaneous measurements of the particle and flow velocity in multiphase flows [19, 20], measurements of the velocity with flow temperature have been limited [21, 22]. Planar measurements of the temperature in particle-laden flows with strong thermal gradients generated by high-flux radiation are currently available for both the particle-phase [23] and gas-phase [24]. The current work extends these measurements by experimentally investigating the effect of particle diameter and volumetric loading on the spatial distribution of the gas-phase temperature in a radiatively heated particle-laden flow.

Laser based techniques are well suited to the measurement of the instantaneous conditions of various parameters in the flow because they can provide planar, spatially resolved data with nanosecond scale temporal resolutions. The technique of LIF, in which the fluorescence emissions from a vapour seeded in trace quantities into the flow are measured, has been used to determine the gas-phase temperature under conditions with strong optical interference, such as in optical engines [25], flows with droplets [26],

and particle-laden flows [27]. The advantage of LIF for measurements in particle-laden flows over other planar techniques, such as Rayleigh scattering, is that the fluorescence is emitted at longer wavelengths than the excitation laser due to Stokes shift, allowing the separation of the fluorescence signal and elastically scattered light using optical filtering. One method commonly used to determine the temperature from the fluorescence emissions is two-colour LIF, which utilises the red-shift of the fluorescence tracer emission spectrum with temperature. This is done by calculating the ratio of the fluorescence intensity measured in two separate wavelength ranges [28]. This technique has already been demonstrated to be suitable for gas temperature measurements in particle-laden flows with volumetric loadings of up to $\phi \approx 10^{-3}$ [27], and for planar measurements in flows heated using high-flux radiation [24]. Importantly, the advantage of using the two-colour ratio is that it corrects for the spatial non-uniformity of the signal intensity that can arise in particle-laden flows due to attenuation of the excitation beam and the mixing of tracers with unseeded, ambient fluid. Furthermore, the experimental arrangement for two-colour LIF is relatively simple, employing a single excitation laser and two detection channels. This technique is therefore highly suitable for systematic measurements of the gas-phase temperature distributions in radiatively heated particle-laden flows.

The aim of this paper is therefore to improve the understanding of heat transfer in particle-laden flows heated with high-flux radiation, utilising two-colour LIF thermometry for spatially resolved, planar measurements of the gas-phase temperature. More specifically, the present investigation aims to determine the effect of particle size and volumetric loading on the gas-phase temperature distributions in a flow with well-defined conditions.

2 Methodology

2.1 Experimental arrangement

Simultaneous measurements of the gas-phase temperature and particle number density, using two-colour LIF and Mie scattering, respectively, were performed in a radiatively heated particle-laden jet arranged as shown in Figure 1. The particle-laden flow issued from a long straight pipe of diameter $D = 12.6$ mm with a length-to-diameter ratio of $L/D = 165$, which is sufficiently long for the particle-laden flow to approach the fully developed condition [29]. A co-annular pipe of diameter 69 mm was used to generate a well-defined co-flow. Each pipe was centrally aligned within a 300×300 mm wind tunnel oriented with the flow direction vertically downwards. The central jet

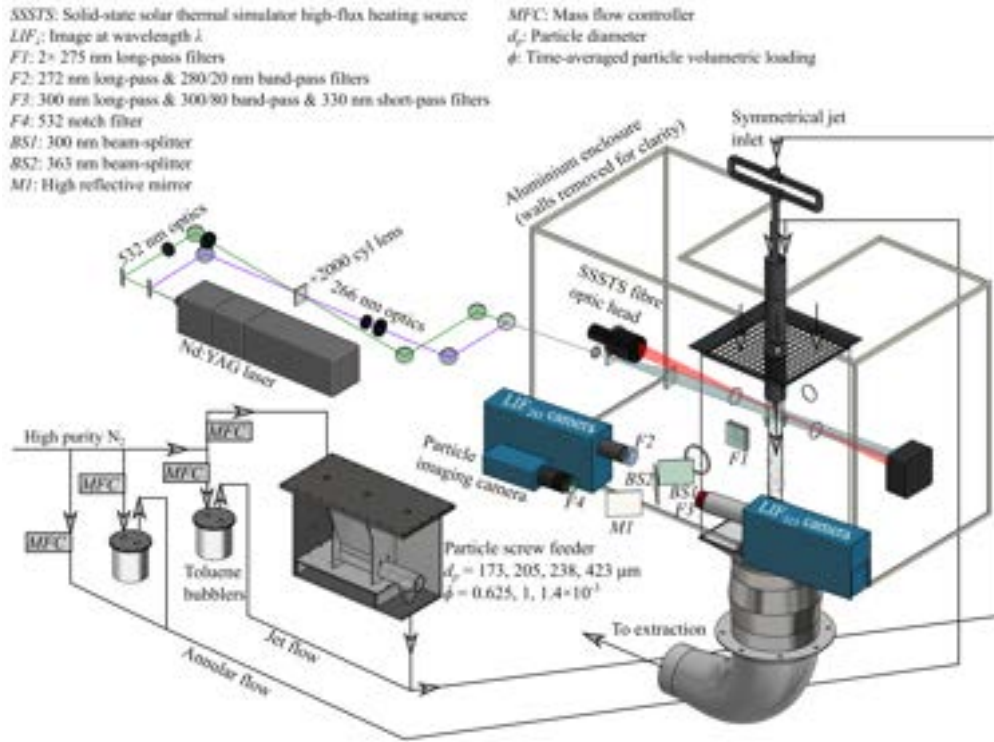


Figure 1: Experimental arrangement for simultaneous two-colour LIF thermometry and particle number density measurements in a flow heated using high-flux radiation.

employed nitrogen with a volumetric flow rate of 25 SLPM. The resultant jet exit Reynolds number was $Re_D = (\rho_f U_b D) / \mu_f = 3000$, where ρ_f and μ_f are the fluid density and dynamic viscosity, respectively, and $U_b = 3.6 \text{ m/s}$ is the gas-phase bulk mean velocity of the jet flow. This flow rate was chosen to maximise the particle residence time in the heating region while remaining sufficiently high to effectively carry the particles. The co-annular flow of 55 SLPM, also of nitrogen, had a bulk mean velocity at the pipe exit of 0.3 m/s . The velocity of the ambient air drawn through the wind tunnel was set to match that of the annular flow to within 20%.

Toluene was chosen as the tracer for two-colour LIF because it is a well characterised species with a relatively strong fluorescence emission that is sensitive to temperature in the range expected for the present investigation of 290-450 K [30, 31]. Both the central jet and annular flow were seeded with toluene vapour to ensure a strong signal throughout the measurement region, with high purity nitrogen used as the carrier gas to prevent quenching of the toluene fluorescence by molecular oxygen [32]. The toluene vapour

Table 1: Summary of experimental parameters.

Parameter	Symbol	Value	
Median particle diameter	\bar{d}_p (μm)	173, 205, 238, 423	
Jet exit Reynolds number	Re_D	3000	
Jet exit Stokes number	Sk_D	86, 121, 163, 514	
Mean particle volumetric loading	$\bar{\phi}$ ($\times 10^{-3}$)	0.625, 1, 1.4	
Heating laser power	\dot{Q}_0 (W)	$\bar{\phi} = 1.4 \times 10^{-3}$	0, 910, 1430, 1950, 2410, 2840
		$\bar{\phi} = 0.625, 1 \times 10^{-3}$	0, 2840

was seeded in each flow by bubbling the nitrogen through a separate bath of liquid toluene held at room temperature. The jet flow and co-annular flows were seeded with toluene at concentrations of approximately 0.75% and 0.25% by volume, respectively, with the concentration chosen to differ in these flows to allow a clear identification of the edges of the jet. Particles were introduced to the jet flow at a series of time-averaged volumetric loadings of $\bar{\phi} = 6.25 \times 10^{-4}$, 1×10^{-3} and 1.4×10^{-3} , with a screw feeder located in a sealed enclosure used to control the of particle flow rate. Four distributions of Aluminosilicate ceramic particles (Carbobeard CP) were used, with median diameters $\bar{d}_p = 173, 205, 238$ and $423 \mu\text{m}$, each of average sphericity 0.9. Each of the particle diameter distributions were measured using a Malvern Mastersizer 2000, with the results presented in Figure 2. The Stokes number of the median diameter for each particle case, evaluated at the jet exit for the large eddy time scale, was $Sk_D = (\rho_p \bar{d}_p^2 U_b) / (18 \mu_f D) = 86, 121, 263$ and 514 , respectively, where $\rho_p = 3270 \text{ kg/m}^3$ is the density of the particles. The distribution of particles at the jet exit for $Sk_D \gg 1$ is expected to be radially non-uniform with a peak number density on the jet centreline, due to the combination of forces applied to the particles within the pipe such as Saffman lift and turbophoresis [33]. A summary of the experimental parameters is presented in Table 1.

The second and fourth harmonic outputs from a single Nd:YAG laser (Quantel Q-smart), with respective wavelengths of 532 (to image scattering from particles) and 266 nm (to generate toluene fluorescence), were each formed into vertical co-planar sheets. Each sheet had an approximate height of 60 mm and thickness of 0.6 mm, and was aligned with the central axis of the

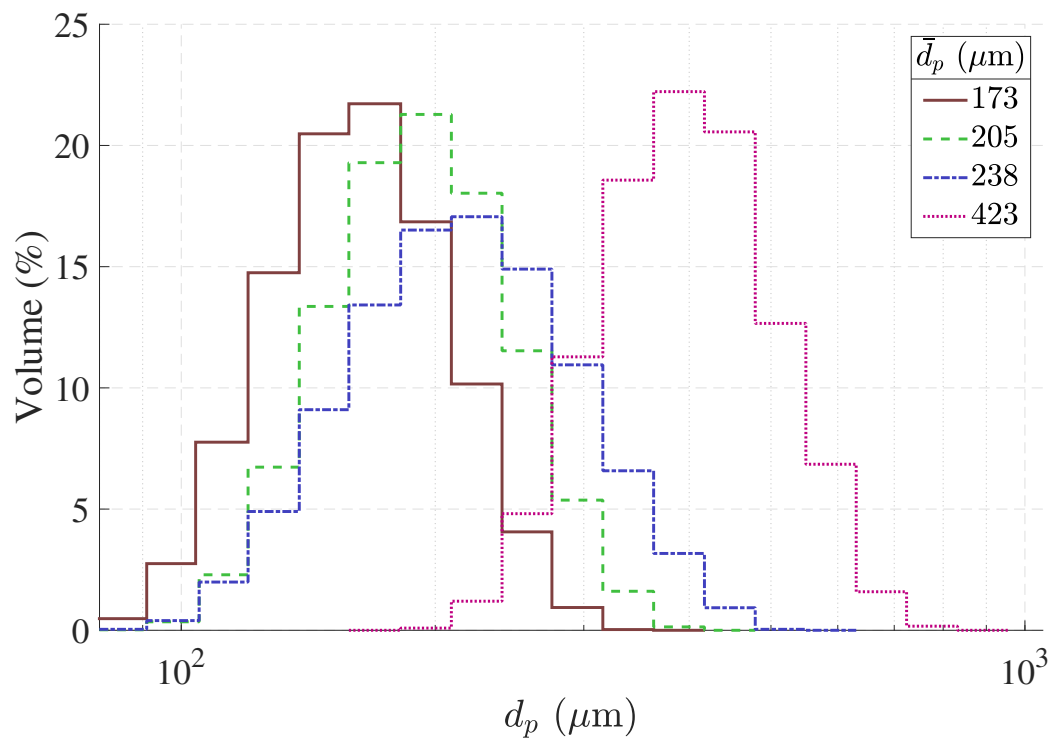


Figure 2: Particle diameter distributions measured using a Malvern Master-sizer 2000.

pipe such that the top edge of the sheet was 3 mm from the jet exit plane. The laser pulse frequency was 10 Hz with pulse energies of 0.5 and 18 mJ/pulse for the 532 nm and 266 nm sheets, respectively. The radiative heating beam was generated with a solid-state solar thermal simulator (SSSTS). The SSSTS combines the output from a bundle of infra-red (910 nm) diode lasers using fibre-optics [34] to provide a collimated beam at output powers up to $\dot{Q}_0 = 2840$ W with an approximate diameter of 15 mm at the focal plane, which was aligned with the jet axis 17.6 mm from the exit plane. The intensity profile of the SSSTS beam on the jet axis is described by Lewis et al. [24], with an approximate peak heating flux on the beam axis of 42.8 MW/m² when operating at $\dot{Q}_0 = 2840$ W. The beam powers used for the current experiments are listed in Table 1. A water-cooled power meter (Gentec model HP100A-4KW-HE) operating at 10 Hz, positioned down-beam from the wind tunnel, measured the power of the SSSTS that was transmitted through the flow, \dot{Q}_{tr} . The total power absorbed by the particles was then estimated using the equation $\dot{Q}_{abs} = \alpha(\dot{Q}_0 - \dot{Q}_{tr})$, where $\alpha \approx 0.89$ is the absorptivity of the particles [35]. This calculation uses the assumption that multiple scattering of the heating beam does not significantly increase the absorbed fraction and that the emitted radiation from the heated particles does not influence the measured power.

Optical filtering was used to separate the fluorescence emissions and scattering from the particles into two channels for two-colour LIF with central wavelengths of 285 nm and 315 nm, named here S_{285} and S_{315} , respectively. One channel to image the scattering of the 532 nm laser sheet by particles was also separated, named S_{532} here. The cameras imaging each of the three channels were positioned on the same side of the wind tunnel and shared the same optical path through the flow. Long-pass filters were used to suppress the scattered 266 nm laser light, with two beam-splitters positioned in series with cut-off wavelengths of 310 nm and 355 nm used to separate the three channels. The positioning of the cameras and beam-splitters can be seen in Figure 1. Additional filters were used to limit the transmitted signal to narrow spectral bands. The details of filters used and the resultant transmission for each channel are presented by Lewis et al. [24]. Each channel was imaged using a separate camera and lens. Two PC Di-Cam intensified s-CMOS cameras imaged the two fluorescence channels with the signal for the channel S_{285} focussed using a spherical UV lens ($f = 100$ mm, Thorlabs LB4821) and for S_{315} using a Sodern UV 100 mm F/2.8 lens. A PCO.2000 CCD with a Tamron macro 80-120 mm lens was used to image S_{532} . Each camera imaged the measurement region of $0.3 < x/D < 3.7$, $|r/D| < 1$, where x is the axial co-ordinate of the jet and r is the radial co-ordinate parallel to the laser sheet.

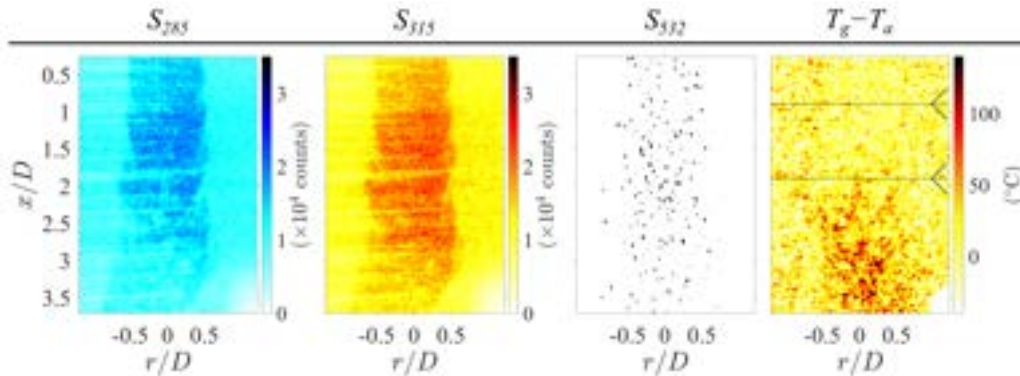


Figure 3: Example instantaneous images taken simultaneously with the two fluorescence cameras, S_{285} and S_{315} , the binary mask of particle locations determined from the scattering image S_{532} , and the resultant temperature calculated from the fluorescence intensity ratio S_{315}/S_{285} . For this figure and following figures including images of the temperature, the dashed lines and arrows indicate the approximate boundaries and direction of the SSSTS heating beam, respectively.

2.2 Image processing

The raw images collected simultaneously from the three cameras were processed using a series of in-house Matlab codes to derive the gas temperature and particle number densities. Examples of the instantaneous images from each camera, together with the calculated gas-phase temperature, are presented in Figure 3. Each step of the process is described in detail by Lewis et al. [24], so that only a summary is presented here. Firstly, the average background signal, collected with the lasers on and camera uncapped but without a flow, was subtracted from the raw images. A common target grid was then imaged with each camera to spatially align the images from the three channels to within approximately ± 1 pixel. The alignment of the fluorescence channels was then improved to approximately ± 0.3 pixels using time-averaged images of the fluorescence emissions from the toluene-seeded jet without heating. This was done by systematically offsetting the image from S_{285} in increments of 0.1 pixel and calculating the signal ratio S_{315}/S_{285} on a pixel-by-pixel basis. Because these measurements were conducted under ambient conditions, the true value of S_{315}/S_{285} should be constant across the field of measurement. Therefore, the image sub-pixel offset location with the smallest variation in the calculated signal ratio was then used to correct all instantaneous images taken on that particular day.

Following spatial alignment, the signal ratio S_{315}/S_{285} was calculated on

a pixel-by-pixel basis for each instantaneous image. Data from S_{285} or S_{315} with a signal of less than 15 times the camera dark charge were removed from further analysis to reduce the influence of camera noise on the measurement [27]. The ratio S_{315}/S_{285} was then converted to temperature using a calibration curve. The calibration was performed in the same jet flow as for the main experiments, except that the jet flow was heated using a controllable electrical tape heater (Briskheat BWH052100LD) fitted to the outside of the central pipe. The heated flow was imaged using S_{285} and S_{315} at a series of specified temperatures, with the actual flow temperature measured simultaneously using a thermocouple. The time- and spatially-averaged ratio S_{315}/S_{285} was then calculated from the potential core region of the jet where the temperature was uniform. The results for the calibration are presented by Lewis et al. [24], with the relationship between S_{315}/S_{285} and temperature well described by a linear function for the temperature range expected in the main experiment of $20\text{ }^\circ\text{C} < T_g < 160\text{ }^\circ\text{C}$. After conversion to temperature, the instantaneous images were smoothed using a 5×5 pixel median filter to reduce the influence of camera shot noise on the results. The uncertainty of the two-colour LIF method in a particle-laden flow with $\bar{d}_p = 173\text{ }\mu\text{m}$ and $\bar{\phi} = 1.4 \times 10^{-3}$, evaluated using the above methods, was found to have a pixel-to-pixel standard deviation in the instantaneous measured temperature of $17.8\text{ }^\circ\text{C}$ [24]. This can be reduced through time-averaging, such that for the mean results the error is expected to be $< 2\text{ }^\circ\text{C}$ for each case.

The instantaneous images of scattering from particles (S_{532}) were formed into a binary mask using a threshold of 10 times the standard deviation of the dark charge, to ensure the particle signals were strongly separated from the background noise. Individual particle locations were then determined from the binary image, using an in-house Matlab code to separate overlapping particles where possible.

3 Analytical models

3.1 One-dimensional heat transfer model

A one-dimensional analytical heat transfer model to estimate the particle and gas temperatures in the jet flow was developed, similar to that presented by Kueh et al. [36]. Both the radiative and convective heat transfer, together with the corresponding change in particle and gas temperature, were calculated for a single spherical particle and the surrounding volume of gas moving axially along the jet centreline. The heat gained by the particle ($\dot{Q}_{p,gain}$) is dependent on the incident radiation absorbed (\dot{Q}_{abs}), emitted radiation

(\dot{Q}_{emit}) and convection with the surrounding fluid (\dot{Q}_{conv}). The resultant heat transfer balance for the particle is given by the following equation:

$$\dot{Q}_{p,gain} = \dot{Q}_{abs} - \dot{Q}_{conv} - \dot{Q}_{emit} = \frac{\alpha\pi d_p^2 \dot{Q}_{rad}''}{4} - h\pi d_p^2 (T_p - T_f) - \epsilon\sigma\pi d_p^2 (T_p^4 - T_a^4), \quad (1)$$

where α is the absorptivity of the particle and \dot{Q}_{rad}'' is the incident radiative heat flux. The convective heat transfer coefficient is $h = Nu k_{film}/d_p$, where Nu is the Nusselt number of the particle and k_{film} is the thermal conductivity of the fluid evaluated at the film temperature. The Nusselt number for a sphere in forced convection is given by:

$$Nu = 2 + (0.4Re_p^{1/2} + 0.06Re_p^{2/3}) Pr^{0.4}, \quad (2)$$

where the Reynolds and Prandtl numbers of the particle are

$$Re_p = \frac{\rho_{film} |U_{slip}| d_p}{\mu_{film}} \quad (3)$$

and

$$Pr = \frac{c_{p,f} \mu_{film}}{k_{film}} \quad (4)$$

respectively. Here, $c_{p,f}$ is the specific heat of the fluid while ρ_{film} and μ_{film} are the fluid's respective density and dynamic viscosity evaluated at the film temperature. The slip velocity $U_{slip} = U_f - U_p$ is the instantaneous difference between the local fluid and particle velocities. The emitted radiation is a function of the particle emissivity, ϵ , and the Stefan-Boltzmann constant $\sigma = 5.67 \times 10^{-8} \text{ W/m}^2\text{K}^4$. The particle, fluid and ambient temperatures are represented by T_p , T_f and T_a respectively. The resultant rate of particle temperature change with time (t) can then be calculated from the following equation:

$$\frac{\partial T_p(t)}{\partial t} = \frac{6}{d_p c_{p,p} \rho_p} \left[\frac{\alpha}{4} \dot{Q}_{rad}''(t) - h (T_p(t) - T_f(t)) - \epsilon\sigma (T_p^4(t) - T_a^4) \right], \quad (5)$$

where $c_{p,p}$ is the specific heat of the particle and ρ_p is the particle density. The local radiative heat flux varies with time as the particle travels through the heating region because of the profile of the heating beam. This is modelled using the measured profile of the heating beam, presented by Lewis et al. [24], and the particle trajectory through the region. For the special case of a uniform particle velocity we obtain $\dot{Q}_{rad}''(t) = \dot{Q}_{rad}''(x/U_p)$, where U_p is the particle velocity in the x direction. The subsequent gas temperature

change, calculated using the assumption that all convective thermal energy is transferred to the gas, is given by:

$$\frac{\partial T_f(t)}{\partial t} = \frac{6h\phi}{d_p c_{p,f} \rho_{film}} (T_p(t) - T_f(t)). \quad (6)$$

In the model, the particle volumetric loading of the flow was assumed to be uniform and constant to match the jet exit values used in the experiments. A constant slip velocity ratio of $U_{slip} = 0.2U_f$ was used, approximated from the value measured by Gillandt et al. [37] for particles with $\bar{d}_p = 110 \mu\text{m}$ and $\rho_p \approx 2000 \text{ kg/m}^3$ at a loading of $\phi \approx 5 \times 10^{-4}$. While the instantaneous slip velocity may vary significantly with time and for each individual particle, these variations are not expected to systematically influence the dependence of gas temperature on either diameter or mass loading. Hence it is reasonable to assume slip-velocity is constant. That is, insights from the model with regards to the influence of the experimentally varied parameters (particle diameter and volumetric loading) are expected to be independent of the slip velocity. Attenuation of the radiation up-beam from the particle is assumed to be negligible. The values for specific heat capacity (as a function of particle temperature), absorptivity and emissivity were estimated from those measured for similar particles [17, 35, 38]. The carrier fluid was modelled as pure nitrogen with the density, viscosity and specific heat calculated as a function of the fluid temperature [39]. The model input parameters are summarised in Table 2.

Figure 4 presents the axial evolution of calculated temperatures of the particle- and gas-phases (a), together with the corresponding values of the absolute power of each heat transfer process (b), for the case with $\bar{d}_p = 173 \mu\text{m}$, $\bar{\phi} = 1.4 \times 10^{-3}$ and $\dot{Q}_0 = 2840 \text{ W}$ (note that data on the y-axis for the heat transfer powers are presented on a logarithmic scale). It can be seen that the particle temperature on the jet centreline is calculated to increase rapidly throughout the heating region, reaching a peak of approximately $300 \text{ }^\circ\text{C}$ at the downstream edge. The particle temperature is predicted to be much higher than that of the gas throughout the measurement. This is consistent with the radiative energy absorbed by particles in the heating region, $0.9 < x/D < 1.9$, being some two orders of magnitude greater than that transferred from the particles, either by radiation or from convection with the gas. The difference can be seen in the bottom sub-figure with $\dot{Q}_{abs} > 100 \times \dot{Q}_{conv}$ and $\dot{Q}_{abs} > 1000 \times \dot{Q}_{emit}$ at $x/D = 1.4$. Downstream from the heating region, the difference between the particle and gas temperatures decreases with axial distance toward the equilibrium that is far downstream from the region of investigation. In the region of $1 < x/D < 4$ convection is predicted to be the dominant mode of particle cooling, with $\dot{Q}_{conv} > 10 \times \dot{Q}_{emit}$.

Table 2: Input parameters used for the analytical heat transfer model. The particle properties used were those previously measured for the Carbobead CP particles or similar. The properties used for the gas were those of pure nitrogen. Temperature dependent parameters are indicated within the brackets in the Symbol column.

Parameter	Symbol	Value
Peak heating flux	\dot{Q}''_{peak}	13.7, 29.4, 36.3, 42.8 MW/m ²
Particle diameter	d_p	173, 205, 238, 423 μm
Particle volumetric loading ($\times 10^{-3}$)	ϕ	0.625, 1, 1.4
Particle density	ρ_p	3270 kg/m ³
Particle specific heat	$c_{p,p}(T_p)$	0.7-1.1 kJ/kgK
Particle absorptivity	α	0.89
Particle emissivity	ϵ	0.85
Particle velocity	U_p	2.9 m/s
Fluid velocity	U_f	3.6 m/s
Fluid density	$\rho_f(T_f)$	1.1-0.8 kg/m ³
Fluid viscosity	$\mu_f(T_f)$	$1.8\text{-}2.2 \times 10^{-5}$ Ns/m ²
Fluid specific heat	$c_{p,f}(T_f)$	1.04 kJ/kgK
Ambient temperature	T_a	20 °C

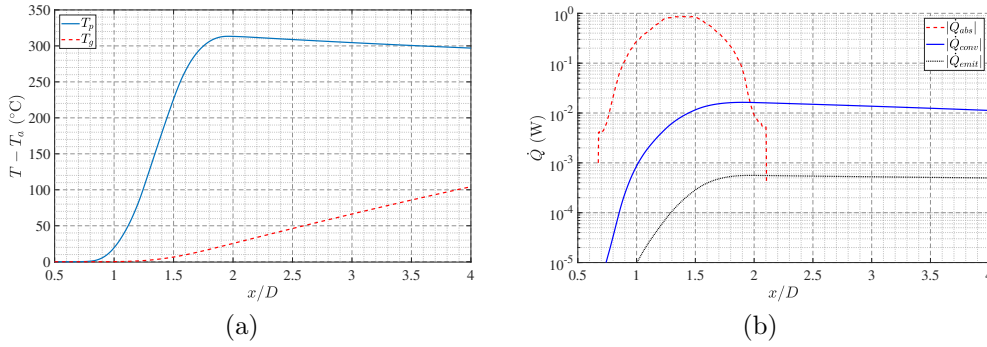


Figure 4: The simulated temperature from the one-dimensional model of both the particle and gas (a) together with the absolute powers of the modelled particle heat transfer components (b) as a function of axial distance, for the parameters listed in Table 2 with $\bar{d}_p = 173 \mu\text{m}$, $\bar{\phi} = 1.4 \times 10^{-3}$ and $\dot{Q}_0 = 2840 \text{ W}$.

3.2 Heating beam attenuation model

The absorption of the heating beam by the particles was predicted numerically using a simplified attenuation model. The model generates a random distribution of particles in a cylindrical spatial domain with both a length and diameter of $1.5D$ positioned such that the centre of the domain coincided with the intersection of the jet axis and that of the SSSTS beam. The particle locations were modelled using a weighted distribution such that the radial profiles of particle number density matched those previously reported for the case with $\bar{d}_p = 173 \mu\text{m}$ [24]. The number of particles in the domain was also selected such that the average volumetric loading matched the experimental cases. Particles were modelled as spheres with a particle size distribution matching that of the present experiment (see Figure 2). Any modelled particles that overlapped in the 3-D space were removed and iteratively replaced until there was no overlap. A 2-D binary mask of the particle locations, projected in the direction of the laser, was then generated with the domain discretised into pixels with sides of length $0.001D$. This length was sufficiently small for the results to converge. The spatial distribution of heating laser flux in each resulting pixel was then calculated using the profile presented by Lewis et al. [24]. Figure 5 presents a typical distribution of the modelled particle locations, for the case with particles of $\bar{d}_p = 423 \mu\text{m}$ at a volumetric loading of $\phi = 1.4 \times 10^{-3}$, together with the intensity profile of the SSSTS beam and the particle cross-sectional area projected in the beam direction. Here, x is the axial co-ordinate of the jet, while r and y are the radial co-ordinates parallel and perpendicular to the heating laser beam direction, respectively. The simulated transmission and attenuation of the heating beam through the flow was then calculated from the element-wise multiplication of the heating flux and the binary mask of projected particles, using the assumption that the particle transmissivity, forward scattering and multiple scattering were negligible.

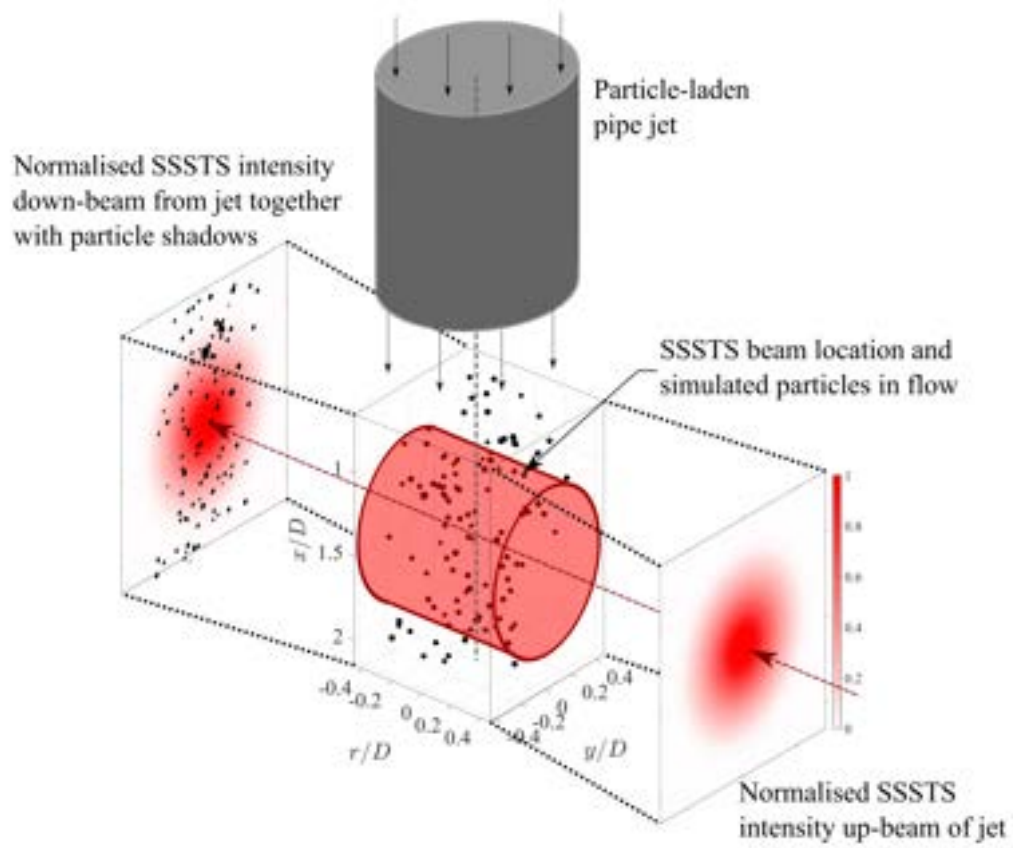


Figure 5: Schematic diagram illustrating the method used to model the attenuation of the SSSTS heating beam. An example of the distribution of the simulated particle locations is shown for the case with $\bar{d}_p = 423 \mu\text{m}$ and $\phi = 1.4 \times 10^{-3}$, together with the intensity of the heating beam.

4 Results

4.1 Instantaneous images

Figure 6 presents typical instantaneous images of the measured temperature above ambient ($T_g - T_a$), the binary particle mask, and the fluorescence intensity from S_{285} , for each particle size distribution. The particle volumetric loading for each image was $\phi = 1.4 \times 10^{-3}$ with a SSSTS beam power of $\dot{Q}_0 = 2840$ W. Additionally, one reference case without heating for the $\bar{d}_p = 406$ μm particles is presented to show the accuracy of the method. The largest particle case was chosen because the reduction in signal due to attenuation, and therefore also the random error, increases with d_p . The dashed lines and arrows overlaying the temperature images indicate the approximate boundaries and direction of the SSSTS heating beam, respectively.

Several qualitative trends can be seen from the temperature images with the heating laser switched on. The gas temperature can be seen to increase with a reduction in particle size, so that it is greatest for the particles with $\bar{d}_p = 173$ μm . This is as expected because the radiation absorption and convective heat transfer increase with total particle cross-sectional area and surface area, respectively, and hence with decreasing particle size for a constant ϕ . The instantaneous distributions of temperature can also be seen to be highly non-uniform in the flow downstream from the heating region, with large-scale coherent regions of high temperature evident for each case with heating. This indicates that the gas is not well mixed, even at the downstream edge of these images, and is also consistent with the particles being distributed with regions of high local volumetric loadings whose position relative to the gas is persistent (i.e., long lived). These local regions of high temperature become more prevalent with decreasing \bar{d}_p , with the temperature difference from the surrounding flow also increasing. More hot regions can be seen on the heating laser in-side of the image, for $r/D > 0$, suggesting that attenuation of the radiation significantly affects the temperature distribution of the flow.

Spatial variations of the fluorescence intensity can be seen throughout the images, driven by the mixing of the jet flow with the surroundings together with the non-uniform laser sheet intensity profile. Temporal changes in the toluene concentration from case to case can also be seen to affect the fluorescence intensity. These variations in signal are corrected for in the temperature measurement because the temperature is derived from the ratio of fluorescence emissions, as described above. However, the influence of random errors increases with decreasing signal. Attenuation of the excitation laser and signal trapping can be seen in the fluorescence images as streaks and circular regions with low intensity, respectively. The size of these regions of re-

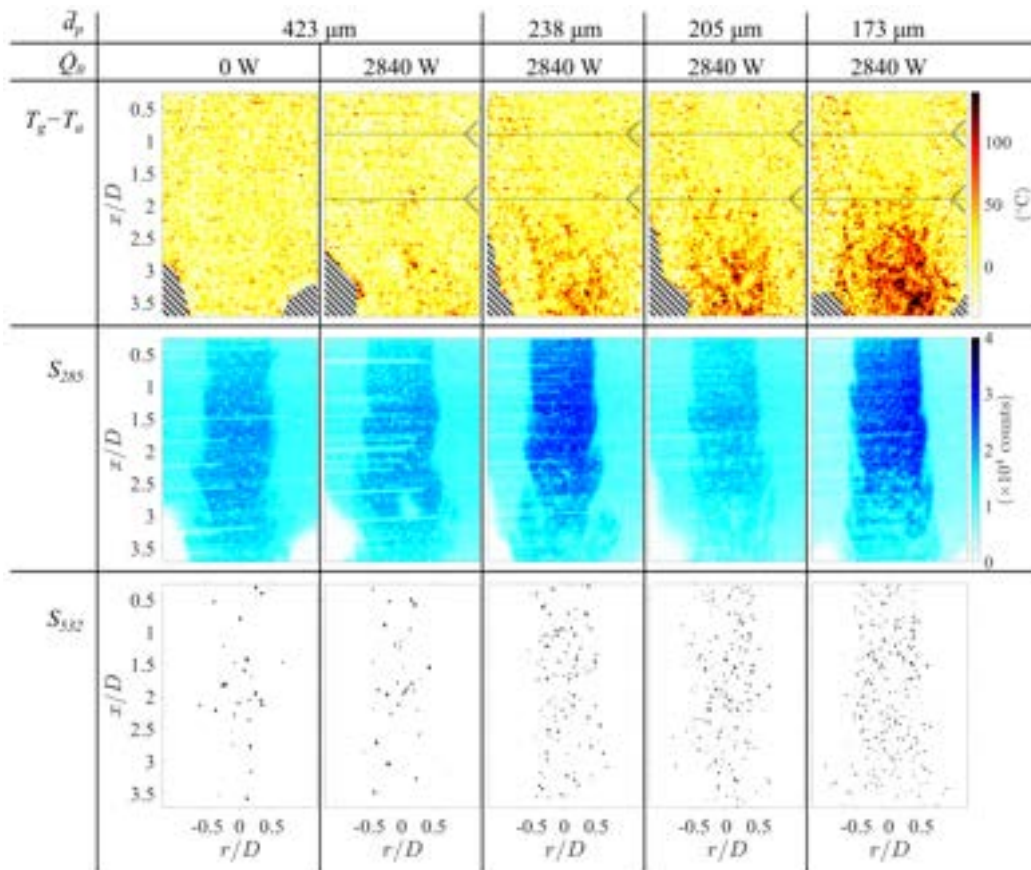


Figure 6: Typical instantaneous images of the calculated temperature, fluorescence intensity and binary particle mask, measured simultaneously, for each particle size with $\phi = 1.4 \times 10^{-3}$ and $\dot{Q}_0 = 2840$ W. Also presented is a reference case without heating, for the $\bar{d}_p = 406$ μm particles. The dotted lines represent the upper and lower extent of the heating laser, where used, while the arrow-head shows its direction. The hatched areas correspond to regions where the signal from one or both of the fluorescence images is below the threshold for reliable measurements.

duced intensity increases with particle diameter. The worst case attenuation is for the $\bar{d}_p = 423 \mu\text{m}$ particles, for which the fluorescence signal inside the streaks is reduced by up to 45% compared to their surroundings. Despite the significant variation in fluorescence signal from these combined sources, the pixel-to-pixel standard deviation of the calculated ratio S_{315}/S_{285} for the case without heating in the region $1 < x/D < 2$, $|r/D| < 0.3$ is $0.076 \times S_{315}/S_{285}$, corresponding to a temperature uncertainty of 18.8 °C. This is a 6% increase of the uncertainty compared to that measured previously for the $\bar{d}_p = 173 \mu\text{m}$ particles of 17.8 °C [24]. These uncertainties were calculated from the images of the flow without heating, with a known, uniform temperature. The uncertainty is expected to increase with temperature because the fluorescence intensity decreases with an increase in temperature. The effect of temperature on the uncertainty was estimated using images of the unheated flow, with the laser power reduced such that the fluorescence intensity matched that measured for the case with the highest heating. The resultant uncertainty for the time-averaged images, to one standard deviation, is estimated to be less than 5 °C for each case across the majority of the image bounded by the region $0.5 < |r/D|$, $0.5 < x/D < 3.7$.

4.2 Time-averaged images

Figure 7 presents the time-averaged temperature above ambient, $\bar{T}_g - T_a$, for each particle size with $\bar{\phi} = 1.4 \times 10^{-3}$ and $\dot{Q}_0 = 2840 \text{ W}$. The trends seen in Figure 6 are also evident here, with the mean temperature downstream from the heating region increasing with a decrease in particle size and a greater temperature rise for the laser-in side, for $r/D > 0$, than for $r/D < 0$. The temperature within the main jet flow, for $|r/D| < 0.5$, can be seen to be greater than the ambient from the start of the heating region, with $\bar{T}_g - T_a$ increasing with x/D to the downstream edge of the image. The majority of the temperature rise is constrained within $|r/D| < 0.6$, suggesting there is little spreading of the jet and/or mixing with the co-flow to the downstream edge of the measurement region. Only one heating flux and loading is presented here because the trends are similar for all cases, with the presented conditions chosen because they exhibit the greatest temperature change.

Figure 8 presents the time-averaged temperature images for a series of particle volumetric loadings, for the flow with $\bar{d}_p = 205 \mu\text{m}$ and $\dot{Q}_0 = 2840 \text{ W}$. Note the condition of $\bar{\phi} = 1.4 \times 10^{-3}$ is repeated from Figure 7, although the colour scale is different. The temperature rise downstream from the heating region increases with particle loading, which is as expected because the greater cross-sectional and surface area of particles leads to an increase

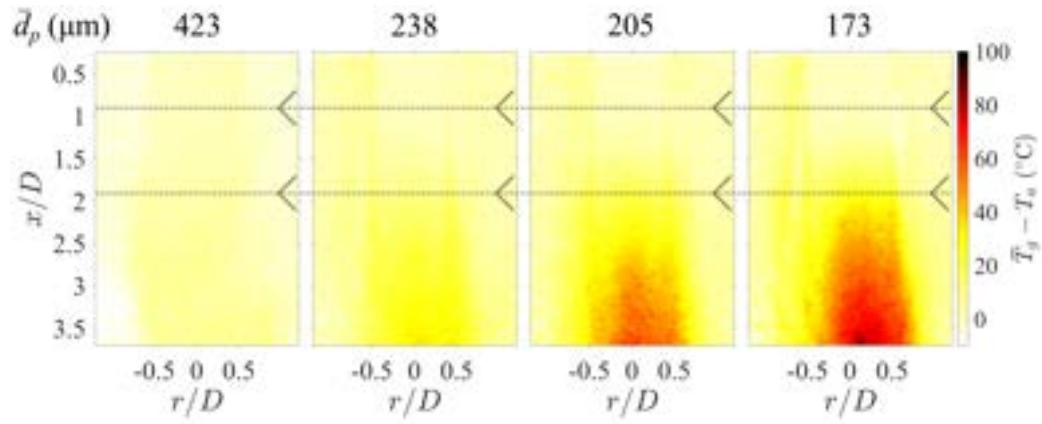


Figure 7: Time-averaged gas-phase temperature distributions for each of the four particle sizes distributions with a fixed particle volumetric loading of $\bar{\phi} = 1.4 \times 10^{-3}$ and a constant power of the heating laser of $\dot{Q}_0 = 2840$ W.

in the total radiation absorption and convective heat transfer, respectively.

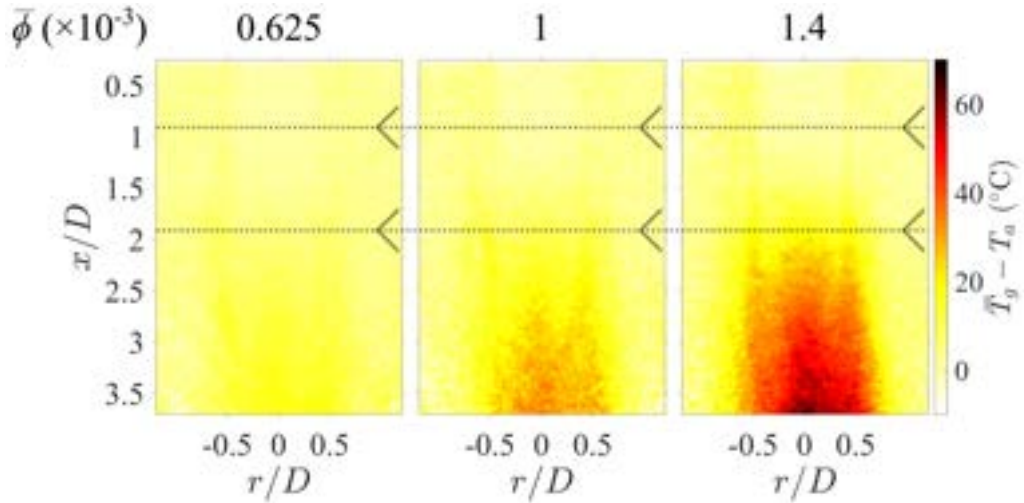


Figure 8: Time-averaged gas-phase temperature distributions for a series of particle volumetric loadings for the particles with $\bar{d}_p = 205 \mu\text{m}$ and $\dot{Q}_0 = 2840 \text{ W}$.

4.3 Heating beam transmission

Figure 9 presents the power from the SSSTS beam that was transmitted through the particle-laden flow, \dot{Q}_{tr} , normalised by the initial beam power, \dot{Q}_0 , as a function of particle diameter for a series of volumetric loadings with $\dot{Q}_0 = 2840 \text{ W}$. Both the measured and simulated transmissions are presented. It can be seen that \dot{Q}_{tr}/\dot{Q}_0 decreases with an increase in $\bar{\phi}$ and a decrease in \bar{d}_p , which is consistent with the results presented in Figures 7 and 8. This is because the total cross-sectional area of particles in the flow increases with an increase in $\bar{\phi}$ for constant \bar{d}_p and a decrease in \bar{d}_p for constant $\bar{\phi}$, resulting in a greater absorption of the heating beam by particles. The lowest measured transmission of the SSSTS beam was $\dot{Q}_{tr}/\dot{Q}_0 = 0.79$ for the particles with $\bar{d}_p = 173 \mu\text{m}$ at a volumetric loading of $\bar{\phi} = 1.4 \times 10^{-3}$. This corresponds to an approximate absorption of the beam by particles of $\dot{Q}_{abs}/\dot{Q}_0 = 0.19$.

The results seen for the measured transmission match sufficiently well with the simulated values calculated using a random distribution of particles to have good confidence in the trends. For each case the measured transmission is lower than that calculated from the model, with the difference increasing with $\bar{\phi}$ for all cases of \bar{d}_p investigated. There are several possible reasons for this discrepancy. These include that the particles are simulated as spherical, whereas the specified sphericity of the particles by the manufacturer is 0.9. The area-to-volume ratio of particles in the flow increases with decreasing sphericity, leading to an increase in the amount of radiation

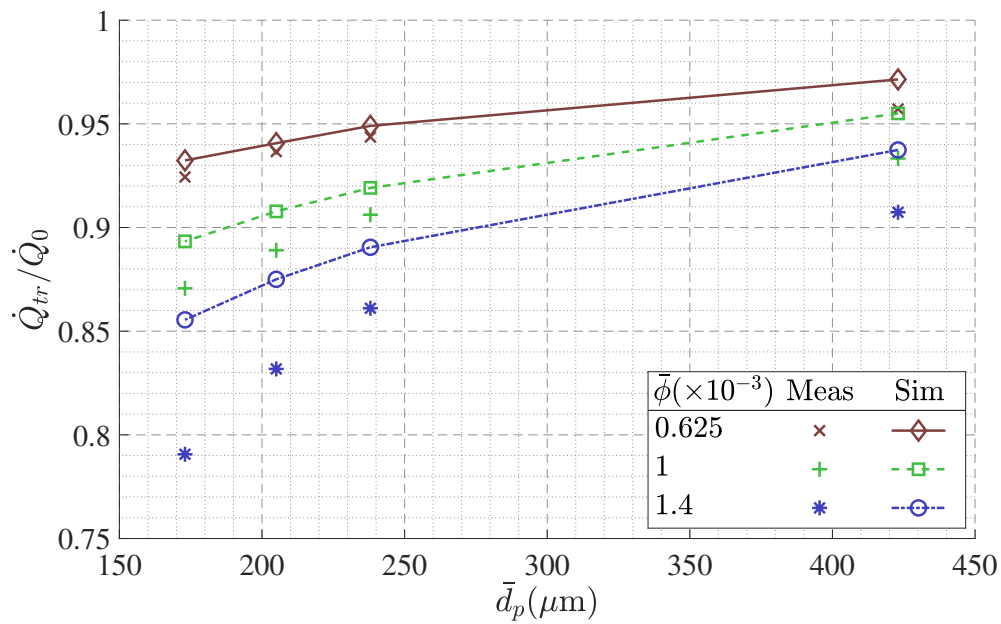


Figure 9: Comparison of the measured (Meas) and simulated (Sim) power of the SSSTS beam transmitted through the particle-laden flow, normalised by the total beam power, as a function of particle diameter for each volumetric loading investigated. The measured results presented are for the cases with $\dot{Q}_0 = 2840$ W.

being attenuated by particles. Breakage of particles or abrasion that generates fine particles in the system could lead to a decrease in the average diameter of particles in the flow relative to that measured, without changing the volumetric loading. This would be more significant for higher loadings because of greater stresses in the feeding system and the increased likelihood of particle-particle collisions in the conveying pipes and jet flow. Additionally, fine particles that occupy a very small volume percent but relatively larger number density may not be recorded when measuring the particle diameter distribution. While these complexities in the real system are not easily predicted or incorporated in models, their contribution is also expected to be modest.

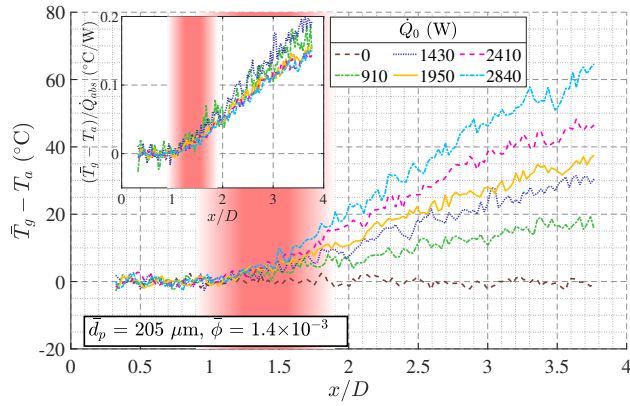
4.4 Centreline temperature profiles

Figure 10 presents the time-averaged temperature above ambient measured on the jet centreline as a function of axial distance for a series of heating powers with $\bar{d}_p = 205 \mu\text{m}$ and $\bar{\phi} = 1.4 \times 10^{-3}$ (a), a series of particle volumetric loadings with $\bar{d}_p = 205 \mu\text{m}$ and $\dot{Q}_0 = 2840 \text{ W}$ (b), and a series of particle diameters with $\bar{\phi} = 1.4 \times 10^{-3}$ and $\dot{Q}_0 = 2840 \text{ W}$ (c). Note that the case for the particles with $\bar{d}_p = 205 \mu\text{m}$, $\bar{\phi} = 1.4 \times 10^{-3}$ and $\dot{Q}_0 = 2840 \text{ W}$ is presented in each sub-figure. The inset in each sub-figure presents the axial profile of the centreline temperature rise relative to the power absorbed by particles, $(\bar{T}_g - T_a)/\dot{Q}_{abs}$. This gives a measure of how efficiently the absorbed radiative energy is transferred to the gas-phase. The trends seen in the normalisation are expected to be reliable even though there is some uncertainty in the absolute values owing to the assumptions used to estimate \dot{Q}_{abs} , because the particle material properties are the same for each case.

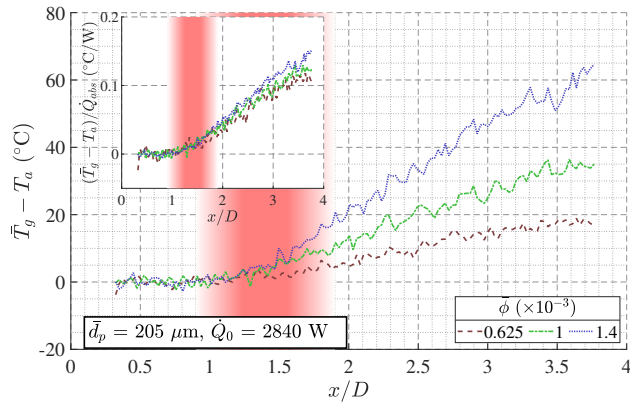
The general trends seen in the time-averaged images are confirmed here, with the temperature increasing monotonically from $x/D \approx 1.1$ to the downstream edge of the measurement region for all cases with heating and $\bar{T}_g - T_a$ increasing with an increase in \dot{Q}_0 , an increase in $\bar{\phi}$, and a decrease in \bar{d}_p . The increase in temperature with axial distance is close to linear for $1.9 < x/D < 3.7$, indicating that the convective heat transfer is nearly constant downstream from the heating beam to the edge of the measurement region. This suggests that the particle temperature after radiative heating remains significantly greater than that of the fluid throughout this region, which agrees well with the trends obtained from the analytical model in Figure 4.

The normalised axial temperature profile $(\bar{T}_g - T_a)/\dot{Q}_{abs}$ collapses well for $x/D < 2.5$ for each heating power. This shows that the temperature rise in this region is proportional to the power absorbed by the particles, for a constant particle diameter and volumetric loading. This is because the

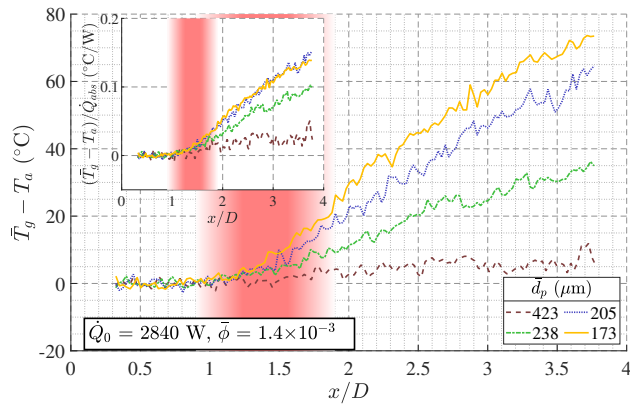
particle temperature rise is directly proportional to the radiative flux and the subsequent temperature rise of the gas is proportional to the temperature differential between the particles and gas, $T_p - T_g$. The trends calculated with the analytical model (see Figure 4) predict that $T_p \gg T_g$ in the region $1.9 < x/D < 2.5$, which would lead to an almost constant rate of convective heat transfer in this region. Downstream from this region, for $x/D > 2.5$, the relative temperature increase $(\bar{T}_g - T_a)/\dot{Q}_{abs}$ can be seen to decrease slightly with increasing heating beam power. This is potentially because buoyancy-induced mixing/convection within the gas-phase increases with an increase in the gradients of temperature in the flow. In the region $1.9 < x/D < 2.5$, the value of $(\bar{T}_g - T_a)/\dot{Q}_{abs}$ also collapses well for the series of values of $\bar{\phi}$, although downstream from this region the value of $(\bar{T}_g - T_a)/\dot{Q}_{abs}$ increases with $\bar{\phi}$. This suggests that, while the heat absorbed by the particles and initial heat transfer is proportional to the volumetric loading, increasing the volumetric loading also decreases the radial gas-phase transport. In the region $x/D > 1.5$, $(\bar{T}_g - T_a)/\dot{Q}_{abs}$ increases significantly with decreasing particle diameter for $\bar{d}_p \geq 205 \mu\text{m}$. However, $(\bar{T}_g - T_a)/\dot{Q}_{abs}$ was found to be similar for the particles with $\bar{d}_p = 173$ and $205 \mu\text{m}$. These trends are consistent for all heating powers and volumetric loadings investigated. This demonstrates the non-linear nature of the relationships between the particle diameter and the convective and radiative heat transfer processes in the flow.



(a)



(b)



(c)

Figure 10: Measured temperature above ambient on the jet centreline for a series of heating fluxes (a), particle loadings (b), and particle diameters (c). The inset in each figure presents the temperature above ambient normalised by the estimated absorbed power.

Figure 11 presents the measured and calculated values of the rate of change of the gas temperature with axial distance on the jet centreline, dT_g/dx , averaged over the region of $2 < x/D < 3$. The results are presented for a series of particle diameter distributions as a function of \dot{Q}_0 with $\bar{\phi} = 1.4 \times 10^{-3}$ (a) and as a function of $\bar{\phi}$ with $\dot{Q}_0 = 2840$ W (b). The measured axial temperature gradient dT_g/dx can be seen to increase approximately linearly with \dot{Q}_0 and monotonically with $\bar{\phi}$ in this region. The gradient dT_g/dx also generally increases with a decrease in \bar{d}_p , except for the particles with $\bar{d}_p = 173$ μm for which the gradient is similar to that seen for the particles with $\bar{d}_p = 205$ μm . For the case with $\dot{Q}_0 = 2840$ W and $\bar{\phi} = 1.4 \times 10^{-3}$, $dT_g/dx \approx 2,200$ $^\circ\text{C}/\text{m}$ for $\bar{d}_p = 173$ and 205 μm . This corresponds to a gas-temperature heating rate of approximately $8,000$ $^\circ\text{C}/\text{s}$, assuming that the axial gas velocity is constant in this region at the jet exit bulk-mean velocity of 3.6 m/s. At this loading and heating power, dT_g/dx decreases with an increase in particle diameter to $1,200$ and 300 $^\circ\text{C}/\text{m}$ for $\bar{d}_p = 238$ and 423 μm , respectively.

The model can be seen to overestimate the gradient for most investigated fluxes, loadings and particle sizes, except for the case with $\bar{d}_p = 238$ μm . Furthermore, the magnitude of difference between the experimental measurements and the modelled results increases with a decrease in the particle diameter. One critical parameter in determining convective heat transfer is the slip velocity, which was assumed to be constant at $U_{slip} = 0.2U_g$ in the model for all cases. There are currently no measurements of both the gas- and particle-phase velocities for the flow conditions and particles used in the experiments, so the value chosen in the model was approximated from that measured for the most similar conditions in the available literature [37]. Additionally, attenuation of the heating beam and particle clustering, which are not accounted for in the model, may change the heat absorbed by particles on the centreline and the subsequent convective heat transfer. Despite these simplifications the trends seen in the model are in good agreement with the experimental results, with the model overestimating the gradient by 19.6% on average for the cases with $dT_g/dx > 500$ $^\circ\text{C}/\text{m}$.

4.5 Radial temperature profiles

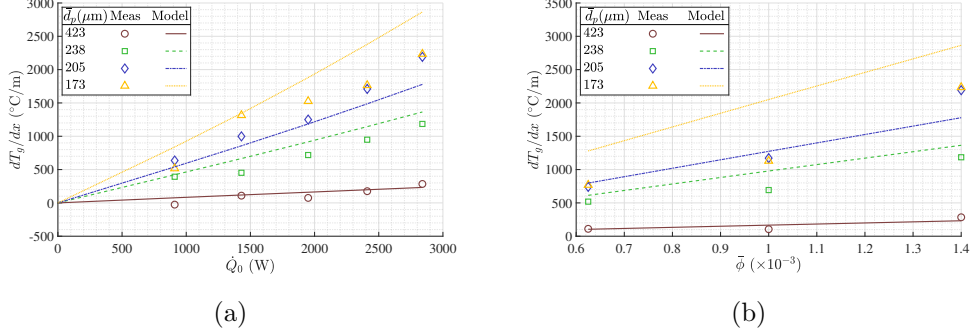


Figure 11: Average rate of temperature increase with axial distance on the jet centreline over the region $2 < x/D < 3$, for both the measurements and the one-dimensional model, as a function of heat flux for each particle diameter with $\bar{\phi} = 1.4 \times 10^{-3}$ (a) and as a function of volumetric loading for each particle diameter with $\dot{Q}_0 = 2840$ W (b).

Figure 12 presents the measured radial profiles of the gas-phase temperature above ambient at $x/D = 3$ for a series of heating powers with $\bar{d}_p = 205$ μm and $\bar{\phi} = 1.4 \times 10^{-3}$ (a), for a series of particle volumetric loadings with $\bar{d}_p = 205$ μm and $\dot{Q}_0 = 2840$ W (b), and for a series of particle diameters with $\bar{\phi} = 1.4 \times 10^{-3}$ and $\dot{Q}_0 = 2840$ W (c). The inset in each subfigure presents the radial temperature profile normalised by the estimated heating power absorbed, $(\bar{T}_g - T_a)/\dot{Q}_{abs}$. The measured temperature rise $\bar{T}_g - T_a$ increases with both \dot{Q}_0 and $\bar{\phi}$, consistent with previous figures, within the region $|r/D| < 1$ at this axial location. The temperature can be seen to generally peak near to the jet centreline and decrease with $|r/D|$, consistent with the particle loading being greatest there for particles with $Sk_D \gg 1$ [24, 33]. However, for the cases with $\bar{d}_p = 406$ μm or $\bar{\phi} \leq 1.4 \times 10^{-3}$ (i.e., the cases with the lowest particle number densities) $\bar{T}_g - T_a$ can be seen to be close to uniform for $|r/D| < 0.5$. The radial profiles for the cases with $\bar{d}_p \leq 238$ μm , $\dot{Q}_0 \geq 1430$ W and $\bar{\phi} = 1.4 \times 10^{-3}$ also show asymmetry consistent with the influence of attenuation of the heating beam, with $\bar{T}_g - T_a$ being up to 10 $^\circ\text{C}$ greater at $r/D = 0.3$ than at $r/D = -0.3$. This suggests that the average gas-phase temperature at any location will also be dependent on the path length of the heating beam through the flow to that location.

The radial profile of the normalised temperature rise, $(\bar{T}_g - T_a)/\dot{Q}_{abs}$, collapses well for the flow with heating powers of $\dot{Q}_0 \geq 1950$ W, for $\bar{d}_p = 205$ μm and $\bar{\phi} = 1.4 \times 10^{-3}$. For $\dot{Q}_0 < 1950$ W the normalised temperature can be seen to increase with a decrease in \dot{Q}_0 , although it should be noted that the influence of noisy data (estimated to be ± 5 $^\circ\text{C}$) on this normalisation increases

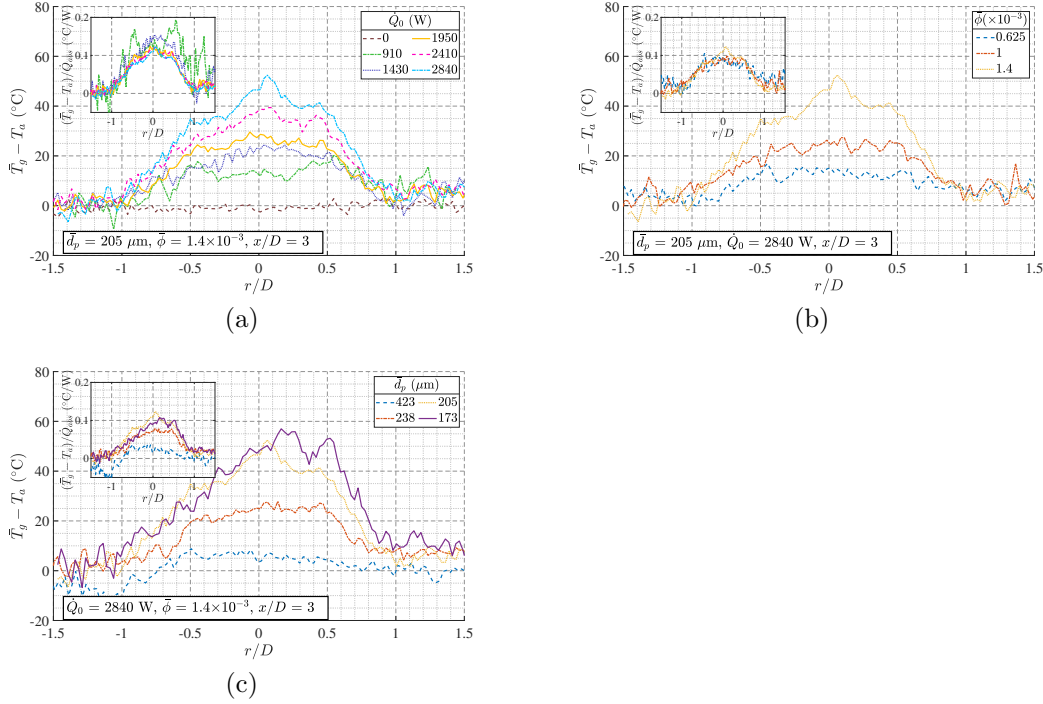


Figure 12: Radial profiles of the temperature above ambient measured at $x/D = 3$ for a series of heating fluxes with $\bar{d}_p = 205 \mu\text{m}$ and $\bar{\phi} = 1.4 \times 10^{-3}$ (a), a series of particle loadings with $\bar{d}_p = 205 \mu\text{m}$ and $\dot{Q}_0 = 2840 \text{ W}$ (b), and for a series of particle diameters with $\dot{Q}_0 = 2840 \text{ W}$ and $\bar{\phi} = 1.4 \times 10^{-3}$ (c). The inset in each sub-figure presents the respective temperature rise normalised by the estimated absorbed power.

with a decrease in $\bar{T}_g - T_a$. As such, there is no clear indication that the mixing/radial transport of the gas-phase is dependent on the heating power at this axial location, although gas-phase velocity measurements are required to confirm this. For each value of $\bar{\phi}$ the normalised temperature profile is similar in the region outside the main core of the jet, for $|r/D| > 0.5$. Nearer to the jet centreline, for $|r/D| < 0.3$, $(\bar{T}_g - T_a)/\dot{Q}_{abs}$ increases with $\bar{\phi}$, suggesting that the radial transport of the gas-phase decreases with an increase in the particle loading. This agrees with previous velocity measurements of the gas phase in a particle-laden jet flow, with the radial velocity fluctuation and turbulence intensity both measured to increase with a decrease in ϕ [40].

5 Conclusions

The combination of systematic and spatially-resolved measurements of the gas-phase temperature in a particle-laden jet and an analytical model of heat transfer for a single particle provide strong evidence of the important roles played by both a) large-scale coherent motions and b) the variable spatial distribution of particles in the heat transfer processes in a particle-laden flow heated with high-flux radiation. The agreement between the model and the experiments was also sufficient to provide confidence in the trends and mechanistic explanations for which they were applied.

Images of the instantaneous gas temperature distribution in the radiatively heated particle-laden jet were found to display localised regions that are significantly hotter or colder than the surrounding areas throughout the imaged area, both within and downstream from the heating zone. These correlate visually with regions where a locally high particle volumetric loading can be observed and are qualitatively consistent with the important role of persistent coherent structures in the flow. The number of distinct regions of high/low temperature, and the temperature difference between these regions and their surroundings, was found to increase with a decrease in particle diameter.

The time-averaged gas-phase temperature measured downstream from the radiative heating zone was found to increase with either an increase in particle loading or a decrease in particle diameter. This is consistent with the total radiation absorption and the subsequent convective heat transfer being proportional to the total cross-sectional area and surface area of the particles, respectively, which both increase with increasing particle loading and decreasing diameter. The gas-phase temperature on the jet centreline was also found to increase approximately linearly with axial distance from the downstream edge of the heating zone to the edge of the measurement region, indicating near-constant convective heat transfer between the particles and gas throughout this region. This is consistent with the analytical model, which shows that the increase in particle temperature is an order of magnitude greater than that of the surrounding gas.

The temperature rise of the gas-phase downstream from the heating region was found to be proportional to the power absorbed by particles, for a series of particle volumetric loadings and heating powers. However, the magnitude of the gas temperature rise, relative to the absorbed power, was found to increase significantly with a decrease in particle diameter. This indicates that the proportion of the total absorbed radiative heat that is transferred to the gas-phase through convection is strongly dependent on the particle diameter, but not on the particle loading or heating power.

The radial profile of temperature was found to peak at, or near to, the jet centreline, consistent with the time-averaged particle volumetric loading being greatest there. However, the temperature profile was found to be close to uniform within the central jet region of $|r/D| < 0.5$ for the cases of comparatively low particle number density, with $\bar{d}_p = 406 \mu\text{m}$ and $\bar{\phi} \leq 1 \times 10^{-3}$. In addition, measurements of the temperature on the heating laser up-beam side of the flow ($r/D > 0$) were found to be up to $10 \text{ }^\circ\text{C}$ greater than that on the down-beam side ($r/D < 0$), consistent with the effect of radiation attenuation. This was especially significant for the flows with $\bar{\phi} \geq 1 \times 10^{-3}$ and $\bar{d}_p \leq 238 \mu\text{m}$.

The measured transmission of the heating beam through the flow was broadly consistent with, although somewhat lower than, that predicted using the particle distribution model, with the relative difference between the measured and predicted attenuations found to increase with ϕ . These differences are consistent with a combination of the slight non-sphericity of the particles that was not accounted for in the model, and/or with a possible role of particle breakage and abrasion in the feeding system leading to the actual particle diameter distribution in the flow differing from that measured beforehand.

The measured axial gradient of the gas-phase temperature on the jet centreline was found to match the values calculated using the simplified one-dimensional model to within 20% for cases with a gradient greater than $500 \text{ }^\circ\text{C/m}$. The magnitude of this difference is consistent with imperfect knowledge of the parameters used in the model, in particular the velocities of the gas and particles, radiation attenuation and particle clustering effects. Nevertheless, the general trends between the model and the experiment are consistent. The quantitative agreement is sufficient to confirm that the rate of radiant heating on the particles under the present conditions is some two orders of magnitude greater than that of convective cooling, while the radiative cooling of the particles is an order of magnitude lower again. Hence, the particle cooling processes are dominated by convection, which is coupled with both the particle-fluid transport and buoyancy induced effects. This, in turn, confirms the ongoing need for the further development and application of both new spatially resolved measurements of multiple flow parameters and of new numerical modelling methods to advance quantitative predictive capability.

References

- [1] W. M. Fish. “Alumina calcination in the fluid-flash calciner”. In: *Essential Readings in Light Metals*. Vol. 1. Switzerland: Springer International Publishers, 2016, pp. 648–652.
- [2] J. A. H. Oates. *Lime and limestone : chemistry and technology, production and uses*. Weinheim, Germany: Wiley-Vch, 1998.
- [3] Energy Transitions Commission. *Making Mission Possible - Delivering a Net-Zero Economy*. Report 1.0. Energy Transitions Commission, 2020.
- [4] C. K. Ho. “A review of high-temperature particle receivers for concentrating solar power”. In: *Special Issue: Solar Energy Research Institute for India and the United States (SERIUS) – Concentrated Solar Power 109* (2016), pp. 958–969.
- [5] A. Steinfeld, A. Imhof and D. Mischler. “Experimental Investigation of an Atmospheric-Open Cyclone Solar Reactor for Solid-Gas Thermochemical Reactions”. In: *Journal of Solar Energy Engineering* 114.3 (1992), pp. 171–174.
- [6] A. Meier, E. Bonaldi, G. M. Cella, W. Lipinski and D. Wuillemin. “Solar chemical reactor technology for industrial production of lime”. In: *Solar Energy* 80.10 (2006), pp. 1355–1362.
- [7] D. Davis, F. Muller, W. Saw, A. Steinfeld and G. Nathan. “Solar-driven alumina calcination for CO₂ mitigation and improved product quality”. In: *Green Chem.* 19.13 (2017), pp. 2992–3005.
- [8] E. K. Longmire and J. K. Eaton. “Structure of a particle-laden round jet”. In: *Journal of Fluid Mechanics* 236 (1992), pp. 217–257.
- [9] T. C. W. Lau, J. H. Frank and G. J. Nathan. “Resolving the three-dimensional structure of particles that are aerodynamically clustered by a turbulent flow”. In: *Physics of Fluids* 31.7 (2019), p. 071702.
- [10] S. Balachandar and J. Eaton. “Turbulent Dispersed Multiphase Flow”. In: *Annual Review of Fluid Mechanics* 42 (2010), pp. 111–133.
- [11] A. Frankel, H. Pouransari, F. Coletti and A. Mani. “Settling of heated particles in homogeneous turbulence”. In: *Journal of Fluid Mechanics* 792 (2016), pp. 869–893.
- [12] R. Zamansky, F. Coletti, M. Massot and A. Mani. “Radiation induces turbulence in particle-laden fluids”. In: *Physics of Fluids* 26.7 (2014), p. 071701.

- [13] A. Kumar, J.-S. Kim and W. Lipiński. “Radiation Absorption in a Particle Curtain Exposed to Direct High-Flux Solar Irradiation”. In: *Journal of Solar Energy Engineering* 140.6 (2018).
- [14] H. Pouransari and A. Mani. “Effects of Preferential Concentration on Heat Transfer in Particle-Based Solar Receivers”. In: *Journal of Solar Energy Engineering* 139.2 (2016), pp. 021008–021008–11.
- [15] A. J. Banko, L. Villafañe, J. H. Kim and J. K. Eaton. “Temperature statistics in a radiatively heated particle-laden turbulent square duct flow”. In: *International Journal of Heat and Fluid Flow* 84 (2020), p. 108618.
- [16] F. Miller and R. Koenigsdorff. “Theoretical analysis of a high-temperature small-particle solar receiver”. In: *Solar Energy Materials* 24.1 (1991), pp. 210–221.
- [17] H. Chen, Y. Chen, H.-T. Hsieh and N. Siegel. “Computational Fluid Dynamics Modeling of Gas-Particle Flow Within a Solid-Particle Solar Receiver”. In: *Journal of Solar Energy Engineering* 129.2 (2006), pp. 160–170.
- [18] N. Siegel, C. Ho, S. S. Khalsa and G. Kolb. “Development and Evaluation of a Prototype Solid Particle Receiver: On-Sun Testing and Model Validation”. In: *Journal Of Solar Energy Engineering-Transactions Of The Asme* 132.2 (2010).
- [19] B. Prakash, H. Parmar, M. T. Shah, V. K. Pareek, L. Anthony and R. P. Utikar. “Simultaneous measurements of two phases using an optical probe”. In: *Experimental and Computational Multiphase Flow* 1.4 (2019), pp. 233–241.
- [20] M. Zhang, M. Xu and D. L. S. Hung. “Simultaneous two-phase flow measurement of spray mixing process by means of high-speed two-color PIV”. In: *Measurement science & technology* 25.9 (2014), p. 95204.
- [21] A. Omrane, P. Petersson, M. Aldén and M. A. Linne. “Simultaneous 2D flow velocity and gas temperature measurements using thermographic phosphors”. In: *Applied Physics B* 92.1 (2008), pp. 99–102.
- [22] B. Fond, C. Abram, A. L. Heyes, A. M. Kempf and F. Beyrau. “Simultaneous temperature, mixture fraction and velocity imaging in turbulent flows using thermographic phosphor tracer particles”. In: *Optics Express* 20.20 (2012), pp. 22118–22133.
- [23] K. C. Y. Kueh, T. C. W. Lau, G. J. Nathan and Z. T. Alwahabi. “Single-shot planar temperature imaging of radiatively heated fluidized particles”. In: *Optics Express* 25.23 (2017), pp. 28764–28775.

- [24] E. W. Lewis, T. C. W. Lau, Z. Sun, Z. T. Alwahabi and G. J. Nathan. “Insights from a new method providing single-shot, planar measurement of gas-phase temperature in particle-laden flows under high-flux radiation”. In: *Experiments in Fluids* 62.4 (2021), p. 80.
- [25] G. Tea, G. Bruneaux, J. T. Kashdan and C. Schulz. “Unburned gas temperature measurements in a surrogate Diesel jet via two-color toluene-LIF imaging”. In: *Proceedings of the Combustion Institute* 33.1 (2011), pp. 783–790.
- [26] C. Jainski, L. Lu, V. Sick and A. Dreizler. “Laser imaging investigation of transient heat transfer processes in turbulent nitrogen jets impinging on a heated wall”. In: *International Journal of Heat and Mass Transfer* 74.Supplement C (2014), pp. 101–112.
- [27] E. W. Lewis, T. C. W. Lau, Z. Sun, Z. T. Alwahabi and G. J. Nathan. “Luminescence interference to two-colour toluene laser-induced fluorescence thermometry in a particle-laden flow”. In: *Experiments in Fluids* 61.4 (2020), p. 101.
- [28] M. Luong, W. Koban and C. Schulz. “Novel strategies for imaging temperature distribution using Toluene LIF”. In: *Journal of Physics: Conference Series* 45.1 (2006), p. 133.
- [29] T. C. W. Lau and G. J. Nathan. “Influence of Stokes number on the velocity and concentration distributions in particle-laden jets”. In: *Journal of Fluid Mechanics* 757 (2014), pp. 432–457.
- [30] W. Koban, J. D. Koch, R. K. Hanson and C. Schulz. “Absorption and fluorescence of toluene vapor at elevated temperatures”. In: *Physical Chemistry Chemical Physics* 6.11 (2004), pp. 2940–2945.
- [31] S. Faust, M. Goschütz, S. A. Kaiser, T. Dreier and C. Schulz. “A comparison of selected organic tracers for quantitative scalar imaging in the gas phase via laser-induced fluorescence”. In: *Applied Physics B* 117.1 (2014), pp. 183–194.
- [32] W. Koban, J. D. Koch, R. K. Hanson and C. Schulz. “Oxygen quenching of toluene fluorescence at elevated temperatures”. In: *Applied Physics B* 80.6 (2005), pp. 777–784.
- [33] T. C. W. Lau and G. J. Nathan. “The effect of Stokes number on particle velocity and concentration distributions in a well-characterised, turbulent, co-flowing two-phase jet”. In: *Journal of Fluid Mechanics* 809 (2016), pp. 72–110.

- [34] Z. T. Alwahabi, K. C. Y. Kueh, G. J. Nathan and S. Cannon. “Novel solid-state solar thermal simulator supplying 30,000 suns by a fibre optical probe”. In: *Optics Express* 24.22 (2016), A1444–A1453.
- [35] N. Siegel, M. Gross, C. Ho, T. Phan and J. Yuan. “Physical Properties of Solid Particle Thermal Energy Storage Media for Concentrating Solar Power Applications”. In: *Energy Procedia* 49 (2014), pp. 1015–1023.
- [36] K. C. Y. Kueh, T. C. W. Lau, G. J. Nathan and Z. T. Alwahabi. “Non-intrusive temperature measurement of particles in a fluidised bed heated by well-characterised radiation”. In: *International Journal of Multiphase Flow* 100 (2018), pp. 186–195.
- [37] I. Gillandt, U. Fritsching and K. Bauckhage. “Measurement of phase interaction in dispersed gas/particle two-phase flow”. In: *International Journal of Multiphase Flow* 27.8 (2001), pp. 1313–1332.
- [38] N. Siegel, M. Gross and R. Coury. “The Development of Direct Absorption and Storage Media for Falling Particle Solar Central Receivers”. In: *Journal of Solar Energy Engineering* 137 (2015), p. 041003.
- [39] F. Incropera, D. Dewitt, T. Bergman and A. Lavine. *Fundamentals of heat and mass transfer*. 6th ed. Wiley, 2007.
- [40] D. Modarress, H. Tan and S. Elghobashi. “Two-component LDA measurement in a two-phase turbulent jet”. In: *AIAA Journal* 22.5 (1984), pp. 624–630.

Appendix F

Paper IV - The effect of instantaneous particle distributions on the gas-phase temperature in an unsteady particle-laden jet heated with high-flux radiation

This chapter presents the published journal article:

Lewis, E. W., Lau, T. C. W., Sun, Z., Alwahabi, Z. T. and Nathan, G. J. (2022), "The effect of instantaneous particle distributions on the gas-phase temperature in an unsteady particle-laden jet heated with high-flux radiation", *International Journal of Multiphase Flow* 153.

The content of this chapter is identical to that of the published article, with the following exceptions:

1. The typesetting and referencing style may have been altered for consistency within the thesis.
2. The position and sizing of the figures and tables may differ.

Statement of Authorship

Title of Paper	The effect of instantaneous particle distributions on the gas-phase temperature in an unsteady particle-laden jet heated with high-flux radiation
Publication Status	<input type="checkbox"/> Published <input type="checkbox"/> Accepted for Publication <input checked="" type="checkbox"/> Submitted for Publication <input type="checkbox"/> Unpublished and Unsubmitted work written in manuscript style
Publication Details	Lewis, E. W., Lau, T. C. W., Sun, Z., Alwahabi, Z. T. and Nathan, G. J., "The effect of instantaneous particle distributions on the gas-phase temperature in an unsteady particle-laden jet heated with high-flux radiation", submitted to International Journal of Multiphase Flow October 2021

Principal Author

Name of Principal Author (Candidate)	Elliott W. Lewis		
Contribution to the Paper	Designed experimental arrangement and undertook experiments, developed data processing methods, interpreted data, wrote manuscript.		
Overall percentage (%)	70		
Certification:	This paper reports on original research I conducted during the period of my Higher Degree by Research candidature and is not subject to any obligations or contractual agreements with a third party that would constrain its inclusion in this thesis. I am the primary author of this paper.		
Signature		Date	1/11/2021

Co-Author Contributions

By signing the Statement of Authorship, each author certifies that:

- i. the candidate's stated contribution to the publication is accurate (as detailed above);
- ii. permission is granted for the candidate to include the publication in the thesis; and
- iii. the sum of all co-author contributions is equal to 100% less the candidate's stated contribution.

Name of Co-Author	Timothy C. W. Lau		
Contribution to the Paper	Co-supervised experimental design, assisted with data analysis, edited the manuscript.		
Signature		Date	1/11/2021

Name of Co-Author	Zhiwei Sun		
Contribution to the Paper	Supervised the experimental setup and data collection, assisted with interpretation of data, and edited the manuscript.		
Signature		Date	1/11/2021

Name of Co-Author	Zeyad T. Alwahabi		
Contribution to the Paper	Designed research concept, co-supervised experimental work and data interpretation.		
Signature		Date	

Name of Co-Author	Graham J. Nathan		
Contribution to the Paper	Co-supervised experimental design, assisted with the interpretation of results and edited the manuscript.		
Signature		Date	9/11/2021

The effect of instantaneous particle distributions on the gas-phase temperature in an unsteady particle-laden jet heated with high-flux radiation

Elliott W. Lewis^{1,3}, Timothy C. W. Lau^{1,3,4}, Zhiwei Sun^{1,3},
Zeyad T. Alwahabi^{2,3}, and Graham J. Nathan^{1,3}

¹*School of Mechanical Engineering, University of Adelaide, Australia*

²*School of Chemical Engineering and Advanced Materials, University of Adelaide, Australia*

³*Centre for Energy Technology, University of Adelaide, Australia*

⁴*UniSA STEM, University of South Australia, Australia*

Abstract

Detailed simultaneous planar measurements of particle number density and gas-phase temperature were performed in radiatively heated particle-laden jet with average particle volumetric loadings in the range $0.625\text{-}1.4 \times 10^{-3}$, which is within the transition region between the two- and four-way coupling regimes, to evaluate the correlation between the local particle volume fraction and temperature for inertial particles with a series of diameter distributions and radiative heating powers. Utilising novel optical measurement and image processing techniques, together with Voronoi analysis, regions of high instantaneous particle number density and localised regions of high/low gas-phase temperatures were identified. The results show that the particle volume fraction measured within the identified ‘hot regions’ was more than 1.5 times greater than the mean value for each case, while within the ‘cold regions’ the particle volume fraction was typically less than the mean. Similarly, the temperature around individual particles was found to increase with an increase in the local particle volume fraction, while the variation in local gas temperature in the vicinity of particles increases with a decrease in particle diameter. Furthermore, the temperature surrounding particles that were determined

to be within closely spaced cluster regions (which form in the present measurements due to the random distribution of particles in the flow) was found to be greater than that around particles outside of clusters, even for the same local particle volume fraction (measured in a radius of 0.1 times the jet pipe diameter around each particle). The particle distributions were found to closely match a random Poisson distribution, consistent with the high particle Stokes numbers ($86 \leq Sk_D \leq 514$), and are not affected by the presence of radiative heating, implying that any flow phenomena induced by thermal gradients in the flow negligibly influence the particles in the near field of the jet for the conditions investigated here.

1 Introduction

Non-isothermal particle-laden flows with strong radiative heat transfer are relevant to a range of processes in industrial systems, including mineral pre-heating [1], in flames with soot formation [2], particulate fuel burners [3], and for the calcination of alumina and limestone [4, 5]. These calcination processes often require temperatures in excess of 1000 °C for efficient operation, with the energy source historically being the combustion of fossil fuels that contribute significantly to global carbon emissions [6]. As such, the equipment required for these processes needs to be redesigned to transition towards a low-carbon future [7, 8]. Energy sources that have been identified to replace, or be used in conjunction with, the existing combustion-based systems include hydrogen, electricity, biomass, and concentrated solar [9]. Efficient and cost-effective optimisation of new systems designed to incorporate non-combusting sources requires reliable, predictive models of the particle-laden flow. However, the current models are limited by a lack of understanding of fundamental heat transfer processes within these flows, partially due to complex, non-linear particle-fluid interactions [10, 11]. Additionally, there is currently a lack of high quality, detailed experimental data for model validation. Therefore, the overall objective of this investigation is to provide high quality experimental data to increase the understanding of heat transfer within non-isothermal particle-laden flows and to support the development of reliable numerical design tools.

Radiative heating of particle suspensions has been increasingly utilised in a range of practical systems such as the indirect calcination in a cement plant [12], combustion devices [3, 13, 14], and in particle-based concentrated solar thermal (CST) receivers [15]. In each of these reactors there is strong radiative heat transfer both from external sources to the particle feedstock (e.g., solar radiation, heated walls, flames) as well as from heated/combusting

particles. The radiative heat transfer becomes particularly significant at the temperatures required for mineral transformation and particle combustion, because: 1) the emissivity of the particles is typically close to 1 [14, 16], and 2) the radiative emission scales with ΔT^4 , where ΔT is the temperature difference to the surroundings, while convection scales linearly with ΔT . As such, understanding of the radiative heat transfer interactions within such systems is critical for the accurate prediction of process temperatures, efficiencies, and emissions [17]. For indirect calcination, the suspended powdered feedstock flows through a cavity with the walls heated using an external source (typically combustion or electrical). The thermal energy is subsequently transferred to the gas and particles by convection and radiation, providing high temperatures while any products from the conversion of feedstock remain physically separated from the heating source. Similarly, CST vortex receivers, in which a swirling particle suspension is transported through an irradiated cylindrical cavity, have shown good potential to replace existing combustion reactors in laboratory-scale experiments [18, 19]. The heated particles in such flows can be used either as a feedstock for material transformation [20] or for the absorption of sensible heat [21]. An alternative CST receiver configuration is the falling particle receiver, in which a curtain of free-falling absorptive particles (typically composed of a ceramic material with a diameter of order 0.1 mm to 1 mm) are directly irradiated by concentrated sunlight for use as heat transfer media or thermal energy storage [22]. Despite the wide range of existing and potential applications utilising highly inertial particles in radiatively heated particle-laden flows, detailed, in-situ measurements of the flow are currently limited [23, 24]. Hence, there is a need for further investigation of the fundamental heat transfer processes and particle-fluid interactions in the flow.

In particle-based systems with strong radiative heating from an external source, the proportion of inlet radiation that is absorbed by the particles increases with particle number density due to an increase in the total particle cross-sectional area [22]. However, for a constant particle diameter distribution, the average temperature of particles at the outlet has been found to decrease with an increase in particle volume fraction, because attenuation of the incident radiation by particles decreases the average radiative heating flux with path length through the flow [25]. Similarly, spatially-resolved measurements of a radiatively-heated particle-laden flow have shown that the gas temperature was greater on the side of the flow closer to the radiative heating source than that on the far side [26]. Additionally, significant variations in the instantaneous gas temperature were observed, with these variations attributed to the non-uniform instantaneous particle distributions. This relationship between local particle volume fraction and temperature has also

been identified and evaluated using single point detectors in a channel flow with radiative heating [24]. Together, these previous studies have demonstrated that the presence of radiation significantly influences the already complex multi-phase dynamics in particle-laden flows. However, despite the advancements made by these studies, current understanding of radiatively heated particle-laden flows is limited by the lack of well-resolved data (both spatially and temporally) of the instantaneous distributions of temperature for either phase in well-characterised particle-laden flows with strong thermal gradients (i.e., high heating rates).

The particle volume fraction ($\phi = \dot{V}_p/\dot{V}_f$, where \dot{V}_p and \dot{V}_f are the respective volumetric flow rates of the particles and fluid) is a key parameter in particle-laden flows that significantly influences the particle-fluid dynamics. For flows with $10^{-6} < \phi < 10^{-3}$, called the two-way coupling regime, the momentum exchange between the particles and fluid is sufficient for the flow field of the fluid to differ significantly from that of the single-phase flow [27]. With further increasing ϕ , the flow transitions to the four-way coupling regime, in which particle-particle interactions are also important in addition to the particle-fluid momentum exchange. Importantly, the majority of applications utilising particle-laden flows operate in turbulent conditions with $\phi > 10^{-4}$, so that these coupling effects must be considered to allow accurate characterisation of the complex particle-fluid interactions within these systems [2, 18, 22]. Additionally, in these regimes optical effects such as radiation attenuation and multiple scattering become important [26], which leads to challenges in obtaining well-resolved experimental data. These flows with relatively high particle volumetric loading are also challenging to model numerically due to the large number of particles that are required to be simulated, leading to the desirability to introduce simplifying assumptions [10]. However, there is currently a lack of experimental measurements available of ‘densely’ seeded particle-laden flows to verify such assumptions, particularly for systems with strong radiative heating.

Another key parameter that influences the particle-fluid interactions is the particle Stokes number $Sk = \frac{\tau_p}{\tau_f}$, which characterises how closely a particle will follow flow motions of a given scale. Here, τ_p is the particle response time and τ_f is a characteristic time scale of the flow. The Stokes number has also been shown to characterise the formation of particle ‘clusters’, which is a term that is used to denote highly localised flow regions in which the particles accumulate [28]. Hence this term should not be confused with aggregates of particles that are physically connected. Regions of locally high particle volume fraction occur in the flow through two primary mechanisms: 1) from random variations in the particle motion, resulting in particle distributions

that are well described by a Poisson distribution and 2) from aerodynamic interactions with the flow, which is particularly significant for particles with $Sk \approx 1$ [29, 30]. In flows with sufficiently strong radiative heating these variations in the particle distribution can lead to thermal gradients in the gas from convection of sufficient magnitude to generate additional flow phenomena such as buoyancy, which can further modify the velocity and temperature of both phases as well as the particle distributions [31, 32]. The strong temperature gradients in the flow arising from the combination of these complex, coupled, non-linear interactions ultimately affect the stability, efficiency, and emissions of processes utilising non-isothermal particle-laden flows. However, the effect of these variable particle distributions on the gas-phase temperature field for flows with radiatively heated inertial particles of relatively high Stokes number ($Sk > 100$) is yet to be analysed.

The gas-phase temperature is one of the key parameters required for full characterisation of the heat transfer in radiatively heated particle-laden flows. Additionally, data with high spatial and temporal resolution are required to evaluate the instantaneous thermal gradients within the flow. While direct numerical simulation (DNS) offers the potential to provide this data, fully-resolved simulations of densely seeded particle-laden flows under radiatively heated conditions remain prohibitively expensive in terms of computational time [10]. Therefore, further improvement of the current understanding requires well-resolved experimental data of the gas-phase temperature distributions. Laser-based methods are well suited to provide non-intrusive measurements [33], with commonly used planar gas-phase thermometry techniques including Rayleigh scattering [34], coherent anti-Stokes Raman scattering [35], and laser induced fluorescence (LIF) of a flow tracer [36]. Utilisation of these methods in a flow with particles requires separation of the thermometry signal from the scattered laser light, with the latter typically stronger than the thermometry signal by several orders of magnitude [37]. Additionally, uncertainties in the signal intensity are influenced by attenuation of the probe laser, signal trapping, and multiple scattering [38]. To overcome these challenges, the technique of two-colour LIF has previously been used in conditions with strong optical interference [39, 40], including in particle-laden flows [41]. Two-colour LIF thermometry utilises the temperature dependence of the fluorescence emission spectrum from a suitable tracer seeded into the flow. The temperature is determined using the ratio of fluorescence emission intensity measured within two wavelength bands, which are separated using optical filtering [42]. The advantage of this method is that the thermometry signal is optically separated from the laser scattering due to Stokes shift (i.e., the fluorescence is emitted at wavelengths longer than that of the excitation laser). Additionally, provided that the two signals traverse the same optical

path through the flow, the calculated ratio is independent of spatial variations in the laser power and tracer concentration. Such variations are particularly significant in particle-laden flows because of attenuation of the excitation beam and signal trapping [26, 38]. Hence, two-colour LIF has been chosen as the method to obtain the requisite planar, well-resolved measurements of the gas-phase temperature for the present investigation.

Despite previous measurements identifying highly variable temperature distributions in radiatively heated particle-laden flows due to the non-uniform particle distribution [24, 26, 43], there is still a need for quantitative assessments of the instantaneous temperature distributions. Therefore, the main objective of the present investigation is to meet this need using simultaneous measurements of the instantaneous spatial distributions of both the gas-phase temperature and particle volume fraction for a radiatively heated particle-laden flow with inertial particles of $Sk \gg 1$ at loadings relevant to practical particle-based systems with strong radiative heat transfer, such as those used in mineral calcination and vortex/falling-particle based CST receivers. The present study investigates in detail the influence of the local, instantaneous particle distribution on the gas-phase temperature of the radiatively heated flow, following recent work by the authors in the same experimental arrangement of a particle-laden pipe jet heated using a circular beam of high-flux radiation near to the jet exit plane [26, 43]. The jet issuing from a long, round pipe used in the present experiments closely matched the arrangement previously used for isothermal particle-laden flow measurements by Lau and Nathan [44, 45] and Njue et al. [46], to provide a well-defined flow. The present investigation aims to quantify the degree of the spatial temperature variations measured in the same well-characterised, radiatively heated particle-laden flow for volumetric loadings within the transition region between the two- and four-way coupling regimes. A further aim of the present study is to assess the correlation between the local particle volume fraction and gas-phase temperature in the flow. Additionally, the present investigation aims to assess the significance of any motions induced by thermal gradients generated following the absorption of high-flux radiation on the spatial distribution of particles in the flow.

2 Methodology

The flow consisted of a particle-laden jet issuing from a long round pipe ($D = 12.6$ mm, $L = 2100$ mm) into a weak co-flow, generated from a co-annular pipe of diameter 69 mm with the outlet plane positioned 6 mm upstream from that of the jet, as shown in Figure 1. The particle-laden flow was heated

using a high-flux beam of infra-red radiation centred $1.4D$ from the jet exit plane, with the gas temperature measured using two-colour LIF with toluene as the tracer and the particle locations determined using laser scattering. The key flow parameters and particle properties are summarised in Table 1. This flow configuration with $L/D > 160$ provides a well-characterised particle-laden jet at the outlet [44]. The experimental arrangement and flow conditions investigated in the present study are identical to those documented by the authors [26, 43], so that only a brief description of the experimental arrangement is provided here.

Toluene was chosen as the fluorescent tracer for two-colour LIF because it has good sensitivity to temperature and has previously been demonstrated to be accurate in conditions with strong optical interference from the combination of laser scattering, particle luminescence, signal trapping, and laser attenuation [39–41]. Nitrogen was employed as the carrier gas for each flow, with both particles and toluene seeded in the jet flow while the annular flow was seeded only with toluene. The pipe jet had a Reynolds number of $Re_D = \frac{\rho_f U_b D}{\mu} = 3000$, where $\rho_f = 1.15 \text{ kg/m}^3$ is the density of the ambient (unheated) flow, $U_b = 3.6 \text{ m/s}$ is the flow bulk mean velocity and $\mu = 1.8 \times 10^{-5} \text{ Ns/m}^2$ is the dynamic viscosity of the ambient flow. The toluene concentration was approximately 0.75% by volume in the jet and approximately 0.25% by volume in the annular flow. A series of distributions of aluminosilicate particles (Carbobeat CP) with median diameters of $\bar{d}_p = 173, 205, 238, \text{ and } 423 \text{ }\mu\text{m}$ were used, with the particle diameter distribution measured for each of these using a Malvern Mastersizer 2000. The measured particle distributions are presented in Figure 2. The resultant jet exit Stokes numbers for each \bar{d}_p are $Sk_D = 86, 121, 163, \text{ and } 514$, respectively. Here, the jet exit Stokes number is based on the large-eddy time-scale, $Sk_D = (\rho_p \bar{d}_p^2 U_b) / (18\mu D)$, where ρ_p is the particle density. Since both the large-eddy length scale and velocity are not expected to vary significantly in the near-field region of the jet [44, 47], this Stokes number is expected to be characteristic of the flow within the entire measurement region investigated in the present experiments ($x/D < 3.7$). The time-averaged particle volumetric loadings in the pipe jet used for the present investigation were $\bar{\phi} = 0.625 \times 10^{-3}, 1 \times 10^{-3}, \text{ and } 1.4 \times 10^{-3}$, which result in the jet flows being in the transition region from the two- to four-way coupling regime.

The thermal response of the particles, together with the particle Biot number, were calculated based on well-established empirical and analytical equations for a heated sphere. The Biot number is given by $Bi = hV_p / A_p k_p$, where V_p is the particle volume, A_p is the particle surface area, $k_p \approx 2$ is a lower bound estimate for the thermal conductivity of the particles [48],

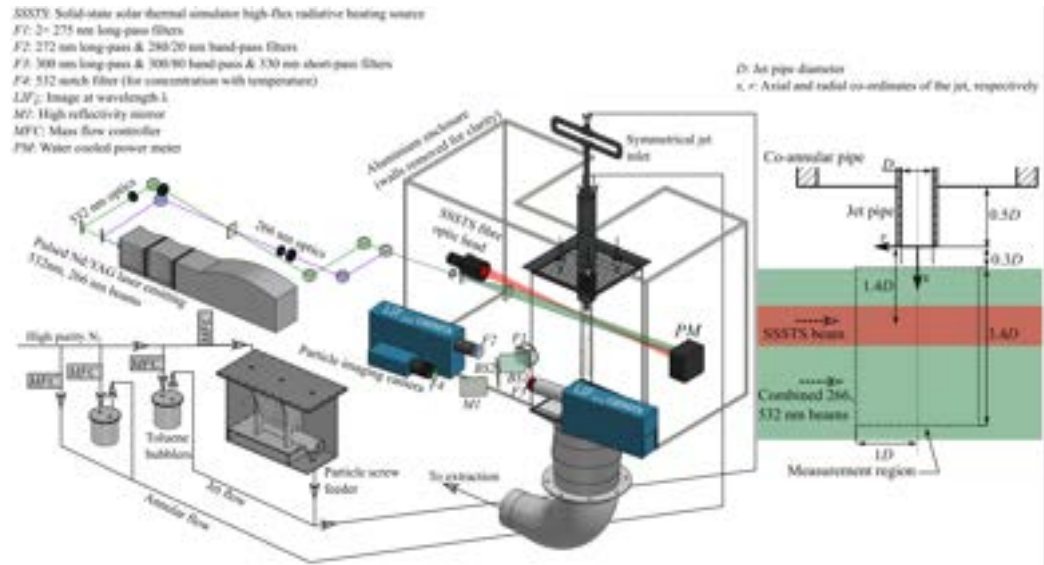


Figure 1: Experimental arrangement for simultaneous planar measurements of the gas-phase temperature, using two-colour LIF, and the particle locations, using laser scattering, in a particle-laden flow heated with high-flux radiation (not to scale).

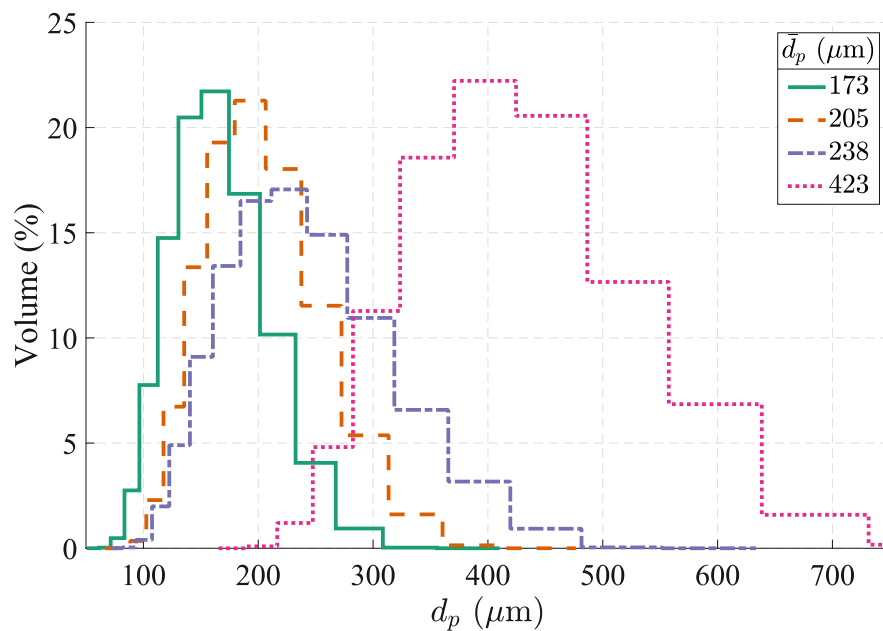


Figure 2: Measured diameter distributions of the particles used in the present investigation.

$h = Nu k_f / \bar{d}_p$ is the convective heat transfer co-efficient, and k_f is the thermal conductivity of the fluid. The Nusselt number for a spherical particle is given by $Nu = 2 + \left(0.4Re_p^{1/2} + 0.06Re_p^{2/3}\right) Pr^{0.4}(\mu/\mu_s)^{0.4}$, and the subscript s indicates the fluid properties estimated at the particle surface. The particle Reynolds number is given by $Re_p = \rho_s U_{slip} \bar{d}_p / \mu_s$, where $U_{slip} \approx 0.7$ m/s is the particle slip velocity, estimated using experimental measurements presented by Gillandt et al. [49] for particles with $\bar{d}_p = 110$ μm , $\bar{\phi} \approx 5 \times 10^{-4}$, and $\rho_p = 2,000$ kg/m^3 measured near to the exit plane of a pipe jet with $Re_D \approx 4,750$ and $Sk_D \approx 39$. The Prandtl number is given by $Pr = c_{p,f} \mu_s / k_{f,s}$, where $c_{p,f}$ is the specific heat capacity of the fluid. The resultant Biot number for the investigated particles is therefore $7.6 \times 10^{-3} < Bi < 9.0 \times 10^{-3}$.

It should be noted that the actual velocity profiles of both the gas and particles are typically dependent on both the particle Stokes number and volumetric loading in the flow, although the influence of Stokes number on the slip velocity is expected to be minor in the near field of the jet for the investigated conditions with $Sk_D \gg 1$ [44]. However, for the present case, even if the slip velocity were to depart from the assumed value by an order of magnitude (i.e., $0.07 < U_{slip} < 7$ m/s), the resultant Biot number range would be $6 \times 10^{-3} < Bi < 0.018$. Since $Bi \ll 1$ for all cases, it can therefore be expected that the temperature distribution within each particle to be uniform throughout the measurement region.

Additionally, the thermal time constant of a radiatively heated spherical particle, given by $\tau_{p,t} = \rho_p c_{p,p} V_p / \dot{Q}'' A_x$, where A_x is the particle cross-sectional area, was calculated to be $6 < \tau_{p,t} < 15$ $\mu\text{s}/\text{K}$ for the investigated particles heated using a radiative flux of $\dot{Q}'' = 42.8$ MW/m^2 . Considering that the bulk velocity of the jet was 3.6 m/s, and assuming that convection is negligible, this implies that the particle temperature would increase by 100 $^\circ\text{C}$ within the central region of the heating beam (which has a diameter of ~ 12 mm) in a distance of 2.2 mm for the $\bar{d}_p = 173$ μm particles and 5.4 mm for the $\bar{d}_p = 423$ μm particles. Similarly, the characteristic particle response time $\tau_{p,a} = \rho_p \bar{d}_p^2 / 18\mu$ was calculated to be in the range of $0.3 < \tau_{p,a} < 1.8$ s, while the particles are within the measurement region for approximately 0.014 s. As such, the observed response of the particles to flow motions is expected to be minor.

The particle-laden flow was heated using high-flux radiation generated using a solid state solar thermal simulator (SSSTS) that provides a collimated, radially-symmetric, infrared (~ 910 nm) beam with a diameter of ~ 12 mm at the focal plane [50]. The SSSTS was operated at a series of output powers up to $\dot{Q}_0 = 2840$ W, with a peak radiative flux on the beam axis of approximately 42.8 MW/m^2 for this power. The beam was aligned per-

Table 1: Key parameters used in the present investigation.

Parameter	Symbol	Value	Units
Pipe jet bulk velocity	U_b	3.6	m/s
Pipe jet Reynolds number	Re_D	3000	-
Annular flow bulk velocity	$U_{a,b}$	0.3	m/s
Particle volumetric loadings	$\bar{\phi}$ ($\times 10^{-3}$)	0.625, 1, 1.4	-
SSSTS heating powers	\dot{Q}_0	0, 910, 1430, 1950, 2410, 2840	W
Particle density	ρ_p	3270	kg/m ³
Particle specific heat	$c_{p,p}(T_p)$	0.7-1.1	kJ/kgK
Particle absorptivity	α	0.89	-
Particle emissivity	ϵ	0.85	-
Median particle diameters	\bar{d}_p	173, 205, 238, 423	μm
Particle Stokes numbers	Sk_D	86, 121, 163, 514	-
Estimated Biot number	Bi	7.6, 7.8, 8.0, 9.0	-
Estimated thermal time constant	$\tau_{p,t}$	($\times 10^{-3}$) 6.1, 7.3, 8.5, 15.1	μs

pendicular to the jet pipe, with the beam axis intersecting the jet centreline 17.5 mm downstream from the exit plane as shown in Figure 1. The power of the beam transmitted through the flow was monitored during operation using a water-cooled power meter positioned down-beam from the wind tunnel (Gentec model HP100A-4KWHE). The fraction of the beam absorbed by the particles was measured to be up to 19% for the flow with $\bar{d}_p = 173 \mu\text{m}$ and $\bar{\phi} = 1.4 \times 10^{-3}$. The absorption of the beam by the particles, estimated from the transmission to the power meter and assuming that the absorptivity of the present particles is similar to that of the particles used by Siegel et al. [16] ($\alpha = 0.89$), was found to decrease with a decrease in total particle cross-sectional area (i.e., an increase in \bar{d}_p and a decrease in $\bar{\phi}$) [43]. The entire region exposed to the heating beam, from the output head to the power meter, was contained within an interlocked aluminium enclosure for safety.

A 266 nm beam from the fourth harmonic of a Nd:YAG laser (Quintel Q-smart), formed into a sheet passing through the jet centreline with a height of 50 mm and thickness 0.6 mm, was used to excite the toluene for two-colour LIF measurements. The second harmonic beam from the same laser (532 nm) was also formed into a sheet co-planar with the 266 nm sheet, with the resultant laser scattering from particles imaged simultaneously with the LIF measurements. The spatially averaged laser pulse fluences for the 266 nm and 532 nm sheets were 50 and 1.4 mJ/cm², respectively.

Optical filters were used to separate the scattered laser light and fluorescence emissions into three channels: two for the two-colour LIF measurements with transmission bands of 285 ± 5 nm and 315 ± 10 nm, respectively, and one to image the scattering from particles at 532 nm. The full details of filters used, together with the transmission bands for the two-colour LIF channels, are presented by Lewis et al. [26]. Each channel shared the same optical path through the flow, so that any attenuation or signal trapping effects were identical. Two separate PCO Di-Cam intensified sCMOS cameras were used to image the filtered fluorescence channels, using a Soderlens Objectif UV 100 F/2.8 lens and a spherical UV lens (Thorlabs LB4821) to focus the channels centred at 315 nm and 285 nm, respectively. The spatial resolution of these channels was 17.8 px/mm for S_{285} and 15.5 px/mm for S_{315} . A PCO.2000 CCD with a Tamron macro 80-120 mm lens was used to image the laser scattering from particles, with a spatial resolution of 27.3 px/mm. Each camera recorded images simultaneously at the laser pulse frequency of 10 Hz, and had a depth of field estimated to be on the order of centimetres (i.e., greater than the laser sheet thickness).

2.1 Image processing

The image processing methods used to determine the gas-phase temperature from the two-colour LIF images and the local particle volume fraction from the images of laser scattering are described in detail by Lewis et al. [26]. Therefore, only a brief summary of the image processing method is presented here, with typical images to illustrate the key processes being presented in Figure 3. Firstly, background images for all cameras, collected under identical conditions to the main experiment except with the flow switched off, were subtracted from each individual image. Images of a target plate of regularly spaced holes backlit using a UV lamp were then used to align channel S_{285} with S_{315} . Matching points were selected on each image with S_{285} then transformed using a least-squares fit with bi-linear interpolation, with the resultant images aligned to within approximately 1 pixel. The fluorescence images were further aligned to sub-pixel accuracy by minimising the spatial variation in the fluorescence intensity ratio within a region upstream from the heating beam but near the edge of the jet. This region was selected because it has strong gradients in the toluene concentration, so that a slight misalignment between cameras leads to a significant variation in the measured ratio. The pixels from each instantaneous fluorescence image with a signal intensity $< 15\times$ that of the dark charge were considered to be unreliable and removed from further analysis [41].

The ratio of intensity for each spatially matched pixel was calculated, from which the temperature was derived using a calibration function. The instantaneous temperature images were then smoothed using a 5×5 median filter to reduce the influence of noise on the data, which resulted in a net measurement volume of approximately $0.3 \times 0.3 \times 0.6 \text{ mm}^3$. The region of interest measured by each camera was bounded by $0.3 < x/D < 3.7$ and $|r/D| < 1$, where x is the axial direction, parallel to the jet axis, and r the radial direction, parallel to the laser sheets, with the origin on the jet axis at the outlet plane.

The calibration of intensity ratio to temperature was completed in the same experimental arrangement as for the main experiment, except without particles in the flow and with the central jet pipe heated directly using a controllable electric tape heater. Fluorescence images were recorded at a series of flow temperatures, with the temperature simultaneously measured using a thermocouple inserted into the flow near to the jet exit plane. The resultant best-fit relationship between the intensity ratio and temperature is well-described by a linear function of the form $S_{315}/S_{285} = 4.50 \times 10^{-3}T_g + 0.98$, for T_g in $^{\circ}\text{C}$ ($R^2 = 0.9989$, see also Lewis et al. [26] for more details). It should be noted that this calibration relationship is accurate only for

the present experimental arrangement, and not valid broadly, because the relationship is dependent on the filters, optics, and cameras used.

For the measurements of laser scattering by particles, a binary mask was generated using a threshold value of $10\times$ the standard deviation of the dark charge, to ensure sufficient separation of the scattering from the camera noise. The centres of individual particles were then measured by calculating the intensity centroid. Overlapping particles in each image (i.e., particles at similar locations within the measurement plane but at different depths within the laser sheet) were separated, where possible, using an in-house Matlab code. This was performed by identifying contiguous regions of intensity greater than the threshold that had an area significantly larger than the expected particle area. If this region contained two or more intensity peaks with the intensity distribution surrounding each peak well approximated by a 2D Gaussian distribution, the region was considered to contain multiple particles (corresponding to the number of peaks). The location of the individual particles was then calculated from the location where the Gaussian distribution was at its peak. The particle number density (n_p) of each image was then calculated from $n_p = N_p/V_{532}$, where N_p is the total number of particles detected in the image, $V_{532} = 3.4D \times 1.1D \times (w + d_p)$ is the effective volume from which particles are detected, and $w = 0.6$ mm is the laser sheet thickness.

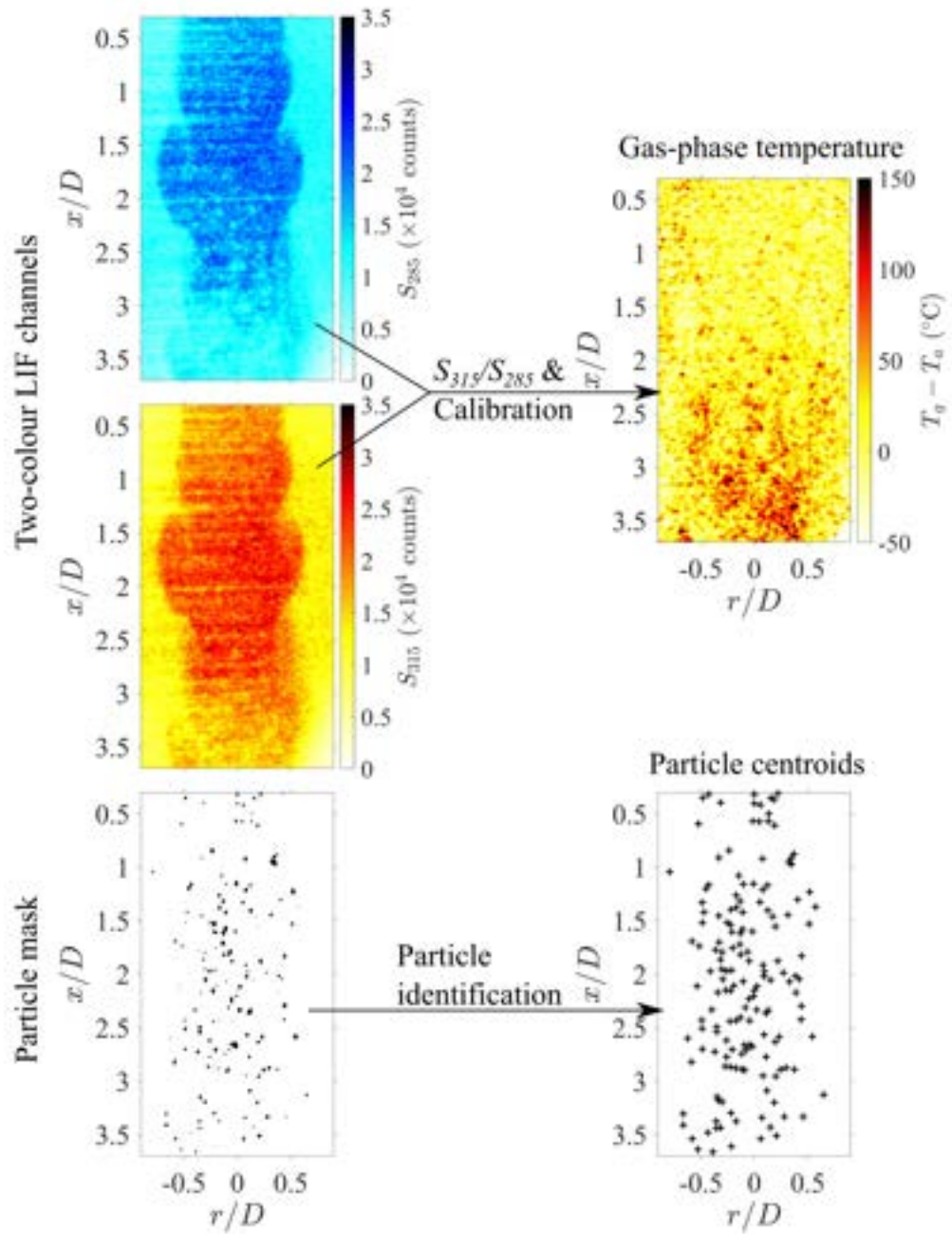


Figure 3: Instantaneous images recorded simultaneously for the two fluorescence channels, S_{285} and S_{315} , and the binary mask of particles from the laser scattering channel, following background subtraction and spatial alignment, together with the processed gas-phase temperature distribution and particle centroid locations.

2.2 Error analysis

Since the errors to the two-colour LIF measurement applied to a particle-laden flow have been previously discussed in detail [26, 41], only a brief summary is provided here. The primary sources of random errors for the present measurement are laser scattering from particles, attenuation of the excitation laser sheet, and signal trapping. Under conditions identical to the present experiment, it was found that the effect of attenuation and signal trapping is to reduce the fluorescence intensity of some regions in the flow by up to 45% [43]. However, in the present experiments, it was found that the signal-to-noise ratio (SNR), defined as the ratio of the signal intensity to the standard deviation of the dark charge, was > 145 even in the regions most impacted by signal trapping and attenuation. Therefore, based on previous measurements of bias error for the conditions used in the present experiments [26], for a SNR > 145 and for $20\text{ }^{\circ}\text{C} \leq T_g \leq 150\text{ }^{\circ}\text{C}$, the bias error of the temperature due to signal trapping and attenuation is estimated to be $< 8^{\circ}\text{C}$.

The measured pixel-to-pixel standard deviation of the unheated flow with particles was $17.7\text{ }^{\circ}\text{C}$, while the pixel-to-pixel uncertainty in the regions most strongly affected by attenuation and signal trapping was measured to be $40\text{ }^{\circ}\text{C}$. While these uncertainties are relatively large, they were significantly reduced by spatial-averaging, with the uncertainty proportional to $1/N_{pix}^{0.5}$ (where N_{pix} is the number of pixels used in the averaging procedure). In the present study, the spatial average of temperature was calculated as the mean temperature of the pixels within a radius of $0.1D$ surrounding each particle (see Section 2.4 for further details). The number of pixels within these regions was typically $N_{pix} \approx 1,200$ pixels, therefore the estimated uncertainty of the spatially-averaged temperature reduced to $< 1.2\text{ }^{\circ}\text{C}$. Noting that the pixel size is $64\text{ }\mu\text{m}$, this results in an effective probe volume in the spatially-averaged temperatures around particles of approximately $2.5 \times 2.5 \times 0.6\text{ mm}^3$.

The detected particles typically have a peak SNR of > 100 . Therefore, the accuracy of the method used to determine the number of particles within each image is relatively high. Furthermore, the particle distribution measured at the pipe jet exit using this method [26] has previously been shown to provide results consistent with literature under similar conditions [44, 51]. The local volume fraction for each investigated region was calculated using the area and number of particles detected within the region, using the assumption that each particle had a volume equal to that of the median particle. Since the actual particles have a size distribution, taking one standard deviation either side of the median particle diameter (see Figure 2) results in a range

of volumes for each individual particle of $\sim 50 - 200\%$ of the volume for the median particle diameter. However, the presented results for the local volume fraction were typically comprised of the average of several hundred individual particles. As such, the presented values of local volume fraction have an uncertainty of approximately 10% of the average due to the size distribution.

There is also uncertainty in the identification of particles (and their positions) for cases where there is significant overlap between particle images. Analysis of the particle identification scheme showed that the uncertainty of locating a particle increases significantly if the centre of one particle is within the radius of another. Using the results from the random particle simulation (see Section 2.5) for the case with the greatest number of overlapping particles (corresponding to $\bar{d}_p = 173 \mu\text{m}$ and $\bar{\phi} = 1.4 \times 10^{-3}$) and the imaging size of particles following scattering (e.g., for the $\bar{d}_p = 173 \mu\text{m}$ the typical pixel diameter is 6 pixels, corresponding to $220 \mu\text{m}$), the total number of particles within the laser sheet will significantly overlap is $\sim 2\%$. Additionally, uncertainty in locating particles may increase with beam distance through the flow due to attenuation of the laser sheet. Using the present particle detection threshold, a reduction of local laser sheet intensity of approximately 90% relative to that of the peak will result in a particle not being counted. On this basis, and using the data from the random particle simulation, fewer than 5.5% of the particles were estimated to be in regions with a local laser sheet intensity less than 10% of the peak at the down-beam edge of the jet. Divergence of the laser sheet is another potential source of uncertainty of the particle volume fraction calculation. However, this was mitigated by the use of a $f = +2000 \text{ mm}$ lens to focus the laser sheet to the $\sim 20 \text{ mm}$ wide region of interest. The resultant divergence of the beam across the measurement region was calculated to be at most $30 \mu\text{m}$, or 5% of the laser sheet width. Therefore, the effects of particle image overlap, laser sheet attenuation, and divergence of the laser sheet are expected to be minor in the present experiments.

2.3 Hot and cold region determination

A new method was developed to determine the regions of the flow where the instantaneous temperature is significantly higher or lower than the average. These are termed ‘hot regions’ and ‘cold regions’, respectively. This method uses quantitative criteria, whose values can be varied systematically, to define the hot and cold regions in a manner that is similar to the method used previously to identify and classify particle clusters [45]. This method is illustrated using a typical instantaneous image for the case with $Sk_D = 86$, $\bar{\phi} = 1.4 \times 10^{-3}$

and $\dot{Q}_0 = 2840$ W, as presented in Figure 4. The spatial variations in the instantaneous image of gas-phase temperature above ambient ($T_g(x, r) - T_a$), within and downstream from the heating region ($0.9 < x/D < 1.9$), can be seen in Figure 4a. The variations in the measured temperature are from a combination of the actual spatial variations in the instantaneous gas temperatures and random errors in the measurements. Although the magnitude of the random errors is typically much smaller than the actual temperature increase measured in the localised hot regions, the pixel-to-pixel random errors result in some pixels registering non-physical values (e.g., regions with $T_g - T_a < 0$ °C). The hot and cold regions within each individual image were determined from a comparison of the instantaneous temperature distribution with the time-averaged value using the following steps:

1. For the time-averaged temperature image $\bar{T}_g(x, r) - T_a$, calculated as the average of > 100 individual images for each flow condition, (Figure 4b), the radially averaged temperature is computed for each row of pixels across the jet over the range $|r/D| < 0.3$. This results in a column vector with values corresponding to the jet temperature as a function of distance down-stream from the jet exit. This column vector was then replicated across the width of the original image to form the image $\bar{T}_{g,CL}(x) - T_a$, as shown in Figure 4c.
2. The normalised temperature was then calculated for the array using the equation:

$$\Theta(x, r) = \frac{T_g(x, r) - T_a}{\bar{T}_{g,CL}(x) - T_a}, \quad (1)$$

which was evaluated on an element-wise (i.e., pixel-by-pixel) basis. This normalisation was performed using $\bar{T}_{g,CL}(x)$, rather than $\bar{T}_g(x, r)$, because large errors can occur in regions with $\bar{T}_g(x, r) \approx 0$, such as near to the jet edge. Regions with $\bar{T}_{g,CL}(x) - T_a < 3$ °C (i.e., where the denominator term used to calculate $\Theta(x, r)$ is close to zero) were considered unreliable and hence were removed from further analysis.

3. Each individual image of $\Theta(x, r)$ was then smoothed using a circular Gaussian filter kernel f with a characteristic smoothing length scale $L_S = 4\sigma$, where σ is the standard deviation of the Gaussian function, expressed as:

$$f(m, n) = \exp \left[-8 \left(\frac{m^2 + n^2}{L_S^2} \right) \right], \quad (2)$$

where m and n are the array indices in the r and x directions with respect to the origin, respectively. Using this, the value of each pixel

(i, j) of the smoothed temperature field $\Theta_S(x, r)$ is given by:

$$[\Theta_S]_{i,j} = \left(\sum_{m=-\delta}^{\delta} \sum_{n=-\delta}^{\delta} f_{m,n} [\Theta]_{i-m,j-n} \right) \times \left(\sum_{m=-\delta}^{\delta} \sum_{n=-\delta}^{\delta} f_{m,n} \right)^{-1}, \quad (3)$$

where $\delta = L_s/2$ is chosen for the bounds of the smoothing kernel size. Figure 4d presents the instantaneous, normalised temperature after smoothing with $L_s = 0.1D$.

4. For each individual image, the reference temperature difference, Θ_{ref} , was calculated as the spatial average of $\Theta(x, r)$ in the region of $2.5 < x/D < 3$ and $|r/D| < 0.25$. The hot and cold regions were then identified as regions with $\Theta_S(x, r)$ that differed significantly from this reference. Threshold values were used to separate the hot and cold regions, with the thresholds for the hot and cold regions, ϵ_H and ϵ_C , respectively, calculated as a function of axial distance from the equations:

$$\epsilon_H(x, L_s) = \Theta_{ref} + \frac{k\sigma_T(x, L_s)}{\bar{T}_{g,CL}(x) - T_a} \quad (4)$$

and

$$\epsilon_C(x, L_s) = \Theta_{ref} - \frac{k\sigma_T(x, L_s)}{\bar{T}_{g,CL}(x) - T_a}, \quad (5)$$

where $\sigma_T(x, L_s)$ is the axial profile of the pixel-to-pixel standard deviation of $\Theta_S(x, r)$, calculated from all pixels with $|r/D| < 0.3$. The symbol k represents a multiplier to the standard deviation. The threshold profile calculated for the example image with $L_s = 0.1D$ and $k = 1$ is presented in Figure 4e. The resultant hot and cold regions, overlaid on the image of $\Theta_S(x, r)$, are presented in Figure 4f.

5. The hot/cold regions with an area less than $0.008D^2$ (corresponding to the area of a circle with diameter $0.1D$) were considered to be too small for reliable measurement and thus removed from further analysis.

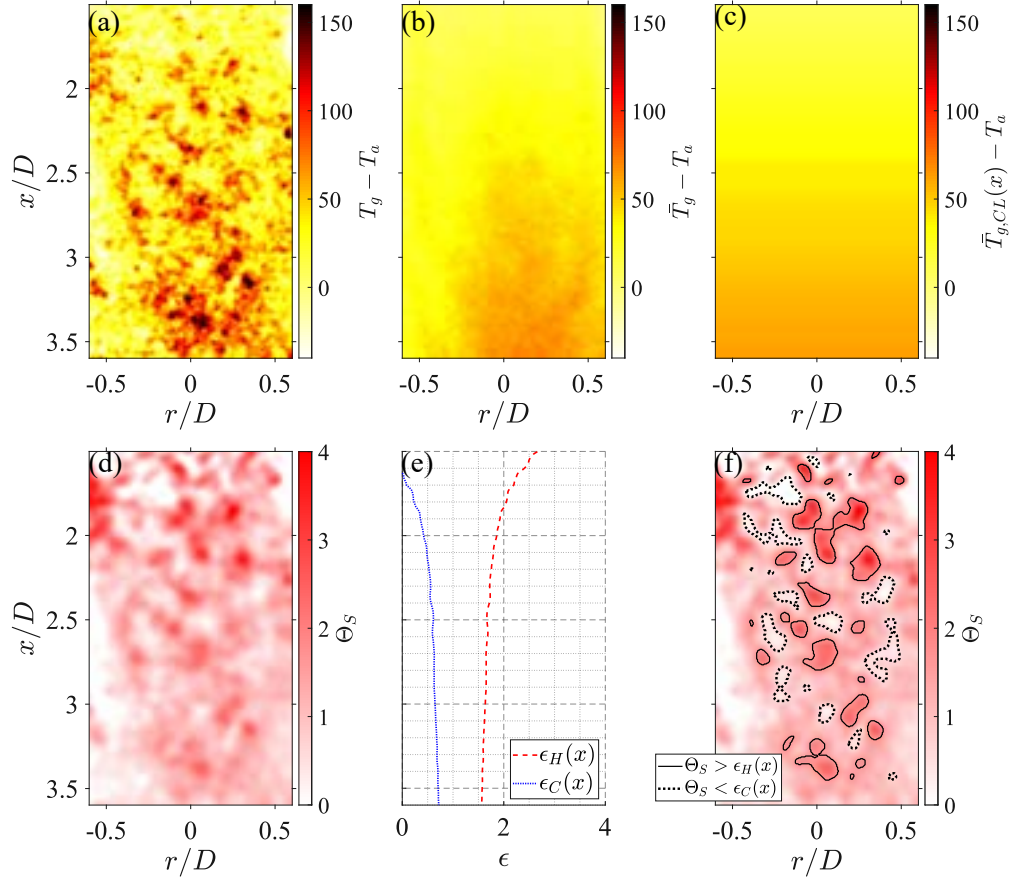


Figure 4: The method used to determine local areas of relative high and low temperature: (a) a typical instantaneous gas-phase temperature image, $T_g - T_a$, (b) the time-averaged temperature image, $\bar{T}_g - T_a$, (c) the axial profile of the time- and radially-averaged temperature in the region $|r/D| < 0.3$ after replication into an array across the width of the original image, $\bar{T}_{g,CL}(x) - T_a$, (d) the smoothed normalised temperature increase from ambient, Θ_S , (e) the thresholds used to determine hot and cold regions, $\epsilon_H(x)$ and $\epsilon_C(x)$, respectively, and (f) Θ_S together with the boundaries of the determined hot and cold regions.

2.4 Particle cluster determination

Flow regions with a relatively high local particle volume fraction (clusters), and those with no nearby particles (voids), were determined from the images of laser scattering using the well-established Voronoi method [30]. An example of the processed laser scattering image is presented in Figure 5a. The Voronoi method involves partitioning the image into cells around each particle centroid, with the region belonging to each cell comprised of the ensemble of locations that are closer to the associated particle than any other. The co-ordinates of the vertices around each cell were used to calculate the area of each individual Voronoi cell, A_{cell} . Cells with vertices outside of the measurement region, such as for particles near to the jet edge, were removed from further analysis. The Voronoi diagram for the example image is presented in Figure 5b.

In the present investigation, particles were defined to be within clusters if two or more adjacent Voronoi cells met the condition:

$$A_{cell}(x) < e_p \bar{A}_{cell}(x) \quad (6)$$

where e_p is a threshold value and \bar{A}_{cell} is the median area of the Voronoi cells, calculated as a function of axial location. A value of $e_p = 0.706$ was chosen for the threshold because this results in 1/3 of all Voronoi cells of a Poisson distribution having an area below the threshold [52]. This constant threshold value was chosen, rather than using an adaptive threshold such as presented by Monchaux et al. [30] for particle cluster determination, because the adaptive threshold method requires the probability density function (PDF) of the cell areas to be calculated. The latter method was considered to be unreliable for the cases with low particle number density investigated here. A constant threshold for cluster determination was also used in the previous analysis performed by Lau et al. [53]. The Voronoi cells that were considered to be clusters are also shown in Figure 5b with blue shading.

Using these definitions, both the gas-phase temperature and local particle volume fraction were calculated within regions of the following size:

1. $< 0.1D$ from the centroid of particles within clusters ($T_{g,Hi}$);
2. $< 0.1D$ from particles that are outside of clusters ($T_{g,Lo}$), and;
3. void regions ($T_{g,Vd}$).

For the present investigation the voids were defined as regions that are further than $0.1D$ from the nearest particle, to match the length scale chosen to identify the hot and cold regions (Section 2.3). The void regions of the

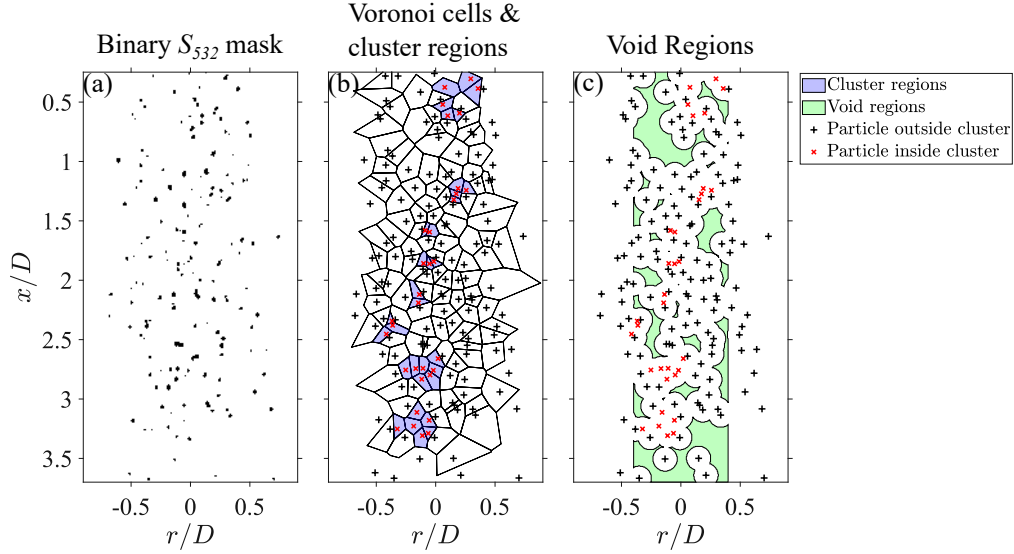


Figure 5: The binary particle mask from S_{532} (a), the resultant particle centroids together with the calculated Voronoi cells and determined clusters (b), and the void locations (c) for a single image from the case with $\bar{d}_p = 173 \mu\text{m}$ and $\phi = 1.4 \times 10^{-3}$.

example image are presented in Figure 5c, together with the locations of particles both inside and outside of clusters. The calculation of the voids was limited to regions with $|r/D| < 0.4$, to avoid bias towards the jet edge regions with a low particle number density and low average local temperature rise. It should be noted that regions where $T_{g,Hi}$ and $T_{g,Lo}$ are measured can overlap for the case where two particles, one of which is considered to be inside of a cluster and the other not, have centroids that are less than a distance $0.2D$ from each other.

2.5 Random particle simulation

A simulation of a random distribution of particles was also performed for each combination of \bar{d}_p and $\bar{\phi}$ employed in the experiment, to assess how closely the random and measured distributions match. This method to simulate the particle distribution is identical to that presented by Lewis et al. [43], so that only a brief summary is presented here. Particle positions were generated randomly in a cylindrical spatial domain with both a length and diameter of $1.5D$ such that the resultant average radial distribution matched previous measurements under identical conditions to the present experiments [26]. In the simulation, only those particles that were located within a volume

corresponding to that of the laser sheet were retained. The particles within this simulated laser sheet were then analysed using the same Voronoi method as was used for the experiments. The results of the Voronoi analysis for the simulated results were compared with the experimental measurements.

3 Results

3.1 Hot and cold region detection sensitivity

The top sub-figure of Figure 6 presents the number of hot and cold regions in the flow that were measured to be larger than the cut-off area of $0.008D^2$ (N_{reg}) normalised by the peak value ($N_{reg,max}$), as a function of L_s for the series of Sk_D investigated in the present study. This assesses the sensitivity of the smoothing length scale used in equations 2 and 3, L_s for the flow with an average particle volume fraction of $\bar{\phi} = 1.4 \times 10^{-3}$ and heating beam power of $\dot{Q}_0 = 2840$ W. The results show that, in general, $N_{reg}/N_{reg,max}$ increases with an increase in L_s for $L_s < 0.075D$ and decreases with an increase in L_s for $L_s > 0.1D$. The peak of $N_{reg}/N_{reg,max}$ occurs for values of $0.075D < L_s < 0.1D$ for each case, which agrees well with what can be visually seen in the instantaneous temperature image (see Figure 4). For these reasons, a smoothing length scale of $L_s = 0.1D$ was used for the present investigation.

The bottom sub-figure of Figure 6 presents the average value of the normalised, smoothed temperature obtained using equations 1-3 within the hot and cold regions (Θ_{reg}) as a function of the standard deviation multiplier used to calculate the threshold in equations 4 and 5, k . The difference between the time-averaged normalised temperature of the flow (i.e., $\Theta = 1$) and the temperature within the detected hot and cold regions can be seen to increase with an increase in k , which is consistent with the threshold values calculated using equations 4 and 5. However, it can be seen that the value of Θ_{reg} is only weakly dependent on k . Because of this, the commonly used statistical value of one standard deviation from the mean (i.e., $k = 1$) was used for the threshold calculations in the present investigation.

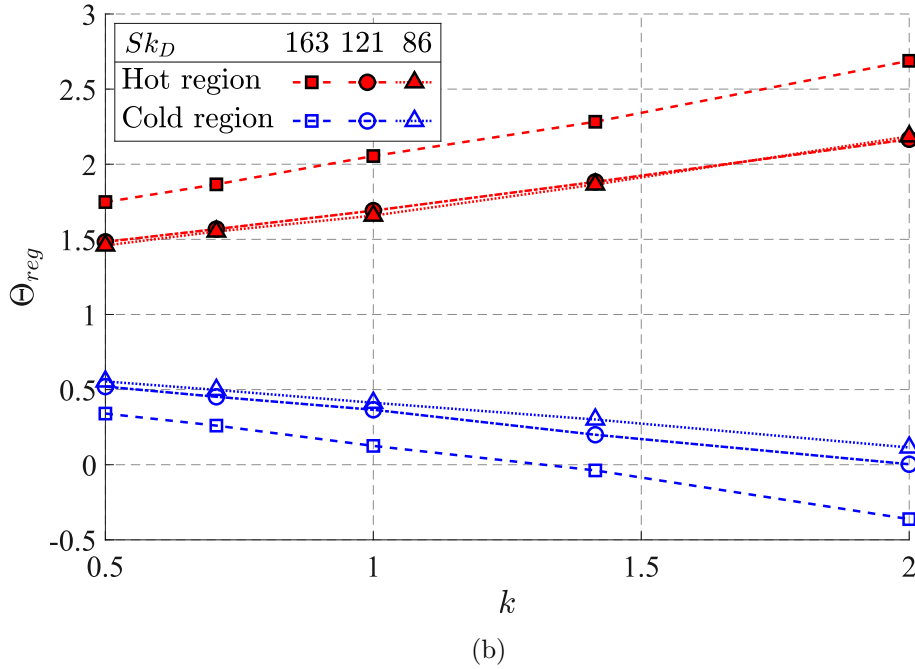
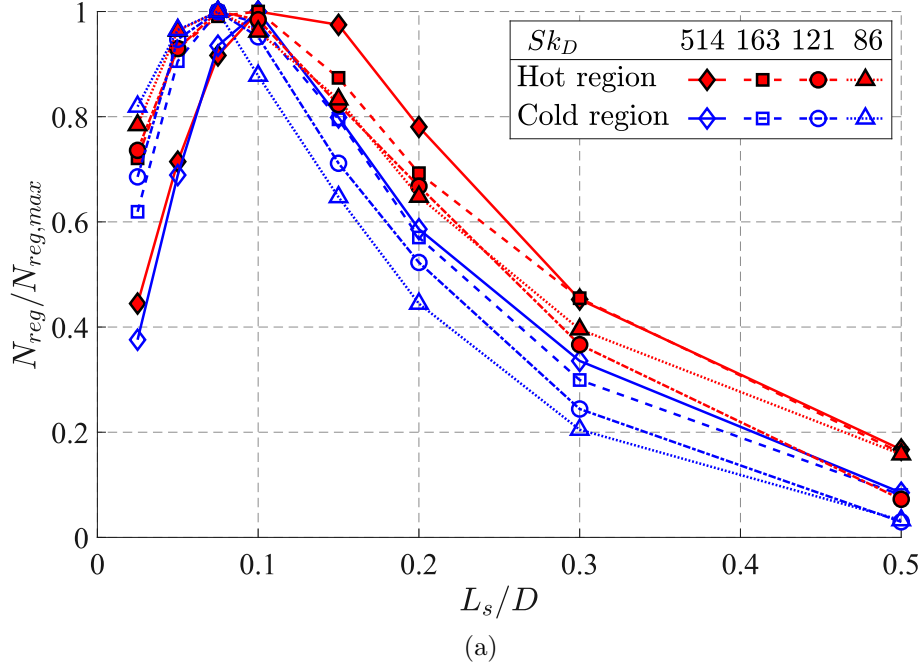


Figure 6: The number of hot and cold regions (N_{reg}) normalised by the peak value as a function of smoothing length scale (a), together with the normalised temperature measured in these regions (Θ_{reg}) as a function of the threshold multiplier, k , (b) for the series of Stokes numbers investigated. The $Sk_D = 514$ case is not presented in the bottom sub-figure because the temperature increase is insufficient for reliable calculation of Θ_{reg} .

3.2 Temperature and particle volume fraction measurements

Figure 7 presents probability density functions (PDF) of both the measured gas-phase temperature above ambient, $T_g - T_a$, (a) and the smoothed normalised temperature, Θ_S , (b) for a series of axial locations for the case with $Sk_D = 86$, $\bar{\phi} = 1.4 \times 10^{-3}$ and $\dot{Q}_0 = 2410$ W. The PDFs at each location were calculated from the ensemble of all pixels, from all relevant images, that are within an axial range of $\pm 0.125D$ about the specified location and within a radial range of $|r/D| < 0.5$. The inset for (a) presents the normalised PDF of $T_g - T_{g,M}$, where $T_{g,M}$ is the modal value of the PDF, while the inset for (b) presents the PDF of Θ_S on a log scale, to better show the tails of the PDF. The shape of the PDF at $x/D = 0.75$ (i.e., upstream from the heating region) is well approximated by a Gaussian curve centred at $T_g - T_a = 0$ °C, with a standard deviation in the measurements of $\sigma_{TG} = 17.7$ °C. This can be seen from comparison with the Gaussian curve with this standard deviation, presented in the inset. The measured temperature variation at $x/D = 0.75$ is not physical, but is due instead to the random errors in the measurement. This standard deviation is consistent with the pixel-to-pixel value of 17.8 °C that was previously determined for the measurement of the unheated jet flow [26]. The results also show that the peak (modal value) of the PDFs increases with axial distance, with the peak for $x/D = 2, 2.75$ and 3.5 at temperatures of $T_g - T_a = 12.5, 22.5$ and 33.5 °C, respectively. This is consistent with the measured increase in the time-averaged temperature [43], of $\bar{T}_g - T_a = 17.3, 31.2$ and 42.6 °C, respectively. Additionally, the range of temperatures that were measured in the flow increases with axial distance, with the standard deviation of the PDFs of $T_g - T_a$ increasing from $\sigma_{TG} = 23.0$ °C at $x/D = 2$ to $\sigma_{TG} = 36.0$ °C at $x/D = 3.5$. The shape of the PDF of $T_g - T_a$ also becomes positively skewed downstream from the heating region. That is, the proportion of the flow with a temperature higher than the peak (modal) value increases with axial distance downstream from the beginning of the heating region at $x/D = 0.9$. This can be seen at $x/D = 2.75$, for which the modal temperature measured was $T_g - T_a = 22.5$ °C with measurements in the range -40 °C $< T_g - T_a < 170$ °C.

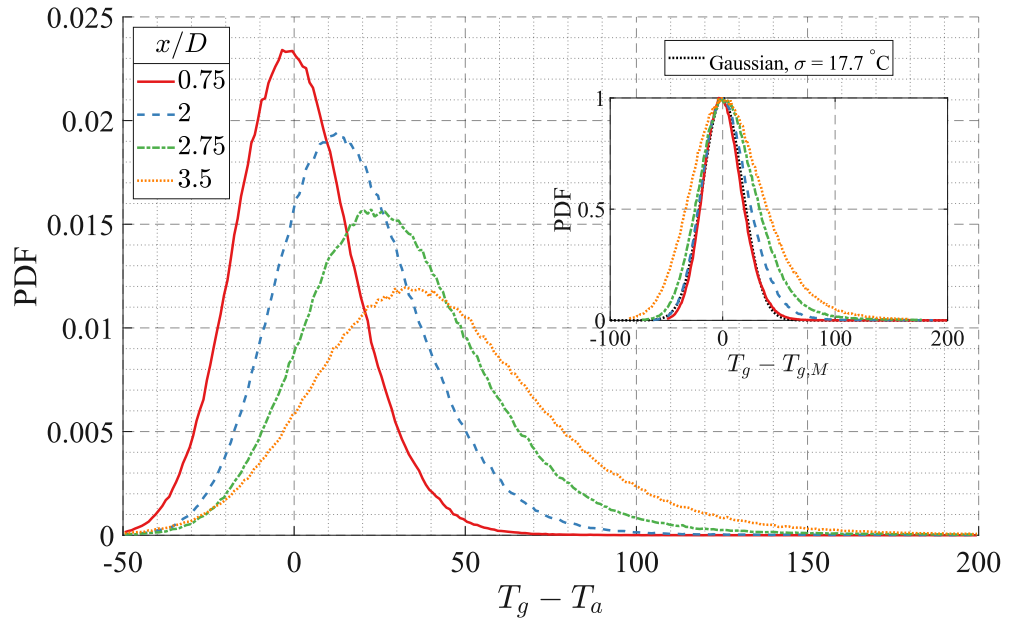
The PDFs of the normalised and smoothed temperature Θ_S collapse closely for $x/D \geq 2.75$, with the shape approaching a skewed Gaussian distribution with a modal value of $\Theta_S = 0.80$. The collapse of the PDFs implies that the relative spread of temperatures measured remains consistent with axial distance from the end of the heating region. For the axial location of $x/D = 2$, the PDF profile has a greater range of values and a lower modal value of $\Theta_S = 0.77$ compared to the downstream locations. The

greater variation that can be seen for the measurements at this axial location is attributed to the measurement uncertainty being more significant in the calculation of Θ_S for relatively low $T_g - T_a$ (i.e., regions with little convective heating). The proportion of the flow with $\Theta_S < \epsilon_C$ (i.e., the cumulative sum of the PDF to the left of the vertical line denoting ϵ_C) for the typical flow, such as at $x/D = 2.75$, was 14.2%, while $\Theta_S > \epsilon_H$ in 9.9% of the flow. This means that there are expected to be more cold regions than hot regions, most likely due to the influence of the flow areas with a low average particle volume fraction near to the jet edge.

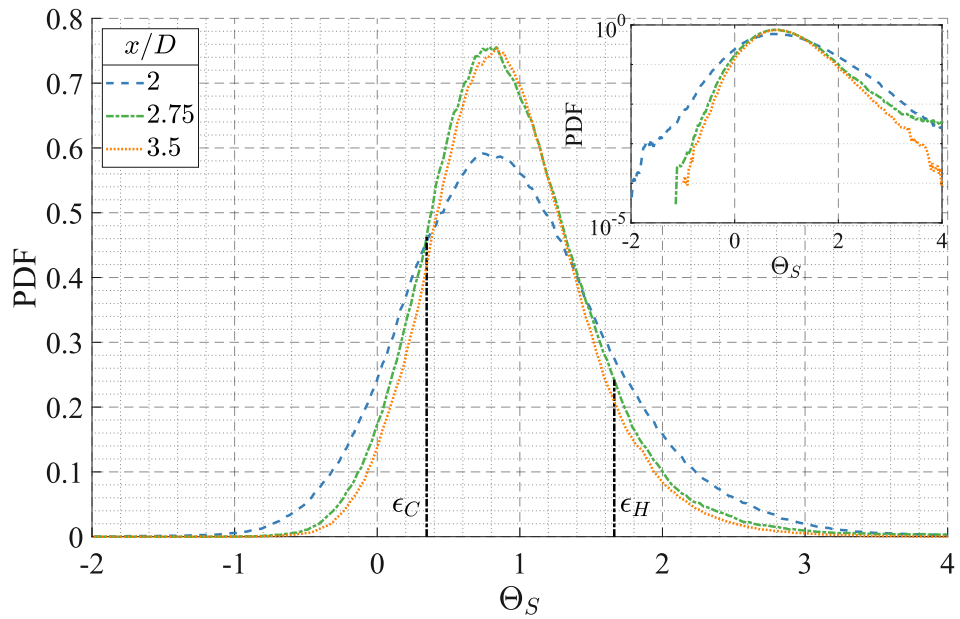
Figure 8 presents the number of particles within clusters from each relevant image normalised by the total number of particles detected, $N_{p,clus}/N_p$, as a function of \dot{Q}_0 for a constant value of $\bar{\phi} = 1.4 \times 10^{-3}$ for the series of particle Stokes numbers/particle number densities investigated (top) and $N_{p,clus}/N_p$ as a function of n_p for each combination of Sk_D and $\bar{\phi}$ (bottom). Also included in the bottom sub-figure is the values of $N_{p,clus}/N_p$ calculated from the simulation of a random particle distribution described in Section 2.5. These results are from the region bounded by $1.5 < x/D < 2.5$ and $|r/D| < 0.3$, in which the time-averaged particle number density is close to uniform [26]. Note that this region contains the flow both within, and immediately downstream from, the heating beam.

The measured proportion of particles in clusters $N_{p,clus}/N_p$ increases with a decrease in particle Stokes number (i.e., an increase in particle number density), with up to 23% of particles being identified as part of clusters for the flow with $Sk_D = 86$ ($n_p = 0.39$ particles/mm³). The proportion of the flow detected to be in clusters for the case with $Sk_D = 514$ is approximately half of that for $Sk_D \leq 163$. This is predominantly attributed to the reduction in particle number density with an increase in Sk_D rather than to any direct role of the Stokes number, since $Sk_D \gg 1$ for all cases. The particle number density is proportional to $1/\bar{d}_p^3$, such that the number of particles detected in the analysed region of each image, for the constant volumetric loading of $\bar{\phi} = 1.4 \times 10^{-3}$, decreases from $n_p = 0.39$ particles/mm³ for $Sk_D = 86$ to $N_p = 0.04$ particles/mm³ for $Sk_D = 514$. This decrease in number density means that the proportion of particles that are removed from the Voronoi analysis due to having an infinite cell area increases (e.g., those near to the jet edge), resulting in fewer valid cells for the cluster analysis.

No trends are evident in $N_{p,clus}/N_p$ as a function of heating power for any of the particle diameter distributions investigated. This implies that for the presented flow particle clustering is not affected by any flow phenomena driven by thermal gradients, including buoyant plumes, thermophoresis, turbulence generation, or particle migration. That is, the particle momentum/inertia dominates over any forces induced by thermal gradients



(a)



(b)

Figure 7: Probability density function of the measured gas temperature for the case with $Sk_D = 86$, $\bar{\phi} = 1.4 \times 10^{-3}$ and $\dot{Q}_0 = 2410$ W before (a) and after (b) normalisation and smoothing, for a series of axial locations. The ensemble of data used for each profile was from pixels in all images with $r/D < 0.5$ and within $0.125D$ axially of the displayed value. The vertical lines represent typical threshold values used to determine hot and cold regions, ϵ_H and ϵ_C , respectively. The inset of (a) presents compares the measured PDFs of temperature to a Gaussian curve, while the inset of (b) presents the PDF of Θ_S with the y-axis on a log-scale.

within the near-field of the jet ($x/D < 3.7$). However, this is not to say that the influence of radiative heating on the gas-phase is insignificant, or that the particle number density and velocity distributions further downstream are unaffected.

The proportion of particles measured to be in clusters can be seen to increase with n_p within the region bounded for these measurements, with the measured results closely matching those of the simulation. This suggests that the spatial variations in the particle distribution that lead to the detected clusters are primarily driven by random fluctuations rather than aerodynamic effects. This is consistent with previous studies that have shown that aerodynamic clustering is predominantly significant for $Sk \sim O(1)$ [29, 30], while in the present measurements the Stokes number is $Sk_D \geq 86$. It should be noted that, while Sk_D is also dependent on the flow temperature through gas viscosity, it is expected to decrease by less than 27% in the range $0 \leq T_g - T_a \leq 150$ °C. Hence, although the clustering in these high-Stokes number flows is not as prevalent as for flows with $Sk \sim O(1)$, the random variations still result in sufficient spatial and temporal variations in the particle volume fraction to generate complex and non-uniform heat transfer processes in the flow. Additionally, it should be noted that henceforth the references to particle clusters identified in the present measurements refers to those that arise from the random variations in particle motions leading to a distribution that closely matches a Poisson process.

Figure 9 presents typical instantaneous images of the temperature above ambient, $T_g - T_a$, (top), the normalised temperature smoothed using a length scale of $L_S = 0.1D$, Θ_S , together with the boundaries of the hot and cold regions (middle) and the locations of particles that have been determined to be either within or outside of clusters (bottom), for each Sk_D with $\phi = 1.4 \times 10^{-3}$ and $\dot{Q}_0 = 2840$ W. The hatched regions in the image correspond to the cases of Θ_S that were removed from the analysis due to having a temperature rise $\bar{T}_{g,CL} - T_a < 3$ °C. The regions for which $\bar{T}_{g,CL} - T_a > 3$ °C include those with $x/D \geq 1.5$ for the cases with $Sk_D \leq 163$ and $x/D > 2.3$ for $Sk_D = 514$. It can be seen that a decrease in Sk_D increases the area of the hot and cold regions, particularly for $x/D > 2$. For each Sk_D the hot and cold regions boundaries typically exhibit an of irregular, ellipse-like shape whose primary axes are aligned at an angle of approximately 45 ° to the jet axis. This shares some similarity with the oblique angles seen for clusters in a particle-laden jet, for particles with $Sk_D \approx 1.4$ and is consistent with a role of large-scale, shear-driven vortical motions [45]. The detected hot regions can be seen to be more prevalent on the jet axis than near to the edge, while the cold regions are more common near to the jet edge. This is consistent with both the particles being preferentially concentrated

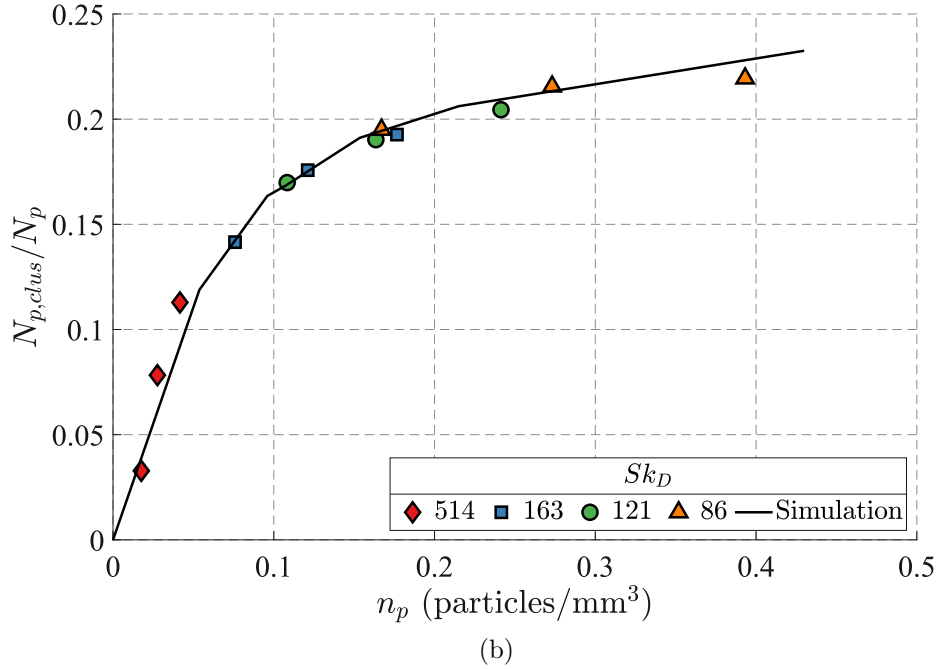
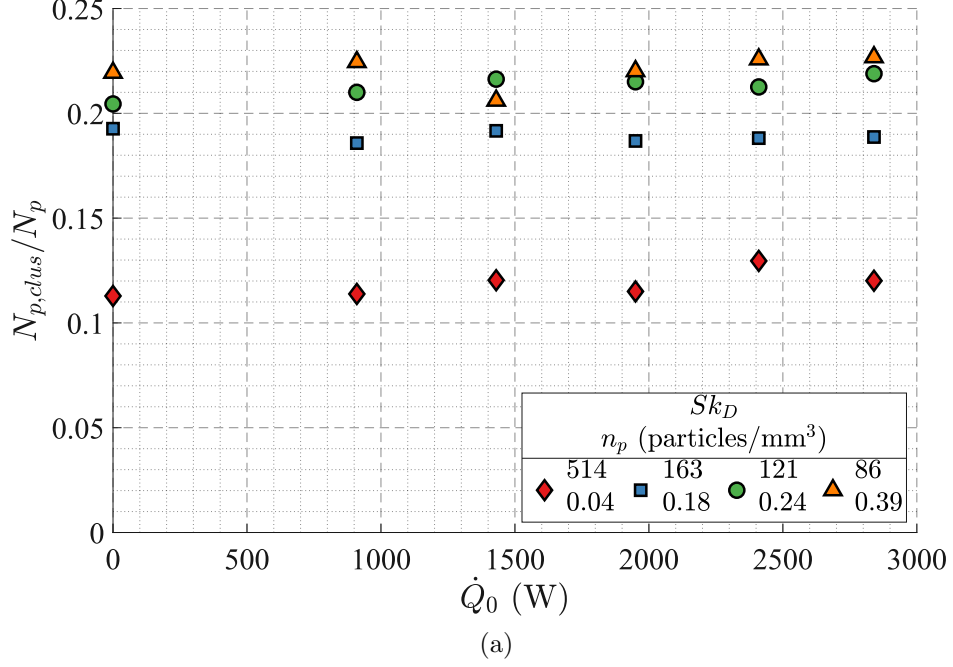


Figure 8: The measured number of particles determined to be in a cluster ($N_{p,clus}$) normalised by the total number of particles (N_p), in the region $1.5 < x/D < 2.5$ and $|r/D| < 0.3$, as a function of the heating beam power with a constant value of $\bar{\phi} = 1.4 \times 10^{-3}$ for a series of particle number densities (a) and $N_{p,clus}/N_p$ as a function of the particle number density n_p for each combination of Sk_D and $\bar{\phi}$ (markers), together with the results from the random particle distribution simulation (line).

towards the jet centreline [26] and with the entrainment of cold flow through convection/mixing with the unheated co-flow being greatest at the jet edge.

The decrease in particle number density with an increase in Sk_D for constant $\bar{\phi}$ can be seen from the number of particles imaged for each case, with the resultant proportion of the gas that is within the void regions increasing significantly with Sk_D from 24% for $Sk_D = 86$ to 79% for $Sk_D = 514$. The location of the hot regions shows good qualitative agreement with regions of high local particle volume fraction, particularly for the case with $Sk_D = 86$. Heat transfer between the gas in the measurement region and particles outside of, but near to, the diagnostic laser sheet also influences the measured gas-phase temperature, such that heated regions can appear where no particles were imaged. However, the influence of these particles on the measured temperature is expected to be less than that of the particles imaged within the laser sheet because of the greater distance between the particle and measurement regions.

Figure 10 presents a series of four consecutive images of $T_g - T_a$, together with the corresponding image of Θ_S , for the flow with $Sk_D = 86$, $\bar{\phi} = 1.4 \times 10^{-3}$ and $\dot{Q}_0 = 2840$ W. The detected boundaries of the hot and cold regions, together with the particle locations, are superimposed on the images of Θ_S to graphically show the correlation between the local particle volume fraction and gas temperature. In the region downstream from the heating beam, for $x/D > 1.9$, the temperature can be seen to vary spatially and temporally (i.e., from image to image) by up to ~ 150 °C, even at similar axial locations. The basic trends identified from the temperature distributions presented in Figure 9 can also be seen in each image here, with the flow exhibiting localised regions of high and low temperature relative to the surroundings. No clear structure can be seen from these temperature variations, with the location, size and shape of the hot and cold regions being irregular. The superimposed particle locations more clearly show the correlation between Θ_S and the particle locations, with the hot regions tending to contain several particles while few particles are detected within the cold regions. These trends are consistent for all combinations of Sk_D and $\bar{\phi}$ with $\dot{Q}_0 > 0$ investigated, but are most clearly demonstrated for the presented case (which has the greatest average temperature increase among all investigated cases). The framing rate of the current measurements is too slow compared with the flow time-scales to assess any coherence between successive frames. Nevertheless, the planar measurements do provide evidence of coherence, because the locations of particles strongly correspond to locations where the gas temperature rise is high at all axial locations downstream from the heating region. This suggests that, within the first few diameters from the exit plane, the particles and fluid surrounding the particles travel coherently with little transport to the bulk

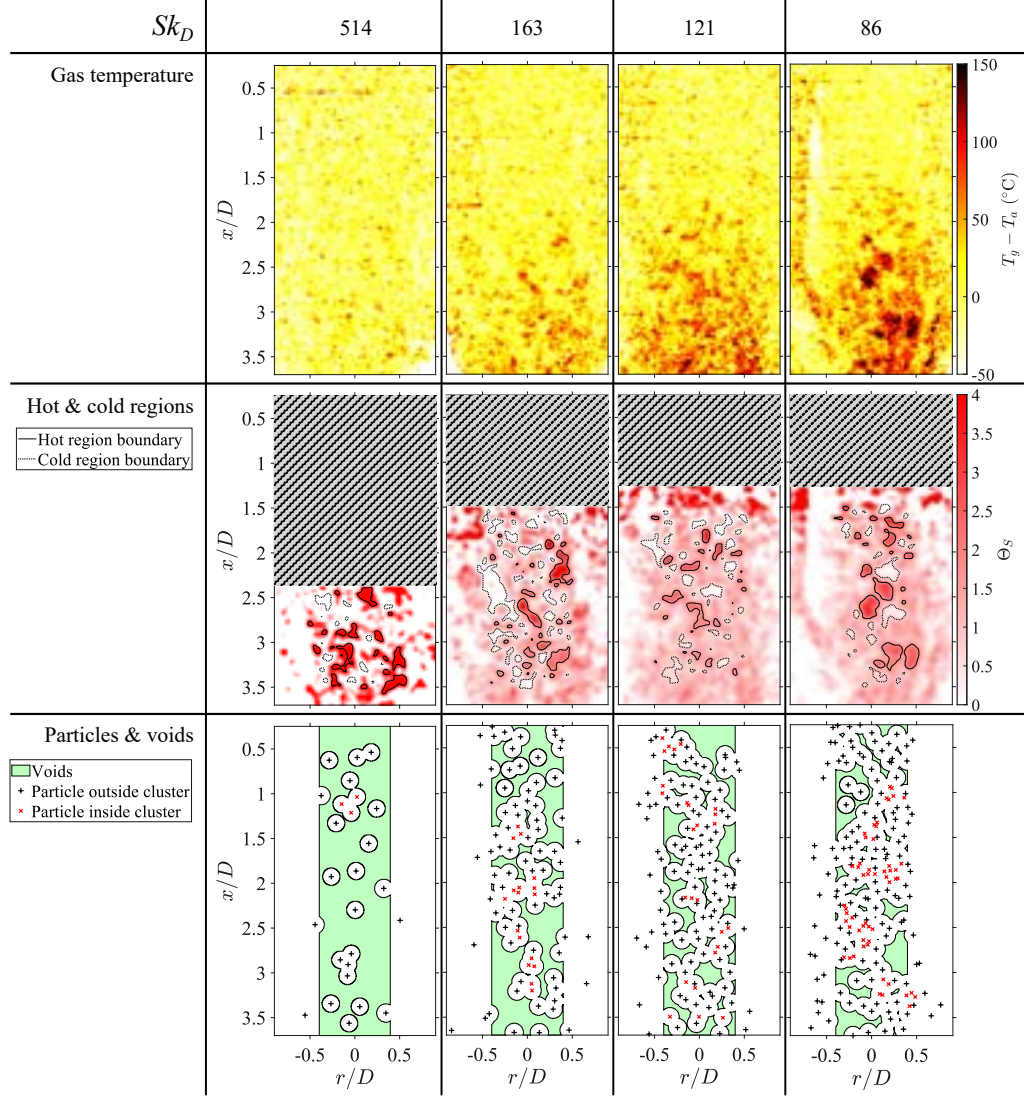


Figure 9: Typical instantaneous images of the temperature above ambient (top), the normalised and smoothed temperature Θ_S together with the boundaries of the determined hot and cold regions (middle), and the particle locations together with the determined void regions (bottom), for each flow Stokes number Sk_D . For each image presented the temporally averaged particle volumetric fraction at the jet exit was $\phi = 1.4 \times 10^{-3}$ and the heating beam power was $\dot{Q}_0 = 2840$ W. The hatched regions denote areas with an insufficient temperature rise for reliable calculation of Θ_S .

flow.

To provide further evidence of the correlation between the particle locations and gas temperature, the instantaneous particle volume fraction within the boundaries of each hot and cold region, ϕ_{reg} , was calculated. The value of ϕ_{reg} was then normalised by the time-averaged volume fraction evaluated at the centroid of the hot/cold regions at the same axial location, $\bar{\phi}$. The ensemble average of $\phi/\bar{\phi}$ within these regions was then calculated for equally spaced bins of length $0.25D$ in the axial direction. The binned data, $\langle\phi_{reg}/\bar{\phi}\rangle$, is presented in Figure 11 as a function of axial location for a series of particle Stokes numbers with $\bar{\phi} = 1.4 \times 10^{-3}$ and $\dot{Q}_0 = 2410$ W. The results show that the average measured particle volume fraction within the determined hot regions is significantly greater than both the mean value and that within the cold regions, for a given value of particle diameter. This is explained by the particle temperatures being greater than that of the gas, owing to the preferential heating of particles by radiation and convection being the primary mode of thermal energy transfer between the two phases. Hence, regions with a higher concentration of particles (i.e., clusters) are expected to have a higher local gas-phase temperature than those with a lower concentration.

A value of $\langle\phi_{reg}/\bar{\phi}\rangle > 3$ was measured in the region $2.3 < x/D < 3.5$ for the case with $Sk_D = 514$, and $\langle\phi_{reg}/\bar{\phi}\rangle > 1.5$ for $Sk_D \leq 163$ throughout the region $1.5 < x/D < 3.5$. The high value at $x/D = 2.375$ for $Sk_D = 514$ is most likely an anomaly due to the combination of the low average temperature rise at this location and low particle number density for this case. The value of $\langle\phi_{reg}/\bar{\phi}\rangle$ was found to be greater than unity in the hot regions for each Sk_D and for all $x/D > 1.5$. This implies that, in the region $1.5 < x/D < 3.5$, the hot regions are coherent and/or that the particles remain sufficiently hot for strong thermal gradients in the surrounding gas to be continually generated through convective heat transfer between the hot particles and gas. Conversely, within the cold regions, it can be seen that $\langle\phi_{reg}/\bar{\phi}\rangle$ is generally less than 1, with $\langle\phi_{reg}/\bar{\phi}\rangle \approx 0.5$ for all x/D for the case with $Sk_D = 86$. The correlation between the gas temperature and particle volume fraction decreases slightly with axial distance, in the region downstream from the end of the heating region ($x/D > 1.5$). This suggests that mixing of the gas-phase becomes increasingly significant, relative to the convective heat transfer with the particles, as the flow moves downstream. While these measurements are limited to the near-field of the jet flow, it is expected that in the far-field these correlations will continue to weaken with axial distance.

Figure 12 presents $T_g - T_a$ as a function of the local particle volume fraction measured within a radius of $0.1D$ around each particle (ϕ_{loc}), normalised by the local time-averaged volume fraction $\bar{\phi}$, for a series of Sk_D

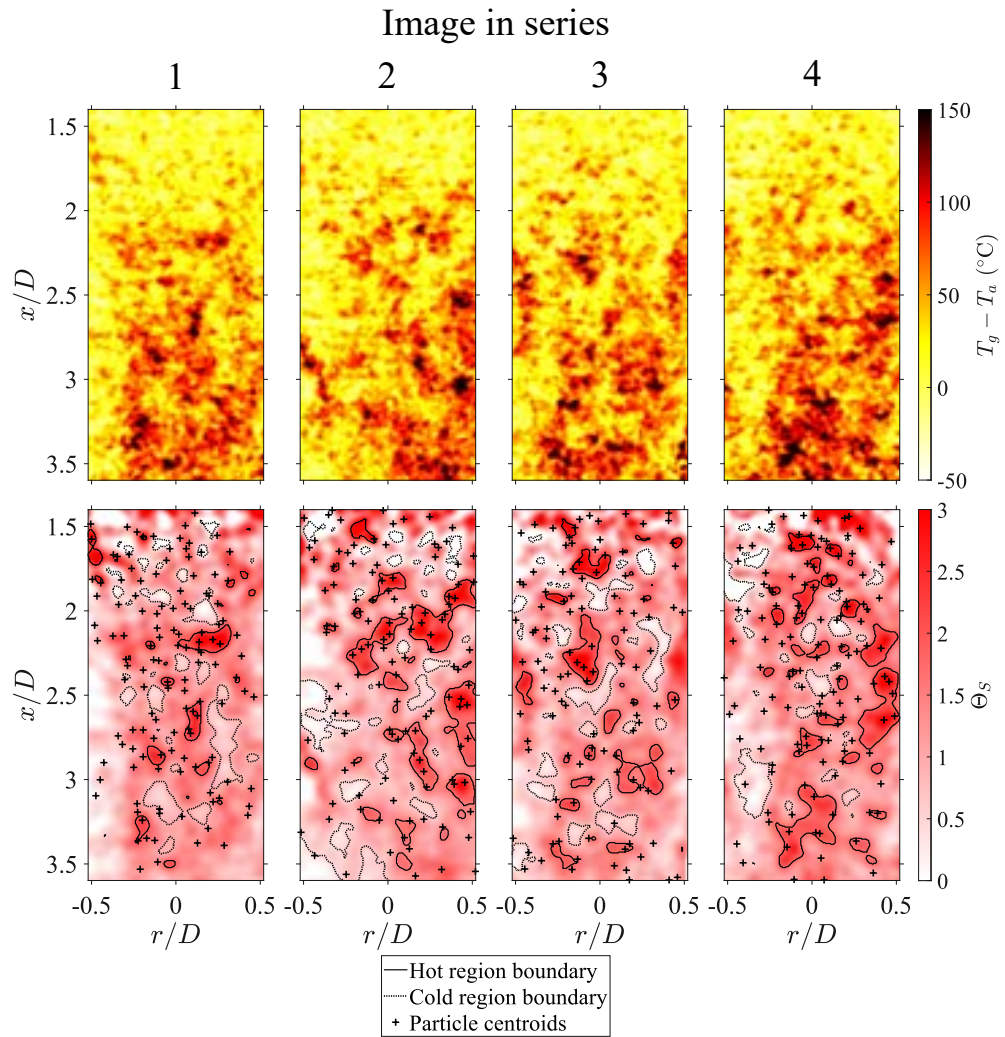


Figure 10: A series of consecutive images of the temperature, together with Θ_S , for the flow with $Sk_D = 86$, $\phi = 1.4 \times 10^{-3}$ and $\dot{Q}_0 = 2840$ W. The particle centroid locations and the boundaries of the detected hot and cold regions are also presented.

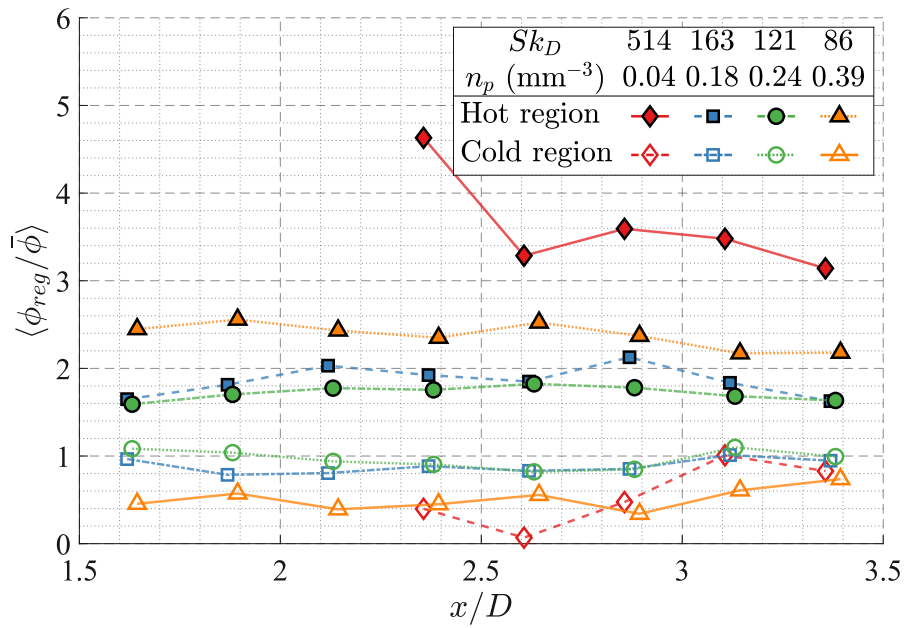


Figure 11: Ensemble average of the measured particle volume fraction within the detected hot and cold regions, ϕ_{reg} , normalised by the time-averaged volume fraction at the same location, $\bar{\phi}(x)$, as a function of axial location for a series of Sk_D and with constant values of $\bar{\phi} = 1.4 \times 10^{-3}$ and $\dot{Q}_0 = 2410$ W.

with $\bar{\phi} = 1.4 \times 10^{-3}$ and $\dot{Q}_0 = 2410$ W (top) together with a series of axial distances with $Sk_D = 86$, $\bar{\phi} = 1.4 \times 10^{-3}$ and $\dot{Q}_0 = 2410$ W (bottom). Three temperatures are presented for the three flow conditions, namely $T_{g,Hi}$, $T_{g,Lo}$ and $T_{g,Vd}$, as defined in Section 2.4. It should be noted that the local volume fraction within all voids is $\phi_{loc} = 0$ by this definition. The value of $\bar{\phi}$ is towards the lower end of the four-way coupling regime ($10^{-3} < \phi < 100$), for which both particle-fluid and particle-particle interactions are significant. Data are only reported within the region of $2 < x/D < 2.25$, $|r/D| < 0.3$, which is immediately downstream from the heating region where the temperature difference between the particles and gas is the greatest. Within this region, the radial profiles of the time-averaged temperature and particle volume fraction are also close to uniform, with the range of \bar{T}_g being less than 15 °C and with ϕ being within 20% of the centreline value for each case [26]. Therefore, the non-uniformities in the particle volume fraction due to the radial distribution at the jet exit are small for this dataset. As such, the random variations in the local volume fraction are expected to be the primary driver for any gas-phase temperature variation.

The results show that the gas temperature is strongly correlated with the local particle volume fraction. The temperature difference in regions with $\phi_{loc}/\bar{\phi} > 0$ is greater than that in regions with $\phi_{loc}/\bar{\phi} = 0$ for all Sk_D and locations downstream from the heating beam. Furthermore, T_g also increases with an increase in $\phi_{loc}/\bar{\phi}$ for each flow condition. For a given value of $\phi_{loc}/\bar{\phi}$, the measured temperature around particles within clusters $T_{g,Hi}$ is generally higher than $T_{g,Lo}$. This implies that regions with clusters have higher local gas-phase temperatures than those that do not, even if the regions have the same local particle number density. This temperature difference is attributed, at least in part, to the coherence between the particle clusters and surrounding gas (as shown in Figure 10). This coherence results in an increase in time at which the fluid ‘parcels’ reside in the same region as the particles, providing greater time for the transfer of thermal energy from the particles to the fluid parcel. Similarly, the apparent lower coherence between the particles and surrounding gas for the cases where particles are not in clusters implies increased mixing with the bulk flow. However, the difference is generally modest with $T_{g,Hi} - T_{g,Lo} < 3$ °C, suggesting that the magnitude of local particle volume fraction has a greater influence on the temperature than the location of the clusters.

The results also show that the peak values of $\phi_{loc}/\bar{\phi}$ are higher in the regions around particles determined to be in clusters than in other regions, consistent with the definition of clusters being local regions of high volume fraction. Within the range of particle volumetric loadings and particle diameters investigated, the effect of ϕ_{loc} on $T_g - T_a$ is small compared to the

effect of \bar{d}_p . For example, for $Sk_D = 121$, $T_{g,Hi} - T_a$ increases from 20 °C to 29 °C for a four-fold increase in the local volume fraction from $\phi_{loc}/\bar{\phi} = 1$ to $\phi_{loc}/\bar{\phi} = 4$. However, for a decrease of the particle diameter by approximately half, from 423 μm to 205 μm (i.e., equivalent to an eight-fold increase in particle number density), but with a fixed volume fraction of $\phi_{loc}/\bar{\phi} = 3$, the value of $T_{g,Hi} - T_a$ increases from 8 °C to 24 °C. The gradient of the increase in temperature with $\phi_{loc}/\bar{\phi}$ (i.e. the slope of the lines in Figure 12, top) increases with $\phi_{loc}/\bar{\phi}$, for the cases with $Sk_D \leq 121$ and $\phi_{loc}/\bar{\phi} > 2.5$. This slope can also be seen to increase with a decrease in Sk_D (i.e., a decrease in particle diameter). Together, these results imply that, for sufficiently small particle diameters, both the diameter and local volume fraction of particles in the flow impact significantly on the instantaneous gas-phase temperature distribution. Therefore, in flows where the local volume fractions can be significantly higher than the mean, such as in flows with aerodynamic particle clustering where $\phi_{loc}/\bar{\phi} > 10$ has been measured [45], variations in the gas phase temperature can be expected to be particularly significant.

At the axial location upstream from the heating laser, for $x/D = 0.75$, all three temperatures $T_{g,Hi}$, $T_{g,Lo}$ and $T_{g,Vd}$ are measured to be approximately zero regardless of the local particle volume fraction. This is as expected, because the particles are yet to be heated directly at this point, although multiple scattering of the heating laser by particles may lead to a broadening of the heating region. However, with an increase in the axial distance downstream from the heating region ($x/D > 0.9$), not only does the temperature rise increase, but the correlation between the local particle volume fraction and temperature rise also increases, as evidenced by the slope of the lines in Figure 12 (bottom). This increase in T_g with $\phi_{loc}/\bar{\phi}$ downstream from the heating region implies that the flow is being heated continually by the particles throughout the measurement region. Additionally, the temperature around particles remains significantly greater than the temperature in the voids, which suggests that the heat transfer from particle-gas convection is dominant throughout the near-field compared to the mixing and convection within the gas-phase. This, in turn, implies that the particle clusters retain strong coherence with time, or are relatively long-lived. Hence, the mechanisms that form particle clusters influence the local distributions of temperature.

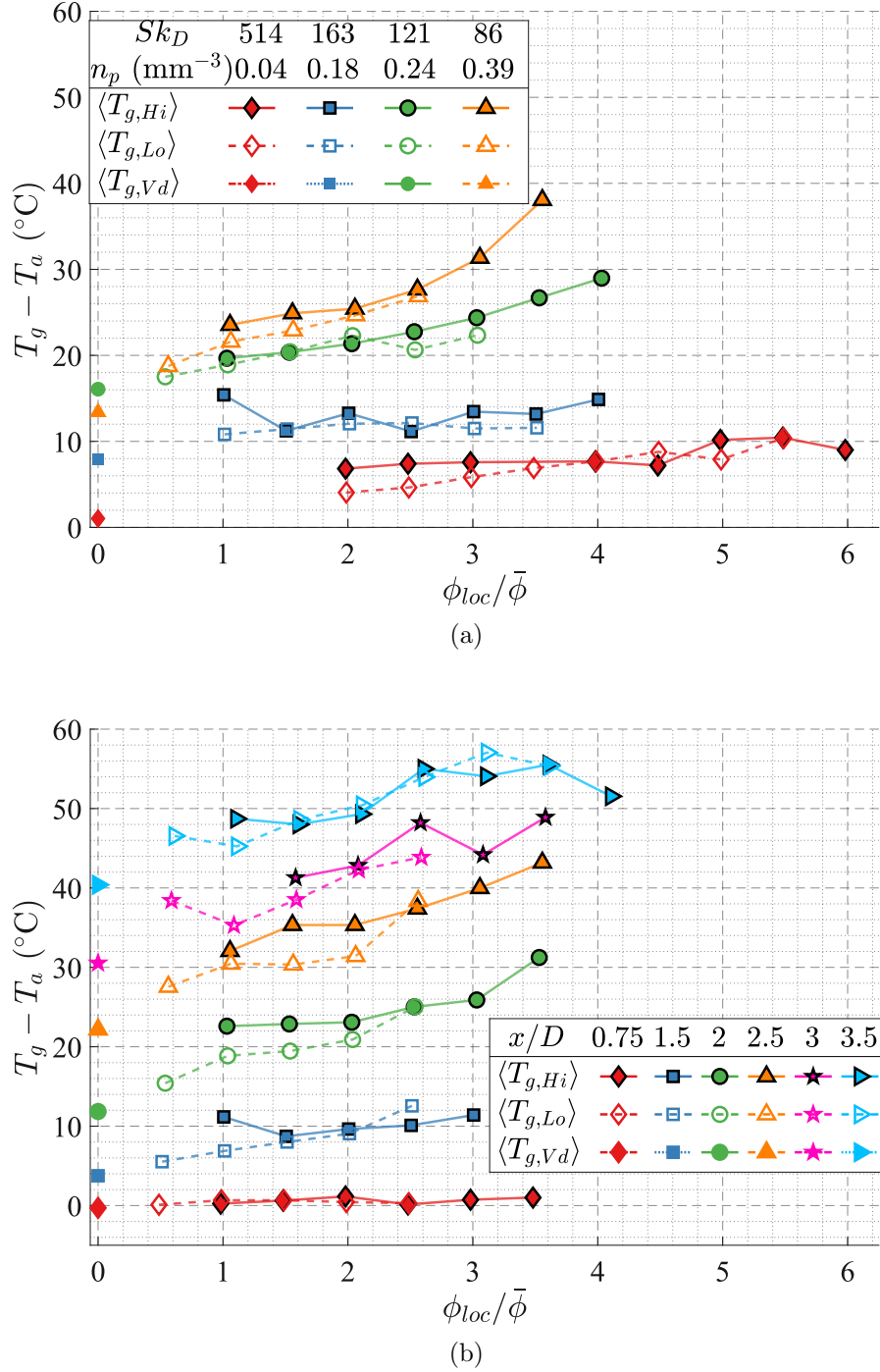


Figure 12: The ensemble average of the temperature above ambient as a function of the local particle volume fraction, for the regions around particles inside clusters, outside cluster, and in voids, for a series of Sk_D with $\bar{\phi} = 1.4 \times 10^{-3}$ and $\dot{Q}_0 = 2410$ W measured in the region immediately downstream from the heating laser of $2 < x/D < 2.25$ (a) and for a series of axial locations for the flow with $Sk_D = 86$, $\bar{\phi} = 1.4 \times 10^{-3}$ and $\dot{Q}_0 = 2410$ W (b).

4 Conclusions

Detailed planar measurements within a radiatively heated particle-laden jet have shown that the instantaneous distributions of both the particle number density and the gas phase temperature are highly non-uniform and correlated, both spatially and temporally. Both the average gas-phase temperature and the range of temperatures measured were found to increase with axial distance downstream from the radiative heating region. Localised regions of high and low temperature were identified from the images of the gas-phase temperature following normalisation by the time-averaged value and smoothing at a suitable length scale, with the location of the ‘hot’ and ‘cold’ regions varying significantly both spatially and temporally. The hot regions were found to be more prevalent near to the jet centreline, while the cold regions were more prevalent near to the jet edge. These results are attributed to the particle volume fraction at the jet exit being preferentially concentrated on the jet axis and the effect of cooling from the unheated co-flow. The local particle volume fraction within the hot regions was $\phi_{reg}/\bar{\phi} > 1.5$ for all investigated cases, while $\phi_{reg}/\bar{\phi} < 1$ was typical within the cold regions. This implies that the convective heat transfer between the hot particles and surrounding gas is faster than its rate of dissipation through the surrounding gases due to mixing and convection, at least within the measurement region and for the conditions investigated. These results were found to be consistent with axial distance, indicating that the regions with both high temperature and particle volume fraction remain coherent over the range $0.3 < x/D < 3.7$. Importantly, this implies that the particle clusters (i.e., regions of locally high particle volumetric loading generated due to random particle motions) are relatively long-lived, so that the local distributions of temperature are influenced by the long history of large-scale flow features.

Furthermore, the temperature in regions surrounding particles was found to be greater than that in the void regions downstream from the radiatively heated region, with the local gas-phase temperature increasing with an increase in the local particle volume fraction. Additionally, the temperature around particles within clusters was greater than those outside of clusters, although the temperature difference was relatively modest. The effect of the local particle volume fraction on the temperature rise was also found to increase with an increase in the particle number density.

For the conditions investigated, the measured proportion of particles in clusters, as calculated using Voronoi diagrams, closely matched that of a dataset simulated using a random particle distribution. The finding that they match a random distribution is consistent with all cases being evaluated in the high Stokes number regime. The particle distributions, both within

and downstream from the radiative heating region, are independent of the radiative flux. This implies that the effects of any thermal gradients on the particle-phase distributions (i.e., any buoyancy-induced effects) are negligible in the near field for these flows in the high Stokes number regime, even for fluxes up to 40 MW/m².

References

- [1] B. Klotz. “New developments in precalciners and preheaters”. In: *1997 IEEE/PCA Cement Industry Technical Conference. XXXIX Conference Record (Cat. No.97CH36076)*. 1997, pp. 255–280.
- [2] G. J. Nathan, P. A. M. Kalt, Z. T. Alwahabi, B. B. Dally, P. R. Medwell and Q. N. Chan. “Recent advances in the measurement of strongly radiating, turbulent reacting flows”. In: *Progress in Energy and Combustion Science* 38.1 (2011).
- [3] A. Williams, M. Pourkashanian and J. M. Jones. “Combustion of pulverised coal and biomass”. In: *Progress in Energy and Combustion Science* 27.6 (2001), pp. 587–610.
- [4] W. M. Fish. “Alumina calcination in the fluid-flash calciner”. In: *Essential Readings in Light Metals*. Vol. 1. Switzerland: Springer International Publishers, 2016, pp. 648–652.
- [5] J. A. H. Oates. *Lime and limestone : chemistry and technology, production and uses*. Weinheim, Germany: Wiley-Vch, 1998.
- [6] IEA. *Renewable Energy for Industry*. Report. IEA, 2017.
- [7] S. J. Davis et al. “Net-zero emissions energy systems”. In: *Science (American Association for the Advancement of Science)* 360.6396 (2018), eaas9793.
- [8] A. de Pee, D. Pinner, O. Roelofsen, K. Somers, E. Speelman and M. Witteveen. *Decarbonization of industrial sectors: the next frontier*. Report. McKinsey and Company, 2018.
- [9] Energy Transitions Commission. *Making Mission Possible - Delivering a Net-Zero Economy*. Report 1.0. Energy Transitions Commission, 2020.
- [10] S. Balachandar and J. Eaton. “Turbulent Dispersed Multiphase Flow”. In: *Annual Review of Fluid Mechanics* 42 (2010), pp. 111–133.

- [11] H. Pouransari and A. Mani. “Effects of Preferential Concentration on Heat Transfer in Particle-Based Solar Receivers”. In: *Journal of Solar Energy Engineering* 139.2 (2016), pp. 021008–021008–11.
- [12] D. C. Ozcan, S. Brandani and H. Ahn. “A Hybrid Carbon Capture System of Indirect Calcination and Amine Absorption for a Cement Plant”. In: *Energy Procedia* 63 (2014), pp. 6428–6439.
- [13] C. H. Birzer, P. A. Kalt, T. C. Lau and G. Nathan. “Renormalisation of particle distributions in an initially-biased turbulent jet by swirl and radial injection”. In: *International Journal of Multiphase Flow* 135 (2021), p. 103509.
- [14] P. J. van Eyk, P. J. Ashman and G. J. Nathan. “Effect of High-Flux Solar Irradiation on the Gasification of Coal in a Hybrid Entrained-Flow Reactor”. In: *Energy & Fuels* 30.6 (2016), pp. 5138–5147.
- [15] C. K. Ho. “A review of high-temperature particle receivers for concentrating solar power”. In: *Special Issue: Solar Energy Research Institute for India and the United States (SERIUS) – Concentrated Solar Power* 109 (2016), pp. 958–969.
- [16] N. Siegel, M. Gross, C. Ho, T. Phan and J. Yuan. “Physical Properties of Solid Particle Thermal Energy Storage Media for Concentrating Solar Power Applications”. In: *Energy Procedia* 49 (2014), pp. 1015–1023.
- [17] B. Jenkins and P. Mullinger. *Industrial and Process Furnaces: Principles, Design and Operation*. eng. Oxford: Elsevier Science and Technology, 2013.
- [18] D. Davis, F. Muller, W. Saw, A. Steinfeld and G. Nathan. “Solar-driven alumina calcination for CO₂ mitigation and improved product quality”. In: *Green Chem.* 19.13 (2017), pp. 2992–3005.
- [19] A. Meier, E. Bonaldi, G. M. Cella, W. Lipinski and D. Wuillemin. “Solar chemical reactor technology for industrial production of lime”. In: *Solar Energy* 80.10 (2006), pp. 1355–1362.
- [20] A Steinfeld, A Imhof and D Mischler. “Experimental Investigation of an Atmospheric-Open Cyclone Solar Reactor for Solid-Gas Thermochemical Reactions”. eng. In: *Journal of solar energy engineering* 114.3 (1992), pp. 171–174.
- [21] D. Davis, M. Jafarian, A. Chinnici, W. L. Saw and G. J. Nathan. “Thermal performance of vortex-based solar particle receivers for sensible heating”. eng. In: *Solar energy* 177 (2019), pp. 163–177.

- [22] N. Siegel, C. Ho, S. S. Khalsa and G. Kolb. “Development and Evaluation of a Prototype Solid Particle Receiver: On-Sun Testing and Model Validation”. In: *Journal Of Solar Energy Engineering-Transactions Of The Asme* 132.2 (2010).
- [23] K. C. Y. Kueh, T. C. W. Lau, G. J. Nathan and Z. T. Alwahabi. “Non-intrusive temperature measurement of particles in a fluidised bed heated by well-characterised radiation”. In: *International Journal of Multiphase Flow* 100 (2018), pp. 186–195.
- [24] A. J. Banko, L. Villafañe, J. H. Kim and J. K. Eaton. “Temperature statistics in a radiatively heated particle-laden turbulent square duct flow”. In: *International Journal of Heat and Fluid Flow* 84 (2020), p. 108618.
- [25] A. Kumar, J.-S. Kim and W. Lipiński. “Radiation Absorption in a Particle Curtain Exposed to Direct High-Flux Solar Irradiation”. In: *Journal of Solar Energy Engineering* 140.6 (June 2018). 061007. eprint: https://asmedigitalcollection.asme.org/solarenergyengineering/article-pdf/140/6/061007/6379341/so1_140_06_061007.pdf.
- [26] E. W. Lewis, T. C. W. Lau, Z. Sun, Z. T. Alwahabi and G. J. Nathan. “Insights from a new method providing single-shot, planar measurement of gas-phase temperature in particle-laden flows under high-flux radiation”. In: *Experiments in Fluids* 62.4 (2021), p. 80.
- [27] S. Elgobashi. “An Updated Classification Map of Particle-Laden Turbulent Flows”. In: *IUTAM Symposium on Computational Approaches to Multiphase Flow: Proceedings of an IUTAM Symposium held at Argonne National Laboratory, October 4–7, 2004*. Ed. by S. Balachandar and A. Prosperetti. Dordrecht: Springer Netherlands, 2006, pp. 3–10.
- [28] J. K. Eaton and J. R. Fessler. “Preferential concentration of particles by turbulence”. In: *International Journal of Multiphase Flow* 20 (1994), pp. 169–209.
- [29] J. R. Fessler, J. D. Kulick and J. K. Eaton. “Preferential concentration of heavy particles in a turbulent channel flow”. In: *Physics of Fluids* 6.11 (1994), pp. 3742–3749.
- [30] R. Monchaux, M. Bourgoïn and A. Cartellier. “Preferential concentration of heavy particles: A Voronoï analysis”. In: *Physics of Fluids* 22.10 (2010), p. 103304.
- [31] A. Frankel, H. Pouransari, F. Coletti and A. Mani. “Settling of heated particles in homogeneous turbulence”. In: *Journal of Fluid Mechanics* 792 (2016), pp. 869–893.

- [32] R. Zamansky, F. Coletti, M. Massot and A. Mani. “Radiation induces turbulence in particle-laden fluids”. In: *Physics of Fluids* 26.7 (2014), p. 071701.
- [33] A. C. Eckbreth. *Laser diagnostics for combustion temperature and species*. 2nd ed. Combustion science and technology book series ; v. 3. Amsterdam: Gordon and Breach, 1996.
- [34] N. J. Kempema and M. B. Long. “Quantitative Rayleigh thermometry for high background scattering applications with structured laser illumination planar imaging”. In: *Applied Optics* 53.29 (2014), pp. 6688–6697.
- [35] A. Bohlin and C. J. Kliewer. “Communication: Two-dimensional gas-phase coherent anti-Stokes Raman spectroscopy (2D-CARS): Simultaneous planar imaging and multiplex spectroscopy in a single laser shot”. In: *The Journal of Chemical Physics* 138.22 (2013), p. 221101.
- [36] C. Schulz and V. Sick. “Tracer-LIF diagnostics: quantitative measurement of fuel concentration, temperature and fuel/air ratio in practical combustion systems”. In: *Progress in Energy and Combustion Science* 31.1 (2005), pp. 75–121.
- [37] J. Lakowicz. *Principles of Fluorescence Spectroscopy*. 3rd ed. New York: Springer, 2006.
- [38] P. A. M. Kalt, C. H. Birzer and G. J. Nathan. “Corrections to facilitate planar imaging of particle concentration in particle-laden flows using Mie scattering, Part 1: Collimated laser sheets”. In: *Applied Optics* 46.23 (2007), pp. 5823–5834.
- [39] M. Cundy, P. Trunk, A. Dreizler and V. Sick. “Gas-phase toluene LIF temperature imaging near surfaces at 10 kHz”. In: *Experiments in Fluids* 51.5 (2011), pp. 1169–1176.
- [40] M. Luong, R. Zhang, C. Schulz and V. Sick. “Toluene laser-induced fluorescence for in-cylinder temperature imaging in internal combustion engines”. In: *Applied Physics B* 91.3 (2008), p. 669.
- [41] E. W. Lewis, T. C. W. Lau, Z. Sun, Z. T. Alwahabi and G. J. Nathan. “Luminescence interference to two-colour toluene laser-induced fluorescence thermometry in a particle-laden flow”. In: *Experiments in Fluids* 61.4 (2020), p. 101.
- [42] M. Luong, W. Koban and C. Schulz. “Novel strategies for imaging temperature distribution using Toluene LIF”. In: *Journal of Physics: Conference Series* 45.1 (2006), p. 133.

- [43] E. W. Lewis, T. C. Lau, Z. Sun, Z. T. Alwahabi and G. J. Nathan. “The effect of particle size and volumetric loading on the gas temperature distributions in a particle-laden flow heated with high-flux radiation”. In: *International Journal of Heat and Mass Transfer* 182 (2022), p. 122041.
- [44] T. C. W. Lau and G. J. Nathan. “The effect of Stokes number on particle velocity and concentration distributions in a well-characterised, turbulent, co-flowing two-phase jet”. In: *Journal of Fluid Mechanics* 809 (2016), pp. 72–110.
- [45] T. C. W. Lau and G. J. Nathan. “A method for identifying and characterising particle clusters in a two-phase turbulent jet”. In: *International Journal of Multiphase Flow* 88 (2017), pp. 191–204.
- [46] J. C. Njue, F. Salehi, T. C. Lau, M. J. Cleary, G. J. Nathan and L. Chen. “Numerical and experimental analysis of poly-dispersion effects on particle-laden jets”. In: *International Journal of Heat and Fluid Flow* 91 (2021), p. 108852.
- [47] J MI, D. S NOBES and G. J NATHAN. “Influence of jet exit conditions on the passive scalar field of an axisymmetric free jet”. eng. In: *Journal of fluid mechanics* 432 (2001), pp. 91–125.
- [48] N. Siegel, M. Gross and R. Coury. “The Development of Direct Absorption and Storage Media for Falling Particle Solar Central Receivers”. In: *Journal of Solar Energy Engineering* 137 (2015), p. 041003.
- [49] I. Gillandt, U. Fritsching and K. Bauckhage. “Measurement of phase interaction in dispersed gas/particle two-phase flow”. In: *International Journal of Multiphase Flow* 27.8 (2001), pp. 1313–1332.
- [50] Z. T. Alwahabi, K. C. Y. Kueh, G. J. Nathan and S. Cannon. “Novel solid-state solar thermal simulator supplying 30,000 suns by a fibre optical probe”. In: *Optics Express* 24.22 (2016), A1444–A1453.
- [51] Y. Tsuji, Y. Morikawa, T. Tanaka, K. Karimine and S. Nishida. “Measurement of an axisymmetric jet laden with coarse particles”. In: *International Journal of Multiphase Flow* 14.5 (1988), pp. 565–574.
- [52] J.-S. Ferenc and Z. Néda. “On the size distribution of Poisson Voronoi cells”. In: *Physica A: Statistical Mechanics and its Applications* 385.2 (2007), pp. 518–526.
- [53] T. C. W. Lau, J. H. Frank and G. J. Nathan. “Resolving the three-dimensional structure of particles that are aerodynamically clustered by a turbulent flow”. In: *Physics of Fluids* 31.7 (2019), p. 071702.

Bibliography

- [1] IEA. *Renewable Energy for Industry*. Report. IEA, 2017.
- [2] Davis, S. J. et al. "Net-zero emissions energy systems". In: *Science (American Association for the Advancement of Science)* 360.6396 (2018).
- [3] de Pee, A., Pinner, D., Roelofsen, O., Somers, K., Speelman, E. and Witteveen, M. *Decarbonization of industrial sectors: the next frontier*. Report. McKinsey and Company, 2018.
- [4] Energy Transitions Commission. *Making Mission Possible - Delivering a Net-Zero Economy*. Report 1.0. Energy Transitions Commission, 2020.
- [5] Jakobsen, H. A. *Chemical Reactor Modeling Multiphase Reactive Flows*. eng. 2nd ed. 2014. Cham: Springer International Publishing, 2014.
- [6] Boateng, A. A. *Rotary kilns : transport phenomena and transport processes*. eng. Second edition. Oxford: Elsevier, 2016.
- [7] Balachandar, S. and Eaton, J. "Turbulent Dispersed Multiphase Flow". In: *Annual Review of Fluid Mechanics* 42 (2010), pp. 111–133.
- [8] Fish, W. M. "Alumina calcination in the fluid-flash calciner". In: *Essential Readings in Light Metals*. Vol. 1. Switzerland: Springer International Publishers, 2016, pp. 648–652.
- [9] Fogler, H. S. *Elements of chemical reaction engineering*. eng. Prentice Hall International Series in the physical and chemical engineering sciences. Pearson Prentice Hall, 2015.
- [10] Giddings, D., Eastwick, C. N., Pickering, S. J. and Simmons, K. "Computational fluid dynamics applied to a cement precalciner". In: *Proceedings of the Institution of Mechanical Engineers, Part A: Journal of Power and Energy* 214.3 (2000), pp. 269–280.
- [11] Williams, A., Pourkashanian, M. and Jones, J. M. "Combustion of pulverised coal and biomass". In: *Progress in Energy and Combustion Science* 27.6 (2001), pp. 587–610.

- [12] Hasanbeigi, A., Arens, M. and Price, L. "Alternative emerging iron-making technologies for energy-efficiency and carbon dioxide emissions reduction: A technical review". In: *Renewable and Sustainable Energy Reviews* 33 (2014), pp. 645–658.
- [13] Steinfeld, A., Imhof, A. and Mischler, D. "Experimental Investigation of an Atmospheric-Open Cyclone Solar Reactor for Solid-Gas Thermochemical Reactions". In: *Journal of Solar Energy Engineering* 114.3 (1992), pp. 171–174.
- [14] Ho, C. K. "A review of high-temperature particle receivers for concentrating solar power". In: *Special Issue: Solar Energy Research Institute for India and the United States (SERIUS) – Concentrated Solar Power* 109 (2016), pp. 958–969.
- [15] Frankel, A., Pouransari, H., Coletti, F. and Mani, A. "Settling of heated particles in homogeneous turbulence". In: *Journal of Fluid Mechanics* 792 (2016), pp. 869–893.
- [16] Elgobashi, S. "An Updated Classification Map of Particle-Laden Turbulent Flows". In: *IUTAM Symposium on Computational Approaches to Multiphase Flow: Proceedings of an IUTAM Symposium held at Argonne National Laboratory, October 4–7, 2004*. Ed. by S. Balachandar and A. Prosperetti. Dordrecht: Springer Netherlands, 2006, pp. 3–10.
- [17] Nathan, G. J., Kalt, P. A. M., Alwahabi, Z. T., Dally, B. B., Medwell, P. R. and Chan, Q. N. "Recent advances in the measurement of strongly radiating, turbulent reacting flows". In: *Progress in Energy and Combustion Science* 38.1 (2011).
- [18] Davis, D., Muller, F., Saw, W., Steinfeld, A. and Nathan, G. "Solar-driven alumina calcination for CO₂ mitigation and improved product quality". In: *Green Chem.* 19.13 (2017), pp. 2992–3005.
- [19] Ho, C. K et al. "Highlights of the high-temperature falling particle receiver project: 2012 - 2016". eng. In: *AIP conference proceedings*. Vol. 1850. 1. 2017.
- [20] Zamansky, R., Coletti, F., Massot, M. and Mani, A. "Radiation induces turbulence in particle-laden fluids". In: *Physics of Fluids* 26.7 (2014), p. 071701.
- [21] Evans, G., Houf, W., Greif, R. and Crowe, C. "Gas-Particle Flow Within a High Temperature Solar Cavity Receiver Including Radiation Heat Transfer". In: *Journal of Solar Energy Engineering* 109.2 (1987), pp. 134–142.

- [22] Chen, H., Chen, Y., Hsieh, H.-T. and Siegel, N. "Computational Fluid Dynamics Modeling of Gas-Particle Flow Within a Solid-Particle Solar Receiver". In: *Journal of Solar Energy Engineering* 129.2 (2006), pp. 160–170.
- [23] Pouransari, H. and Mani, A. "Effects of Preferential Concentration on Heat Transfer in Particle-Based Solar Receivers". In: *Journal of Solar Energy Engineering* 139.2 (2016), pp. 021008–021008–11.
- [24] Fond, B., Abram, C., Heyes, A. L., Kempf, A. M. and Beyrau, F. "Simultaneous temperature, mixture fraction and velocity imaging in turbulent flows using thermographic phosphor tracer particles". In: *Optics Express* 20.20 (2012), pp. 22118–22133.
- [25] Kueh, K. C. Y., Lau, T. C. W., Nathan, G. J. and Alwahabi, Z. T. "Non-intrusive temperature measurement of particles in a fluidised bed heated by well-characterised radiation". In: *International Journal of Multiphase Flow* 100 (2018), pp. 186–195.
- [26] Eckbreth, A. C. *Laser diagnostics for combustion temperature and species*. 2nd ed. Combustion science and technology book series ; v. 3. Amsterdam: Gordon and Breach, 1996.
- [27] Kohse-Höinghaus, K. and Jeffries, J. B. *Applied combustion diagnostics*. Combustion, an international series. New York ; Taylor & Francis, 2002.
- [28] Kueh, K. C. Y., Lau, T. C. W., Nathan, G. J. and Alwahabi, Z. T. "Single-shot planar temperature imaging of radiatively heated fluidized particles". In: *Optics Express* 25.23 (2017), pp. 28764–28775.
- [29] Miller, F. and Koenigsdorff, R. "Theoretical analysis of a high-temperature small-particle solar receiver". In: *Solar Energy Materials* 24.1 (1991), pp. 210–221.
- [30] Siegel, N., Ho, C., Khalsa, S. S. and Kolb, G. "Development and Evaluation of a Prototype Solid Particle Receiver: On-Sun Testing and Model Validation". In: *Journal Of Solar Energy Engineering-Transactions Of The Asme* 132.2 (2010).
- [31] Banko, A. J., Villafañe, L., Kim, J. H. and Eaton, J. K. "Temperature statistics in a radiatively heated particle-laden turbulent square duct flow". In: *International Journal of Heat and Fluid Flow* 84 (2020), p. 108618.

- [32] Lewis, E. W., Lau, T. C. W., Sun, Z., Alwahabi, Z. T. and Nathan, G. J. "Luminescence interference to two-colour toluene laser-induced fluorescence thermometry in a particle-laden flow". In: *Experiments in Fluids* 61.4 (2020), p. 101.
- [33] Lewis, E. W., Lau, T. C. W., Sun, Z., Alwahabi, Z. T. and Nathan, G. J. "Insights from a new method providing single-shot, planar measurement of gas-phase temperature in particle-laden flows under high-flux radiation". In: *Experiments in Fluids* 62.4 (2021), p. 80.
- [34] Lewis, E. W., Lau, T. C., Sun, Z., Alwahabi, Z. T. and Nathan, G. J. "The effect of particle size and volumetric loading on the gas temperature distributions in a particle-laden flow heated with high-flux radiation". In: *International Journal of Heat and Mass Transfer* 182 (2022), p. 122041.
- [35] Lewis, E. W., Lau, T. C. W., Sun, Z., Alwahabi, Z. T. and Nathan, G. J. "The effect of instantaneous particle distributions on the gas-phase temperature in an unsteady particle-laden jet heated with high-flux radiation". In: *Submitted to Physics of Fluids* (2021).
- [36] Klotz, B. "New developments in precalciners and preheaters". In: *1997 IEEE/PCA Cement Industry Technical Conference. XXXIX Conference Record (Cat. No.97CH36076)*. 1997, pp. 255–280.
- [37] Modarress, D., Tan, H. and Elghobashi, S. "Two-component LDA measurement in a two-phase turbulent jet". In: *AIAA Journal* 22.5 (1984), pp. 624–630.
- [38] Modarress, D., Wuerer, J. and Elghobashi, S. "An experimental study of a turbulent round two-phase jet". In: *Chemical Engineering Communications* 28.4-6 (1984), pp. 341–354.
- [39] Tsuji, Y., Morikawa, Y., Tanaka, T., Karimine, K. and Nishida, S. "Measurement of an axisymmetric jet laden with coarse particles". In: *International Journal of Multiphase Flow* 14.5 (1988), pp. 565–574.
- [40] Hardalupas, Y., Taylor, A. M. K. P. and Whitelaw, J. H. "Velocity and Particle-Flux Characteristics of Turbulent Particle-Laden Jets". In: *Proceedings of the Royal Society of London. Series A, Mathematical and Physical Sciences* 426.1870 (1989), pp. 31–78.
- [41] Mostafa, A. A., Mongia, H. C., McDonnell, V. G. and Samuelsen, G. S. "Evolution of particle-laden jet flows - A theoretical and experimental study". In: *AIAA Journal* 27.2 (1989), pp. 167–183.
- [42] Longmire, E. K. and Eaton, J. K. "Structure of a particle-laden round jet". In: *Journal of Fluid Mechanics* 236 (1992), pp. 217–257.

- [43] Gillandt, I., Fritsching, U. and Bauckhage, K. "Measurement of phase interaction in dispersed gas/particle two-phase flow". In: *International Journal of Multiphase Flow* 27.8 (2001), pp. 1313–1332.
- [44] Lau, T. C. W. and Nathan, G. J. "The effect of Stokes number on particle velocity and concentration distributions in a well-characterised, turbulent, co-flowing two-phase jet". In: *Journal of Fluid Mechanics* 809 (2016), pp. 72–110.
- [45] Lau, T. C. W., Frank, J. H. and Nathan, G. J. "Resolving the three-dimensional structure of particles that are aerodynamically clustered by a turbulent flow". In: *Physics of Fluids* 31.7 (2019), p. 071702.
- [46] Evans, M. J. and Medwell, P. R. "Understanding and Interpreting Laser Diagnostics in Flames: A Review of Experimental Measurement Techniques". In: 5.65 (2019).
- [47] Nieuwstadt, F. T. M., Westerweel, J. and Boersma, B. J. *Turbulence: Introduction to Theory and Applications of Turbulent Flows*. 1st ed. 2016. Cham: Springer International Publishing, 2016.
- [48] Gore, R. A. and Crowe, C. T. "Effect of particle size on modulating turbulent intensity". In: *International Journal of Multiphase Flow* 15.2 (1989), pp. 279–285.
- [49] Bagchi, P. and Balachandar, S. "Response of the wake of an isolated particle to an isotropic turbulent flow". In: *Journal of Fluid Mechanics* 518 (2004), pp. 95–123.
- [50] Kulick, J. D., Fessler, J. R. and Eaton, J. K. "Particle response and turbulence modification in fully developed channel flow". In: *Journal of Fluid Mechanics* 277 (1994), pp. 109–134.
- [51] Kussin, J. and Sommerfeld, M. "Experimental studies on particle behaviour and turbulence modification in horizontal channel flow with different wall roughness". In: *Experiments in Fluids* 33.1 (2002), pp. 143–159.
- [52] Mittal, R. "Response of the Sphere Wake to Freestream Fluctuations". In: *Theoretical and Computational Fluid Dynamics* 13.6 (2000), pp. 397–419.
- [53] Eaton, J. K. and Fessler, J. R. "Preferential concentration of particles by turbulence". In: *International Journal of Multiphase Flow* 20 (1994), pp. 169–209.

- [54] Fessler, J. R., Kulick, J. D. and Eaton, J. K. "Preferential concentration of heavy particles in a turbulent channel flow". In: *Physics of Fluids* 6.11 (1994), pp. 3742–3749.
- [55] Crowe, C. T., Chung, J. N. and Troutt, T. R. "Particle mixing in free shear flows". In: *Progress in Energy and Combustion Science* 14.3 (1988), pp. 171–194.
- [56] Monchaux, R., Bourgoïn, M. and Cartellier, A. "Analyzing preferential concentration and clustering of inertial particles in turbulence". In: *International Journal of Multiphase Flow* 40 (2012), pp. 1–18.
- [57] Lau, T. C. W. and Nathan, G. J. "Influence of Stokes number on the velocity and concentration distributions in particle-laden jets". In: *Journal of Fluid Mechanics* 757 (2014), pp. 432–457.
- [58] Zheng, F. "Thermophoresis of spherical and non-spherical particles: a review of theories and experiments". In: *Advances in Colloid and Interface Science* 97.1 (2002), pp. 255–278.
- [59] Grena, R. "Thermal simulation of a single particle in a falling-particle solar receiver". In: *Solar Energy* 83.8 (2009), pp. 1186–1199.
- [60] Kalt, P. A. M., Birzer, C. H. and Nathan, G. J. "Corrections to facilitate planar imaging of particle concentration in particle-laden flows using Mie scattering, Part 1: Collimated laser sheets". In: *Applied Optics* 46.23 (2007), pp. 5823–5834.
- [61] González-Portillo, L. F., Abbas, R., Albrecht, K. and Ho, C. "Analysis of optical properties in particle curtains". In: *Solar Energy* 213 (2021), pp. 211–224.
- [62] Anoop, K. B., Sundararajan, T. and Das, S. K. "Effect of particle size on the convective heat transfer in nanofluid in the developing region". In: *International Journal of Heat and Mass Transfer* 52.9 (2009), pp. 2189–2195.
- [63] Bertocchi, R., Karni, J. and Kribus, A. "Experimental evaluation of a non-isothermal high temperature solar particle receiver". In: *Energy* 29.5 (2004), pp. 687–700.
- [64] Meier, A., Bonaldi, E., Cella, G. M., Lipinski, W. and Wuillemin, D. "Solar chemical reactor technology for industrial production of lime". In: *Solar Energy* 80.10 (2006), pp. 1355–1362.
- [65] Monazam, E. R. and Maloney, D. J. "Temperature transients associated with pulsed heating of single particles". In: *Journal of Applied Physics* 71.6 (1992), pp. 2552–2559.

- [66] Nikulshina, V., Halmann, M. and Steinfeld, A. "Coproduct of Syn-gas and Lime by Combined CaCO₃-Calcination and CH₄-Reforming Using a Particle-Flow Reactor Driven by Concentrated Solar Radiation". In: *Energy & Fuels* 23.12 (2009), pp. 6207–6212.
- [67] Spjut, R. E., Sarofim, A. F. and Longwell, J. P. "Laser heating and particle temperature measurement in an electrodynamic balance". In: *Langmuir* 1.3 (1985), pp. 355–360.
- [68] Rahmani, M., Geraci, G., Iaccarino, G. and Mani, A. "Effects of particle polydispersity on radiative heat transfer in particle-laden turbulent flows". In: *International Journal of Multiphase Flow* 104 (2018), pp. 42–59.
- [69] van Eyk, P. J., Ashman, P. J. and Nathan, G. J. "Effect of High-Flux Solar Irradiation on the Gasification of Coal in a Hybrid Entrained-Flow Reactor". In: *Energy & Fuels* 30.6 (2016), pp. 5138–5147.
- [70] Bohren, C. F. and Huffman, D. R. *Absorption and scattering of light by small particles*. eng. Weinheim, Germany: Wiley-VCH Verlag GmbH and Co. KGaA, 2004 - 2004.
- [71] Väisänen, T., Martikainen, J. and Muinonen, K. "Scattering of light by dense particulate media in the geometric optics regime". In: *Journal of Quantitative Spectroscopy and Radiative Transfer* 241 (2020), p. 106719.
- [72] Miles, R. B., Lempert, W. R. and Forkey, J. N. "Laser Rayleigh scattering". In: *Measurement Science and Technology* 12.5 (2001), R33–R51.
- [73] Sutton, J. A. and Driscoll, J. F. "Rayleigh scattering cross sections of combustion species at 266, 355, and 532 nm for thermometry applications". In: *Optics Letters* 29.22 (2004), pp. 2620–2622.
- [74] Hruby, J., Steeper, R., Evans, G. and Crowe, C. "An Experimental and Numerical Study of Flow and Convective Heat Transfer in a Freely Falling Curtain of Particles". In: *Journal of Fluids Engineering* 110.2 (1988), pp. 172–181.
- [75] Tobiasson, J. R., Egbert, S. C., Adams, B. R. and Tree, D. R. "An optical method for the measurement of combustion gas temperature in particle laden flows". In: *Experimental Thermal and Fluid Science* 98 (2018), pp. 704–711.
- [76] Ma, L., Ning, H., Wu, J., Cheong, K.-P. and Ren, W. "Characterization of Temperature and Soot Volume Fraction in Laminar Premixed Flames: Laser Absorption/Extinction Measurement and Two-Dimensional Computational Fluid Dynamics Modeling". In: *Energy & Fuels* 32.12 (2018), pp. 12962–12970.

- [77] Lakowicz, J. *Principles of Fluorescence Spectroscopy*. 3rd ed. New York: Springer, 2006.
- [78] Bohlin, A. and Kliever, C. J. "Communication: Two-dimensional gas-phase coherent anti-Stokes Raman spectroscopy (2D-CARS): Simultaneous planar imaging and multiplex spectroscopy in a single laser shot". In: *The Journal of Chemical Physics* 138.22 (2013), p. 221101.
- [79] Miller, J. D., Slipchenko, M. N., Mance, J. G., Roy, S. and Gord, J. R. "1-kHz two-dimensional coherent anti-Stokes Raman scattering (2D-CARS) for gas-phase thermometry". In: *Optics Express* 24.22 (2016), pp. 24971–24979.
- [80] Roy, S., Gord, J. R. and Patnaik, A. K. "Recent advances in coherent anti-Stokes Raman scattering spectroscopy: Fundamental developments and applications in reacting flows". In: *Progress in Energy and Combustion Science* 36.2 (2010), pp. 280–306.
- [81] Eichler, H. J., Günter, P. and Pohl, D. W. *Laser-Induced Dynamic Gratings*. 1st ed. 1986. Springer Series in Optical Sciences, 50. Berlin, Heidelberg: Springer Berlin Heidelberg, 1986.
- [82] Kiefer, J. and Ewart, P. "Laser diagnostics and minor species detection in combustion using resonant four-wave mixing". In: *Progress in Energy and Combustion Science* 37.5 (2011), pp. 525–564.
- [83] Ewart, P. and Kaczmarek, M. "Two-dimensional mapping of temperature in a flame by degenerate four-wave mixing in OH". In: *Applied Optics* 30.27 (1991), pp. 3996–3999.
- [84] Ehn, A., Zhu, J., Li, X. and Kiefer, J. "Advanced Laser-Based Techniques for Gas-Phase Diagnostics in Combustion and Aerospace Engineering". In: *Applied Spectroscopy* 71.3 (2017), pp. 341–366.
- [85] Schulz, C. and Sick, V. "Tracer-LIF diagnostics: quantitative measurement of fuel concentration, temperature and fuel/air ratio in practical combustion systems". In: *Progress in Energy and Combustion Science* 31.1 (2005), pp. 75–121.
- [86] Medwell, P. R., Masri, A. R., Pham, P. X., Dally, B. B. and Nathan, G. J. "Temperature imaging of turbulent dilute spray flames using two-line atomic fluorescence". In: *Experiments in Fluids* 55.11 (2014), p. 1840.
- [87] KRONEMAYER, H, BESSLER, W. G and SCHULZ, C. "Gas-phase temperature imaging in spray systems using multi-line NO-LIF thermometry". eng. In: *Applied physics. B, Lasers and optics* 81.8 (2005), pp. 1071–1074.

- [88] Koban, W., Koch, J. D., Hanson, R. K. and Schulz, C. "Absorption and fluorescence of toluene vapor at elevated temperatures". In: *Physical Chemistry Chemical Physics* 6.11 (2004), pp. 2940–2945.
- [89] Luong, M., Koban, W. and Schulz, C. "Novel strategies for imaging temperature distribution using Toluene LIF". In: *Journal of Physics: Conference Series* 45.1 (2006), p. 133.
- [90] Aldén, M., Omrane, A., Richter, M. and Särner, G. "Thermographic phosphors for thermometry: A survey of combustion applications". In: *Progress in Energy and Combustion Science* 37.4 (2011), pp. 422–461.
- [91] Abram, C., Fond, B. and Beyrau, F. "Temperature measurement techniques for gas and liquid flows using thermographic phosphor tracer particles". In: *Progress in Energy and Combustion Science* 64 (2017), pp. 93–156.
- [92] Luong, M., Zhang, R., Schulz, C. and Sick, V. "Toluene laser-induced fluorescence for in-cylinder temperature imaging in internal combustion engines". In: *Applied Physics B* 91.3 (2008), p. 669.
- [93] Cundy, M., Trunk, P., Dreizler, A. and Sick, V. "Gas-phase toluene LIF temperature imaging near surfaces at 10 kHz". In: *Experiments in Fluids* 51.5 (2011), pp. 1169–1176.
- [94] Faust, S., Goschütz, M., Kaiser, S. A., Dreier, T. and Schulz, C. "A comparison of selected organic tracers for quantitative scalar imaging in the gas phase via laser-induced fluorescence". In: *Applied Physics B* 117.1 (2014), pp. 183–194.
- [95] Tran, K. H., Guibert, P., Morin, C., Bonnet, J., Pounkin, S. and Legros, G. "Temperature measurements in a rapid compression machine using anisole planar laser-induced fluorescence". In: *Combustion and Flame* 162.10 (2015), pp. 3960–3970.
- [96] Attar, M. A., Zhao, H., Herfatmanesh, M. R. and Cairns, A. "Turbulent flame boundary and structure detection in an optical DISI engine using tracer-based two-line PLIF technique". In: *Experimental Thermal and Fluid Science* 68 (2015), pp. 545–558.
- [97] Wang, Q., Zhang, Y., Jiang, L., Zhao, D., Guibert, P. and Yang, S. "Fluorescence and absorption characteristics of p-xylene: applicability for temperature measurements". In: *Applied Physics B* 123.9 (2017), p. 242.

- [98] Peterson, B., Baum, E., Böhm, B., Sick, V. and Dreizler, A. "Evaluation of toluene LIF thermometry detection strategies applied in an internal combustion engine". In: *Applied Physics B* 117.1 (2014), pp. 151–175.
- [99] Yoo, J., Mitchell, D., Davidson, D. F. and Hanson, R. K. "Near-wall imaging using toluene-based planar laser-induced fluorescence in shock tube flow". In: *Shock Waves* 21.6 (2011), p. 523.
- [100] Jainski, C., Lu, L., Sick, V. and Dreizler, A. "Laser imaging investigation of transient heat transfer processes in turbulent nitrogen jets impinging on a heated wall". In: *International Journal of Heat and Mass Transfer* 74.Supplement C (2014), pp. 101–112.
- [101] Yu, Y. "Theoretical modelling and experimental investigation of the performance of screw feeders". Thesis. 1997.
- [102] Rodnyi, P. and Khodyuk, I. "Optical and luminescence properties of zinc oxide (Review)". In: *Optics and Spectroscopy* 111.5 (2011), pp. 776–785.
- [103] Siegel, N., Gross, M., Ho, C., Phan, T. and Yuan, J. "Physical Properties of Solid Particle Thermal Energy Storage Media for Concentrating Solar Power Applications". In: *Energy Procedia* 49 (2014), pp. 1015–1023.
- [104] Miller, V. A., Gamba, M., Mungal, M. G. and Hanson, R. K. "Single- and dual-band collection toluene PLIF thermometry in supersonic flows". In: *Experiments in Fluids* 54.6 (2013), p. 1539.
- [105] Burton, C. S. and Noyes, W. A. "Electronic Energy Relaxation in Toluene Vapor". In: *The Journal of Chemical Physics* 49.4 (1968), pp. 1705–1714.
- [106] Koban, W., Koch, J. D., Hanson, R. K. and Schulz, C. "Oxygen quenching of toluene fluorescence at elevated temperatures". In: *Applied Physics B* 80.6 (2005), pp. 777–784.
- [107] Faust, S., Tea, G., Dreier, T. and Schulz, C. "Temperature, pressure, and bath gas composition dependence of fluorescence spectra and fluorescence lifetimes of toluene and naphthalene". In: *Applied physics. B, Lasers and optics* 110.1 (2013), pp. 81–93.
- [108] Yaws, C. L. *Handbook of vapor pressure*. v. 4: Library of physico-chemical property data. Houston: Gulf Pub. Co., 1994.
- [109] Fuhrmann, D. et al. "Self-quenching in toluene LIF". In: *Proceedings of the Combustion Institute* 36.3 (2017), pp. 4505–4514.

- [110] Alwahabi, Z. T., Kueh, K. C. Y., Nathan, G. J. and Cannon, S. "Novel solid-state solar thermal simulator supplying 30,000 suns by a fibre optical probe". In: *Optics Express* 24.22 (2016), A1444–A1453.
- [111] Siegel, N., Gross, M. and Coury, R. "The Development of Direct Absorption and Storage Media for Falling Particle Solar Central Receivers". In: *Journal of Solar Energy Engineering* 137 (2015), p. 041003.
- [112] Incropera, F., Dewitt, D., Bergman, T. and Lavine, A. *Fundamentals of heat and mass transfer*. 6th ed. Wiley, 2007.
- [113] Lau, T. C. W. and Nathan, G. J. "A method for identifying and characterising particle clusters in a two-phase turbulent jet". In: *International Journal of Multiphase Flow* 88 (2017), pp. 191–204.
- [114] Monchaux, R., Bourgoïn, M. and Cartellier, A. "Preferential concentration of heavy particles: A Voronoï analysis". In: *Physics of Fluids* 22.10 (2010), p. 103304.
- [115] Ferenc, J.-S. and Néda, Z. "On the size distribution of Poisson Voronoi cells". In: *Physica A: Statistical Mechanics and its Applications* 385.2 (2007), pp. 518–526.
- [116] Abram, C., Fond, B. and Beyrau, F. "High-precision flow temperature imaging using ZnO thermographic phosphor tracer particles". In: *Optics Express* 23.15 (2015), pp. 19453–19468.
- [117] Mi, J., Nobes, D. S. and Nathan, G. J. "Influence of jet exit conditions on the passive scalar field of an axisymmetric free jet". In: *Journal of Fluid Mechanics* 432 (2001), pp. 91–125.
- [118] Papadopoulos, G. and Pitts, W. M. "Scaling the Near-Field Centerline Mixing Behavior of Axisymmetric Turbulent Jets". In: *AIAA Journal* 36.9 (1998), pp. 1635–1642.
- [119] Schefer, R. W. and Dibble, R. W. "Mixture Fraction Field in a Turbulent Nonreacting Propane Jet". In: *AIAA Journal* 39.1 (2001), p. 64.
- [120] Munson, B., Young, D., Okiishi, T. and Huebsch, W. *Fundamentals of fluid mechanics*. 6th ed. Hoboken, N.J.: Wiley, 2010.
- [121] Uematu, T. and Nakamura, S. "A Study of the Screw Conveyor". In: *Bulletin of JSME* 3.12 (1960), pp. 449–455.
- [122] Carleton, A. J., Miles, J. E. P. and Valentin, F. H. H. "A Study of Factors Affecting the Performance of Screw Conveyers and Feeders". In: *Journal of Engineering for Industry* 91.2 (1969), pp. 329–333.